Fat Suppression in Magnetic Resonance Imaging Near Metal Implants

Laura Jane King

A thesis presented for the degree of
Doctor of Philosophy
in
Electrical and Computer Engineering
at the
University of Canterbury
Christchurch, New Zealand

August 22, 2017

Abstract

Magnetic resonance imaging (MRI) is one of the most outstanding developments in medical diagnosis in recent decades. It is used in a wide range of clinical imaging applications, and is particularly effective for producing high quality images of soft tissues. It should therefore be well-suited to evaluating complications arising in patients with orthopaedic metal implants which are considered safe for MRI scanning. However, the presence of the metal produces large variations in the magnetic field, and the resulting images have significant artifacts.

Performing accurate fat suppression near metal implants remains an unsolved challenge in MRI. The ability to use multipoint fat suppression techniques close to metal would be greatly beneficial, as it would allow for easier diagnosis of certain soft tissue complications through contrast-enhanced imaging. To succeed, multipoint techniques require a robust and accurate method for estimating the magnetic field variation induced by the metal. Existing methods tend to fail near the boundary of the metal where the field is rapidly varying.

This thesis explores new methods for estimating the phase shift due to the magnetic field variation in the three-point Dixon technique near metal. The problem of phase unwrapping in regions where the phase varies rapidly is investigated. Magnetic field variation simulations are used throughout for developing and assessing these new methods.

The most significant contribution presented is the development and evaluation of the *Phase Onion Peeling (POP)* algorithm. POP is a novel approach to phase estimation in the three-point Dixon technique. POP estimates the phase across a two-dimensional slice using a set of closed paths which enclose the implant boundary. The phase is first estimated at the outer edges of the slice. The method incrementally works inwards along a set of adjacent paths, finishing at the boundary of the implant. The phase along each path is represented by a Fourier series, and the coefficients for each path are estimated by minimising an objective function. The main advantage of POP over existing techniques is that the phase unwrapping problem is converted to one of parameter estimation. POP was tested on data acquired from three phantoms and seven human participants, with results presented and evaluated. POP is shown to have superior performance compared to existing phase unwrapping methods

and better or comparable performance to the IDEAL reconstruction method.

This thesis also presents a number of other contributions: a detailed assessment of the performance of existing phase unwrapping methods in the vicinity of metal; an analysis of existing iterative techniques in regions of rapid magnetic field variation; a proposed extension to POP to use a different objective function form; an exploration into using POP in conjunction with the matching pursuit algorithm; and a description of three phase estimation methods developed before POP.

Acknowledgements

Ehara taku toa i te toa takitahi,
engari he toa takitini.

There are many people I need to thank for offering me wisdom, support, encouragement, and love over the course of my thesis.

To my supervisors, Phil Bones and Rick Millane. For the unwavering support and positivity; for the astute observations and robust discussions; for the advice on writing, constructing mathematical arguments, and the craft of research - thank you.

Many people and organisations provided practical support and guidance for my research. To Brian Hargreaves and the Body MRI group at Stanford University, for your generous assistance with collecting data and advice on getting my project off the ground. Thank you for letting me pick your brains. To Julian and Jana Maclaren, for kindly hosting me in your garage. To Tracy Melzer, Mustafa Almuqbel, and the staff at Hagley Radiology, for all your time and patience with helping me collect data. Thank you for answering all my questions about MRI. To Gary Hooper and staff at the Department of Orthopaedic Surgery and Musculoskeletal Medicine, especially Jen Dunn, Debbie Snell, and Lyn Jefferies. Thank you for going out of your way to help me with the ethics approval process, recruiting participants, and giving advice on the clinical aspects of my research. To UC and the NZOA, thank you for the financial support.

I am hugely grateful to the ECE department for providing a truly collegial environment to learn and thrive in. I will miss the Cake Club, the Staff Club beers, and the banter and good humour. To Richard Lane, Michael Hayes, Philippa Martin, and Mike Shurety - thank you for the nuggets of wisdom and moments of silliness, right when I needed them. To the "Postgrad Social Club", for all the morning teas, afternoon teas, and Tandoori lunches. In between the eating and drinking we worked our way through all the problems, and figured out how to "do research". To Blair, for always being a listening ear over a beer - the very definition of a Postgrad Rep.

To my flatmates, Matt, Rory, and Tristan (and Yanosh, of course) - for all the late night discussions on politics, feminism, and cooking. To the tramping club - for the many trips, TWALK, and being an endless source of procrastination. To all my friends and family - for the countless cups of tea, outdoor adventures, hugs and laughter, and for being on belay. To Yanosh - for everything. Thank you for all your love. Without you, this would have been impossible. Aroha nui.

Deputy Vice-Chancellor's Office
Postgraduate Office

UNIVERSITY OF CANTERBURY
Te Whare Wānanga o Waitaha
CHRISTCHURCH NEW ZEALAND

Co-Authorship Form

This form is to accompany the submission of any thesis that contains research reported in co-authored work that has been published, accepted for publication, or submitted for publication. A copy of this form should be included for each co-authored work that is included in the thesis. Completed forms should be included at the front (after the thesis abstract) of each copy of the thesis submitted for examination and library deposit.

Publication 1: *L.J. King, R.P. Millane, H. Weber, B.A. Hargreaves, P.J. Bones: "Path-based phase estimation for fat suppression near metal implants" in Proceedings of the 24th Meeting of the ISMRM, Singapore, 2016.*

Components of thesis extracted from Publication 1:

Chapter 5, particularly sections 5.3-5.5.

Chapter 6, particularly sections 6.1 and 6.3.

Chapter 7, particularly section 7.1.

Publication 2: *P.J. Bones, L.J. King, R.P. Millane: "Phase estimation for magnetic resonance imaging near metal prostheses" in Proceedings of the SPIE 9600, Image Reconstruction from Incomplete Data VIII, San Diego, 2015.*

Components of thesis extracted from Publication 2:

Chapter 3, particularly section 3.3.

Chapter 4, particularly section 4.1.

Appendix A, particularly sections A.1 and A.2.

Publication 3: *L.J. King, R.P. Millane, P.J. Bones: "Phase unwrapping near metal implants with prior knowledge of the implant geometry" in Proceedings of the 23rd Meeting of the ISMRM, Toronto, 2015.*

Components of thesis extracted from Publication 3:

Chapter 5, particularly section 5.2.

Appendix A, particularly section A.2.

Please detail the nature and extent (%) of contribution by the candidate:

Publication 1:

Method developed through discussions with P.J. Bones and R.P. Millane. Data collected with assistance from H. Weber and B.A. Hargreaves. Results produced by candidate. Written content and figures produced by candidate. All co-authors provided comments and review.

Publication 2:

Content mostly extracted from candidate's mid-term report and compiled and written by P.J. Bones (lead author). Figures produced by candidate. All co-authors provided comments and review.

Publication 3:

Method developed largely by candidate with guidance and review from co-authors. Written content and figures produced by candidate.

Certification by Co-authors:

If there is more than one co-author then a single co-author can sign on behalf of all

The undersigned certifies that:

- The above statement correctly reflects the nature and extent of the PhD candidate's contribution to this co-authored work
- In cases where the candidate was the lead author of the co-authored work he or she wrote the text

Name: *Philip J. Bones* Signature:  Date: *22 Feb 2017*

Contents

Abbreviations

Abbreviations used in this thesis are listed here for easy reference.

2D	two-dimensional
3D	three-dimensional
BW	bandwidth
CT	computed tomography
DCT	discrete cosine transform
DFT	discrete Fourier transform
FFT	fast Fourier transform
FOV	field of view
FSE	fast spin echo
GE	General Electric (Healthcare)
IDEAL	iterative decomposition of water and fat with echo asymmetry and least squares estimation
ISMRM	International Society for Magnetic Resonance in Medicine
MAVRIC	multi-acquisition variable-resonance image combination
MR	magnetic resonance
MRI	magnetic resonance imaging
MSE	mean square error
MSI	multispectral imaging
POP	phase onion peeling
RF	radio frequency
SEMAC	slice encoding for metal artifact correction
SNR	signal-to-noise ratio
SPI	single point imaging
STIR	short tau (inversion time) inversion recovery
STL	stereolithographic (file)
TE	echo time
TI	inversion time
TR	repetition time
VARPRO	variable projection (least squares)
VAT	view angle tilting

1

Introduction

This chapter contains three sections: an overview of the research and its objectives; a summary of the major contributions; and a guide to the structure of this thesis. A list of publications is included.

1.1 OVERVIEW AND OBJECTIVES

Metal implants are commonly used in orthopaedic surgery to treat a wide range of conditions, from fractures to osteoarthritis. Patients with orthopaedic implants may suffer from complications such as inflammation, bone loss, and fracture. Medical imaging is necessary for evaluating these complications, as they do not usually produce characteristic symptoms. X-ray and CT are both used clinically, but perform poorly in identifying soft tissue complications. Magnetic resonance imaging (MRI) has potential to be the best technique for assessing complications arising from MRI safe implants, as it produces images with excellent soft tissue contrast. Also, unlike X-ray and CT, it requires no ionising radiation.

Acquiring high quality magnetic resonance (MR) images of patients with metal implants is challenging. First, the presence of many types of metal in the scanner can be unsafe. This thesis only considers passive metal implants which are classified as safe for MR imaging, although these implants still severely disrupt the imaging process. The presence of the metal produces large variations in the magnetic field. The resulting images have significant artifacts, including signal loss and pile-up, distortion of the imaged anatomy, and failure of fat suppression. By carefully selecting the imaging sequence and parameters, the artifacts can be reduced to some extent. Several advanced imaging techniques which produce images near metal with few artifacts and good contrast have been developed and are becoming clinically available worldwide. These include three-dimensional (3D) multispectral imaging techniques such as MAVRIC and SEMAC. However, existing techniques for fat suppression perform inadequately near metal.

Fat suppression is an important technique used frequently in MRI

to produce images which contain no contribution from the fat tissue. Fat tends to appear brighter than fluid in many MR imaging sequences, and can prevent the visualisation of fluid-based abnormalities. Near metal, the presence of fat interferes with the detection of certain complications such as pseudotumours. Being able to perform robust fat suppression near the boundary of metal implants would enable a more accurate diagnosis of these complications.

Three main approaches are used for fat suppression: fat saturation, inversion recovery, and multipoint techniques. Near metal, fat saturation fails due to the large magnetic field variation. Inversion recovery methods can successfully suppress fat near metal, but the images have a low signal-to-noise ratio. Also, inversion recovery can only be used in some imaging applications as interpretation of the images can be ambiguous. In particular, it cannot be used reliably in conjunction with contrast-enhanced imaging. Multipoint fat suppression techniques, such as the three-point Dixon method and IDEAL, have potential. However, for these techniques to succeed, the magnetic field variation induced by the metal must be correctly estimated. Existing methods generally assume that the field is slowly varying.

The aim of the research presented here is to contribute to a better understanding of how multipoint fat suppression techniques near metal might be improved. The main focus of this thesis is to investigate new methods for estimating the magnetic field variation in the three-point Dixon technique. The development, testing, and evaluation of the new algorithms is described. In particular, the algorithms have an emphasis on using prior knowledge of the magnetic field variation to guide the estimation.

The main algorithm developed in this thesis is the *Phase Onion Peeling (POP)* algorithm. Extensions to POP and early algorithms developed before POP are also described. A major focus of these algorithms has been on achieving a more accurate estimate of the rapidly varying magnetic field near the implant boundary, where existing algorithms tend to fail. The algorithms take advantage of the fact that the magnetic field variation induced by the implant can be predicted and incorporated using a model-based approach.

1.2 THESIS CONTRIBUTIONS

The most significant contribution to the field made by this thesis is the *Phase Onion Peeling (POP)* algorithm. POP adopts a new approach to estimating the phase shift, which is proportional to the magnetic field variation. It uses a set of one-dimensional (1D) paths which circumnavigate the implant. The phase along these paths is modelled using the Fourier series. The presented results demonstrate that this method is capable of accurately separating fat and water near metal implants in phantoms and participants. Other contributions include:

- THE DEVELOPMENT OF AN EFFICIENT METHOD to distribute a set of 1D paths over a two-dimensional (2D) slice which intersects one or more implants. The paths are calculated using distance transforms, and the spacing between the paths is adjustable.

- AN EVALUATION of the performance of existing branch cut and minimum-norm phase unwrapping algorithms near metal. Results are shown for both phantom and participant datasets, and the limitations of these algorithms are discussed in detail.

- THE EXTENSION OF POP to be used in conjunction with the VARPRO least squares method. It is shown that the basic POP algorithm can be extended to use a different objective function and achieve consistent results.

- AN INVESTIGATION INTO modelling the phase along the paths with an alternative basis to the Fourier series. A potential method for directly estimating the phase using a pre-determined model basis is described.

- THREE METHODS FOR USING an imperfect model of the phase shift to simplify the phase unwrapping are described. These comprise early research performed before POP was developed, but have provided numerous useful insights into the problem of phase unwrapping near metal.

- OTHER, MORE MINOR, contributions can be found throughout the thesis. These include the use of a white light scanner to acquire the stereolithographic geometry of two implants, and a simulated analysis of the performance of IDEAL in regions of rapid magnetic field variation. These are unlikely to be original contributions, but the approach taken may be unique. It is anticipated that the described practical developments, including the construction of the phantoms and the data acquisition and reconstruction process, will be of benefit to others in the future.

1.2.1 *Publications*

The following publications have resulted from this work, to date:

- P.J. Bones, L.J. King, R.P. Millane: "MR imaging near metal: the POP algorithm" in *Proceedings of the 31st International Conference on Image and Vision Computing New Zealand*, 2016 [Bones et al., 2016].

- L.J. King, R.P. Millane, H. Weber, B.A. Hargreaves, P.J. Bones: "Path-based phase estimation for fat suppression near metal implants" in *Proceedings of the 24th Meeting of the ISMRM*, Singapore, 2016 [King et al., 2016].

- P.J. Bones, L.J. King, R.P. Millane: "Phase estimation for magnetic resonance imaging near metal prostheses" in *Proceedings of*

the SPIE 9600, Image Reconstruction from Incomplete Data VIII, San Diego, 2015 [Bones et al., 2015].

- L.J. King, R.P. Millane, P.J. Bones: "Phase unwrapping near metal implants with prior knowledge of the implant geometry" in *Proceedings of the 23rd Meeting of the ISMRM*, Toronto, 2015 [King et al., 2015].
- L.J. King, R.P. Millane, P.J. Bones: "Phase unwrapping for magnetic resonance imaging near metal prostheses" in *Proceedings of the 29th International Conference on Image and Vision Computing New Zealand*, 2014 [King et al., 2014].

The work described in this thesis has also been presented in various forms:

- Poster presentation, "Path-based phase estimation for fat suppression near metal implants", 24th Meeting of the ISMRM, Singapore, 7-13 May 2016.
- Oral presentation, "Magnetic resonance imaging, fat suppression, and phase unwrapping", Departmental Seminar, Department of Electrical and Computer Engineering, University of Canterbury, 18 March 2016.
- Oral presentation, "Magnetic resonance imaging near metal implants", Christchurch MRI Mini-Symposium, 16 October 2015.
- Oral presentation, "Magnetic resonance imaging: the ultimate application of electrical engineering?", ENEL420 lecture, 10 August 2015.
- Poster presentation, "Phase unwrapping near metal implants with prior knowledge of the implant geometry", 23rd Meeting of the ISMRM, Toronto, 30 May - 5 June 2015.
- Oral presentation, "Phase unwrapping for magnetic resonance imaging near metal prostheses", Image and Vision Computing New Zealand, University of Waikato, Hamilton, New Zealand, 19-21 November 2014.
- Oral presentation, "Improved fat suppression in magnetic resonance imaging near metal implants", Departmental Seminar, Department of Electrical and Computer Engineering, University of Canterbury, 22 August 2014.
- Oral presentation, "Improved fat suppression in magnetic resonance imaging near metal implants", Centre for Bioengineering Mini-Conference, University of Otago, 2 July 2014.

1.3 THESIS STRUCTURE

This thesis is separated into two parts. The first part consists of three background chapters, and contains a review of the main literature used during this research. The second part presents the original contributions.

- CHAPTER 2 provides an overview of the issues with performing MR imaging of patients with metal implants. The clinical reasons for acquiring MR images near metal are outlined, and the mechanisms which produce artifacts near metal are described.

- CHAPTER 3 outlines the motivation for fat suppression and separation imaging sequences. The three standard techniques, fat saturation, inversion recovery, and multipoint or Dixon techniques, are summarised and compared in terms of suppressing fat near metal implants.

- CHAPTER 4 introduces phase unwrapping and the issues which make phase unwrapping a complicated problem to solve. It gives a summary of three main types of phase unwrapping algorithms: branch cut methods, minimum-norm methods, and model-based methods.

- THE FIRST CHAPTER IN Part II, Chapter 5, describes how phantom data were obtained and reconstructed, and outlines simulation work performed.

- CHAPTERS 6–8 present the POP method. Chapter 6 describes the theory and implementation of POP. Chapter 7 provides results from testing POP on three phantom datasets. Chapter 8 presents the results from testing POP on a cohort of participants with hip implants.

- CHAPTER 9 analyses the performance of existing iterative methods near metal. It describes an extension to use POP as an iterative method, and gives a brief set of results.

- CHAPTER 10 examines the performance of the set of basis functions used in POP, and describes an alternative approach using the matching pursuit algorithm.

- CHAPTER 11 provides a summary of the research presented in this thesis, and gives recommendations for future work. Finally, Appendix A presents three preliminary techniques which were initially developed to simplify phase unwrapping methods.

Part I

BACKGROUND

2

Magnetic Resonance Imaging Near Metal

This chapter introduces the problem of magnetic resonance imaging (MRI) near metal. The first section describes the clinical motivation for MR imaging of people with metal implants. A summary of how MR images are produced is given next, with a brief description of the history of medical imaging. The third section describes how metal induces artifacts in MRI, and summarises existing techniques used to mitigate these artifacts. The final section in this chapter gives an overview of modelling techniques which are used to understand metal-induced artifacts.

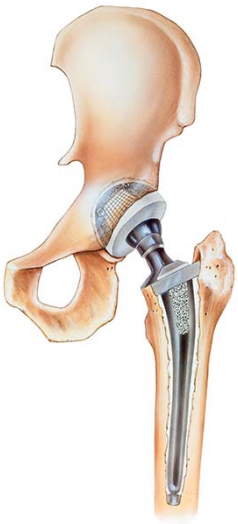

Figure 2.1: Drawing of a typical hip replacement.

Figure 2.2: Drawing of a typical knee replacement.

▶ Metal components are used in many orthopaedic applications. Pins, screws, and plates are commonly inserted in people to fix fractured joints in place. Total joint replacement surgery is used to improve the mobility and reduce the pain of people with chronic joint diseases. The majority of spinal fixations and hip, knee, and shoulder implants are made primarily of metal. Figures 2.1 and 2.2 show drawings of typical hip and knee implants.

This thesis is largely focused on imaging hip implants. The human hip is a ball-and-socket joint. The rounded upper end of the femur forms the ball, and is generally referred to as the femoral head. This sits inside a socket in the pelvis, called the acetabulum. During total hip replacement surgery, the bone in the joint is replaced with an implant. Modern hip implant designs differ in their geometry and size, but generally consist of the following components:

1. Femoral stem: this is embedded in the top of the femur. It may be fixed in place with bone cement.
2. Femoral head: this is a ball which sits on top of the femoral stem.
3. Acetabular shell: this replaces the acetabulum. It may be fixed to the pelvis with cement or screws.
4. Acetabular liner: this sits inside the acetabular shell.

Figure 2.3 shows a diagram of the main components.

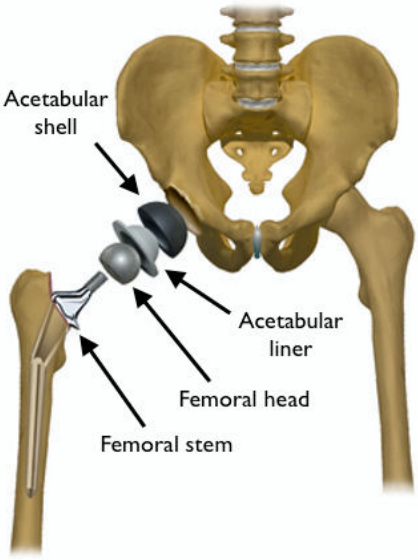

Figure 2.3: Exploded diagram showing the main components of a hip replacement, and how these components slot into the pelvis and femur.

The main tensile strength of a hip implant is most commonly formed by metal. The femoral stem and acetabular shell are often made of titanium or cobalt-chromium. The femoral head is usually metal or ceramic. The acetabular liner may be metal, ceramic, or polyethylene. Several combinations of the materials used for the head and liner are possible, such as ceramic-on-ceramic, metal-on-metal, and ceramic-on-polyethylene. In all cases the combination of materials enables smooth motion at the interface between the two components. This imitates the ball-and-socket motion in a normal hip.

Due to ageing of the population, the demand for total joint replacement surgeries is increasing. In the United States the rate of knee replacement surgeries almost tripled between 1990 and 2002, while the rate of hip replacements increased by 50 % [Kurtz et al., 2005]. In New Zealand, the National Joint Registry provides information on patients who undergo joint replacement. Between 1999 and 2012, the registry recorded a 158 % increase in knee replacements and a 75 % increase in hip replacements [Hooper, 2013].

On average, around 12 % of joint replacements need revision surgery ten years after the initial surgery [Labek et al., 2011]. This is necessary when a patient's joint replacement suffers from complications to the extent that the implant must be replaced. This rate is expected to increase as people are living for longer periods after the initial surgery. In the United States, it is predicted that between 2005 and 2030, revision rates will increase by 601 % for knee replacements and 137 % for hip replacements [Kurtz et al., 2007].

The most common complication is caused by long-term wear between the surfaces of the implant. Over time, particulate matter rubs off the surface, and makes its way into the surrounding tissue. This can cause chronic inflammation, which leads to the formation of os-

teoclasts. These are a type of bone cell which break down and absorb bone tissue. Normally, this is an important part of the continuous maintenance of bone, and occurs in proportion with bone formation. However, ongoing inflammation leads to osteolysis, which is when abnormally high osteoclast production occurs, and the existing bone deteriorates without replacement [Gallo et al., 2002]. Bone loss occurs, causing loosening of the implant and fracture in severe cases. Other complications that can arise from joint replacement include the production of inflammatory masses, dislocation, and torn tendons [White et al., 2000].

Apart from ongoing pain, osteolysis does not generally produce characteristic symptoms. Medical imaging is therefore important for diagnosing long-term complications, and is needed for assessing whether a patient needs revision surgery. Radiographic techniques such as X-ray are currently used routinely for imaging patients with metal implants. Computed tomography (CT) is also used to evaluate complications, but images suffer from beam-hardening artifacts [Stradiotti et al., 2009, Verburg and Seco, 2012]. All X-ray based methods offer poorer soft-tissue contrast than is possible with MRI.

Ultrasound provides several advantages for imaging complications near metal, as it is a relatively low cost modality and has no ionising radiation. It is recommended as an initial screening tool for identifying the presence of inflammatory masses [Garbuz et al., 2014]. As it is portable, ultrasound can also be used for guidance during medical procedures. However, repetitive reflection of the sound waves between the ultrasound transducer and the metal produces reverberation artifacts in the ultrasound images. This causes the metal to appear larger than it truly is, and also produces a characteristic "comet-tail" artifact. Overall, MRI may be a superior modality for evaluating the extent of complications, particularly in relation to the surrounding anatomy [Ostlere, 2011].

- MRI provides excellent soft tissue contrast, and so is potentially the best technique for evaluating most complications, especially the early symptoms of osteolysis [Toms et al., 2008, Heyse et al., 2012]. However, the presence of metal implants in the MRI scanner can be unsafe. Ferromagnetic objects experience a torque in the vicinity of the strong scanner magnetic field. This can cause the implanted objects to move or become dislodged, and loose objects can become dangerous projectiles. Certain implants, including electronically active devices such as pacemakers, may also experience induced currents which produce unsafe levels of heating [Shellock, 2002, McRobbie et al., 2006a].

  This thesis only focuses on passive metal orthopaedic implants which are classed as safe for MR imaging. These are made from materials such as titanium, cobalt-chromium, or non-ferrous stainless steel. However, despite the safety of these implants, the presence of the metal in the scanner can produce images with artifacts so severe that the images provide no useful information.

Some MRI applications involve imaging near a metal implant, but the desired information is unrelated to the implant itself. In this case it is important that the implant does not produce artifacts which interfere with the rest of the image and that it can be treated as another part of the anatomy. For example, patients may have an abnormality such as a cancerous tumour, which is situated close to the metal [Viano et al., 2000]. Small implants such as dental fillings and aneurysm clips can also hinder brain imaging.

Image artifacts due to the presence of metal are primarily caused by large distortions in the static magnetic field. A number of techniques exist to mitigate these artifacts. These include basic adjustments to the image parameters and more sophisticated methods such as multispectral imaging [Koch et al., 2010] [1].

[1] A summary of these techniques is given in Section 2.2.

Multispectral imaging techniques are able to produce spin echo images with few artifacts and good contrast. However, techniques for achieving reliable fat suppression near metal are currently limited. Being able to acquire accurate fat-suppressed images is valuable, as the presence of fat can obscure diagnostically important features near the implant [2]. The objective of the work reported in this thesis is to improve the performance of fat suppression near metal, using the three-point Dixon technique.

[2] Fat suppression techniques and their performance near metal are described in detail in Chapter 3.

2.1 MAGNETIC RESONANCE IMAGING

Up until the turn of the twentieth century, the only reliable way to see inside a patient was to cut them open and look inside. Anaesthesia was crude, the use of antiseptics was not widespread, and antibiotics had not yet been discovered. Surgery was brutally invasive, painful, and was generally seen as a last resort [3].

[3] *[Surgery is] "a humiliating spectacle of the futility of science [and the surgeon is] a savage armed with a knife"*– John Hunter, anatomist, 1750.

In the latter half of the 19th century, three monumental breakthroughs started a shift towards modern medicine. Two of these were the development of general anaesthesia, and an understanding of the germ theory of diseases. The third breakthrough was the discovery of X-rays. In 1895, Wilhelm Röntgen produced the first medical X-ray of his wife's hand. This ushered in a new era of medicine, one where we could produce images of the human interior. The following century saw the development of a broad range of medical imaging techniques, including ultrasound, CT, positron emission technology (PET), and MRI.

Figure 2.4: The first medical X-ray, of Anna Bertha Ludwig's hand. The 'lump' in the image is her wedding ring. It should be noted that even the first medical image suffered from a metal-induced artifact.

In 2017, imaging is an essential component of modern medicine. It is used daily for diagnosis, planning, and evaluating treatment, and for researching and understanding the human body[4]. MRI is arguably the most versatile imaging technique, as it can be used for both

- anatomical imaging, or finding out what the body "looks like" and
- functional imaging, or understanding how the body "is working".

[4] Medical imaging techniques are also commonly used on many other animals, especially by veterinarians for treating domesticated animals.

In particular, MRI produces high-quality images of the structure of our soft tissue, organs, and bone. Figure 2.5 shows two examples of standard anatomical MR images. Beyond anatomical imaging, there are a wide range of MRI techniques used to understand physiological processes in the body. Three common techniques are

- functional MRI (fMRI), which is used to measure brain activity,
- MR angiography, which is used to image blood flow and vessels,
- and diffusion MRI, which is used for looking at how easily water molecules diffuse and interact with the tissue they are in.

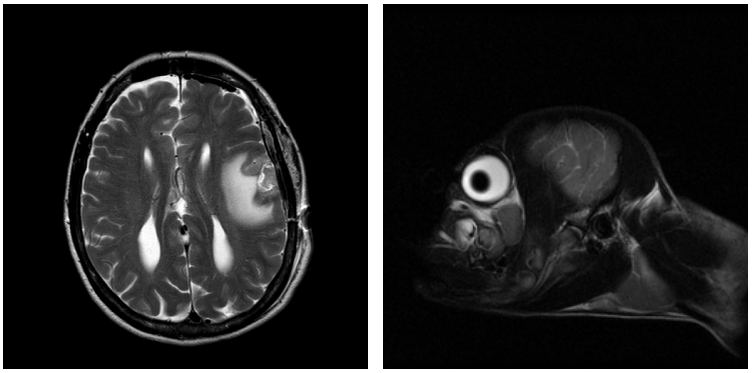

(a) Human brain, with tumour (b) Cat brain

Figure 2.5: Two examples of MR images of the brain: a) shows a human brain with a tumour and b) shows a cat brain. Source: [Osi].

This section provides a brief overview of the main components of MR imaging: nuclear magnetic resonance, signal generation, and image formation [5].

[5] The information presented is summarised from *"Principles of Magnetic Resonance Imaging"* by Nishimura [1995a] and *"MRI from Picture to Proton"* by McRobbie et al. [2006a].

2.1.1 *Nuclear magnetic resonance*

MRI is based on the phenomenon of nuclear magnetic resonance (NMR). Atoms with an odd number of protons or neutrons have a property called nuclear spin. The behaviour of these atoms in a varying magnetic field is the basis of NMR. Hydrogen atoms have a single proton, as shown in Fig. 2.6, and so have a net spin (Fig. 2.7). Hydrogen is abundant in the human body in water and lipids.

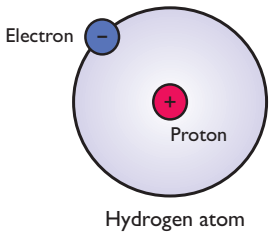

Figure 2.6: The nucleus of a hydrogen atom has a single proton.

The behaviour of a three-dimensional (3D) population of spins is analysed using a magnetisation vector, $\mathbf{M}$. This vector is the net magnetisation produced by the sum of the magnetic moments of the spins. Spins are normally randomly oriented, and $\mathbf{M} = 0$. When the ensemble of spins is placed into a static external magnetic field, $\mathbf{B}$, they become oriented in two possible states: parallel with the magnetic field direction, or anti-parallel. A larger proportion of the spins take on the parallel state, and so $\mathbf{M}$ is non-zero and is oriented in the direction of $\mathbf{B}$. Figure 2.8 shows a diagram depicting the behaviour of a group of spins (shown in two dimensions for simplicity).

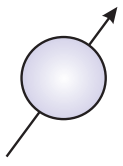

Figure 2.7: Depiction of a proton with net spin used in this section.

By convention, the main static magnetic field in MRI lies along the z-direction, or longitudinal direction. This is referred to as $\mathbf{B}_0$, and is

non-zero only in the z-direction:

$$\mathbf{B}_0 = [0, 0, B_0]. \tag{2.1}$$

The resonant frequency of the spins is linearly proportional to the applied magnetic field strength. If the only applied field is $\mathbf{B}_0$, all spins in the ensemble have the same resonant frequency given by

$$f = \frac{\gamma}{2\pi} B_0, \tag{2.2}$$

where both γ and $\frac{\gamma}{2\pi}$ are called the gyromagnetic ratio. For hydrogen protons in water, $\frac{\gamma}{2\pi}$ has a value of 42.58 MHzT^{-1}. This is known as the Larmor equation, and f is the Larmor frequency.

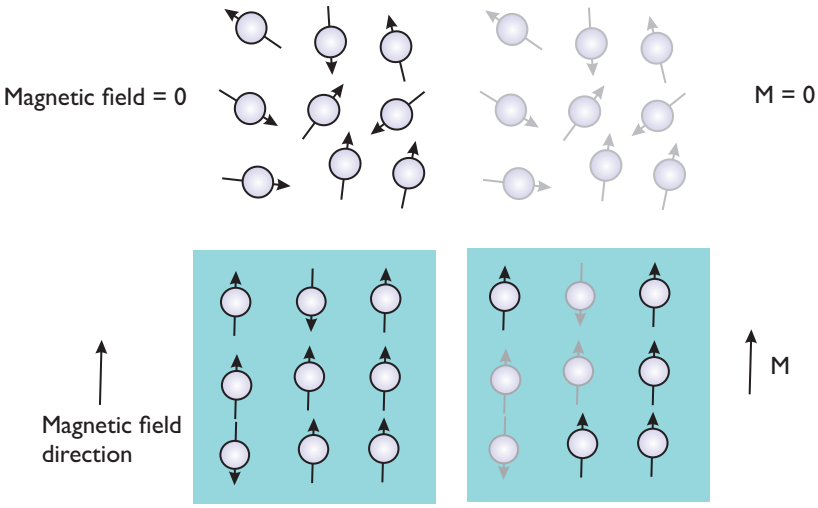

Figure 2.8: A depiction of the behaviour of a sample of spins when it is placed in an external magnetic field. The spins in the top row are not subject to an external magnetic field, and so are randomly oriented. Their individual magnetic dipoles cancel, and $\mathbf{M} = 0$, as depicted in the top right diagram. The spins in the bottom row have been placed in a magnetic field. A greater proportion of the spins are oriented in the direction of the magnetic field, and so the individual dipoles do not cancel (bottom right).

2.1.2 *Signal generation*

With only the $\mathbf{B}_0$ field present, $\mathbf{M}$ is at equilibrium aligned with the z-axis (in the direction of $\mathbf{B}_0$). When a radiofrequency (RF) magnetic field, $\mathbf{B}_1$, is applied at the Larmor frequency, the spins are excited[6]. The $\mathbf{B}_1$ field is applied in the transverse, or $x-y$ plane. The magnetisation vector is pushed away from the z-axis and towards the transverse plane. $\mathbf{M}$ begins to precess about the z-axis at the Larmor frequency, as shown in Fig. 2.9. The angle by which $\mathbf{M}$ is tipped away from the z-axis is determined by the magnitude and duration of the $\mathbf{B}_1$ field. This is known as the *flip angle*. A 90° flip angle tips $\mathbf{M}$ completely into the $x-y$ plane.

After the RF field is turned off, $\mathbf{M}$ eventually relaxes back to its equilibrium state. Two main time constants are associated with the relaxation of $\mathbf{M}$:

1. The longitudinal relaxation time constant, T_1. This is the rate at which the z-direction component of $\mathbf{M}$, M_z, returns to equilibrium.

2. The transverse time constant, T_2. This is the rate at which the transverse component of $\mathbf{M}$, M_{xy}, returns to equilibrium.

[6] Note that the RF magnetic field is also known as an RF *pulse*.

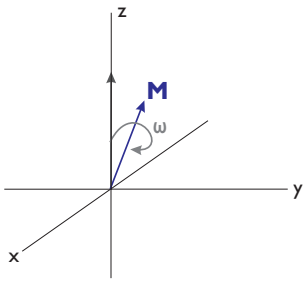

Figure 2.9: The magnetisation vector precesses at the Larmor frequency, $\omega = 2\pi f$.

The values of T_1 and T_2 vary between tissues. The density of the hydrogen atoms also varies between tissues [7]. These properties produce the contrast in an MR image.

After the $\mathbf{B}_1$ field excites the spin ensemble located in the $\mathbf{B}_0$ field, we can acquire the signal induced by the transverse component of $\mathbf{M}$ in an RF receiver coil.

[7] This is commonly referred to as the proton density.

2.1.3 *Image formation*

Placing a sample of spins in a static magnetic field and applying an RF field allows a signal to be acquired from the sample. However, with $\mathbf{B}_0$ uniform, we have no way of differentiating between spins in different locations, as all spins in the sample have the same resonant frequency. Linear magnetic field gradients G_x, G_y, and G_z are used in addition to $\mathbf{B}_0$ for spatial localisation of the spins in the x, y, and z directions, respectively. These gradients can be applied in linear combinations to acquire images of the patient in any plane. Figure 2.10 shows the main components of an MRI scanner:

- The $\mathbf{B}_0$ magnet, which produces the static $\mathbf{B}_0$ background field.
- The RF coil, which produces the RF excitation ($\mathbf{B}_1$) and receive fields.
- The gradient coils, which produce the linear magnetic field gradients.

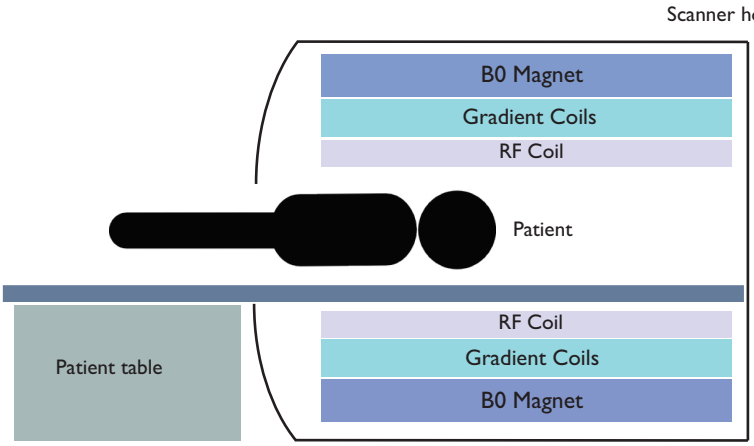

Figure 2.10: The main components of a MRI scanner. Electronics such as RF amplifiers and gradient amplifiers are not shown.

There are three components to spatial localisation: slice selection, frequency encoding, and phase encoding. Slice selection excites a 2D slice of spins in the 3D object, using a slice selection gradient. This is depicted in Fig. 2.11. Slices can be acquired in the three perpendicular imaging planes:

1. When G_z alone is used, the excited slice is in the *axial* plane [8].
2. Using G_x produces a slice in the *sagittal* plane.
3. Using G_y produces a *coronal* slice.

[8] By convention, the longitudinal axis of the patient, aligned with $\mathbf{B}_0$, is the z "laboratory" coordinate. Positive z is towards the head.

Slices which are selected using a combination of the gradients are known as *oblique*.

When a frequency encoding gradient is applied, the frequencies of the spins in the slice vary linearly with their position. For example, if the frequency encoding gradient is applied along the x-direction, the frequency is dependent on the x-position, by the Larmor equation

$$f(x) = \frac{\gamma}{2\pi}(B_0 + G_x x). \tag{2.3}$$

Similarly, when a phase encoding gradient is applied, this causes the phase of the spins to vary linearly with their position.

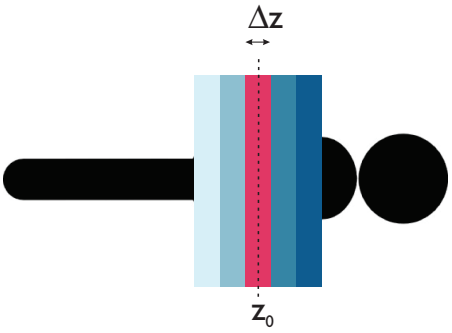

Figure 2.11: A simple illustration of axial slice selection. Each strip is an acquired slice. The position z_0 and thickness Δz of each slice are determined by the magnetic field gradient (such as G_z) and the bandwidth and centre frequency of the RF pulse.

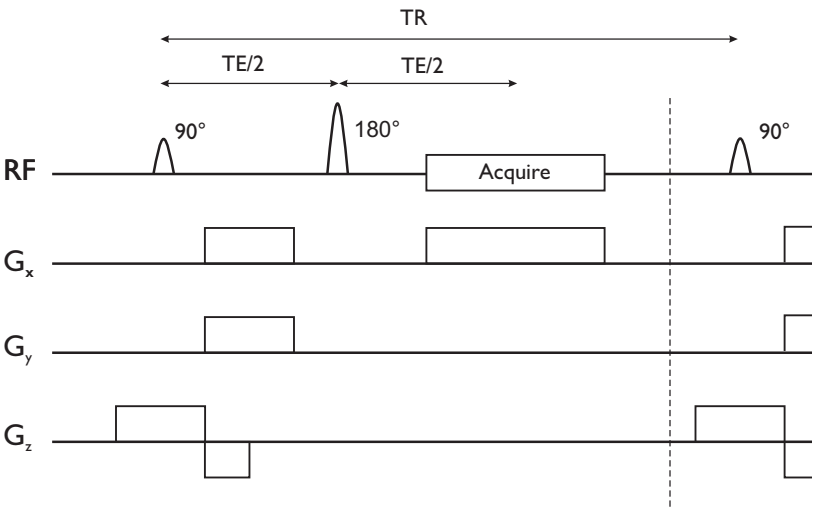

Figure 2.12: Diagram of a spin echo pulse sequence. The RF pulses and gradients are shown. The echo time, TE, and repetition time, TR, are also labelled. In this example the frequency encoding is along the x-axis, the phase encoding along the y-axis, and the slice selection along the z-axis.

In an imaging sequence, gradients are applied sequentially in conjunction with RF excitation pulses. The type of image which is produced is influenced by a range of image parameters, such as the echo time (TE), repetition time (TR) and the bandwidth of the RF pulses. The order and relative timing of the gradients and pulses are generally represented using a pulse sequence diagram. Figure 2.12 shows a simplified pulse sequence diagram for a spin echo sequence.

In 2D imaging, for each slice, the acquired signals produce a 2D matrix in Fourier space, or k-space. As the positions of the spins are linearly related to the measured frequency and phase, a 2D Fourier transform can be used to reconstruct an image of the measured slice (Fig. 2.13).

2.1.4 *Notation*

Signal is acquired from the spins within a 3D imaging volume, as depicted in Fig. 2.14. The size of this volume is given by the field of view, $\mathbf{FOV} = [FOV_x, FOV_y, FOV_z]$. This is generally given in millimetres (mm). In 3D imaging, the volume is segmented into a grid of 3D voxels of tissue. The size of this grid is generally referred to as the image acquisition matrix size, $\mathbf{RES} = [RES_x, RES_y, RES_z]$.

In 2D imaging, a set of slices are excited within the volume. Slices may be contiguous, or there may be a gap between two successive slices. For example, if the slice is axial (selected by G_z),

$$RES_z = \text{Number of slices} \tag{2.4}$$

and

$$FOV_z = \text{Number of slices} \times \text{Slice spacing}, \tag{2.5}$$

where

$$\text{Slice spacing} = \text{Slice thickness} + \text{Slice gap}. \tag{2.6}$$

The slice thickness and gap is generally given in millimetres. The excited slice is segmented into a grid of 2D pixels.

The position of the voxel (or pixel) is a vector quantity, $\mathbf{x} = [x, y, z]$. The size of the voxel in millimetres, $[\Delta x, \Delta y, \Delta z]$, is given by

$$[\Delta x, \Delta y, \Delta z] = [\frac{FOV_x}{RES_x}, \frac{FOV_y}{RES_y}, \frac{FOV_z}{RES_z}]. \tag{2.7}$$

The 3D imaging volume, or patient, is placed in the MRI scanner bore. By convention, the direction of the static $\mathbf{B_0}$ magnetic field acts along the z-dimension. This is along the long axis of the bore. The patient table also lies along this axis. The x and y directions are conventionally aligned horizontally and vertically across the scanner bore, respectively.

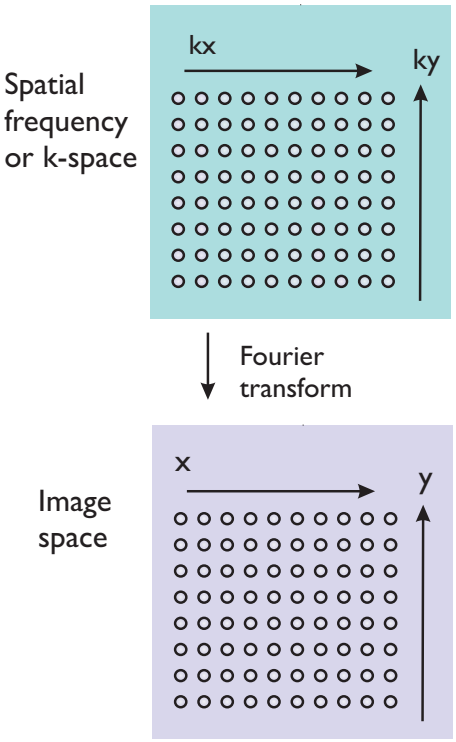

Figure 2.13: Illustration showing the relationship between acquired signals in k-space and image space.

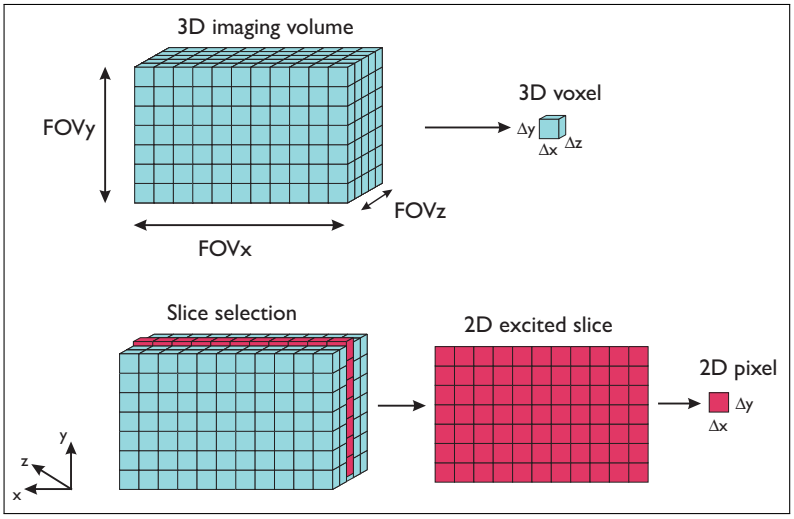

Figure 2.14: Diagram showing the difference between 3D imaging (top) and 2D imaging (bottom). In this example the slices are contiguous.

2.2 METAL INDUCED ARTIFACTS

This section describes how the presence of metal produces artifacts in MR images. The main types of image artifacts are described. This is followed by an overview of basic techniques to reduce artifacts and more advanced methods such as SEMAC and MAVRIC [9].

[9] The content in this section is largely comprised of information from Koch et al. [2010] and Hargreaves et al. [2011].

Metal implants have a magnetic susceptibility (χ) which is significantly different from the surrounding tissue. This produces large variations in the static $\mathbf{B_0}$ magnetic field. The orthopaedic implants considered in this thesis are paramagnetic, with a magnetic susceptibility of $\chi << 1$. Figure 2.15 shows a diagram showing the susceptibility of these implants compared to other common materials. For $\chi << 1$, the maximum B_0 variation, ΔB_{max}, is approximately proportional to the susceptibility [Schenck, 1996]:

$$\Delta B_{max} \approx \chi B_0. \tag{2.8}$$

By the Larmor equation, the resonant frequency of imaged spins at voxel $\mathbf{x}$ is shifted by an amount ($\Delta f[\mathbf{x}]$) which is directly proportional to B_0 field inhomogeneities $\Delta B_0[\mathbf{x}]$:

$$\Delta f[\mathbf{x}] = f_{off}[\mathbf{x}] - f_0[\mathbf{x}] = \frac{\gamma}{2\pi}\Delta B_0[\mathbf{x}], \tag{2.9}$$

where $f_0[\mathbf{x}]$ is the resonant frequency of the spin in a homogeneous magnetic field and $f_{off}[\mathbf{x}]$ is the new frequency, both in hertz [10].

[10] The B_0 variation, $\Delta B_0[\mathbf{x}]$, is commonly referred to by the term *field map*. Methods for modelling $\Delta B_0[\mathbf{x}]$ are described in Sec. 2.3.1.

Typical susceptibility values of materials used in metal orthopaedic implants include:

- Titanium: 180 ppm,
- Cobalt-chromium: 900 ppm,
- Non-ferrous stainless steel: $3000 - 5000$ ppm.

In comparison, tissue and bone have a susceptibility of approximately -9.2 ppm [Koch et al., 2010]. Due to the large susceptibility difference, the measured resonant frequency variations near metal implants are in the order of tens of kilohertz. This is significantly larger than frequency variations that occur at boundaries of air and tissue, which are in the range of a few hundred hertz.

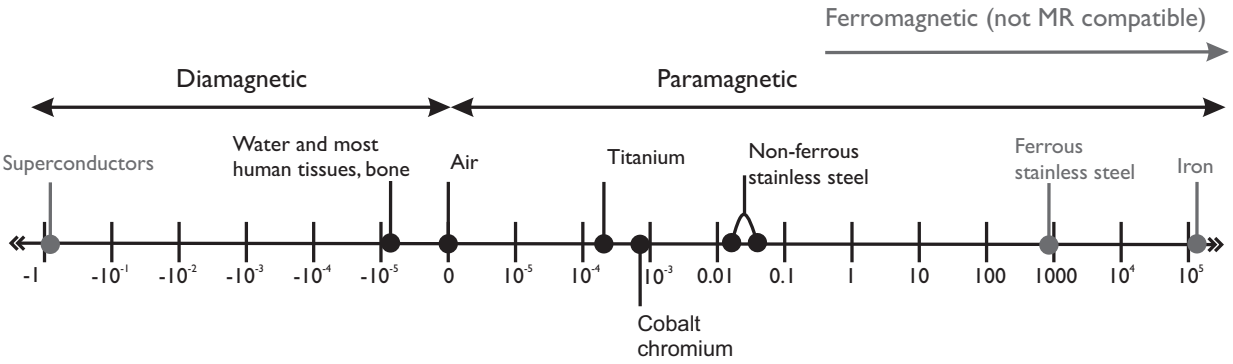

Figure 2.15: Diagram showing a susceptibility spectrum of common materials. Recreated from Schenck [1996], Fig. 2.

▶ MAGNETIC FIELD PERTURBATIONS are the main cause of image artifacts, which can be separated into four main types:

- Signal dephasing
- Signal loss and pile-up
- Image distortion
- Failure of fat suppression.

Signal loss, pile-up, and image distortion occur in the readout and slice selection directions, but not in the phase encoding direction [Koch et al., 2010] [11]. In areas of particularly large field gradients, the spins within each voxel precess at multiple rates. The spins therefore dephase rapidly, resulting in signal loss at readout. This can be seen in the image as black areas with no signal.

In a homogeneous magnetic field to which a uniform gradient is applied, the resonant frequency of the spin is a linear function of its physical location. The slope is dependent on the amplitude of the applied gradient. However, field inhomogeneities due to metal cause this relationship to become nonlinear [Lu et al., 2009]. The resonant frequency of a spin no longer directly corresponds to its position, as it also depends on where the spin is located in relation to the metal. This nonlinear function is complicated and depends on the field map induced by the metal implant. The field map is determined by the shape, size, and orientation of the implant, and the type of metal.

A nonlinear mapping between the frequency and position of the spins results in errors in the frequency encoding. These are generally referred to as "in-plane" artifacts. Spins which precess faster or slower than they would in a homogeneous field appear to be shifted away from their true location. This is illustrated in Fig. 2.17.

Shifts of groups of spins cause geometric distortion in the reconstructed image. A more severe artifact occurs when multiple spins are shifted to the same voxel. This is called signal pile-up and appears as bright hyper-intense areas in the image. Moving several spins to the same place causes signal loss in the original locations of the shifted spins. These appear as black voids in the image. An example of typical image artifacts near a hip replacement is shown in Fig. 2.16.

Errors in the slice selection are usually called "through-plane" artifacts. Normally, slice selection involves exciting a group of frequencies, where the centre frequency and bandwidth determines the location and width of the slice. However, in the presence of metal, the actual slice which is excited is different from the desired slice. The slice location may be shifted, as the centre frequency is no longer linearly related to the position. Spins from other slice locations may be excited, causing signal pile-up and thickening of the slice. Spins in the intended slice can also be shifted away to other slices, causing signal loss and thinning [Hargreaves et al., 2011]. This is illustrated in Fig. 2.18.

[11] In 2D multislice imaging, the presence of B_0 field inhomogeneities cause the signal model to be distorted in the frequency encoding and slice selection directions, with no dependency on the phase encoding direction. For further detail on the mathematical relationship between the acquired signal and the B_0 variation, the reader is referred to the comprehensive descriptions given by Nishimura [1995a] (p. 137) and Chang and Fitzpatrick [1992].

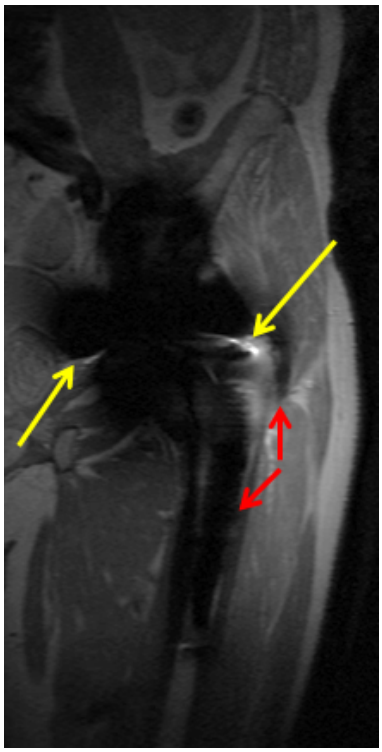

Figure 2.16: Image artifacts near a hip implant with cobalt-chromium and titanium components. The black void in the centre of the image is where the implant is located and the boundary between the implant and the tissue cannot be clearly identified. The red arrows indicate two regions of signal loss, and the yellow arrow shows two areas where has pile-up has occurred.

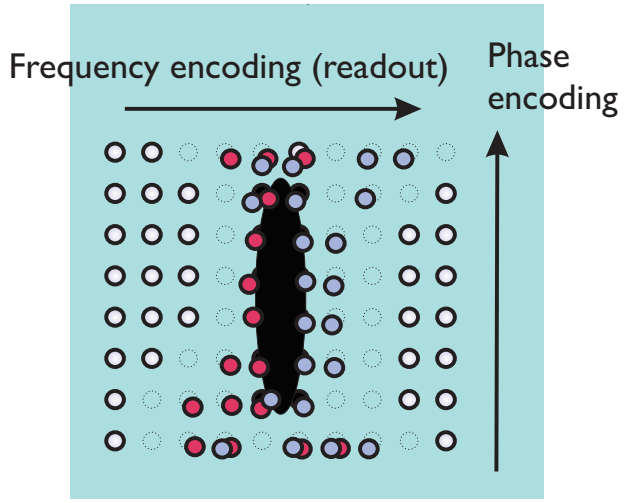

Figure 2.17: Illustration of in-plane shifting of spins near a simplistic metal object (shown in black). Some spins have shifted to the left (blue) and others have shifted to the right (pink). Locations where spins have shifted and have left behind a void are shown with a faint dotted outline. Signal pile-up is depicted where multiple spins have shifted to the same location. Note that no shifting occurs in the phase encoding direction. Figure based on Hargreaves et al. [2011], Fig. 4.

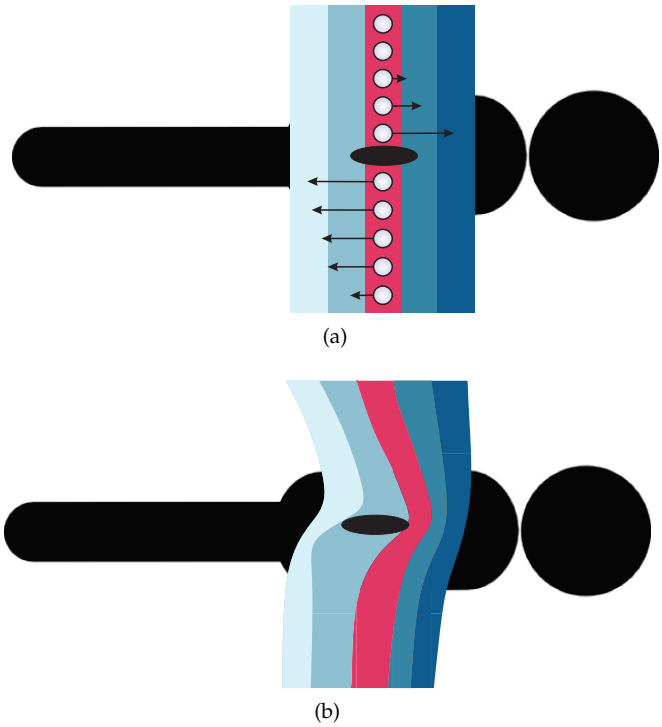

Figure 2.18: A depiction of through-plane slice distortion. A slice splitting into multiple slices is not pictured but may also occur near metal.

a) A possible scenario showing how spins shift to other slices.

b) The resulting distorted slice profiles after spins are shifted. Figure based on Hargreaves et al. [2011], Fig. 6 and Lu et al. [2009], Fig. 4.

In-plane and through-plane artifacts occur simultaneously, so it is difficult to identify the cause of any particular image artifact. For example, pixels showing signal pile-up may be due to spin displacement during slice selection or readout. It is challenging to resolve artifacts retrospectively, as they originate from multiple sources. In general, signal loss is not recoverable [Koch et al., 2011b]. Most techniques to mitigate artifacts near metal aim to avoid incorrect slice selection and frequency encoding, rather than attempting to correct by post-processing.

2.2.1 *General techniques for reducing artifacts*

Rapid spin dephasing resulting in signal loss occurs in gradient echo images. Spin echo sequences are preferred near metal as the 180° pulse refocuses spins before readout and recovers the signal. Short echo times are also recommended as this reduces the time available for spins to dephase [Vandevenne et al., 2007].

The distortion of spins in the frequency encoding direction is proportional to the resonant frequency shift (Δf) and inversely proportional to the readout gradient amplitude (G_r):

$$\text{Distortion} \propto \frac{\Delta f}{G_r}, \tag{2.10}$$

where the readout gradient amplitude is defined by

$$G_r = \frac{2\pi BW_r}{\gamma FOV_r}. \tag{2.11}$$

BW_r is the readout bandwidth (in hertz) and FOV_r is the field of view (in millimetres) along the readout, or frequency encoding, direction. The distortion in millimetres is dependent on these two parameters by

$$\text{Distortion (mm)} \propto \frac{FOV_r \times \Delta f}{BW_r}. \tag{2.13}$$

A similar expression can be written for the distortion in pixels,

$$\text{Distortion (pixels)} \propto \frac{RES_r \times \Delta f}{BW_r}. \tag{2.12}$$

In-plane distortion is reduced by increasing the readout bandwidth and reducing the size of the image matrix. However, increasing the readout gradient reduces the SNR [Hargreaves et al., 2011]. Venook et al. [2006] show that image distortion is inversely proportional to the radius of the object. Small objects and sharp corner features of larger implants are therefore more likely to suffer from pile-up artifacts.

Slice selection aims to excite spins in the range

$$z_0 - \frac{\Delta z}{2} < z < z_0 + \frac{\Delta z}{2}, \tag{2.14}$$

where z_0 is the spatial centre of the intended slice and Δz is the slice thickness. The spins are excited by applying an RF pulse during the slice-selection gradient, G_s. The centre frequency (f_{RF}) and bandwidth (Δf_{RF}) of the pulse are determined by the desired location and thickness of the slice and G_s:

$$f_{RF} = \frac{\gamma}{2\pi}(B_0 + G_s z_0) \tag{2.15}$$

$$\Delta f_{RF} = \frac{\gamma}{2\pi} G_s \Delta z. \tag{2.16}$$

In an inhomogeneous magnetic field, the range of excited spins expands to include the resonant frequency shift:

$$z_0 - \frac{\Delta z}{2} < z + \frac{2\pi\Delta f}{\gamma G_s} < z_0 + \frac{\Delta z}{2}. \tag{2.17}$$

The through-plane distortion is therefore dependent on the frequency shift and slice selection gradient amplitude. Rearranging Eq. 2.16

gives an expression for the distortion in terms of the slice width and pulse bandwidth:

$$\text{Distortion} \propto \frac{\Delta f}{G_s} \propto \frac{\Delta z \Delta f}{\Delta f_{RF}}. \tag{2.18}$$

Using a smaller slice thickness reduces the through-plane distortion. However, this requires longer scan times, as more slices are necessary for a given field of view. Increasing the pulse bandwidth also reduces the distortion. However, the ability to increase this parameter is limited as a higher than normal RF bandwidth results in a larger deposition of energy in the tissue being imaged [Hargreaves et al., 2011]. This can cause significant heating of the metal implant and tissue. Unsafe levels of heating may affect cardiac function and cause burns [McRobbie et al., 2006b].

Other techniques to reduce image artifacts exist, but may not be able to be used in all situations. Placing the long axis of the implant parallel to the z-axis of the $\mathbf{B_0}$ field reduces the artifacts along the axis. This can be done for some implants by positioning joints (such as knees and wrists) at particular angles, but may not be practical for some implants in the torso. Swapping the frequency and phase encoding direction changes the orientation of the artifacts. This does not reduce the size of the artifacts, but may allow previously obscured anatomy to be seen [Vandevenne et al., 2007].

Even with a careful choice of sequence parameters, significant image artifacts can still exist near metal, especially at high field strengths and near large implants (such as hip and knee replacements). The extent to which parameters can be adjusted is constrained by the need to maintain good SNR and physical limitations in generating the gradients.

2.2.2 *Advanced techniques*

More advanced techniques have been developed to obtain diagnostically reliable MR images near metal. These include 3D multispectral imaging techniques (3D-MSI) and the closely related view angle tilting (VAT), single point imaging, and prepolarized MRI.

▶ VIEW ANGLE TILTING (VAT) removes in-plane distortion with a modification to a standard spin echo sequence. A compensation gradient is applied during readout, in the slice-selective direction. The amplitude of the compensation gradient is equal to the slice-selection gradient. This has the effect of changing the angle at which the slice is read out, from 0^o to $\theta = \tan^{-1}(G_s/G_r)$ [12]. As there is a constant ratio between the slice and in-plane distortion, shifts in the readout-direction are cancelled by an equivalent shift in the slice direction, removing in-plane distortions [13].

VAT was first described by Cho et al. [1988] as a method to remove artifacts from the chemical shift and susceptibility differences in tissues [14]. Several studies have applied VAT during imaging of metal [Butts et al., 1999, Lee et al., 2001, Kolind et al., 2004]. The main lim-

[12] Recall from Sec. 2.2.1 that G_r is the readout gradient amplitude and G_s is the slice-selection gradient amplitude.

[13] The reader is referred to the paper by Cho et al. [1988] for a pulse sequence diagram and a more detailed description of the VAT sequence.

[14] The chemical shift is introduced in Chapter 3.

itation of VAT is that it does not resolve through-plane distortions and so images still contain significant artifacts. Using VAT can also introduce blurring into the image, although this can be managed by using a high bandwidth during readout [Butts et al., 2005]. VAT can be considered as a precursor to multispectral imaging techniques.

Multispectral imaging techniques: 3D multispectral imaging (3D-MSI) is a general term for techniques such as SEMAC and MAVRIC, which resolve both in-plane and through-plane artifacts by acquiring additional information.

- SLICE ENCODING FOR METAL ARTIFACT CORRECTION (SEMAC) applies a VAT compensation gradient during readout, but also uses additional phase encoding in the slice-selective direction to resolve through-plane distortions. As resonant frequency variations arising from ΔB_0 cause the spins from the intended slice to be spread out over a range of different locations, multiple slices must be acquired to resolve through-plane distortions. For each nominal slice location, SEMAC phase encoding obtains a set of distorted 2D slices, or "sub-encodes". These are registered with each other during image reconstruction and then combined into a single undistorted slice. The number of sub-encodes must span the expected range of ΔB_0 for the slice [Lu et al., 2009].

- MULTI-ACQUISITION VARIABLE-RESONANCE IMAGE COMBINATION (MAVRIC) is a similar technique to SEMAC as it also uses a set of acquisitions to resolve artifacts. However SEMAC is a spatially-selective method, as each set of sub-encodes is based on a specific slice location. Instead of exciting a range of spatial locations, MAVRIC excites bands of frequencies by acquiring multiple 3D fast spin echo (FSE) images. Slice selection gradients are not used, so through-plane distortions are removed. Instead, the region which is imaged is determined by the RF centre frequency, spectral properties of the pulse and the change in resonant frequencies induced by the implant [Koch et al., 2009].

  MAVRIC acquires a set of 3D-FSE images at incremented values of the RF centre frequency. This splits the resonant frequency variation into discrete frequency bins, as shown in Fig. 2.19. Each bin captures a different proportion of the spins, depending on their resonant frequency. The frequency variation in each bin is limited by the bandwidth of the applied RF pulse. For example, when a 2 kHz pulse is applied, the maximum frequency variation is limited to ± 1 kHz, which limits the distortion within that bin. Each of the 3D bins is independently reconstructed to give a series of volumetric images. These are combined using a sum-of-squares method to give a composite 3D image.

  The advantages of MAVRIC and SEMAC have been combined to give a hybrid method [Koch et al., 2011a]. A clinical 3D-MSI sequence called MAVRIC-SL has been developed, based on these tech-

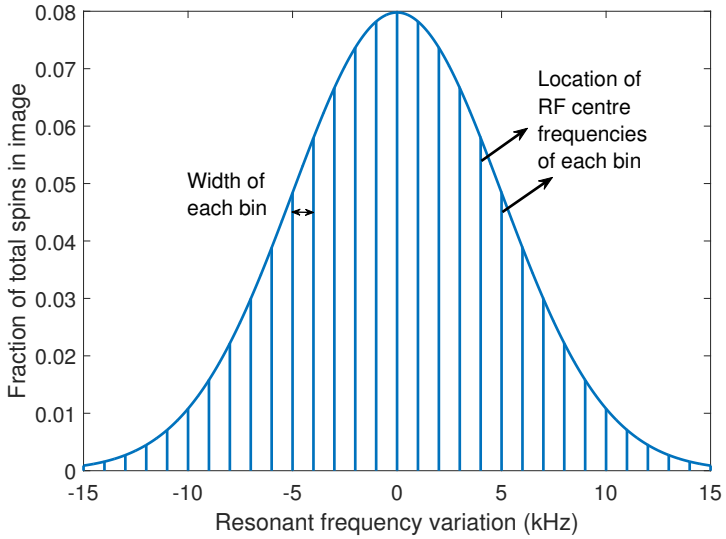

Figure 2.19: A possible distribution of the resonant frequency variation of spins in an image. In this example the resonant frequency variation lies in the range ± 16 kHz. The location and width of MAVRIC bins are marked to show the proportion of the total spins captured by each bin. Figure recreated from Koch et al. [2009], Fig. 2.

niques. This is available on GE MRI scanners. As multiple acquisitions are required for each image, the scan time is increased compared to a standard FSE acquisition which does not resolve artifacts.

Further developments on 3D-MSI techniques have focused on reducing the scan time. This can be done by using parallel imaging and partial Fourier acquisition [Hargreaves et al., 2010], compressed sensing [Koch and King, 2011, Worters et al., 2012], and with prior knowledge [Smith et al., 2014, Shi et al., 2016]. However, with the use of acceleration techniques comes the need to balance an acceptable level of SNR in the image against the reduction of scan time.

While 3D-MSI techniques effectively remove geometric distortions present in FSE images, pile-up artifacts remain. These could be removed in post-processing by using information from the field map of the resonant frequency variation [Koch et al., 2009]. An alternative algorithm could also be used in the image reconstruction [Hernando et al., 2009]. However, in regions where the gradient of the resonant frequency variation exceeds the readout gradient, signal pile-up and loss are not recoverable [Koch et al., 2011b, Smith et al., 2015]. Other recent work on improving the performance of 3D-MSI has included reducing blurring in the reconstruction process [Quist et al., 2016], and combining 3D-MSI with other imaging sequences [Kaushik et al., 2016].

- SINGLE POINT IMAGING:
  One disadvantage of 3D-MSI techniques is that pile-up artifacts cannot be completely eliminated, as long as frequency encoding is used [Koch et al., 2011b]. An alternative is to use a single point imaging (SPI) method, where all three dimensions of the image are phase encoded. This approach produces distortion free images and has been tested on metal devices in-vitro [Ramos-Cabrer et al., 2004]. However, as only one point of k-space is acquired after each excitation,

early implementations of SPI methods were reported to have excessively long imaging times of up to nine hours. Acceleration techniques such as parallel imaging and partial Fourier acquisition have been used to reduce the scan time to 7–12 minutes [Artz et al., 2013]. Recently, a new technique has been proposed to reduce the scan time of SPI methods. It uses multiple RF pulses offset at different frequencies. The clinical feasibility of this method has been demonstrated on a volunteer with a full knee replacement [Artz et al., 2016].

- PREPOLARIZED MRI:
  As the magnitude of the resonant frequency variation increases with the field strength, the image distortions can be reduced by using MRI with a low magnetic field. This results in a significant loss of SNR in standard imaging, but this can be mitigated by using a prepolarized MRI (PMRI) system. Two magnets are used for imaging: the first is a high field (0.4–1.0 T) which excites the spins before acquisition and the second is a low field (20–180 mT) applied during readout.

  PMRI has been used to scan human wrists with plates and screws and produces high quality images with few distortions [Venook et al., 2006]. The main disadvantage of this approach is the small bore size used in PMRI. For example, Venook et al. [2006] used a 9 cm diameter bore, compared to a standard bore diameter of around 60 cm. In order to image the torso, a considerably wider bore would be required.

- IN CONCLUSION, 3D-MSI techniques are currently the most well developed techniques for imaging near metal. However, a number of significant challenges to imaging near metal still exist, including resolving residual artifacts, and tradeoffs between SNR, resolution, and scan time. Alternative techniques such as single point imaging have demonstrated potential but are not currently clinically feasible. Finally, fat suppression is a major unsolved issue in MR imaging near metal, as discussed in Sec. 3.4.

2.3 MODELLING TECHNIQUES

Large susceptibility differences between the metal implant and the surrounding tissue induce significant inhomogeneities in the $\mathbf{B_0}$ magnetic field. Understanding the nature of these inhomogeneities is an important requirement for developing improved imaging techniques near metal. This section describes tools which can be used to understand and mitigate metal-induced artifacts in MR images.

2.3.1 *Magnetic field modelling*

There are several ways of estimating the $\mathbf{B_0}$ magnetic field variation near metal.

- ONE TECHNIQUE uses knowledge of the distribution of susceptibility values across an object to estimate the field variation. A rapid method for calculating this relationship using the FFT was proposed by two independent groups. Salomir et al. [2003] use Maxwell's equations and 3D Fourier transforms to obtain the expression. Marques and Bowtell [2005] derive the same equation, using dipolar field models. The equation has been applied to in-vivo data of the human brain and a metal hip replacement cup [Koch et al., 2006, Koch and Hinks, 2008].

  Given a 3D matrix of the susceptibility across an object, $\chi(\mathbf{x})$, a 3D map of the field variation can be determined using the equation developed by Salomir et al. [2003] and Marques and Bowtell [2005],

$$\Delta B_0[\mathbf{x}] = FT^{-1}\left[B_0\left(\frac{1}{3} - \frac{k_z^2}{k_x^2 + k_y^2 + k_z^2}\right)FT\left(\chi[\mathbf{x}]\right)\right], \tag{2.19}$$

  where $\mathbf{x} = [x, y, z]$ is a position vector in the spatial domain, $\mathbf{k} = [k_x, k_y, k_z]$ is a position vector in k-space, and $FT[\cdot]$ is the 3D FFT.

- ANALYTICAL SOLUTIONS have been derived for the magnetic field variation induced by objects of simple shapes such as spheres and cylinders [Haacke et al., 1999, Koch et al., 2006].

- THE MAGNETIC FIELD VARIATION can also be measured by acquiring two gradient echo images at two different echo times [Haacke et al., 1999]. The field variation is calculated from the phase difference between the two images. This method is not generally used near metal as gradient echo images suffer from significant signal loss. Bartusek et al. [2006] used a spin echo sequence to map phase shifts near metal dental implants. This technique was able to measure resonant frequency offsets of up to 10 kHz but may not perform as well near larger implants.

- FIELD MAPS CAN ALSO BE CALCULATED from the MAVRIC-SL sequence. During MAVRIC-SL, a set of N_b 3D bin images $I_b[\mathbf{x}]$ are acquired at a range of discrete resonant frequency offset values, $\{f_b\} = \{-f_b^{max}, ..., 0, ..., f_b^{max}\}$, where f_b^{max} is the maximum frequency offset measured and $\frac{2f_b^{max}}{N_b}$ is the bin width. The simplest method of calculating the resonant frequency variation (or field map) uses a weighted average of the bin image magnitudes [Koch et al., 2011a]. At each pixel, the magnitude of the bin images is normalised by

$$|\bar{I}_b[\mathbf{x}]| = \frac{|I_b[\mathbf{x}]|}{\sum_{b=1}^{N_b} |I_b[\mathbf{x}]|}. \tag{2.20}$$

  The resonant frequency variation is then estimated by weighting the normalised bin image magnitudes by their corresponding frequency offset value,

$$\Delta f[\mathbf{x}] = \sum_{b=1}^{N_b} |\bar{I}_b[\mathbf{x}]| f_b. \tag{2.21}$$

An improved method for estimating the resonant frequency variation using a matched-filter has recently been proposed [Quist et al., 2016]. Compared to the weighted average approach, this method is less sensitive to noise and is less biased towards the central bin. In a standard MAVRIC-SL acquisition, the bins are generally combined using a sum-of-squares method. This process introduces blurring, and includes information from bins which may only contain noise and no useful signal. The proposed method uses the matched-filter to reduce blurring. A better quality MAVRIC-SL image is produced.

2.3.2 *Recovering image distortion*

In-plane and through-plane distortions can be resolved retrospectively if the $\Delta B_0[\mathbf{x}]$ field is known exactly [Skare and Andersson, 2005]. This allows the geometric distortion, $\mathbf{d}[\mathbf{x}]$, to be calculated. The distortion in the image intensity at each voxel is then calculated using the Jacobian of $\mathbf{d}[\mathbf{x}]$. The acquired image is corrected by resampling the data at each voxel. It should be noted that this approach is not able to resolve near-metal artifacts such as signal loss and pile-up. It assumes that all spins in a single voxel undergo the same resonant frequency shift [Koch et al., 2010]. However, spins in voxels near the boundary of the metal are subject to several frequency offsets, as described in Sec. 2.2.

- Chang and Fitzpatrick [1992] developed a *reverse encoding (RE)* method where two images are acquired using spin echo pulse sequences. The only difference between the two pulse sequences is that the sign of the frequency encoding and the slice selection gradients are switched. This produces two images which are distorted in alternating directions. The two images are combined during post-processing to produce a single undistorted image.

  However, there are several issues with this approach. Most importantly, the equations used to correct for the distortion are ill-conditioned in regions of rapid $\Delta B_0[\mathbf{x}]$ variation [Koch et al., 2010]. Numerical errors can also result in the estimated $\mathbf{d}[\mathbf{x}]$ map having discontinuities, and it can be difficult to identify a required set of common features between the two images before correction [Skare and Andersson, 2005]. A number of developments have been made to the original RE method, and it has been used in rectifying the distortions in echo-planar imaging [Morgan et al., 2004].

- Skare and Andersson [2005] further extended the RE techniques by modelling the distortion, $\mathbf{d}[\mathbf{x}]$, by a set of B-spline basis functions. Instead of estimating the distortion at each voxel, the basis function coefficients are optimised using an objective function which minimises the difference between the two images. The use of B-splines enforces smoothness in the estimated $\mathbf{d}[\mathbf{x}]$ map.

  Proof of concept of this method has been demonstrated by successfully correcting for the distortion induced by two small metal

aneurysm clips. The first clip was embedded in a phantom, and the second was implanted in a patient. However, this method is computationally demanding, as it requires several thousand parameters to be estimated for each 3D image. The processing time depends on the number of parameters and the image matrix size, with times of between 30 minutes and 18 hours reported. The phantom data was shown to be successfully corrected in approximately 50 minutes.

2.4 SUMMARY

In conclusion, MRI could be a powerful technique for diagnosing and assessing soft tissue complications near metal orthopaedic implants. However, the quality of a standard MR image is reliant on the $\mathbf{B}_0$ field being uniform. Introducing metal produces inhomogeneities in the $\mathbf{B}_0$ field, resulting in several types of image artifacts. A range of techniques for reducing artifacts have been proposed. These include simple changes to the image sequence parameters, and advanced techniques including 3D-MSI and SPI. Finally, mathematical models of both the $\mathbf{B}_0$ field variations and the image distortions are useful tools for understanding how to alleviate artifacts.

3

Fat Suppression and Separation Techniques

Fat suppression is used routinely in MR imaging to suppress the signal from fat-bound protons. Fat has a dominant signal which can obscure underlying abnormalities in surrounding fluid-based tissue, such as inflammation and edema (swelling caused by the accumulation of fluid) [Bley et al., 2010]. Totally successful fat suppression produces an image which does not contain signal from fat tissue.

Several fat suppression methods exist, and all take advantage of the fact that hydrogen nuclei behave differently in fat tissue than in water. Fat saturation and multipoint techniques take advantage of chemical shift differences. Inversion recovery techniques are independent of chemical shift differences, and are based on fat and water protons having different T_1 relaxation times [Delfaut et al., 1999].

Fat is comprised of long triglyceride chains with two hydrogen atoms connected to each carbon atom. Each hydrogen atom is surrounded by many other atoms, whose electron fields act as a shield. This reduces the apparent strength of the external magnetic field which is experienced by the hydrogen nuclei. In comparison, each water molecule only has two hydrogen atoms and one oxygen atom, so there is less shielding effect. Fat molecules therefore precess at a lower resonant frequency than water. The fractional shift between fat and water is known as the chemical shift, δ_{cs}, and has a value of approximately 3.5 ppm (Fig. 3.1). The resonant frequency difference between fat and water, f_{cs} increases with the magnetic field strength by

$$f_{cs} = \frac{\gamma}{2\pi} B_0 \delta_{cs}[\text{ppm}] \times 10^{-6} \tag{3.1}$$

and is approximately 220 Hz at 1.5 T and 440 Hz at 3 T [Bley et al., 2010].

The difference in resonant frequency between fat and water can cause noticeable artifacts in MR images. RF (or slice selection) bandwidths generally vary between 1–3 kHz. With a chemical shift of 220 Hz at 1.5 T, the selected slice can be shifted by a significant frac-

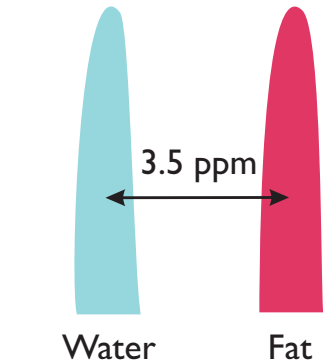

Figure 3.1: Fat-water peaks.

tion of the slice width. Likewise, typical readout bandwidths vary in the range of 50–200 Hz/pixel, leading to a chemical shift artifact in the frequency encoding direction in the order of several pixels [Bernstein et al., 2004a].

Fat suppression is used for a number of reasons, including reducing artifacts due to the chemical shift, improving visualisation of water signal enhanced by contrast agents, and identifying anatomic details that may be obscured by fat. The best fat suppression technique depends on the application and the amount of fat which needs to be suppressed. For example, fat saturation is used to image tissues with a large amount of fat, whereas multipoint techniques are most effective on tissues comprised of a mixture of fat and water [Delfaut et al., 1999]. Fat suppression is an important technique used in near-metal imaging to identify complications such as fluid build up and the presence of inflammatory masses.

It should be clarified that in this thesis, the term *fat suppression* refers to producing a single image which contains no fat signal. Fat saturation and inversion recovery are fat suppression techniques. *Fat separation* refers to producing two separate images: a water-only image and a fat-only image. Fat suppression is therefore a component of fat separation. Multipoint techniques perform fat separation, as described in Sec. 3.3.

This section provides an overview of standard fat suppression and separation techniques including fat saturation, inversion recovery, and multipoint techniques. Recent developments based on multipoint techniques are also summarised. Finally, the reasons for the failure of existing fat suppression and separation methods near metal implants are described.

3.1 FAT SATURATION

In a fat saturation sequence, a 90° RF pulse with the same resonant frequency as fat and a narrow bandwidth is applied before the beginning of the conventional pulse sequence. This excites the fat protons. Immediately afterwards, a spoiler gradient is applied in all three dimensions, which dephases the transverse magnetisation from the fat signal. The image acquisition then continues as normal, but contains no contribution from the fat protons [Bernstein et al., 2004b]. An example where fat saturation is applied to a spin echo sequence is shown in Fig. 3.2.

Fat saturation is most effective at suppressing tissues with a large amount of fat. It is also a reliable technique for contrast-enhanced imaging and avoiding chemical shift artifacts. As the fat suppression component is independent of the rest of the acquisition, this technique can be used with any imaging sequence [Delfaut et al., 1999].

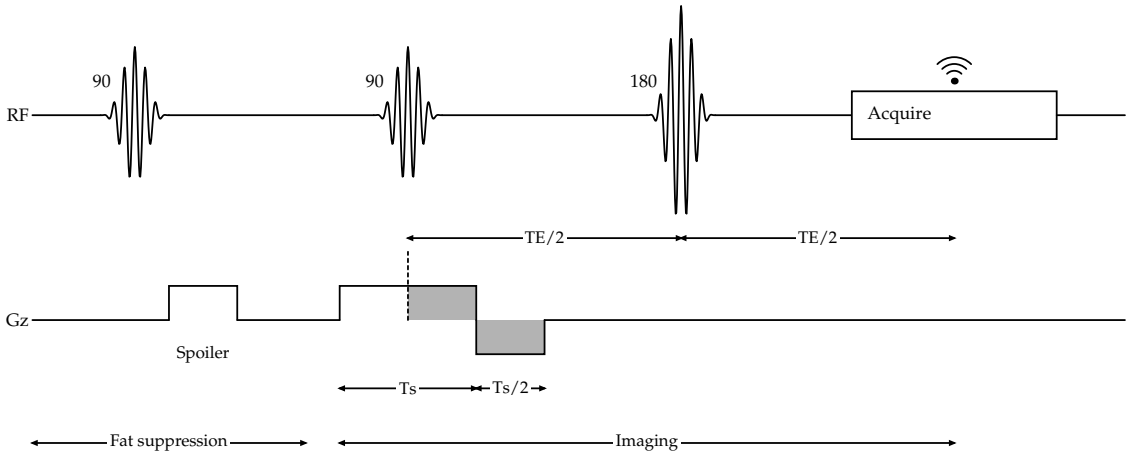

Figure 3.2: Fat saturation with a spin echo sequence. The spoiler gradient is applied in all three dimensions, with only one shown here. TE is the echo time, which is the interval between the 90° excitation pulse and the centre of the spin echo. Ts is the time period for which the slice-select gradient is applied.

▶ DISADVANTAGES:

Fat saturation fails in the presence of $\mathbf{B}_0$ magnetic field variations. The effectiveness of fat saturation is dependent on the frequency of the RF saturation pulse accurately matching the resonant frequency of fat. $\mathbf{B}_0$ variations shift the resonant frequencies of fat and water, so the RF pulse fails to excite the fat component. In some situations the pulse saturates water instead of fat, resulting in a water-suppressed image. Areas where $\mathbf{B}_0$ variations affect fat saturation include air-tissue interfaces, near sharp variations in anatomic structures, and around metal implants.

Imperfections in the RF transmitter field also influence the final image. Ideally, the RF pulse should deposit a uniform amount of energy throughout the imaged region. However, inhomogeneities in the RF field cause the flip angle to vary across the region. The fraction of spins which are tipped into the transverse plane is proportional to $\sin(\theta)$, so deviations from $\theta = 90^o$ cause uneven excitation [Bernstein et al., 2004c]. Also, the actual bandwidth of the pulse may differ from the desired bandwidth. A non-uniform saturation pulse does not excite all of the fat protons, resulting in incomplete suppression of the fat signal.

RF pulses are also distorted by large metal implants. The metal absorbs a proportion of the RF energy intended for the neighbouring tissues. Therefore the amount of transverse magnetisation which is excited in these tissues is less than tissues far from the implant, and so residual fat signal remains in the vicinity of the metal [McRobbie et al., 2006a].

Another main disadvantage of fat saturation is the increase in imaging time. The saturation pulse is applied for approximately 10–20 ms to satisfy the requirements for a narrow bandwidth pulse [Bernstein et al., 2004b]. In gradient echo imaging, this is a similar order of magnitude to the acquisition time, leading to a significant increase in total imaging time.

3.2 INVERSION RECOVERY IMAGING

Spins in fat tissue relax faster than those in water. The difference between the T_1 relaxation rate of the two tissue types is exploited in inversion recovery techniques. An exponential relationship is used to represent the relaxation of the longitudinal magnetisation of a tissue after a 180° inversion pulse is applied:

$$M_z(t) = M_0(1 - 2e^{-t/T_1}), \tag{3.2}$$

where M_z is the longitudinal magnetisation over time, $-M_0$ is the initial longitudinal magnetisation, and T_1 is the tissue-dependent relaxation rate. By equating M_z to zero, the null time (TI) for a particular tissue can be found. Figure 3.3 compares the relaxation of typical fat and water-based tissues during inversion recovery. The null time for fat is marked TI. This is when the longitudinal magnetisation of fat is zero but the water magnetisation has not fully recovered.

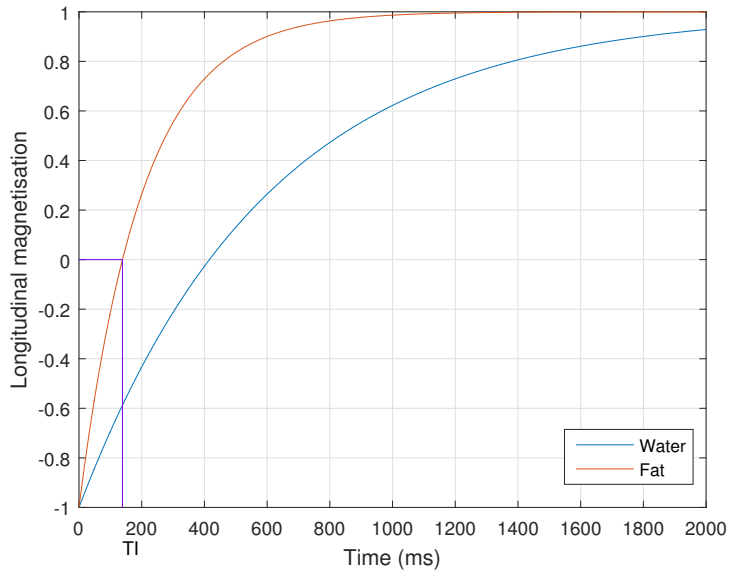

Figure 3.3: Exponential relationship describing the relaxation of the longitudinal magnetisation of water and fat. -1 corresponds to the complete inversion of the longitudinal magnetisation after the 180° inversion pulse is applied. The null time for fat is labelled TI and marked with a purple line.

In a short tau (inversion time) inversion recovery (STIR) sequence, a 180° inversion pulse is first applied, followed by a 90° excitation pulse at a time of TI after the first pulse, as shown in Fig. 3.4. The image acquisition then proceeds as normal. TI is chosen so that the 90° pulse occurs at the null point of fat. There is a contribution to the acquired signal from water but none from fat [Nishimura, 1995b].

STIR is not dependent on the chemical shift between fat and water, so is not affected by magnetic field inhomogeneities. Unlike fat saturation, inversion recovery sequences accurately suppress fat near metal implants. STIR produces images with sharp contrast, especially in tissues with long T_1 and T_2, which can improve the detection of tumours.

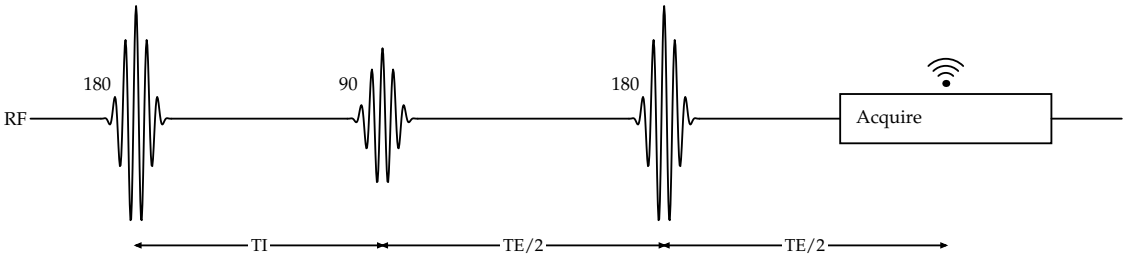

Figure 3.4: Inversion recovery RF pulse sequence. TI is the null time and TE the echo time.

▶ DISADVANTAGES:

When the 90° pulse is applied in STIR, as shown in Fig. 3.4, the spins in water have not fully recovered and are still partially saturated. A smaller magnetisation vector is therefore flipped into the transverse plane than in a normal imaging sequence, so fewer spins contribute to the acquired signal. This results in a loss of SNR [Delfaut et al., 1999].

Interpretation of the signal intensities in T_1-weighted STIR images can be ambiguous. Fat and some fluids including hemorrhage, proteinaceous fluid, and gadolinium based contrast agents (in certain concentrations) have similar T_1 values, so these fluids are suppressed along with the fat. The chosen TI value is based on the relaxation time of white fat, but some tumours and fat deposits have different T_1 values. Also, the T_1 for white fat varies between individuals and within the anatomy of each individual. For these reasons, STIR is mainly used with T_2 and proton density weighted sequences, and T_1-weighted acquisitions are not generally recommended [Bley et al., 2010]. STIR is not generally used with gadolinium based contrast agents as abnormalities (such as tumours) which should have enhanced contrast become suppressed along with the fat.

3.3 MULTIPOINT TECHNIQUES

The material in this section is based on content from the *"Handbook of MRI Pulse Sequences"*, by Bernstein et al. [2004a], and a collection of papers written by Reeder et al. [2004, 2005], Yu et al. [2005, 2012], and Hernando et al. [2008, 2010b]. The review paper by Ma [2008] also provides a comprehensive review of Dixon techniques.

Multipoint fat suppression techniques acquire multiple images at different echo times. These are combined to produce separated images of the fat and water components in the tissue. These techniques can be used in the presence of $\mathbf{B}_0$ field variations and in conjunction with contrast enhancement agents.

Multipoint techniques are based on the principle that fat and water have different resonant frequencies. By separating the peaks, individual images of the two components are obtained. In comparison, a single fat-suppressed image is acquired in fat saturation and STIR. This approach is useful for estimating the relative proportion of fat and water in tissues. This can assist with the diagnosis of conditions such as bone marrow disease and some liver diseases [Bley et al., 2010].

The Dixon technique is an example of a multipoint technique. The original two-point method was first introduced by Dixon [1984]. The extended two-point and the three-point techniques have since been developed to correct for magnetic field inhomogeneities. Further ex-

tensions to an arbitrary number of points have been developed by Reeder et al. [2004], and are used clinically on GE scanners.

As fat and water protons precess at different resonant frequencies, the phase difference between the fat and water components of the magnetisation changes over time. The Dixon technique uses this principle to obtain in-phase and out-of-phase images. The fat and water spins are in phase directly after the 90° excitation pulse, when Image 1 is acquired, but go out of phase as the water spins precess at a slightly faster rate than the fat spins. After a short time period the water and fat spins are out of phase by π, and Image 2 is acquired. The spins continue to precess until they are again in phase, and the process repeats. Figure 3.5 shows how the phase between the fat and water spins changes over time.

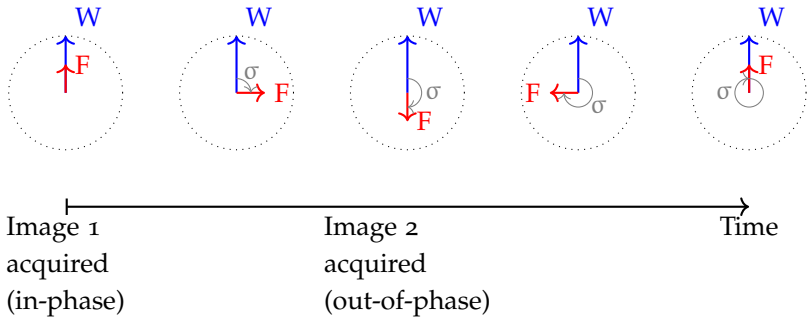

Figure 3.5: Relative phase shift σ between fat and water spins during the two-point Dixon method. The timing of the in-phase and out-of-phase images are marked.

3.3.1 *Two-point method*

The standard two-point Dixon technique acquires two images for each slice location. These can be obtained in two separate TR intervals or as different echoes within the same TR, where TR is the repetition time for the sequence. In spin echo sequences, the first image is a normal in-phase acquisition where the spins are in phase at the centre of the readout gradient. The out-of-phase image is acquired by shifting the 180° pulse in time by $t_n/2$. This offsets the location of the spin echo by t_n, so the spins are out of phase at readout. A pulse sequence diagram for the two acquisitions is shown in Fig. 3.6. The spins have a phase offset of

$$\sigma = 2\pi f_{cs} t_n \tag{3.3}$$

at the centre of the readout, where f_{cs} is the resonant frequency difference due to the chemical shift, defined by Eq. 3.1. Given a desired phase offset of $\sigma = \pi$ and $f_{cs} = 220\,\text{Hz}$ at 1.5 T, t_n and therefore TE can be calculated using this equation. Gradient echo sequences can also be used with this approach, where the centre of the readout gradient is shifted instead of the refocusing pulse.

As shown in Fig. 3.5, the in-phase image contains the sum of the fat and water signals, whereas the out-of-phase image contains the

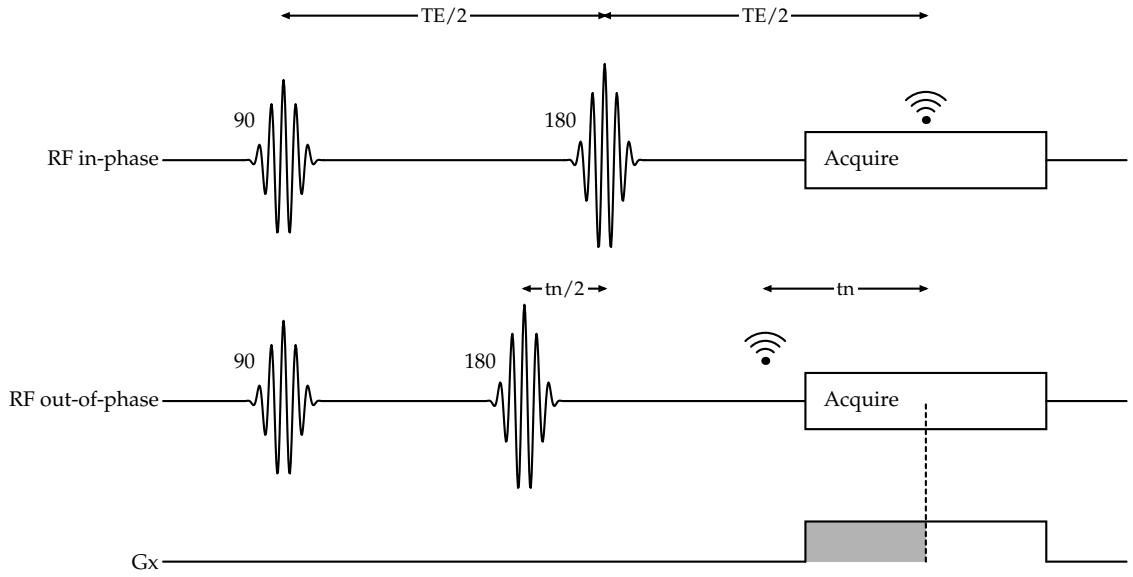

Figure 3.6: Abbreviated pulse sequences used in the two-point Dixon technique. The first line is a standard RF pulse sequence, where the echo occurs at the centre of the readout. The second line shows the 180° pulse advanced by $t_n/2$. The echo occurs at a time t_n before the centre of the readout, so an out-of-phase signal is acquired.

difference:

$$\begin{aligned} S_{in}[\mathbf{x}] &= W[\mathbf{x}] + F[\mathbf{x}] \\ S_{out}[\mathbf{x}] &= W[\mathbf{x}] - F[\mathbf{x}], \end{aligned} \tag{3.4}$$

where $\mathbf{x} = [x, y, z]$ is the position of the voxel in the spatial domain. Spatial dependence is only indicated in this section where necessary. A water-only image can be obtained by adding the in-phase and out-of-phase images. Likewise, a fat-only image can be obtained by subtracting the out-of-phase image from the in-phase image:

$$\begin{aligned} W &= \tfrac{1}{2}(S_{in} + S_{out}) \\ F &= \tfrac{1}{2}(S_{in} - S_{out}). \end{aligned} \tag{3.5}$$

The amount of water and fat in a particular tissue can be estimated from the separated images.

A major disadvantage of the two-point Dixon technique is that it assumes that the chemical shift is the only contributor to the phase difference. It ignores the effect of $\mathbf{B}_0$ inhomogeneities and susceptibility variations. A perturbation in the magnetic field, ΔB_0, which produces a resonant frequency shift, Δf, causes the phase offset to shift further by ψ:

$$\psi = 2\pi \Delta f t_n. \tag{3.6}$$

Figure 3.7 shows the effect of the additional phase shift produced by the field variation on the fat and water phase. $\mathbf{B}_0$ inhomogeneities cause the supposedly water-only and fat-only images to contain a mixture of fat and water.

3.3.2 *Extended two-point method*

The extended two-point Dixon technique resolves the problems caused by $\mathbf{B}_0$ inhomogeneities with post-processing techniques, instead of

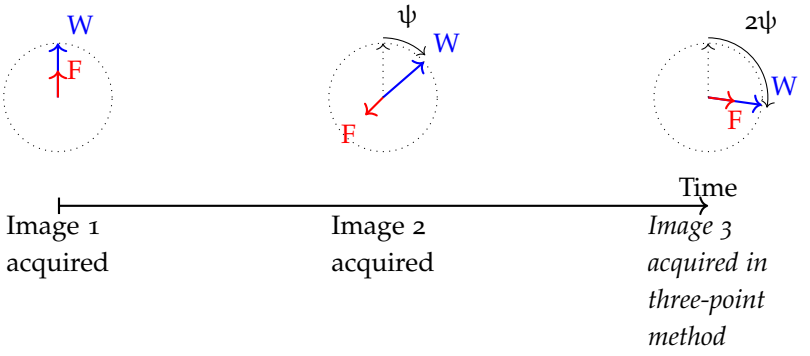

Figure 3.7: Relative phase between fat and water spins during the two-point Dixon method, with the additional phase shift ψ induced by the field variation.

acquiring additional information. The in-phase and out-of-phase images are modelled as

$$\begin{aligned} \mathbf{S}_{in}[\mathbf{x}] &= (W[\mathbf{x}] + F[\mathbf{x}])e^{j\psi_0} \\ \mathbf{S}_{out}[\mathbf{x}] &= (W[\mathbf{x}] - F[\mathbf{x}])e^{j(\psi_0+\psi[\mathbf{x}])}, \end{aligned} \tag{3.7}$$

where $\psi[\mathbf{x}]$ is the phase shift due to local $\mathbf{B}_0$ field inhomogeneities, and ψ_0 includes all other effects which cause phase shifts such as eddy currents and imperfections in the RF pulse. These two equations contain four unknowns: $W[\mathbf{x}]$, $F[\mathbf{x}]$, $\psi[\mathbf{x}]$, and ψ_0. $\mathbf{S}_{in}$ and $\mathbf{S}_{out}$ are complex, so the magnitude and phase of the two images form four independent equations which are used to solve for the unknowns [Bernstein et al., 2004a, Coombs et al., 1997]. The first equation takes the magnitude of $\mathbf{S}_{in}$ to eliminate ψ_0:

$$|\mathbf{S}_{in}| = W + F \tag{3.8}$$

An intermediate variable, $\hat{\mathbf{S}}_{out}$, is used to solve for ψ and $\mathbf{S}_{out}$. It is defined by

$$\hat{\mathbf{S}}_{out} = \mathbf{S}_{out}e^{-j\psi_0} = \frac{\mathbf{S}_{out}\mathbf{S}_{in}^*}{|\mathbf{S}_{in}|} = (W - F)e^{j\psi}, \tag{3.9}$$

where * is the complex conjugate. Calculating ψ directly from the phase of Eq. 3.9 may not give the correct result as the sign of $W - F$ changes depending on the relative amounts of water and fat in the tissue [Skinner and Glover, 1997]. By squaring $\hat{\mathbf{S}}_{out}$ instead and taking the phase of $(\hat{\mathbf{S}}_{out})^2$, ψ can be calculated:

$$(\hat{\mathbf{S}}_{out})^2 = |W - F|^2 e^{j2\psi} \tag{3.10}$$

$$\angle(\hat{\mathbf{S}}_{out})^2 = 2\psi \tag{3.11}$$

$$\psi = \frac{\angle(\hat{\mathbf{S}}_{out})^2}{2}. \tag{3.12}$$

Once ψ is calculated and eliminated from Eq. 3.10, the water and fat images can be calculated from

$$\begin{aligned} W &= \tfrac{1}{2}(|\mathbf{S}_{in}| + p_c|\mathbf{S}_{out}|) \\ F &= \tfrac{1}{2}(|\mathbf{S}_{in}| - p_c|\mathbf{S}_{out}|), \end{aligned} \tag{3.13}$$

where $-1 < p_c \leqslant 1$ is a coefficient which is positive when there is more water than fat in the tissue, and negative when there is less water than fat [Bernstein et al., 2004a, Skinner and Glover, 1997]. p_c is calculated as

$$p_c = \cos(\angle(\hat{\mathbf{S}}_{out} e^{-j\psi})) = \frac{\mathrm{Re}\{\hat{\mathbf{S}}_{out} e^{-j\psi}\}}{|\hat{\mathbf{S}}_{out}|}. \tag{3.14}$$

As ψ is not restricted to an interval of length 2π, wrapping of the phase shift occurs. Therefore, directly calculating ψ from Eq. 3.12 does not always give the correct solution. Instead, $\hat{\mathbf{S}}_{out}$ is treated as the image containing the wrapped value of the phase shift. Phase unwrapping algorithms are generally used to estimate ψ, and are discussed in more detail in Chapter 4.

The extended two-point Dixon technique is usually able to separate fat and water successfully, except at boundaries between the two species [Coombs et al., 1997]. In this situation $W \approx F$, and so $\mathbf{S}_{out} \approx 0$. Noise in $\mathbf{S}_{out}$ can cause ψ to be incorrectly calculated, resulting in water being wrongly labelled as fat and vice versa.

3.3.3 *Three-point method*

The first three-point method was introduced by Glover and Schneider [1991]. Images are acquired at three different phase offsets: $(0, \pi, -\pi)$. This gives one in-phase and two out-of-phase images, with the phase difference between the out-of-phase images used to calculate ψ. A map of ψ values is used to correct one of the out-of-phase images, then the water and fat images are calculated as in the two-point method. Because ψ is estimated from an out-of-phase image, it fails or can be ambiguous when $W \approx F$, like the two-point methods.

The three-point technique is improved by acquiring two in-phase and one out-of-phase image at phase offsets of $(0, \pi, 2\pi)$. The relative timing of the three images is shown in Fig. 3.7, with the third image marked in italics. The difference between the two in-phase images is used to calculate ψ. The three images are described by:

$$\begin{aligned} \mathbf{S}_0[\mathbf{x}] &= (W[\mathbf{x}] + F[\mathbf{x}])e^{j\psi_0} \\ \mathbf{S}_1[\mathbf{x}] &= (W[\mathbf{x}] - F[\mathbf{x}])e^{j(\psi_0 + \psi[\mathbf{x}])} \\ \mathbf{S}_2[\mathbf{x}] &= (W[\mathbf{x}] + F[\mathbf{x}])e^{j(\psi_0 + 2\psi[\mathbf{x}])}. \end{aligned} \tag{3.15}$$

This approach is less sensitive to voxels which contain similar amounts of water and fat, as $\mathbf{S}_0$ and $\mathbf{S}_2$ are made up of the sum of water and fat contributions instead of the difference. Also, a more accurate estimate of ψ is possible as in-phase images have higher SNR than opposed-phase images.

Obtaining three images gives an overdetermined system, with four unknowns (W, F, ψ, and ψ_0) and six equations. In a similar approach to Eq. 3.9 in the extended two-point technique, intermediate variables $\hat{\mathbf{S}}_1$ and $\hat{\mathbf{S}}_2$ are used to determine the phase shift,

$$\hat{\mathbf{S}}_1 = \mathbf{S}_1 e^{-j\psi_0} = \frac{\mathbf{S}_1 \mathbf{S}_0^*}{|\mathbf{S}_0|} = (W - F)e^{j\psi} \tag{3.16}$$

$$\hat{\mathbf{S}}_2 = \mathbf{S}_2 e^{-j\psi_0} = \frac{\mathbf{S}_2 \mathbf{S}_0^*}{|\mathbf{S}_0|} = (W + F)e^{j2\psi}. \tag{3.17}$$

Once these are calculated, ψ is extracted by taking the angle of Eq. 3.17. It then can be estimated using techniques such as phase unwrapping.

Eliminating ψ from Eq. 3.15 gives the following system of equations,

$$\begin{aligned} W + F &= |\mathbf{S}_0| \\ W - F &= \hat{\mathbf{S}}_1 e^{-j\psi} = p_c |\mathbf{S}_1| \\ W + F &= |\mathbf{S}_2|, \end{aligned} \tag{3.18}$$

where p_c is calculated using Eq. 3.14 and substituting $\hat{\mathbf{S}}_1$ for $\hat{\mathbf{S}}_{out}$. Two solutions exist to this set of equations. Both are usually calculated and combined to improve the SNR of the final result.

3.3.4 *Generalised N-point method*

In the three-point Dixon technique, the images are acquired using symmetrically placed spin echoes. This allows the phase shift due to the magnetic field variation to be directly extracted from Eq. 3.17. Reeder et al. [2005] have demonstrated that the best noise performance occurs when the echoes are asymmetrically placed so the relative phase offset between the fat and water in each of the three images is $(-\pi/6, \pi/2, 7\pi/6)$ or $(-7\pi/6, -\pi/2, \pi/6)$. This particular set of phase offsets is called IDEAL (iterative decomposition of water and fat with echo asymmetry and least squares estimation). It is used as the standard Dixon technique in GE MRI scanners. Figure 3.8 shows the relative fat and water phase shift in IDEAL images, ignoring the phase shift due to the field variation.

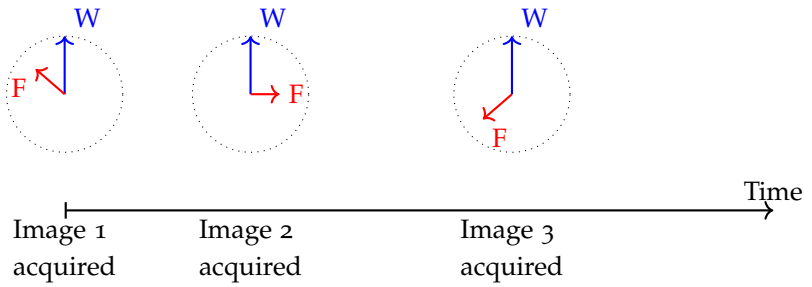

Figure 3.8: Relative asymmetric phase shift between fat and water signals in images acquired using IDEAL imaging. The additional phase shift due to the field variation is ignored in this diagram.

The set of equations describing the three-point Dixon method in Eq. 3.15 can be generalised to describe the water and fat signal in a set of N_S images acquired at an arbitrary set of echo times. The signal at each voxel $\mathbf{x} = [x, y, z]$ in the nth image can be described by

$$\mathbf{S}(t_n)[\mathbf{x}] = (W[\mathbf{x}] + F[\mathbf{x}]e^{j2\pi f_{cs} t_n})e^{j2\pi \Delta f[\mathbf{x}] t_n}, \tag{3.19}$$

where f_{cs} is the chemical shift between fat and water in hertz, t_n is the echo time offset, and Δf is the resonant frequency shift due to the

$\mathbf{B}_0$ field variation, in hertz. For simplicity, the spatial dependence on $\mathbf{x}$ is ignored in the following equations in this section.

It can be seen that for $t_n = (0, 1/2f_{cs}, 1/f_{cs})$, $n = 1, 2, 3$, this set of equations is equivalent to the three-point Dixon technique, described in Eq. 3.15. For asymmetric combinations of t_n, this system of equations cannot be solved directly, and a more complicated reconstruction method is required. This is because the phase shift due to the chemical shift is not separable from the phase shift due to the field variation. Instead, Reeder et al. [2004] use an iterative least squares method to simultaneously estimate the unknown quantities F, W, and Δf.

Equation 3.19 is solved by minimising the following residual, R:

$$R = \|\mathbf{S}(t_n) - (W + Fe^{j2\pi f_{cs} t_n})e^{j2\pi \Delta f t_n}\|_2, \tag{3.20}$$

where $\|\cdot\|_2$ is the 2-norm. This is done by linearising the system of equations in Eq. 3.19 and solving it using linear least squares. An initial estimate of the field variation, Δf_0, is used to rearrange Eq. 3.19 into a linear system of equations. This is done by removing Δf_0 from $\mathbf{S}(t_n)$:

$$\hat{\mathbf{S}}(t_n) = \mathbf{S}(t_n)e^{-j2\pi \Delta f_0 t_n} = (W + Fe^{j2\pi f_{cs} t_n}). \tag{3.21}$$

The remainder of the model, $W + Fe^{j2\pi f_{cs} t_n}$, can be linearised by separating the water and fat into their real and imaginary components using Euler's identity [1]. This allows the signal model to be rewritten in matrix format and solved using an iterative linear least squares method on a voxel-by-voxel basis. At the end of each iteration error terms in Δf, W, and F are calculated, and used as updates for the next step. The method is repeated over several iterations until the error in Δf is smaller than a set tolerance [2].

[1] $e^{j\theta} = \cos(\theta) + j\sin(\theta)$

[2] The reader is referred to the paper by Reeder et al. [2004] titled *"Multicoil Dixon chemical species separation with an iterative least-squares estimation method"* for a full derivation of the method.

For correct convergence to occur, the initial estimate of Δf_0 must be sufficiently close to the true solution. This assumption allows a first order Taylor series approximation to be made while calculating the error terms.

In reality the residual in Eq. 3.20 has many local minima for each voxel, so it is possible to converge to the incorrect solution for Δf. If this occurs, the estimated water and fat signals will be incorrect. This appears in the final reconstructed images as regions where the water and fat have been swapped. Yu et al. [2005] address this issue by using a region-growing method to more reliably estimate the initial field variation at each voxel. The starting value for each voxel is calculated using a neighbouring region of voxels. The field variation is assumed to be locally smooth and slowly varying throughout the image.

- VARIABLE PROJECTION (VARPRO) is used by Hernando et al. [2008] to rewrite Eq. 3.20 to be a separable least squares problem. VARPRO is a method for solving non-linear least squares problems by splitting the problem into non-linear and linear parameters [Golub and Pereyra, 2003, O'Leary and Rust, 2013].

Equation 3.20 describes a non-linear least squares problem, as Δf is a non-linear, unknown parameter. However, this equation can be rewritten using VARPRO to isolate Δf from W and F. First, Eq. 3.20 is rewritten as

$$R_V = \|\mathbf{S}_V(t_n)[\mathbf{x}] - \Psi(\Delta f[\mathbf{x}], t_n)\mathbf{Y}[\mathbf{x}]\|_2, \tag{3.22}$$

where

$$\mathbf{S}_V(t_n)[\mathbf{x}] = \begin{bmatrix} \mathbf{S}(t_1)[\mathbf{x}] \\ \mathbf{S}(t_2)[\mathbf{x}] \\ \vdots \\ \mathbf{S}(t_{N_S})[\mathbf{x}] \end{bmatrix} \qquad \mathbf{Y}[\mathbf{x}] = \begin{bmatrix} W[\mathbf{x}] \\ F[\mathbf{x}] \end{bmatrix}$$

$$\Psi(\Delta f[\mathbf{x}], t_n) = \begin{bmatrix} e^{j2\pi f_{cs} t_1} & e^{j2\pi (f_{cs}+\Delta f[\mathbf{x}]) t_1} \\ e^{j2\pi f_{cs} t_2} & e^{j2\pi (f_{cs}+\Delta f[\mathbf{x}]) t_2} \\ \vdots & \vdots \\ e^{j2\pi f_{cs} t_{N_S}} & e^{j2\pi (f_{cs}+\Delta f[\mathbf{x}]) t_{N_S}} \end{bmatrix} \tag{3.23}$$

$\mathbf{Y}$ contains the linear parameters, W and F, while Ψ is dependent on the non-linear parameter Δf. Given Δf, $\mathbf{Y}$ is obtained from

Note that the spatial dependence on $\mathbf{x}$ and reference to t_n is omitted in the following equations for simplicity.

$$\mathbf{Y} = \Psi(\Delta f)^+ \mathbf{S}_V \tag{3.24}$$

where $\mathbf{A}^+$ denotes the pseudo-inverse of $\mathbf{A}$. This expression allows us to remove $\mathbf{Y}$ from Eq. 3.22 to obtain

$$R_V = \|[I - \Psi(\Delta f)\Psi(\Delta f)^+]\mathbf{S}_V\|_2, \tag{3.25}$$

where I is the $N_S \times N_S$ identity matrix. R_V is now only dependent on one unknown parameter, the field variation, Δf. In the previously described iterative least squares method, W, F, and Δf must be estimated simultaneously in each iteration. VARPRO simplifies the problem, as R_V can be minimised for Δf alone. Once the optimum value for Δf is obtained, W and F can be calculated using Eq. 3.24.

▶ THE EXPRESSIONS in Eq. 3.20 and Eq. 3.25 describe the residual for a single voxel. Minimising these expressions on a voxel-by-voxel basis assumes that the solution for each voxel is independent of the other voxels in the image. This can lead to an estimated field map which is not smooth, and which is not the globally optimum solution. To deal with this, Hernando et al. [2010a] estimate the field variation for all voxels in the image jointly.

Equation 3.25 is rewritten into the following cost function for all voxels in the image,

$$\Delta f_T[\mathbf{x}] = \arg\min\Big(\sum_{v=1}^{V} R_V + \mu \sum_{v=1}^{V} \sum_{j \in \delta_V} w_{v,j} W\Big), \tag{3.26}$$

where v is the voxel index and V is the number of voxels in the image[3]. $\Delta f_T[\mathbf{x}]$ is the final estimated resonant frequency shift. The first

[3] For example, in a 2D image with 256×256 pixels, $V = 256^2$.

part of the equation sums the residual across all voxels, enforcing data consistency. The second part of the equation applies a smoothness constraint. μ is a regularisation parameter, and W is a quadratic function which encourages smoothness over a small neighbourhood of voxels, δ_V. $w_{v,j}$ is a weighting map. This equation is minimised using a graph cuts algorithm.

3.3.5 *Multipeak model*

The described variations of the Dixon technique assume that both water and fat have a single resonant frequency peak. This is a simplification, as the fat spectrum actually has at least six spectral peaks, while water has one. For example, the fat spectrum for peanut oil is known to have a similar chemical shift spectrum to certain types of human fat tissue. The spectrum at 3 T is shown in Fig. 3.9, with the location and magnitude of the peaks obtained from experimental data in Yu et al. [2008]. The magnitudes indicate the fraction of the total fat signal contained in each peak. Although around 60 % of the signal power is contained within the main fat peak, the locations of the other peaks can reduce the contrast between the fat and water signals.

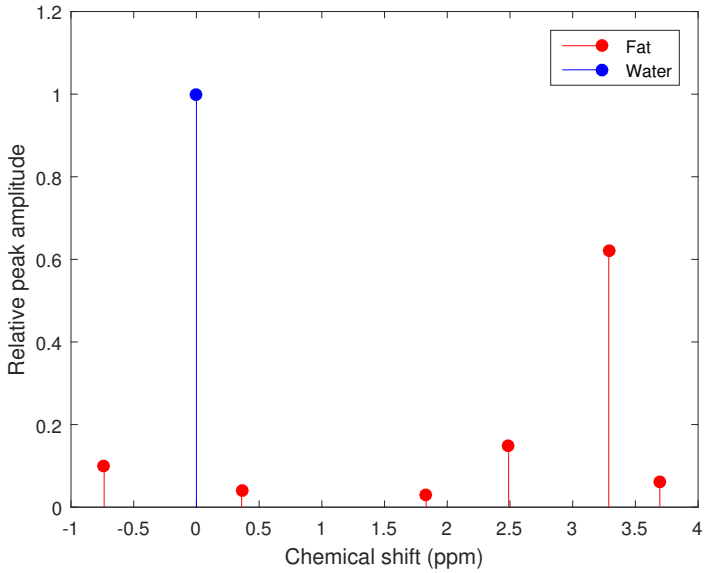

Figure 3.9: Frequency spectrum for peanut oil showing the location of six fat peaks, relative to the water peak.

The set of equations described by Eq. 3.19 is used to separate two chemical species: fat and water. This can be generalised to a multipoint method which can be used to separate M species as

$$\mathbf{S}(t_n) = \left(\sum_{m=1}^{M} \rho_m e^{j2\pi f_{cs_m} t_n}\right) e^{j2\pi \Delta f t_n}, \tag{3.27}$$

where ρ_m is the intensity of the mth species and f_{cs_m} describes the corresponding unique chemical shift. With $M = 7$, Equation 3.27 can be used to describe a fat spectrum model which has six fat peaks and

The signal model given by Eq. 3.27 can be extended to account for T_2^* decay. Significant T_2^* dephasing can affect estimation of the fat and water images if not included in the model. The extended model is useful when imaging conditions such as fatty liver disease, where iron overload in the liver contributes to T_2^* dephasing. The reader is referred to the paper by Yu et al. [2007] for a full description of the method.

one water peak. Yu et al. [2012] use the difference between the shape of the fat and water spectra to improve the accuracy of the field map.

3.4 FAT SUPPRESSION NEAR METAL IMPLANTS

The presence of fat can interfere with the identification of fluid-based complications near metal implants, including inflammation, edema, and pseudotumours [4]. In contrast-enhanced MR imaging, fat appears to have the same image intensity as lesions such as cancerous tumours and pseudotumours. Fat suppression is therefore important for diagnosing these complications. In particular, being able to perform robust fat suppression near the boundary of metal implants would allow for improved identification of contrast-enhanced abnormalities.

[4] A pseudotumour is a type of cystic or solid mass occurring due to an adverse reaction to the metal implant [Campbell et al., 2010, Davis and Morrison, 2016].

The resonant frequency offsets induced by metal implants can be in the order of tens of kilohertz. This is significantly larger than the chemical shift between fat and water. For example, an offset of 16 kHz is around 70x greater than the chemical shift at 1.5 T, which is 220 Hz. Fat saturation methods generally fail near metal implants because the resonant frequency of the fat protons is shifted by an amount which is significantly larger than the chemical shift. The fat saturation pulse misses the fat protons altogether, resulting in unsuccessful fat suppression.

Inversion recovery methods are the most reliable techniques as they are independent of the chemical shift. STIR is currently the standard clinical technique used for fat suppression near metal [Hargreaves et al., 2011]. However, STIR images have low SNR, as the contribution by the non-fat protons is reduced by the inversion pulse. STIR also suppresses the signal from common concentrations of gadolinium. It is not generally used near metal to diagnose complications which are more easily identified with gadolinium, such as inflammatory masses (including pseudotumours).

Multipoint techniques have the potential to be able to accurately separate fat and water near metal [5]. A major advantage of the multipoint methods over the fat saturation and inversion recovery methods is that they can a) be used in regions of magnetic field variation, and b) be used reliably in conjunction with contrast-enhanced imaging. Therefore, in principle, these methods could be well-suited to imaging near metal.

[5] For published examples of fat suppression near metal, Vandevenne et al. [2007] compare the performance of fat saturation and STIR near a titanium screw. Del Grande et al. [2014] compare the performance of fat saturation, STIR, and IDEAL for a range of metal implants at 3 T, including hip and knee replacements, spinal fixations, and a screw.

However, the main challenge is finding an accurate method of calculating the resonant frequency shift due to the magnetic field variation, Δf. Direct calculation is not practical near metal because it can only be used for resonant frequency shifts Δf which are less than $f_{cs}/2$, as phase wrapping occurs for larger shifts [Bernstein et al., 2004a]. A robust phase unwrapping or iterative reconstruction method is therefore required. Existing phase estimation methods can resolve small phase changes some distance from metal but fail near the boundaries of the implant and tissue, where large $\mathbf{B}_0$ perturbations cause greater phase wrapping [Hargreaves et al., 2011]. In

addition, in-plane and through-plane distortions mean that the estimated phase at locations near the metal may not accurately represent the true phase.

In summary, options for obtaining fat suppressed images near metal are currently limited, and do not produce high quality images. Being able to accurately suppress fat near metal and produce images with good diagnostic quality is a significant unsolved challenge in MRI. Multipoint techniques have potential but further development of phase estimation methods is needed in order to be able to successfully suppress fat near the boundaries of metal.

4

Phase Unwrapping

This chapter describes phase unwrapping techniques which are necessary for accurate fat-water separation in the three-point Dixon technique. An introduction to the theory of phase unwrapping is given first. This is followed by a summary of common two-dimensional phase unwrapping techniques, including branch cut methods, minimum-norm methods, and model-based methods.

It should be noted that *phase unwrapping* is a term used for the mechanism for estimating the phase shift. In other words, *phase unwrapping* forms one component of the broader problem of *phase estimation*.

The material presented in this chapter is largely based on the book by Ghiglia and Pritt [1998a] titled "*Two Dimensional Phase Unwrapping. Theory, Algorithms and Software*".

4.1 INTRODUCTION

For a complex signal, $\mathbf{s} = |\mathbf{s}|e^{j\phi}$, the phase is extracted by taking the inverse four quadrant tangent of the quotient of the imaginary and real components,

$$\phi_w = \arctan\left(\frac{\mathrm{Im}\{\mathbf{s}\}}{\mathrm{Re}\{\mathbf{s}\}}\right). \tag{4.1}$$

The estimated value of the phase, ϕ_w, is restricted to lie in the principal period, $[-\pi, \pi]$.

In the three-point Dixon technique, the true phase induced by $\mathbf{B}_0$ inhomogeneities is given by Eq. 3.6. The phase is extracted from

$$\hat{\mathbf{S}}_2 = (W + F)e^{j2\psi}. \tag{4.2}$$

Without loss of generality, let $\phi = 2\psi$.

In reality, the true phase of the signal, ϕ, may be greater than 2π, especially in the presence of metal. The estimated phase is wrapped into the principal period. The estimate by Eq. 4.1 is therefore wrapped,

$$\phi_w = \mathcal{W}_r[\phi], \tag{4.3}$$

where $\mathcal{W}_r[\phi]$ is the wrapping operator defined by

$$\mathcal{W}_r[\phi] = \mathrm{mod}(\phi + \pi, 2\pi) - \pi. \tag{4.4}$$

Phase unwrapping is required to estimate the true phase shift ϕ from the wrapped values ϕ_w. This is a common problem in signal processing and several different methods for unwrapping have been developed. This chapter provides an overview of the main phase unwrapping techniques.

4.1.1 *One-dimensional phase unwrapping*

Figure 4.1 shows the wrapped phase shift $\phi_w[x]$ and the corresponding true phase $\phi[x]$ for a one-dimensional discrete signal [1]. In 1D, phase unwrapping involves calculating the number of integer multiples of 2π, $c[x]$, which must be added to the phase $\phi_w[x]$ at each sample point x in order to unwrap it:

$$\phi[x] = \phi_w[x] + 2\pi c[x]. \tag{4.5}$$

If we define the phase difference between two points as

$$\Delta\phi[x] = \phi[x+1] - \phi[x], \tag{4.6}$$

the true phase can be expressed as

$$\phi[x+1] = \phi[x] + \Delta\phi[x]. \tag{4.7}$$

In order for the true phase to be correctly determined from $\Delta\phi[x]$, the condition

$$|\Delta\phi[x]| \leqslant \pi. \tag{4.8}$$

must be met. If this condition is satisfied, the true phase difference is equal to the wrapped difference of the wrapped phase shift,

$$\Delta\phi[x] = \mathcal{W}_r[\Delta\phi_w[x]]. \tag{4.9}$$

$\mathcal{W}_r[\Delta\phi_w[x]]$ can be determined from the extracted, wrapped phase values $\phi_w[x]$. If the phase value at the first sample point, $\phi[0]$, is known, the phase at any subsequent point, m, can be unwrapped. This is done by evaluating the following path integral:

$$\phi[m] = \phi[0] + \sum_{x=0}^{m-1} \mathcal{W}_r[\Delta\phi_w[x]]. \tag{4.10}$$

4.1.2 *Two-dimensional phase unwrapping*

Equation 4.5 can be extended to an expression which describes phase unwrapping for a two-dimensional signal:

$$\phi[x,y] = \phi_w[x,y] + 2\pi c[x,y]. \tag{4.11}$$

Similarly to Fig. 4.1, Fig. 4.2 shows an equivalent 2D example of a wrapped and true phase shift. For the phase extracted from the Dixon images, the phase unwrapping involves finding the unique set of integer values $c[x,y]$ which remove the phase wraps from every pixel $[x,y]$. Unwrapping the phase of a 2D image is achieved

[1] $x = [1:240]$ is the index of each sample in the signal.

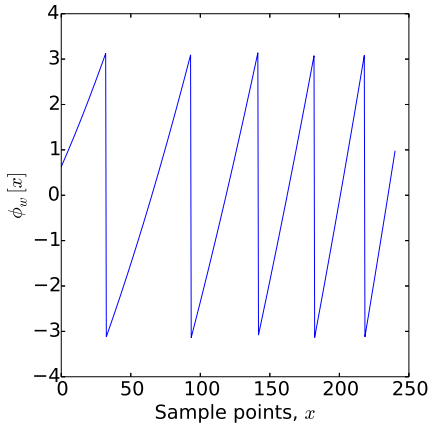

(a) Wrapped phase

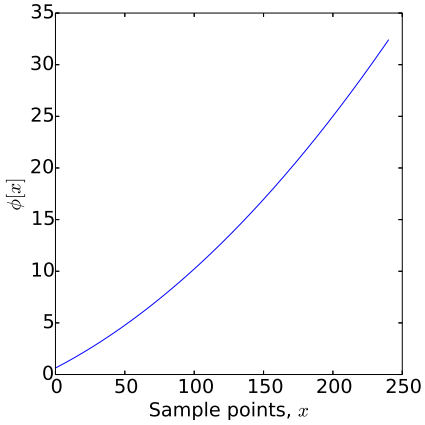

(b) Unwrapped phase

Figure 4.1: One-dimensional phase shift.

by performing a set of path integrals, similar to the 1D line integral in Eq. 4.10. In an ideal situation, the phase can be unwrapped along any path in the image; the unwrapping is path-independent. However, noise and discontinuities cause the integration to be path-dependent. Points that cause problems in the phase unwrapping are called residues [Ghiglia and Pritt, 1998c].

The complexity of the 2D phase unwrapping required can be assessed by calculating the number of phase wraps, or discontinuities, E, in a wrapped phase image. E is obtained from taking the sum of the horizontal and vertical jump counts, $h[x, y]$ and $v[x, y]$, across every pixel in the image. A horizontal jump count has a value of one if the difference between two adjacent horizontal pixels exceeds π radians in magnitude:

$$h[x, y] = \text{Ceiling}\left[\frac{\phi[x+1, y] - \phi[x, y]}{2\pi}\right] \tag{4.12}$$

The vertical jump counts are obtained using a similar expression. E is calculated using the following equation,

$$E = \sum_{x=0}^{M-1}\sum_{y=0}^{N-1} |h[x, y]| + \sum_{x=0}^{M-1}\sum_{y=0}^{N-1} |v[x, y]|, \tag{4.13}$$

where M and N are the number of pixels in the x and y dimensions of the image, respectively. Clearly E scales with the total number of pixels.

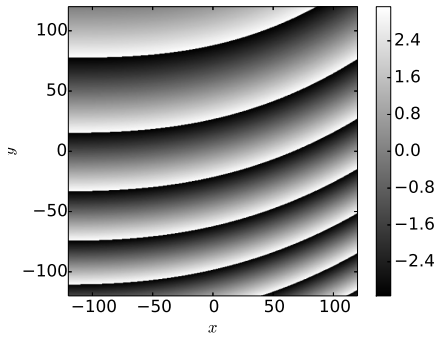

(a) Wrapped phase

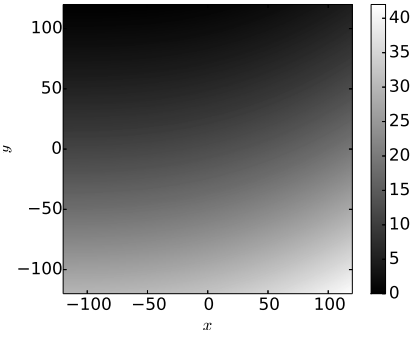

(b) Unwrapped phase

Figure 4.2: Two-dimensional phase shift.

4.1.3 *Undersampled data*

In order for the phase to be correctly unwrapped using straightforward path integration, the condition in Eq. 4.8, $|\Delta\phi[x]| \leqslant \pi$, must be true. This is analogous to the Nyquist sampling criterion. If the sampling rate of a signal fails to meet the Nyquist criterion, aliasing occurs and the true signal cannot be exactly recovered. Similarly, if Eq. 4.8 is not met, ambiguity in the unwrapped phase exists.

The largest phase change $\Delta\phi$ which can be resolved without aliasing is $|\pi|$ per sample. An alternative way of understanding this requirement is that between two adjacent wrapped samples $\phi_w[x_1]$ and $\phi_w[x_2]$, where x_1 and x_2 are adjacent on any path, the integer 2π values used to unwrap these samples must not increase or decrease by more than one:

$$|c[x_1] - c[x_2]| \leqslant 1. \tag{4.14}$$

For signals with a rapidly varying phase shift, this condition does not hold as the phase shift is undersampled. The phase unwrapping therefore produces one of many possible solutions.

4.2 RESIDUES

Residues exist at locations where inconsistencies in the phase unwrapping occur if an integration path includes these pixels. The

presence of a residue indicates path dependence at this point; integrating across this residue along two different paths gives two different results. This is demonstrated in Fig. 4.3.

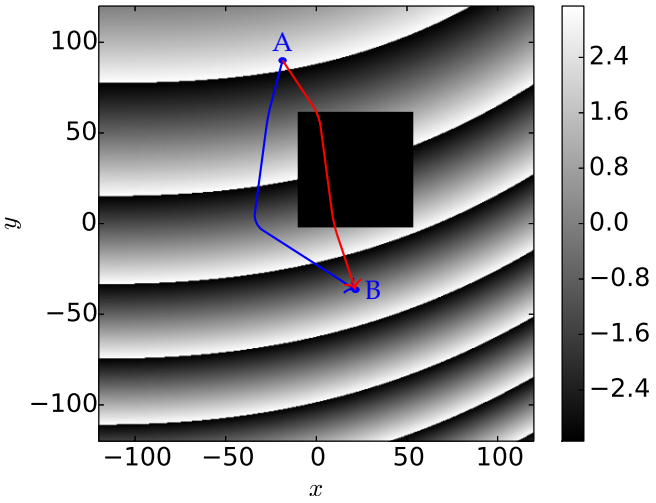

Figure 4.3: Pixels in this two-dimensional wrapped phase shift can be unwrapped by traversing multiple paths through the image. However, the black square produces discontinuities in the phase, which affects the phase unwrapping. Integrating along the red line between points A and B produces a different result compared to integrating along the blue line; the phase unwrapping is therefore path-dependent. Figure recreated from Ghiglia and Pritt [1998b], Fig. 4.1.

The requirements for path independence state that the integral around a closed path must be zero:

$$\oint_C \mathbf{F} \cdot d\mathbf{r} = 0, \tag{4.15}$$

where C is any closed path (loop) in N-dimensional space, and $\mathbf{F}$ is a conservative vector field defined at each point $\mathbf{r}$ [2]. By comparison, the theory of residues states that the loop integral around a residue is a nonzero multiple of 2π,

$$\oint_C \mathbf{F} \cdot d\mathbf{r} = 2\pi k, \tag{4.16}$$

where k is an integer which gives the number (and order) of residues enclosed by the path.

The existence of residues in a 2D phase map is identified by taking the sum of the wrapped phase differences around a 2x2 array of adjacent pixels. This is the smallest loop which can be constructed on a 2D discrete image. Loops which contain residues sum to a multiple of 2π, while those without residues have a value of zero. Each residue has a positive or negative value for k, depending on the direction in which the loop is traversed. By convention, a positive residue corresponds to k positive for an anti-clockwise loop. Fig. 4.4 shows a diagram demonstrating how the loop integral is calculated, with:

$$\Delta_1 = \mathcal{W}_r[\phi_{w,2} - \phi_{w,1}], \tag{4.17}$$

where $\phi_{w,1}$ and $\phi_{w,2}$ are the wrapped phase values at points 1 and 2, respectively, and so on for the other three sides.

There are three main contributors to residues in phase maps extracted from Dixon images near metal, with examples labelled in

[2] Refer to Chapter 2 of Ghiglia and Pritt [1998c], *Line Integrals, Residues, and 2D Phase Unwrapping*, for a proof and explanation.

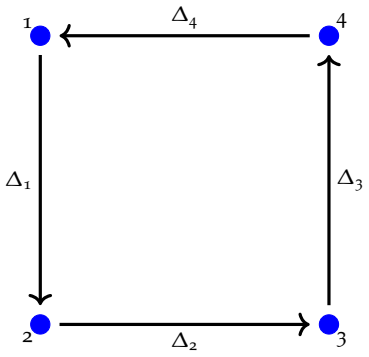

Figure 4.4: Diagram showing the loop integral used to identify residues in the wrapped phase. By convention, the location of the residue is associated with point 1, at the top left corner. The actual location of the residue is enclosed within the four points.

Fig. 4.5. Noisy pixels and discontinuities in the phase, such as at the implant-tissue boundary, can produce inconsistent data. There is no signal from the metal, so the extracted phase within these pixels is noisy. We must avoid unwrapping across these pixels if we wish to correctly unwrap the field map. The third cause of residues is adjacent pixels where the magnitude of the true phase difference is greater than π. These pixels are undersampled but need to be unwrapped. Using the residue test, there is no way of distinguishing between inconsistent and undersampled data. In general, the most difficult regions of the image to unwrap occur close to the implant, where it is necessary to unwrap the rapidly varying phase while coping with discontinuities and noisy data.

Figures 4.5 and 4.6 illustrate an attempt to unwrap a simulated phase map while ignoring the presence of residues. Errors originate from incorrectly estimating the phase at the location of the residues. These are propagated in the unwrapping of the following pixels and are shown as streaks in Fig. 4.6. These images demonstrate how residues corrupt the unwrapped phase if they are not identified correctly and avoided.

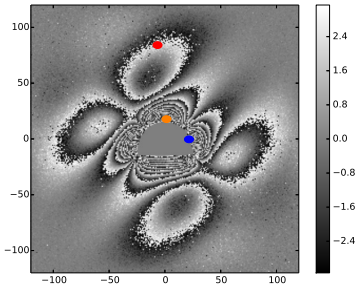

Figure 4.5: Wrapped phase shift displaying three main sources of residues. The red marker is located at a noisy pixel, the blue marker at a discontinuity and the orange marker at an undersampled pixel.

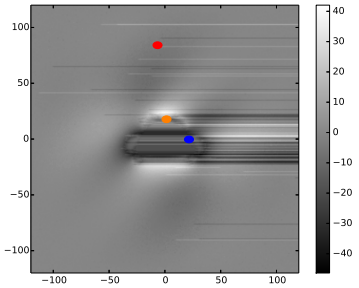

Figure 4.6: Result obtained from unwrapping the phase shift in Figure 4.5. The phase shift was unwrapped horizontally across the image from left to right and the residues were ignored.

4.3 BRANCH CUT METHODS

Phase unwrapping paths must be carefully chosen to ensure that noise and discontinuities do not cause errors to accumulate. Branch cut algorithms are used to calculate a suitable set of integration paths. First, the residues in the image are located. Each positive residue is matched to a nearby negative residue. This creates a set of branch cuts. These are lines in the image which the integration paths must not intersect if the phase unwrapping is to succeed.

The standard branch cut phase unwrapping method was developed by Goldstein et al. [1988]. In this method, after the branch cuts are generated, the phase is unwrapped using a flood-fill algorithm. The unwrapping begins at a seed pixel, where the phase is known and is not wrapped. The four adjacent pixels of the seed pixel are then unwrapped. The subsequent adjacent pixels are unwrapped, and so the set of unwrapped pixels grows outwards from the seed pixel. Pixels which lie across branch cuts are avoided during the flood-fill unwrapping, and are dealt with in the final step of the algorithm.

▶ MATCHING EACH POSITIVE RESIDUE with an appropriate negative residue is not straightforward and becomes more complicated as the number of residues increases. In general, it is desirable that the branch cuts are as short as possible. This is because long branch cuts increase the chance that large regions of the image will be isolated and will not be able to be unwrapped. In practice, it is impractical to measure the length of every possible set of branch cuts [3].

Figure 4.7 shows two possible branch cut arrangements for three positive and three negative residues in a 4×3 grid. Figure 4.7(a)

[3] In Goldstein's method, the branch cuts are generated by passing a 3×3 box over the image and matching residues within the box. Chapter 4 of Ghiglia and Pritt [1998b], *Path-following methods*, gives a comprehensive description of the method.

shows the best configuration, where all positive residues are balanced by an immediately adjacent negative residue. However, if the red and blue branch cuts are placed as shown in Fig. 4.7(b), this forces the purple branch cut to be 5x longer than in Fig. 4.7(a). This demonstrates how changing the location of a single branch cut can result in a poor arrangement overall.

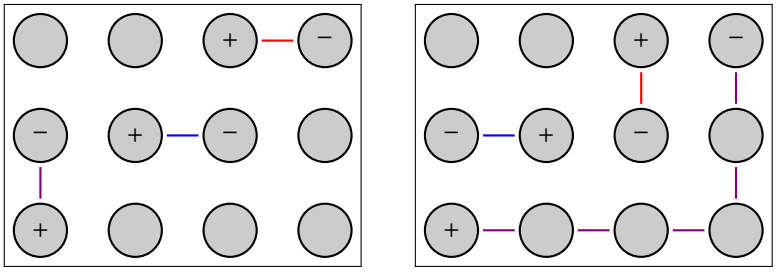

(a) (b)

Figure 4.7: Two possible sets of branch cuts for a group of six residues.
a) Optimal branch cut arrangement.
b) Poorly placed branch cuts.

In images (or regions of images) with a low SNR, the number of residues increases significantly. Generating a suitable set of branch cuts from the residues becomes more difficult, as it is less likely that positive residues will be matched correctly with negative residues.

4.4 MINIMUM-NORM METHODS

Instead of using branch cut methods, the phase unwrapping can be expressed as a least squares problem [Ghiglia and Romero, 1994]. With the known wrapped phase difference between adjacent pixels, $\Delta\phi_w$, and the unknown true phase difference, $\Delta\phi$, the least squares solution finds the unwrapped phase, $\phi[x, y]$, which minimises the least squares difference between $\Delta\phi_w$ and $\Delta\phi$. This assumes that the true phase difference between adjacent pixels is less than π in magnitude.

Similar to the 1D phase difference given by Eq. 4.6, in 2D the difference in the true phase between adjacent pixels in the x-direction and y-direction is defined as:

$$\Delta\phi_x = \phi[x+1, y] - \phi[x, y] \tag{4.18}$$

$$\Delta\phi_y = \phi[x, y+1] - \phi[x, y]. \tag{4.19}$$

This is a first order discrete derivative, approximated using a forward difference. Correspondingly, the wrapped differences of the wrapped phase values in the x-direction and y-direction are

$$\Delta\phi_{w,x} = \mathcal{W}_r[\phi_w[x+1, y] - \phi_w[x, y]] \tag{4.20}$$

$$\Delta\phi_{w,y} = \mathcal{W}_r[\phi_w[x, y+1] - \phi_w[x, y]], \tag{4.21}$$

where $\mathcal{W}_r[\cdot]$ is the wrapping operator. The phase $\phi[x, y]$ which minimises

$$\sum_{x=0}^{M-2}\sum_{y=0}^{N-1}(\Delta\phi_x - \Delta\phi_{w,x})^2 + \sum_{x=0}^{M-1}\sum_{y=0}^{N-2}(\Delta\phi_y - \Delta\phi_{w,y})^2 \tag{4.22}$$

is the least squares solution, where M and N are the dimensions of the image. This equation states that in 2D the least squares solution satisfies the phase differences summed over all pixels in the x-direction and the y-direction. Equation 4.22 is often written in matrix form [4].

Hunt [1979] and Ghiglia and Romero [1994] showed that Eq. 4.22 can be simplified to a discrete form of Poisson's equation. This can be solved efficiently with the discrete cosine transform (DCT) to obtain the unwrapped phase $\phi[x, y]$.

[4] The reader is referred to Hunt [1979] and Ghiglia and Romero [1994] for a full derivation.

4.5 WEIGHTED BRANCH CUT AND MINIMUM-NORM METHODS

The described branch cut and minimum-norm phase unwrapping methods assume that every measured value of the wrapped phase has equal importance. However, some measured values are more important or more accurate than others. Weighted branch cut and minimum-norm methods are used to prevent "poor-quality" pixels from unduly influencing the phase unwrapping.

In the weighted minimum-norm method, weighted least squares is used to prioritise the measured values by their relative validity, on a scale of $[0, 1]$. Values with a weighting of 0 make no contribution to the final unwrapped phase. In the weighted branch cut method, pixels with a high weighting are unwrapped first, and pixels with a weighting of 0 are avoided completely.

Weighting masks can be calculated using several different methods. They are often derived from "quality maps", which provide a quantitative measure of the quality of the phase at each pixel. Common methods used to calculate quality maps include:

- Calculating the variance of the derivative of the phase.
- Calculating the maximum phase gradient in a small neighbourhood of each pixel.
- Using additional signal information [5].

[5] For example, when performing phase unwrapping on synthetic aperture radar data, a correlation map can be used to generate the quality map.

The weighting mask is generally calculated by applying a threshold to the quality map.

Near metal, there are discontinuities in the wrapped phase differences across the boundary between the metal object and the surrounding tissue. Additionally, certain pixels in the vicinity of the metal may be significantly altered by signal loss and noise. These pixels need to be assigned a low weighting so their influence on the unwrapped phase is minimised.

4.6 OTHER PHASE UNWRAPPING METHODS

Basic models have been used to assist the estimation of the phase. Liang [1996] describes the two-dimensional unwrapped phase as

$$\phi[x, y] = P[x, y] + r[x, y], \tag{4.23}$$

where $P[x, y]$ is a two-dimensional polynomial model of order N_P and $r[x, y]$ is the residual, composed of errors in the model and noise. By using this model, the phase unwrapping is transformed into estimating the coefficients of the polynomial model.

This approach assumes that the phase in MR images is smooth, and can be modelled accurately by a polynomial. In standard MR imaging, this assumption is generally valid. However, the phase in MR images near metal is not globally smooth, due to the discontinuous boundary between the tissue and the implant. In addition, a high order polynomial would be needed to accurately fit the rapidly varying phase near the implant boundary. A set of piecewise continuous polynomials may be a more suitable model [Skare and Andersson, 2005] [6].

Statistical methods have been used to estimate the phase, including incorporating prior knowledge in the form of a Markov random field or total variation model. Some methods use global optimisation techniques such as simulated annealing to minimise the formulated objective function [Nico et al., 2000, Stramaglia et al., 2000, Ying et al., 2006]. Costantini [1998] expresses the phase unwrapping problem as a network of integers to be optimised.

Flynn [1997] developed a visually intuitive phase unwrapping method. The discontinuities along 1D lines in the 2D wrapped phase images are identified. In other words, these are the lines where the wrapped phase goes from $+\pi$ to $-\pi$, or where the image pixel intensities go from light to dark (as shown in Fig. 4.2). These lines are then joined into loops. Multiples of 2π are then added to the pixels inside the loops, until the number of discontinuities in the image, E (Eq. 4.13), is minimised.

There are a number of common features in the methods described in this chapter. First, all have a mechanism for preventing residues or "poor quality" pixels from influencing the unwrapped result. Examples given include arranging unwrapping paths around residues, using a weighting map, or imposing smoothness on the phase using a model-based approach. Second, all methods involve efficiently minimising some type of objective function. Branch cut methods aim to minimise the length of the generated branch cuts, minimum-norm methods use an objective function based on least-squares, and model-based methods use a range of objective functions.

The third common feature of the methods described in this chapter is that all assume the phase is adequately sampled, and the condition in Eq. 4.8 is true. This cannot be assumed near metal, where the $\mathbf{B}_0$ field variation varies rapidly. Some degree of prior knowledge is required to accurately unwrap undersampled phase shifts.

[6] The main contribution in this thesis, the Phase Onion Peeling method (POP), is based on a similar approach, but uses a Fourier series model instead of a polynomial model. The method is described in Chapter 6.

Part II

CONTRIBUTIONS

In this part the major contributions of the thesis are presented. There are seven chapters. The first describes the acquisition and reconstruction of phantom data. The following three chapters present the major contribution made by this thesis, the *Phase Onion Peeling (POP)* algorithm. Results of testing this method on phantoms and participants are included. Then, two extensions to POP are introduced: a modification to the POP objective function based on the VARPRO iterative least squares method, and an investigation into using an alternative set of basis functions in POP. The final chapter outlines the key contributions and conclusions made by this research, and makes recommendations for future work.

5

Magnetic Field Simulation and Phantom Data Acquisition

This chapter outlines work done on simulating the field variation induced by metal orthopaedic implants. It also describes the process for attaining phantom data, including phantom construction, data acquisition, and reconstruction.

Phantoms are often used in MRI research as they allow for data to be acquired from a known object. Phantom studies were carried out in this thesis to assess the performance of fat suppression techniques near metal implants in a controlled environment. The phantoms contained implants with a known composition and piecewise homogeneous regions of water and peanut oil, or "fat".

Phantom data were acquired for three types of implants:

1. Implant 1: total hip replacement with a titanium femoral stem and acetabular shell, and a ceramic-on-ceramic femoral head and acetabular liner.
2. Implant 2: total hip replacement with a titanium stem and shell, and cobalt-chromium head and liner.
3. Implant 3: non-ferrous stainless steel femur implant.

Each implant was embedded in a plastic container of agar gel doped with copper sulfate. Vials of peanut oil were used to simulate regions of fat. The phantom construction is described in Sec. 5.3. Photos of the Implant 1 and Implant 3 components are shown in Figures 5.1 and 5.2.

During scanning, each implant was oriented in the coronal plane. The femoral stem of the hip replacements and the long axis of the femur replacement were aligned with the long axis of the scanner bore: along the direction of the static $\mathbf{B}_0$ field. Figure 5.3 shows a diagram of the orientation of the implants in the scanner, where $x-y$ is the transverse or axial plane, $y-z$ is the sagittal plane, and $x-z$ is the coronal plane. All 2D slices used in this thesis are in the coronal plane.

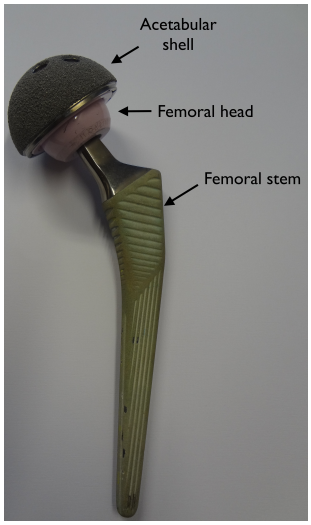

Figure 5.1: Implant 1 components: titanium stem and shell, and ceramic head and liner. The liner is not visible but sits within the shell.

Figure 5.2: Implant 3.

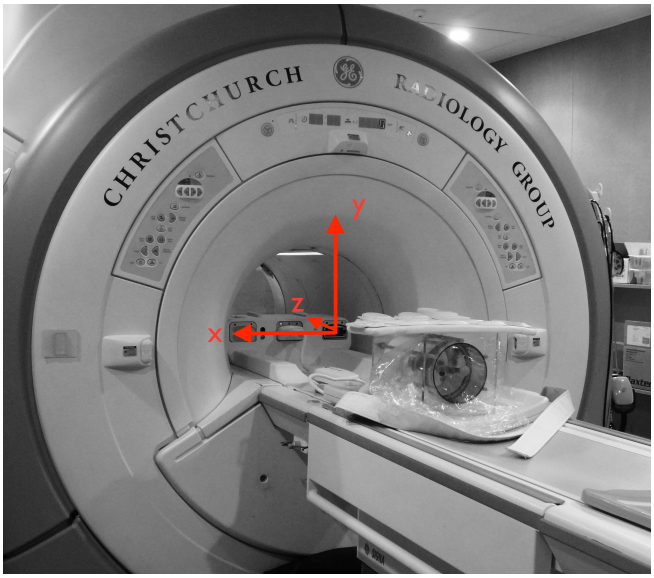

Figure 5.3: An early phantom in the GE scanner at the New Zealand Brain Research institute. Arrows show the coordinate system used in this thesis. $\mathbf{B}_0$ is oriented in the z-direction along the bore of the magnet.

5.1 ACQUIRING IMPLANT GEOMETRY

The 3D geometries of Implants 1 and 3 were obtained using a white light scanner [1]. This produced a stereolithographic (STL) file, which was then converted to a 3D matrix of voxels.

An STL file describes the surface geometry of a 3D object by a set of contiguous triangular facets. Each facet has three vertices and a unit normal indicating its orientation (Figure 5.4). The position of each vertex and the normal are specified using Cartesian coordinates, $\mathbf{x} = [x, y, z]$. The voxelisation process converts these to a grid of cubic voxels which are ordered with Cartesian coordinates [2].

The STL files were first aligned to approximately the same orientation as the acquired phantom images. This was done in *MeshLab*, an open source STL editing software package [Mes, 2014]. Before voxelisation, affine transforms were applied to the STL facets to refine the orientation and position of the geometry.

The voxelisation algorithm first finds the bounding box of the STL model. This is used to calculate the dimensions of the voxel grid. Rays are then projected along each axis in a pre-set order. The intersections of the rays with the facets are used to determine the locations of voxels where the object is present. This voxelisation process converts the STL surface geometry to a binary grid. Voxels with a value of 1 indicate they originate from "inside the surface". This process therefore assumes that the STL file describes a solid object with no internal cavities.

The dimensions of the voxel grid are determined by the 3D field of view **FOV** and resolution **RES** of the image [3]. The number of voxels in the x direction are calculated by

$$(\text{Number of voxels})_x = \text{Ceiling}\left[(\text{Bounding box resolution})_x \times \left(\frac{\text{FOV}_x}{\text{RES}_x}\right)\right], \tag{5.1}$$

and similarly for the y and z directions. The corner coordinates of

[1] The scanner was manufactured by *Arctec 3D*, with the geometries reconstructed with the accompanying software, *Artec Studio* [Arctec 3D, 2015].

[2] Patil and Ravi [2005] give a detailed description of the voxelisation algorithm which was used.

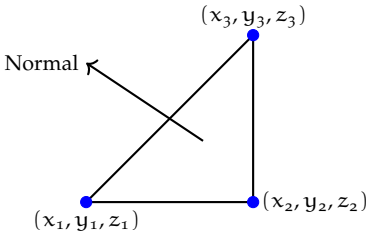

Figure 5.4: Depiction of a single facet in an STL file.

[3] Recall that **FOV** and **RES** are defined on P. 17.

the voxel grid bounding box are used to place the voxel grid into a 3D grid with the same dimensions as the image resolution, **RES**.

Converting from a continuous representation of the object geometry to a discrete voxel grid can cause the object to appear voxelated. This effect is reduced by increasing the image resolution to $n \times$ **RES**, $\{n = 2, 4, 8, ...\}$ during the voxelisation. The image is then resampled back to a resolution of **RES**.

The geometry of the acetabular shell, femoral head, and femoral stem of Implant 1 were obtained in separate scans, and combined during the voxelisation process. Susceptibility values were assigned to each component during the voxelisation. The susceptibility values were not known exactly but were estimated to be:

- Titanium: $\chi = 180\,\text{ppm}$
- Ceramic: $\chi = -18\,\text{ppm}$ [4]
- Non-ferrous stainless steel: $\chi = 4000\,\text{ppm}$.

Figure 5.5 shows the rendered STL geometries for the Implant 1 and Implant 3 components. Figure 5.6 shows a 2D slice through the centre of the voxelised objects for Implants 1 and 3.

[4] The ceramic components were made of Biolox®, which is approximately 75 % aluminium oxide and 25 % zirconium oxide [Dalla Pria, 2007]. Aluminium oxide has a susceptibility of -18.1 ppm and zirconium oxide -8.3 ppm [Schenck, 1996].

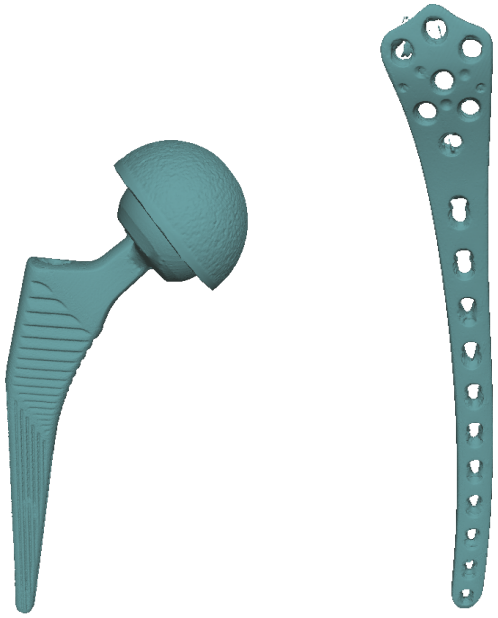

(a) (b)

Figure 5.5: Rendered STL geometries:
a) Implant 1.
b) Implant 3.

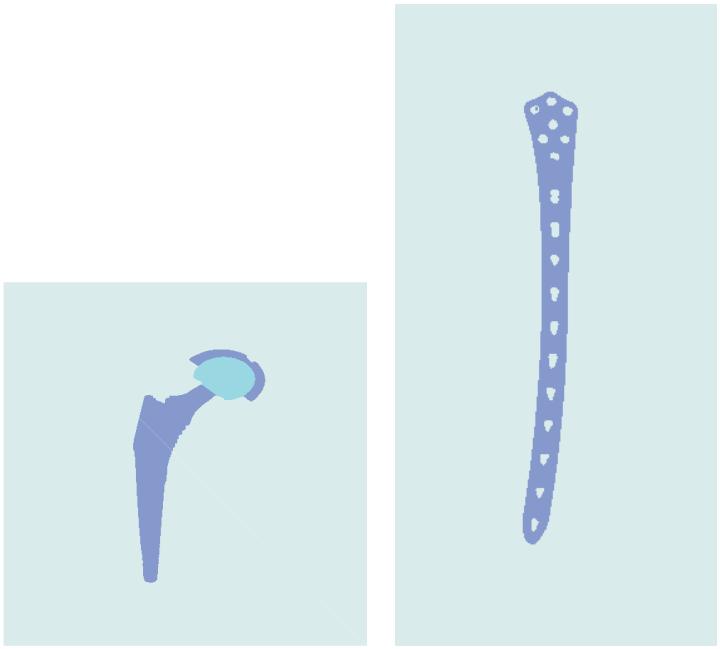

(a) (b)

Figure 5.6: Voxelised implant geometry:
a) Voxelised geometry for the centre slice for Implant 1. The titanium component is shown in dark blue and the ceramic in light blue.
b) Voxelised geometry projected across all slices for Implant 3. The projection is shown instead of just the centre slice to better visualise the implant geometry.

5.2 MAGNETIC FIELD SIMULATION

The voxelisation process produced a 3D susceptibility map for Implants 1 and 3. This was used to estimate the induced magnetic field variation with the susceptibility distribution method described by Eq. 2.19 in Section 2.3.1. This was converted to a resonant frequency variation, Δf, using the Larmor equation [5]. In these simulations, $B_0 = 3\,T$. A 2D $x-z$ slice through the centre of the Δf map for Implants 1 and 3 is shown in Figure 5.7. The displayed resonant frequency variations are important data used for simulation and analysis throughout this thesis.

[5] Recall from Eq. 2.9,

$$\Delta f = \frac{\gamma}{2\pi}\Delta B_0. \qquad (5.2)$$

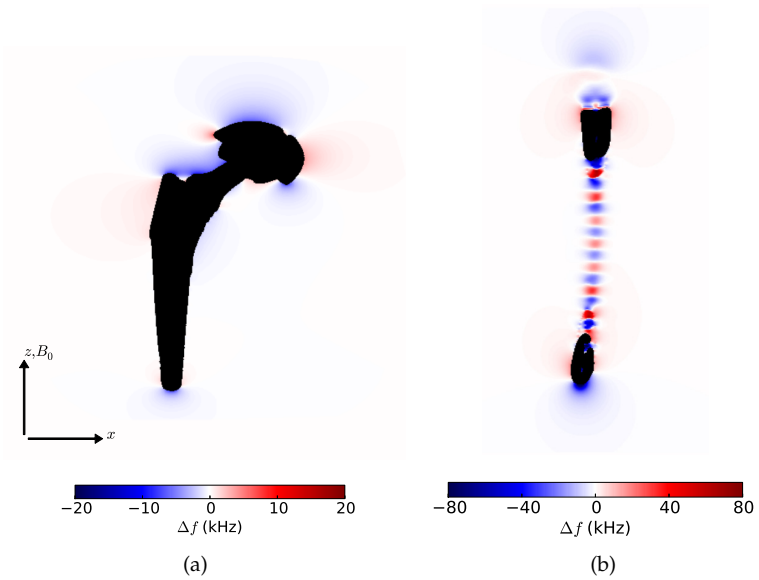

(a) (b)

Figure 5.7: Simulated resonant frequency variations:
a) Centre slice for Implant 1.
b) Centre slice for Implant 3.

5.3 PHANTOM CONSTRUCTION

Phantom 1 was constructed at the Lucas Imaging Center at Stanford University in June 2015. It consisted of a plastic container holding Implant 1 suspended in agar gel. Three vials of peanut oil were arranged around the implant.

Phantom 2 was built at the Lucas Center for other applications. It consisted of a plastic container with Implant 2 embedded inside a plastic grid, which was held suspended in agar gel. The grid was 3D-printed with a known uniform spacing to examine distortion near the implant boundary. No peanut oil was present in this phantom. The geometry of Implant 2 could not be obtained using the white light scanner as the implant was fixed in place inside the grid and agar.

Phantom 3 was built in Christchurch in May 2016. Similar to Phantom 1, it contained Implant 3 suspended in agar gel with six vials of peanut oil arranged around the implant.

▶ THE AGAR GEL for each of the phantoms was prepared using the following procedure, based on the process described by Mitchell et al. [1986].

The implant and vials of oil were first suspended in the container using removable supports. The concentration of agar powder used was 2 % weight/volume. This is equal to 20 g of powder per litre of water. The agar was doped with copper sulfate $CuSO_4.5H_20$. The concentration of copper sulfate used was 1 mmol/L. This is equal to 0.25 g per litre of water.

The agar and copper sulfate were dissolved in the required volume of cold water. This was brought to a boil over a moderate heat, while stirring constantly. Once boiling point was reached, the mixture was kept at a rolling boil while stirring for 10 minutes, to ensure a full transition from liquid to gel. The gel was then poured into the container and left to set overnight. Finally, the supports were removed once the gel had fully set.

5.4 DATA ACQUISITION

Data for Phantoms 1 and 2 were acquired on a GE 750 3 T MRI scanner at the Lucas Imaging Center in June 2015. Data for Phantom 3 were acquired on a GE 750 3 T scanner at the New Zealand Brain Research Institute at Hagley Radiology in May 2016. Raw k-space data were acquired for each phantom, with the reconstruction of this data outlined in Section 5.5.

Phantoms 1 and 2 were scanned with the 2D-FSE IDEAL and 3D MAVRIC-SL protocols [6]. The scan parameters are given in Table 5.1. For each phantom, the IDEAL protocol was repeated seven times. A different set of echo time offsets was used for each acquisition, and these are shown in Table 5.2. This produced a set of 21 images, each with a different phase evolution.

[6] The MAVRIC-SL reconstruction process is outlined in Appendix A.3. The reconstructed MAVRIC-SL images do not form a central part of this thesis, but may be useful for the development of future methods.

Phantom 3 was scanned with the 2D-FSE IDEAL protocol. The scan parameters for Phantom 3, which were different to those used for Phantoms 1 and 2, are shown in Table 5.3. The protocol was repeated for three different sets of echo time offsets. These are shown in Table 5.4. Phantom 3 was also scanned using 2D-FSE STIR (inversion recovery) and 2D-FSE fat saturation protocols, for comparison between existing fat suppression techniques.

5.5 DATA RECONSTRUCTION

The "Orchestra" software development kit (SDK) provided by GE Healthcare was used to reconstruct the acquired raw k-space data [Orchestra, 2015]. The reconstruction was done in MATLAB® [MATLAB, 2015].

For each 2D IDEAL acquisition with N_S echo time offsets (with $n = 1, 2, ..., N_S$ and $N_S = 3$ for the acquired data) and M_S slices, there are $N_S \times M_S$ images to reconstruct. The reconstruction process can be summarised in the following steps:

1. Load the data for each acquisition into MATLAB.
2. Extract relevant header information from the raw header.
3. Reconstruct each of the N_S echo time offset images for each of the M_S slices. This involves four steps:
   (a) Extract the k-space data for the current n and m indices.
   (b) Zero pad the k-space data to the desired resolution.
   (c) Take the inverse 2D FFT to get the complex image data.
   (d) Store the complex image data in a structure indexed by n and m.

In order to assist the reader with visualising the composition of each phantom, reconstructed magnitude images are shown. Figures 5.8 and 5.9 show three reconstructed 2D-FSE magnitude images for Phantoms 1, 2, and 3. These were obtained by taking the magnitude of the IDEAL complex image data which was obtained as described above in Steps 1–3. The central slice is shown for each phantom, and all slices are the first ($n = 1$) IDEAL echo time offset images. These slices show the location of the fat vials in Phantoms 1 and 3, in relation to the implant. The plastic grid in Phantom 2 is also visible.

Parameter	Value
Echo time (TE)	10 ms
Repetition time (TR)	3400 ms
Slice thickness	3 mm
Slice gap	0 mm
Readout bandwidth (BW_r)	125 kHz
Echo train length (ETL)	16
Refocus flip angle	135
Parallel imaging	disabled
Matrix size	384×136
Field of view	300×210 mm
Number of slices	16
Scan plane	coronal
Shim	auto
IDEAL	*Water* and *Fat* boxes enabled for FSE-IDEAL imaging.
Coil	Single-channel head coil

Table 5.1: Scan parameters used for Phantoms 1 and 2.

Acquisition	1	2	3	4	5	6	7
Echo time	-0.2	0	-2.8	-2.4	-2.0	-1.6	-1.2
offsets (ms)	0.6	1.1	-0.8	-0.4	0	0.4	0.8
	1.4	2.2	1.2	1.6	2.0	2.4	2.8

Table 5.2: Echo time offsets used in FSE-IDEAL imaging of Phantoms 1 and 2.

Acquisition 1 used the default IDEAL echo time offsets, and Acquisition 2 used the three-point Dixon offsets.

Parameter	Value
Echo time (TE)	12 ms
Matrix size	512×256
Field of view	390×390 mm
Number of slices	33
Coil	Eight-channel cardiac coil

Table 5.3: Scan parameters which were altered for Phantom 3.

Acquisition	1	2	3
Echo time	0	-0.2	-1.1
offsets (ms)	1.1	0.6	0
	2.2	1.4	1.1

Table 5.4: Echo time offsets used in FSE-IDEAL imaging of Phantom 3.

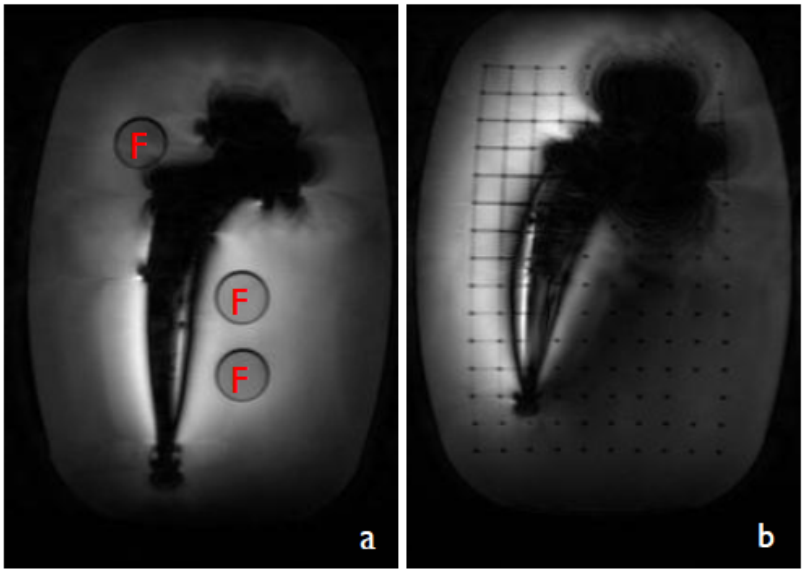

Figure 5.8: 2D-FSE magnitude images of the central slice of Phantom 1 (a) and Phantom 2 (b). The three vials of peanut oil in Phantom 1 are marked in red with 'F'.

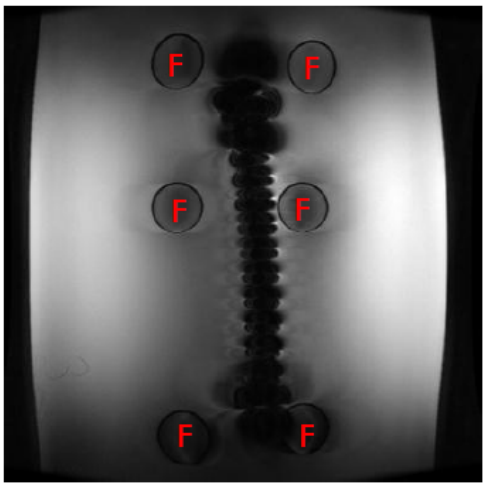

Figure 5.9: 2D-FSE magnitude images of the central slice of Phantom 3. The six vials of peanut oil are marked in red with 'F'.

5.6 DISCUSSION

The constructed phantoms were simplistic, to allow for straightforward construction. However, the phantoms were not representative of in-vivo tissue composition near metal. Each implant was embedded in a homogeneous block of agar gel. The peanut oil, or fat, was confined to small piecewise homogeneous regions of the phantom, with a clear boundary between the oil and agar. Also, in all three phantoms, the implants were a considerable distance from the outer boundary of the phantom. In other words, each implant was well-surrounded by agar [7]. Finally, each phantom contained a single metal implant.

[7] For example, the field-of-view for Phantom 3 was 390×390 mm whereas the cross-sectional dimensions of the implant were 275×30 mm.

In reality, human MR images contain a mixture of tissue types, often with indistinct boundaries between objects. Discontinuities occur at the interface between different tissue types, or at the boundary of an air gap and tissue. Metal implants may be located near the skin or an air gap. Also, in a single MR slice, there may be more than one metal implant. For example, a patient may have multiple screws and a plate implanted to fix a fracture in place. A more realistic set of phantoms would address these issues, by incorporating several tissue types and implants in a single phantom.

5.7 SUMMARY

Data were acquired for three metal orthopaedic implant phantoms: two hip replacements, and a femur implant. The STL geometries of the implants used in Phantoms 1 and 3 were obtained and voxelised, allowing for the resonant frequency variation induced by the implants to be estimated. Details of the phantom construction were provided, and the MR data acquisition and reconstruction process was outlined. Finally, limitations of the constructed phantoms were discussed.

6

Phase Onion Peeling

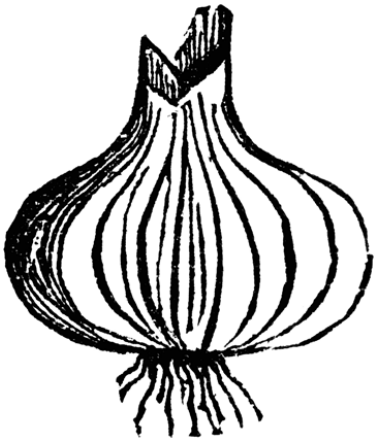

Figure 6.1: An onion.

This chapter introduces a new approach to phase estimation for the three-point Dixon technique. It is described for a 2D slice which intercepts an implant. The phase is estimated at the outer regions of each slice first. It proceeds inwards over a set of closed enveloping paths, ending at the implant boundary. The new method is called *Phase Onion Peeling (POP)*, as the process is comparable to peeling the layers of an onion.

The phase is estimated incrementally using a set of closed 1D paths which circumnavigate the implant boundary. Instead of unwrapping the phase at each individual pixel, the coefficients of a Fourier series representing the phase are estimated for the path. This simplifies the phase unwrapping, as it is now a parameter estimation problem. Fitting a Fourier series to the phase along a set of 1D paths automatically enforces (a) the recovered phase to be smooth along each path, and (b) the loop integral along each path to be zero. Due to the arrangement of the paths, this method avoids unwrapping across the discontinuous implant boundary.

This chapter is separated into the following three sections:

- Section 6.1 introduces the motivation for POP, illustrated using the simulated phase shift induced by Implant 1.
- Section 6.2 describes the path generation process. This section first introduces the nomenclature used in defining a path, and then outlines the path calculation method using distance transforms. Path generation in a range of different situations is also considered.
- Section 6.3 outlines the process of iteratively estimating the phase along the generated paths. This section describes the Fourier series representation of the phase, and explains the formulation and minimisation of the objective function used to calculate the Fourier series coefficients. Then, the stages defining how the phase estimation proceeds between adjacent paths are outlined. Finally, methods for calculating the order of the Fourier series are described.

6.1 MOTIVATION

In general, the $\mathbf{B_0}$ field variation ΔB_0 induced by a metal implant is continuous in most regions of the image and discontinuous across the implant boundary. The gradient of ΔB_0 increases as the distance to the implant boundary decreases, with the largest slopes at locations which are adjacent to the boundary.

Figure 6.2 shows the simulated phase shift $\phi[x, z]$ through the central slice of Implant 1. This was obtained by converting the simulated $\Delta f[x, z]$ map shown in Figure 5.7(a) to a phase shift by

$$\phi[x, z] = 2\pi\Delta f[x, z]t_{N_S}, \tag{6.1}$$

where $t_{N_S} = 2.2\,\text{ms}$.

Figure 6.3 shows the phase along the two paths shown in Fig. 6.2 circumnavigating the object, and Fig. 6.4 shows the phase along the three radial lines. For the circumnavigating paths, the distance along the path is shown for a clockwise traversal, commencing where the paths intersect radial line 2. For the radial lines, the distance is from the outer boundary of the simulated region to the outer boundary of the implant. The magnitude of the gradient of the phase along radial lines 1 and 2 from the edge of the image to the boundary has an increasing trend.

Note however that the phase gradient magnitude does not increase monotonically along all radial lines. An example is shown in the phase along the third radial line, which ends near concavities in the implant geometry. However, in general the gradient is steeper near the implant boundary. Likewise, the phase shift along the inner of the two circumnavigating paths contains features with a steeper gradient. The phase is therefore more difficult to estimate close to the implant.

Figure 6.3 also shows the phase shift along the paths with a 10th order Fourier series fitted to the outer path and a 30th order series fitted to the inner path. Similarly, Figure 6.5 shows the phase shift for one slice of Implant 3, with two paths marked. Figure 6.6 shows the phase along these paths, with a 30th order Fourier series fitted to both.

In conclusion, the properties of the simulated phase shifts demonstrated in this section provide the key motives for POP. In general, the phase estimation increases in difficulty the closer pixels are situated to the implant boundary. Major discontinuities in the phase occur across the implant boundary, and must be avoided to ensure accurate phase unwrapping. The simulated phase along closed 1D paths which circumnavigate the implant boundary is smooth. Finally, Figs. 6.3 and 6.6 demonstrate that the phase along these paths can be modelled by an Nth order Fourier series.

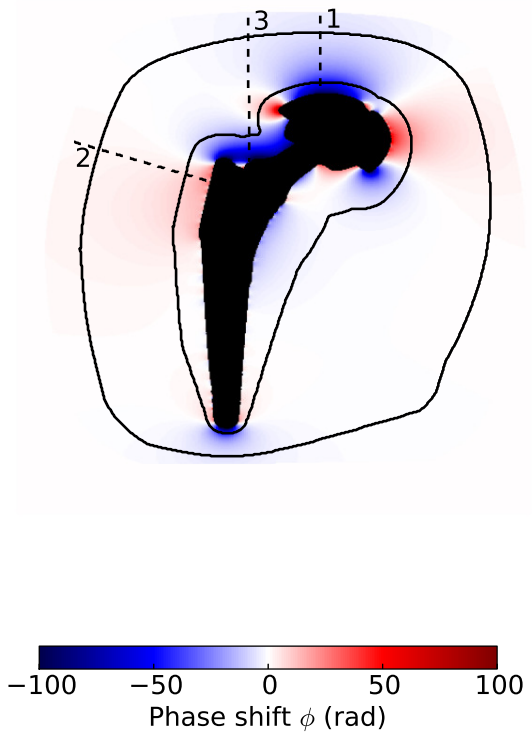

Figure 6.2: Simulated phase shift $\phi[x, z]$ produced by Implant 1. Two paths around the implant are marked with solid black lines. Three radial paths from the boundary of the simulated region to the implant boundary are marked with dashed black lines.

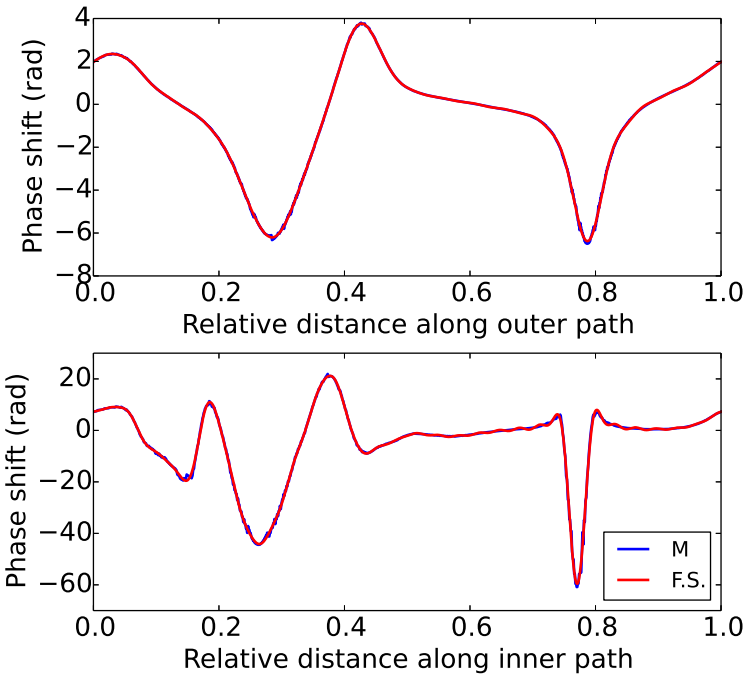

Figure 6.3: Phase shift ϕ along the outer path (top) and inner path (bottom) marked in Fig. 6.2, with 10th and 30th order Fourier series fitted, respectively. The simulated model phase (M) is shown in blue and the Fourier series fit (F.S.) in red.

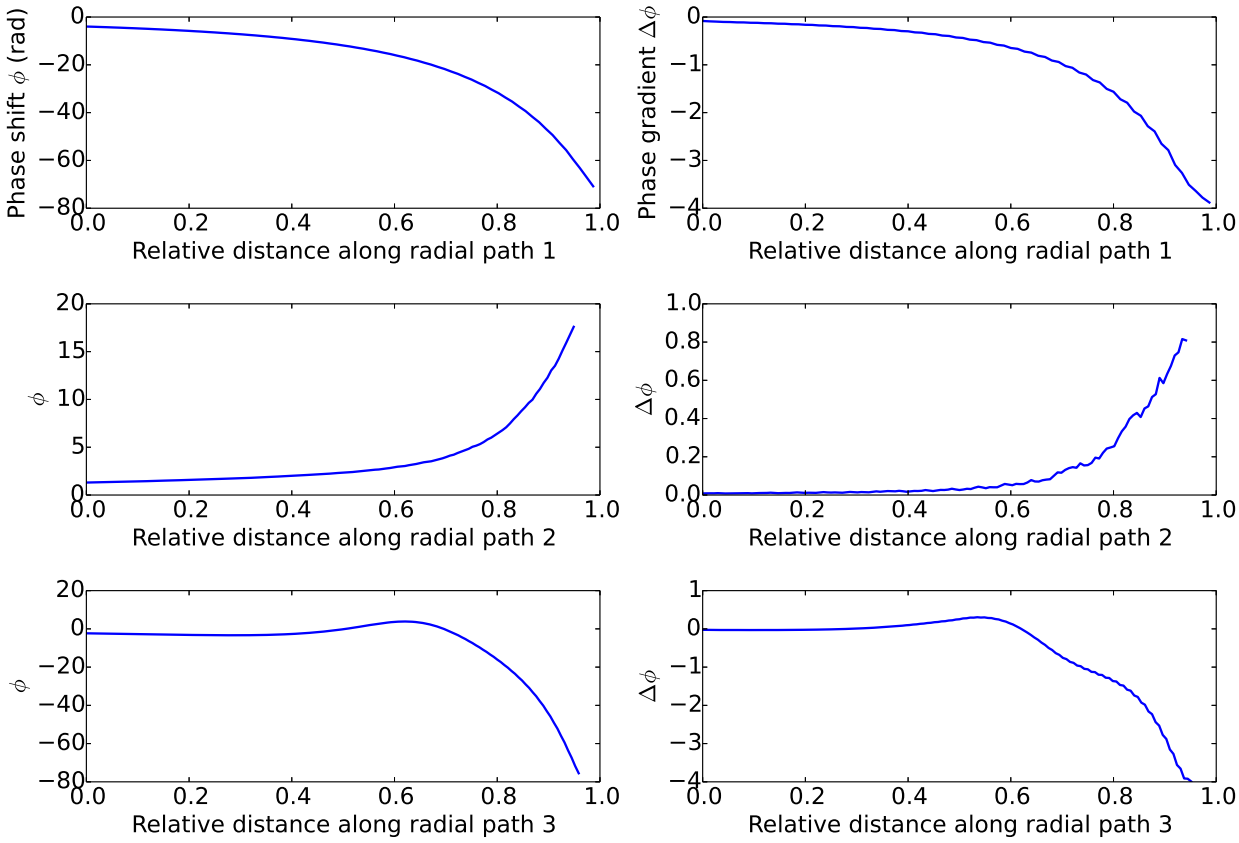

Figure 6.4: Phase shift ϕ along the three radial paths marked in Fig. 6.2, and the first order discrete derivative of the phase, $\Delta\phi$. The phase shift is plotted from the outer boundary of the imaged region to the tissue-implant boundary.

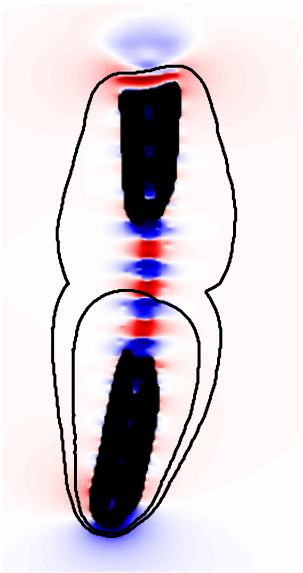

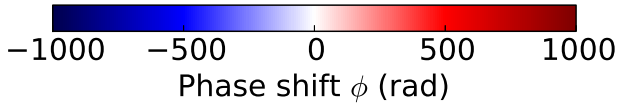

Figure 6.5: Simulated phase shift $\phi[x, z]$ produced by Implant 3. Two paths around the implant are marked with solid black lines.

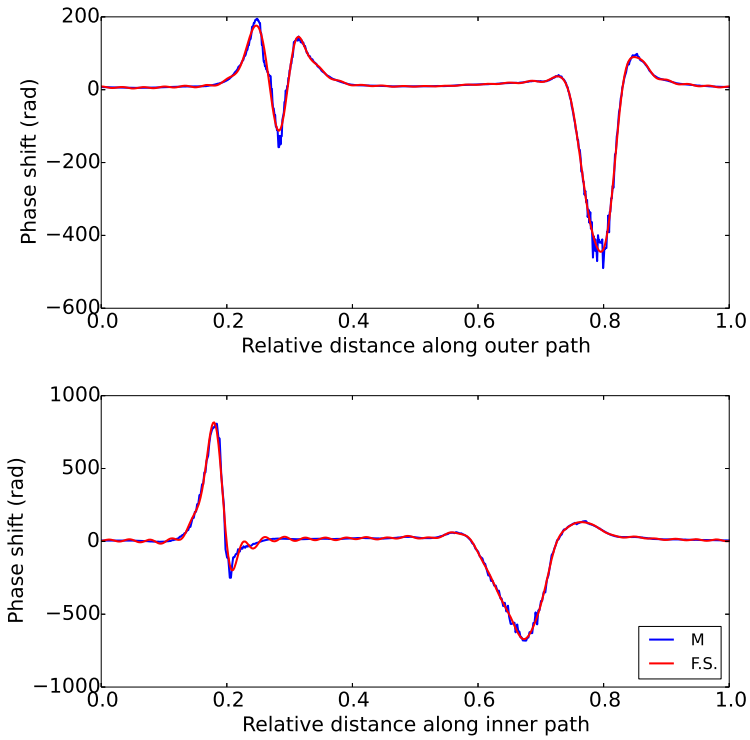

Figure 6.6: Phase shift ϕ along the outer path (top) and inner path (bottom) marked in Fig. 6.5, both with 30th order Fourier series fitted. The simulated model phase (M) is shown in blue and the Fourier series fit (F.S.) in red.

6.2 PATH GENERATION

This section outlines a method for calculating a set of closed 1D paths distributed across a 2D slice which intersects one or more implants, suitable for use in POP. Distance transforms are used to efficiently construct the paths in the region between the implant boundary and the outer boundary of the slice. This method produces a set of non-overlapping paths which do not intersect with the discontinuities present at the implant boundary and the outer boundary of the slice. The described method allows for flexible spacing between the paths, and is applicable to slices which contain more than one implant.

There are three main components to this section. First, the terminology used in defining the paths is introduced. This is followed by a description of the distance transform method used to produce the set of paths. Finally, the application of the described method to different imaging situations is considered, including when multiple implants are present in the slice.

6.2.1 *Path definition*

First consider the diagram shown in Fig. 6.7. There are two boundary paths:

- Γ_i: the boundary around the edge of the object (or implant), and

- Γ_o: the boundary around the outer edge of the image.

Γ_o is closed, completely encloses Γ_i, and has no points in common with Γ_i. In Fig. 6.7 there is only one object in the image, but Γ_i may comprise multiple closed sub-boundaries. This is shown in Fig. 6.8, where there are two objects and Γ_i is split into two sub-boundaries: Γ_{i1} and Γ_{i2}. None of the sub-boundaries overlap or enclose each other. This can be extended to an image with S objects, with the sub-boundaries for each object labelled Γ_{is}, $s = 1, 2, ..., S$. The space between the inner and outer boundaries is labelled Ω. This is the region within which the paths are formed.

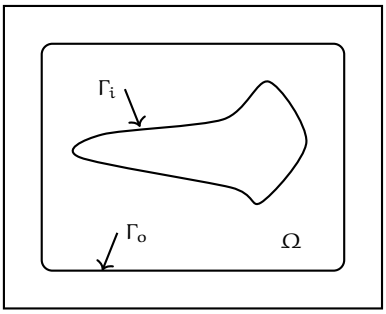

Figure 6.7: A hypothetical image slice with one object present. This has a single closed inner boundary.

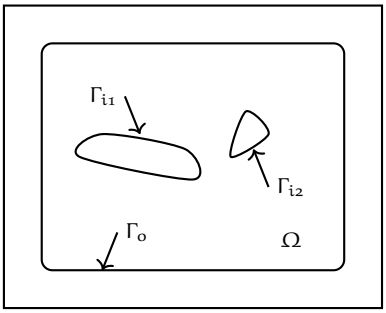

Figure 6.8: A slice with multiple distinct and closed inner boundaries.

▶ THE SET OF PATHS for a particular 2D slice are calculated with the assistance of two 2D binary masks, $M_i[x, y]$ and $M_o[x, y]$. $M_i[x, y]$ is a mask of the implant geometry, such that Γ_i is the set of boundary pixels of M_i [1]. $M_o[x, y]$ is a mask indicating the extent of the imaged region of interest (such as the tissue-air boundary at the edge of the anatomy). Γ_o is the set of boundary pixels of M_o. Pixels inside Γ_i and outside Γ_o are given a value of 0, and are shown in black. The region outside Γ_i where pixels have a value of 1 is marked Ω_i. Likewise, the region inside Γ_o where pixels have a value of 1 is marked Ω_o. Note that $\Omega = \Omega_i \cap \Omega_o$. Figure 6.9 shows the masks calculated for Phantom 1. In this example M_o indicates the inside edge of the container used in the phantom.

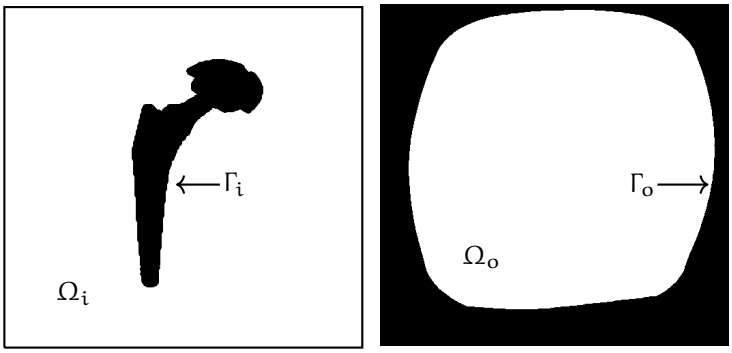

(a) M_i (b) M_o

Figure 6.9: Masks generated for Phantom 1. Γ_i, Γ_o, Ω_i, and Ω_o are indicated.

These masks are used to calculate a suitable set of K paths $\{\rho_k, k = 1, 2, ..., K\}$. ρ_1 is the outermost path, immediately adjacent to Γ_o. ρ_K is the innermost path, immediately adjacent to Γ_i. These are closed, and path ρ_k entirely encloses path ρ_{k+1}. The paths are grouped close together near the implant boundary where the field is rapidly varying.

▶ A PATH IS DEFINED by an ordered set of eight-connected pixels. These approximate a closed smooth curve, with each pixel identified by the index $i = 1, 2, ..., D_k$, where the path ρ_k contains D_k pixels. The distance along the path to the ith pixel, r_i, is defined as the sum of the Euclidean distances between adjacent pixel centres. The total distance along the path is R_k. As the paths are closed, any pixel can

[1] The implant mask M_i may be obtained in several ways, such as using prior knowledge of the implant, thresholding the magnitude image, using MAVRIC field maps to reconstruct the implant geometry [Koch et al., 2013], or by using phase quality mapping methods as described in Chapter 3 of Ghiglia and Pritt [1998a].

be chosen as the first pixel.

6.2.2 *Path calculation*

This section outlines the method used to calculate the set of paths, $\{\rho_k\}$, given the boundaries described in the previous section. The method is first defined for the case where one object is present in the slice, and is then applied to multiple objects in Sec. 6.2.3.

The paths are calculated by taking Euclidean distance transforms of $M_i[x,y]$ and $M_o[x,y]$ to obtain $d_i[x,y]$ and $d_o[x,y]$, respectively. This allows for the location of the pixels along the generated paths to be dependent on the relative distance from the implant boundary and the outer boundary. d_i is the distance from each point $[x,y]$ in Ω_i to the nearest point on the inner boundary, Γ_i. Likewise, d_o is the distance from each point $[x,y]$ in Ω_o to the nearest point on the outer boundary, Γ_o. Figure 6.10 shows d_i and d_o calculated for the boundaries in Fig. 6.9.

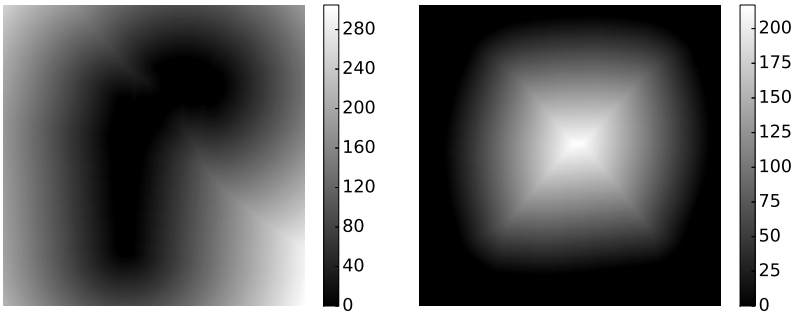

(a) d_i (b) d_o

Figure 6.10: Euclidean distance transforms for Phantom 1.

In order to produce a set of non-overlapping paths, a scalar quantity $\sigma[x,y]$ is defined for all points $[x,y] \in \Omega$,

$$\sigma[x,y] = \frac{d_i[x,y]}{d_i[x,y] + d_o[x,y]}. \tag{6.2}$$

Along any straight line between the inner and outer boundaries, $\sigma[x,y]$ varies monotonically between 0 and 1. Figure 6.11 shows $\sigma[x,y]$ calculated for the boundaries in Fig. 6.9.

$\sigma[x,y]$ is raised to a power P by

$$\sigma_P[x,y] = \sigma[x,y]^P, \tag{6.3}$$

where P is a constant, $0 < P \leqslant 1$, which alters the rate at which σ_P changes in traversing Ω between Γ_o and Γ_i. By choosing an appropriate value for P the paths can be distributed more closely together near the implant. This is illustrated in Fig. 6.13.

Closed contour lines are formed using an method based on level sets. Given a constant value $\hat{\sigma}$, where $0 < \hat{\sigma} < 1$, and considering only pixels within Ω, let the set of pixels Ω^- be defined by

$$\{\Omega^- : \sigma_P[x,y] \leqslant \hat{\sigma}\}. \tag{6.4}$$

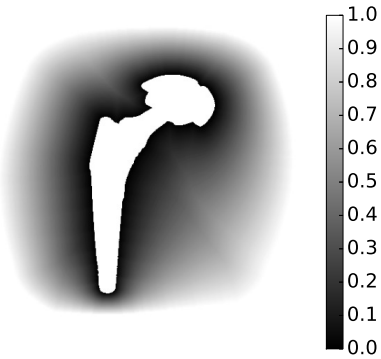

Figure 6.11: Distance ratio function σ for Phantom 1. Pixels inside the implant mask are given a value of 1.0.

This partitions the region Ω into sub-regions Ω^- and Ω^+, as demonstrated in Fig. 6.12. For all pixels in Ω^+, $\sigma_P[x,y] > \hat{\sigma}$. The path ρ_k is then defined by the set of eight-connected pixels which form the closed boundary of Ω^-.

A set of K closed paths is calculated by evaluating Eq. 6.4 over an ordered set of K $\hat{\sigma}_k$ values, $\{\hat{\sigma}_k, k = 1, 2, ..., K\}$. The properties of the distance transforms (and so the properties of $\sigma_P[x,y]$) and the definition of Eq. 6.4 ensures that no pixel forming part of the path ρ_{k+1} does not lie outside the immediately adjacent outer path ρ_k. However, ρ_{k+1} and ρ_k may share some common pixels.

Each $\hat{\sigma}_k$ value produces an array of pixel indices along the path, ρ_k, with D_k rows and 2 columns. D_k is the number of pixels in the path. The ith row of the array is $[x_i, y_i]$, where x_i is the x-index of the ith pixel along the path and y_i is the y-index. The pixel index array for all paths is stored as:

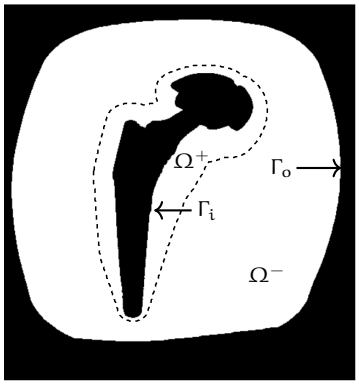

Figure 6.12: Evaluating Eq. 6.4 for a specific $\hat{\sigma}$ value segments the region Ω into Ω^- and Ω^+. The extracted closed path, ρ_k, is marked with a dotted line. Γ_i and Γ_o are also indicated.

$$\{\rho\}$$
$$\downarrow$$
$$\{\rho_1 \quad \rho_2 \quad \dots \quad \rho_K\}$$
$$\downarrow$$
$$\left\{\rho_1 = \begin{bmatrix} x_1 & y_1 \\ x_2 & y_2 \\ \dots & \dots \\ x_{D_1} & y_{D_1} \end{bmatrix} \quad \rho_2 = \begin{bmatrix} x_1 & y_1 \\ x_2 & y_2 \\ \dots & \dots \\ x_{D_2} & y_{D_2} \end{bmatrix} \quad \dots \quad \rho_K = \begin{bmatrix} x_1 & y_1 \\ x_2 & y_2 \\ \dots & \dots \\ x_{D_K} & y_{D_K} \end{bmatrix}\right\} \tag{6.5}$$

Figure 6.13(a) shows nine evenly spaced paths calculated for Phantom 1 with $P = 1$, using $\hat{\sigma}_k = \{0.1, 0.2, ..., 0.9\}$, and Fig. 6.13(b) shows nine paths calculated with $P = 0.7$.

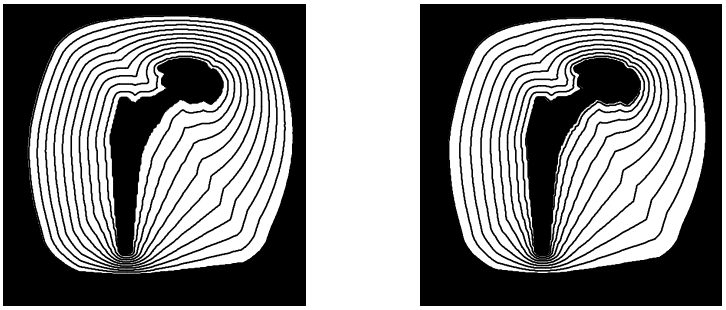

(a) $P = 1$ (b) $P = 0.7$

Figure 6.13: Two sets of paths calculated for Phantom 1, using differing values of P.

6.2.3 *Multiple objects*

The described path generation method using distance transforms and Eq. 6.4 is valid for slices with more than one object present. The only significant difference between the paths generated for a slice with a single object and those generated for slices with several objects lies in how the paths are ordered.

Figure 6.14(a) shows eight paths calculated for an outer slice of Phantom 1, with $S = 2$ objects present. In this situation, the exterior paths form individual closed loops, similar to Fig. 6.13. The interior paths split into two separate loops, or "sub-paths", one for each object. These are marked in blue. Figure 6.14(b) shows paths generated for a hypothetical slice with $S = 3$ objects present. In this example, the exterior paths initially split into two sub-paths (as shown in the outermost blue path), and then split again to form three separate sub-paths around each object.

With $S > 1$ objects present in a slice, evaluating Eq. 6.4 for certain constant $\hat{\sigma}$ values produces multiple Ω^- pixel sets, $\Omega_1^-, \Omega_2^-, ..., \Omega_S^-$. The paths for each $\hat{\sigma}$ value are subsequently constructed by identifying the boundary pixels of the Ω_s^- pixel sets. The paths are then ordered as described below.

With one object, $\{\rho_k\}$ is a list of arrays, as shown in Diagram 6.5. With $S > 1$ object, $\{\rho_k\}$ is a list of K levels. Each level comprises a list of $1 \leqslant s \leqslant S$ sub-paths, $\{\rho_k\} = \{\rho_{k1}, \rho_{k2}, ..., \rho_{ks}\}$. The innermost level has S sub-paths. The pixel indices for each sub-path are stored in an array, as shown in Diagram 6.6.

$$
\begin{array}{c}
\Big\{\rho\Big\} \\
\downarrow \\
\Big\{\rho_1 \quad \rho_2 \quad \cdots \quad \rho_K\Big\} \\
\downarrow \\
\left\{\rho_1 = \Big\{\rho_{11}\Big\} \quad \rho_2 = \begin{Bmatrix}\rho_{21}\\ \rho_{22}\end{Bmatrix} \quad \cdots \quad \rho_K = \begin{Bmatrix}\rho_{K1}\\ \rho_{K2}\\ \vdots \\ \rho_{KS}\end{Bmatrix}\right\} \\
\downarrow \\
\left\{\Big\{\rho_{11} = \begin{bmatrix}x_i & y_i\end{bmatrix}\Big\} \quad \left\{\begin{matrix}\rho_{21} = \begin{bmatrix}x_i & y_i\end{bmatrix}\\ \rho_{22} = \begin{bmatrix}x_i & y_i\end{bmatrix}\end{matrix}\right\} \quad \cdots \quad \left\{\begin{matrix}\rho_{K1} = \begin{bmatrix}x_i & y_i\end{bmatrix}\\ \rho_{K2} = \begin{bmatrix}x_i & y_i\end{bmatrix}\\ \vdots \\ \rho_{KS} = \begin{bmatrix}x_i & y_i\end{bmatrix}\end{matrix}\right\}\right\}
\end{array}
\tag{6.6}
$$

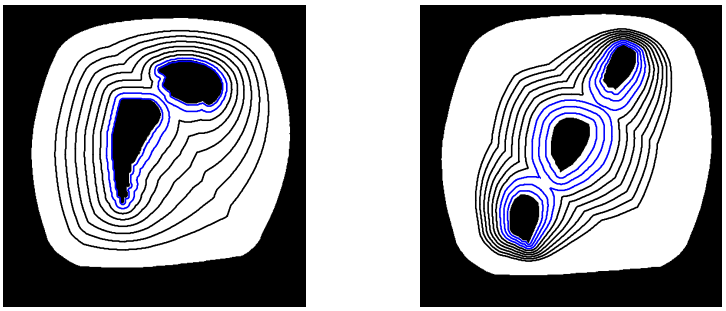

(a) Two objects

(b) Three objects

Figure 6.14: Paths calculated for two examples of slices with multiple objects present.

▶ THE GENERATED PATHS must form a closed loop. However, this can cause issues in sharp concavities near the implant boundary, and in regions between multiple objects. Figure 6.15 shows an example of the paths calculated for a hypothetical object with a sharp concavity. Within the concavity, the density of the paths is lower compared to immediately outside it. These paths also have sharp corners. When the phase is extracted along these paths, the assumption that the phase is continuous may no longer be valid.

In regions between multiple objects, points which are equidistant between the objects act as a type of "asymptote". This is shown in Fig. 6.16(a), which shows a close up of the region between the two objects, with 30 paths originally generated. In this example, the paths which form a single closed loop (before the paths split into two loops) have a sharp corner, near the "asymptote", marked in red. Also, there is a key region between the two objects which has no paths allocated. This can also be visualised in Fig. 6.16(b). There are two distinct regions between the three objects where the path density is lower than in other regions of the image. Further work is needed to address these issues.

6.2.4 *Summary of path generation*

▶ THE PATH GENERATION PROCESS can be summarised by the following steps:

1. Generate masks for the slice, $M_i[x, y]$ and $M_o[x, y]$.
2. Calculate the distance transforms $d_i[x, y]$ and $d_o[x, y]$.
3. Calculate $\sigma_P[x, y]$.
4. Extract the pixel indices in each path by evaluating Eq. 6.4 over an ordered set of K constant values, $\{\hat{\sigma}_k\}$.
5. Store each pixel index array in a list, $\{\rho_k\}$.

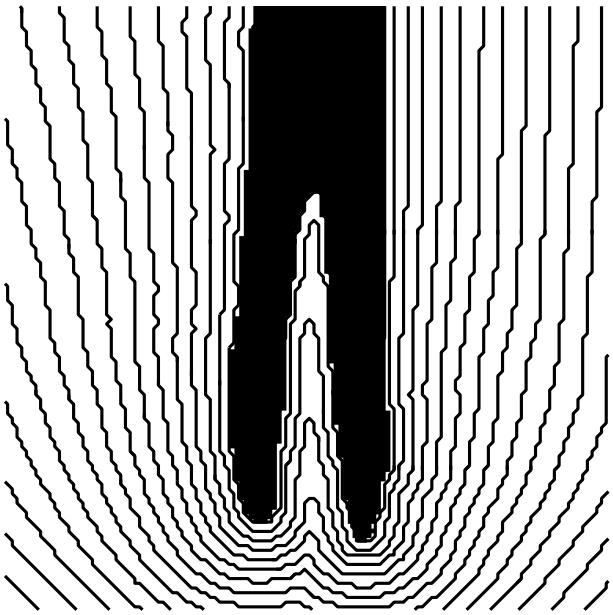

Figure 6.15: Close up of the paths generated for a simulated object with a sharp concavity.

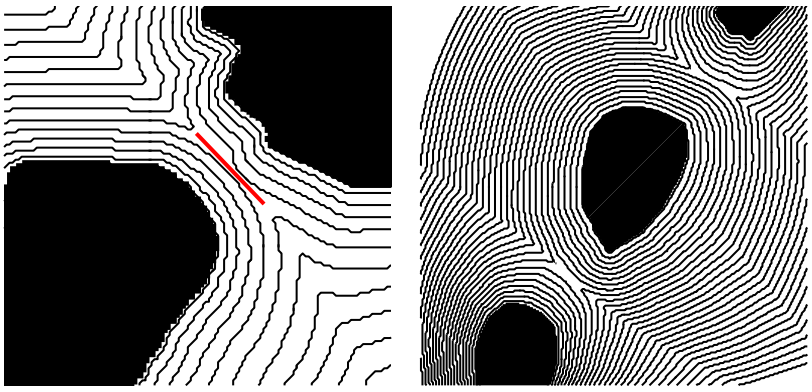

(a) Two objects

(b) Three objects

Figure 6.16: Close up of the paths generated near multiple objects.

6.3 ITERATIVE PHASE ESTIMATION

This section describes the method used to estimate the phase along the generated paths. First, the equations defining the three-point Dixon technique are rearranged into a form which allows the phase along each path to be modelled by a set of basis functions. This is followed by Sec. 6.3.1, which consists of three main points: the expressions used to represent the phase by an Nth order Fourier series, the objective function used to calculate the Fourier series coefficients, and the process used to minimise the objective function. Section 6.3.2 describes the iterative stages of the algorithm, which govern how the phase estimation proceeds inwards from path to path. Finally, Sec. 6.3.3 discusses two methods for estimating the Fourier series order for each path.

▶ As described in Sec. 3.3.3, in the three-point Dixon technique the phase is estimated from $\hat{\mathbf{S}}_2$ [2],

$$\hat{\mathbf{S}}_2[\mathbf{x}] = (W[\mathbf{x}] + F[\mathbf{x}])e^{j2\psi[\mathbf{x}]}. \tag{6.9}$$

As shown by Liang [1996], Equation 6.9 can be scaled to be a complex image with a magnitude of 1,

$$\bar{\mathbf{S}}_2[\mathbf{x}] = \frac{\hat{\mathbf{S}}_2[\mathbf{x}]}{|\hat{\mathbf{S}}_2[\mathbf{x}]|} = e^{j2\psi[\mathbf{x}]}. \tag{6.10}$$

For simplicity, let

$$\hat{\phi}[\mathbf{x}] = \mathcal{W}_r[2\psi[\mathbf{x}]], \tag{6.11}$$

where $\mathcal{W}_r[\cdot]$ is the wrapping operator and noting that $e^{j\hat{\phi}[\mathbf{x}]} = e^{j\mathcal{W}_r[2\psi[\mathbf{x}]]}$, and

$$\hat{s}[\mathbf{x}] = e^{j\hat{\phi}[\mathbf{x}]}. \tag{6.12}$$

Once the paths are generated, the acquired complex data at the pixel indices along each path are extracted and stored in a list, $\{s_k\}$. The extracted data along the kth path is therefore

$$s_k(i) = e^{j\hat{\phi}_k(i)}. \tag{6.13}$$

The distance along each path, r_i is also calculated and stored in an associated list, $\{r_{i_k}\}$. Henceforth, in this section the subscript k, referring to the specific path, has been neglected to simplify the notation.

6.3.1 *Objective function*

The true phase along each path, $\phi(i)$, is modelled with a set of basis functions,

$$\phi(i) = \sum_{n=1}^{N} \alpha_n \beta_n(i), \tag{6.14}$$

where $\{\alpha_n\}$ are the parameters to estimate, and $\{\beta_n\}$ are the basis functions. In this chapter an Nth order Fourier series is used as a basis. This is expressed as

$$\phi(i) = F^N(r_i), \quad i = 1, 2, ..., D, \tag{6.15}$$

[2] Recall that the three images have the signal model

$$\begin{aligned} \mathbf{S}_0[\mathbf{x}] &= (W[\mathbf{x}] + F[\mathbf{x}])e^{j\psi_0} \\ \mathbf{S}_1[\mathbf{x}] &= (W[\mathbf{x}] - F[\mathbf{x}])e^{j(\psi_0+\psi[\mathbf{x}])} \\ \mathbf{S}_2[\mathbf{x}] &= (W[\mathbf{x}] + F[\mathbf{x}])e^{j(\psi_0+2\psi[\mathbf{x}])}. \end{aligned} \tag{6.7}$$

and

$$\hat{\mathbf{S}}_2 = \mathbf{S}_2 e^{-j\psi_0} = \frac{\mathbf{S}_2\mathbf{S}_0^*}{|\mathbf{S}_0|}. \tag{6.8}$$

where $F^N(r_i)$ is the Fourier series which is expanded as

$$F^N(r_i) = \frac{a_0}{2} + \sum_{n=1}^{N} [a_n \cos(\frac{2\pi n r_i}{R}) + b_n \sin(\frac{2\pi n r_i}{R})]. \tag{6.16}$$

D is the number of pixels along the path and R is the total distance along the path.

The aim is to find the set of Fourier coefficients $\{a_n, b_n\}$ for each path which minimises the objective function

$$H = \sum_{i=1}^{D} |e^{j\hat{\phi}(i)} - e^{jF^N(r_i)}|, \tag{6.17}$$

This objective function forces congruence between the measured complex data along each path and the estimated solution.

Using Euler's identity [3], Eq. 6.17 is rewritten as

[3] $e^{j\theta} = \cos(\theta) + j\sin(\theta)$

$$H = \sum_{i=1}^{D} \sqrt{[\cos(\hat{\phi}(i)) - \cos(F^N(r_i))]^2 + [\sin(\hat{\phi}(i) - \sin(F^N(r_i))]^2}. \tag{6.18}$$

The first derivatives of the objective function with respect to the coefficients $\{a_n, b_n\}$ are

$$\begin{aligned}
\frac{\partial H}{\partial a_0} &= \sum_{i=1}^{D} \frac{0.5[\cos(\hat{\phi}(i))\sin(F^N(r_i)) - \sin(\hat{\phi}(i))\cos(F^N(r_i))]}{\sqrt{[\cos(\hat{\phi}(i)) - \cos(F^N(r_i))]^2 + [\sin(\hat{\phi}(i)) - \sin(F^N(r_i))]^2}} \\
\frac{\partial H}{\partial a_n} &= \sum_{i=1}^{D} \frac{\cos(\frac{2\pi n r_i}{R})[\cos(\hat{\phi}(i))\sin(F^N(r_i)) - \sin(\hat{\phi}(i))\cos(F^N(r_i))]}{\sqrt{[\cos(\hat{\phi}(i)) - \cos(F^N(r_i))]^2 + [\sin(\hat{\phi}(i)) - \sin(F^N(r_i))]^2}} \\
\frac{\partial H}{\partial b_n} &= \sum_{i=1}^{D} \frac{\sin(\frac{2\pi n r_i}{R})[\cos(\hat{\phi}(i))\sin(F^N(r_i)) - \sin(\hat{\phi}(i))\cos(F^N(r_i))]}{\sqrt{[\cos(\hat{\phi}(i)) - \cos(F^N(r_i))]^2 + [\sin(\hat{\phi}(i)) - \sin(F^N(r_i))]^2}}.
\end{aligned} \tag{6.19}$$

The calculation of this derivative allows H to be minimised with an efficient gradient-based optimisation routine. There are a number of suitable routines, including those based on conjugate gradient methods. Currently POP uses a trust-region algorithm which solves each trust-region subproblem with the preconditioned conjugate gradient method [Conn et al., 2000].

6.3.2 *Iterative stages*

This subsection outlines the key iterative stages in POP. The phase estimation begins at the outermost path. It then advances inwards over the generated paths towards the implant boundary. This approach offers several advantages. The phase is slowly varying at the outer paths compared to the inner paths, so fewer Fourier series coefficients are required to model the phase along the outer paths. The phase estimation therefore proceeds from being relatively straightforward to more difficult at the innermost path. Also, if the phase

estimation fails along an inner path, the errors are restricted to the region between this path and the implant boundary. In comparison, in the branch cut phase unwrapping method, a single unbalanced branch cut can cause errors to spread throughout a significant portion of the image.

There are three steps which occur before the iterative stages begin. First, the paths are generated, using the steps described in Sec. 6.2.4. Second, the acquired data along the paths is extracted. The third step calculates the order of the Fourier series, N, for each path. This process is described in Sec. 6.3.3.

▶ THE ITERATIVE STAGES OF POP then proceed as follows:

The phase along the outermost path is unwrapped first. It is assumed that this is sufficiently far from the implant that it is slowly varying and standard 1D phase unwrapping can be used [4]. For this path, the initial set of coefficients $\{a_n, b_n\}$ is calculated by fitting a Fourier series to the unwrapped phase.

[4] Refer to Sec. 4.1.1 for details of this method.

For each subsequent path, the final phase estimate on the previous path is first mapped to the new path pixel-by-pixel. The pixel mapping is performed on a nearest neighbour basis for each pixel on the new path by identifying the pixel on the previous path which is located at the smallest Euclidean distance. More efficient methods are possible, but experience indicates that these are not required.

The initial set of Fourier coefficients is then obtained by fitting the Nth order Fourier series (as defined in Sec. 6.3.1) to the mapped phase along the new path. This is a suitable starting point for the new path because the phase functions along two adjacent paths exhibit a similar shape, even for paths which are close to the object boundary. For example, Fig. 6.18 shows the simulated phase shift along the two adjacent paths marked in Fig. 6.17. Figure 6.19 shows the difference in $\{a_n, b_n\}$ values between them. Similarly, Fig. 6.20 shows how four fitted low-order coefficient values (a_0, a_1, a_2, b_1) change across 50 paths generated for Fig. 6.17. The Fourier series is therefore an efficient method for representing the phase along a set of circumnavigating paths.

Given the extracted data along the path, $e^{j\hat{\Phi}(i)}$, the initial objective function value, H, is evaluated with the initial set of coefficients, $\{a_n, b_n\}$. The coefficient values are then refined by minimising H as described in Sec. 6.3.1.

Figure 6.17: Simulated phase shift ϕ with two adjacent paths marked.

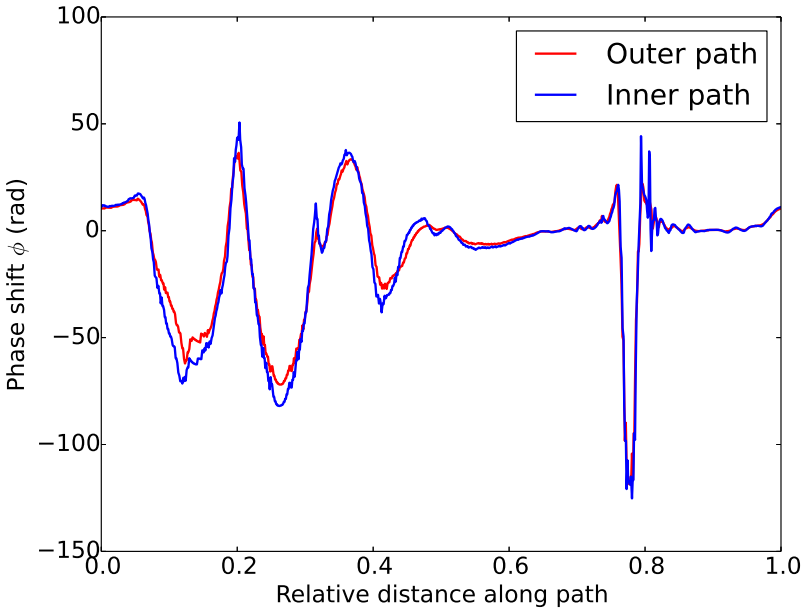

Figure 6.18: Phase shift along the adjacent paths marked in Fig. 6.17.

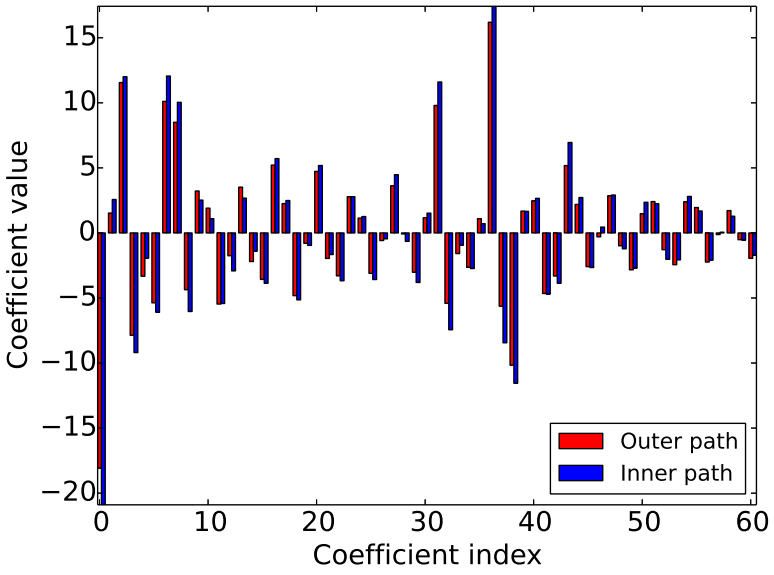

Figure 6.19: Difference in Fourier series coefficient values between the two adjacent paths.

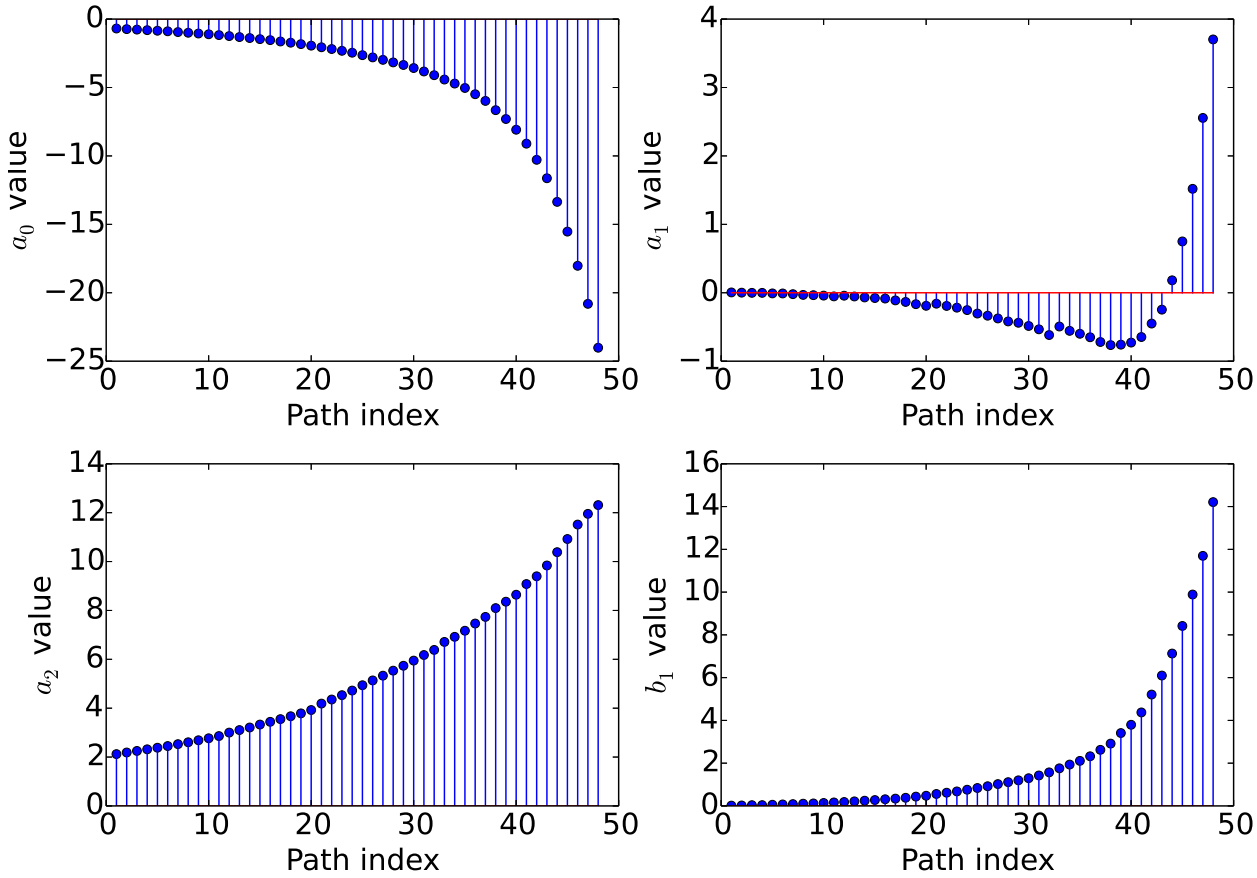

Figure 6.20: Difference in four Fourier series coefficient values across 50 paths generated for Fig. 6.17.

- In the case of multiple implants in the same slice, the iterative stages of POP proceed in much the same manner as the described method. First, the paths are generated and ordered as a list of K levels containing sub-paths, as described in Sec. 6.2.3. Next, the acquired data along each sub-path is extracted, and the Fourier series order for each sub-path is determined.

  It is assumed that the outermost level contains only one path. The phase along this path is unwrapped first. For all following levels, the initial phase estimate at each pixel along the sub-paths is mapped from the nearest pixel in the sub-paths in the previous level. It is noted that although this method of performing the mapping is simple, it is not the most efficient. This is discussed further in Sec. 11.2. The initial Fourier coefficients for each sub-path are then adjusted using the previously described optimisation method.

- The POP method can be summarised by the following steps:

  1. Generate the set of K paths $\{\rho_k\}$.
  2. Extract the measured data along each path.
  3. Estimate the Fourier series order, N, for each path.
  4. Unwrap phase along the outermost path, ρ_1.
  5. Fit Nth order Fourier series to the phase along the path.
  6. Adjust the Fourier coefficients to minimise the objective function, H.
  7. Set the initial phase at each pixel on the next path in to be equal to the final phase at the closest pixel on the previous path.

  Steps 5-7 are repeated for each path until the path closest to the boundary of the object is reached.

- In the final step of the algorithm, the phase at pixels which do not belong to any path is estimated using a 2D inpainting method. In image inpainting, values of pixels in "holes" in the image are calculated by interpolating inwards from the boundaries of the holes [Bertalmio et al., 2000]. Currently, POP uses an inpainting method developed by D'Errico [2014]. This method forms elliptical partial differential equations (PDEs) across "holes" of pixels which are not associated with any POP path. Boundary values of the PDEs are obtained from the boundary pixels of each hole. A large sparse set of equations is then solved to calculate the phase at the pixels within the holes.

  The number of paths and spacing between the paths (controlled by the value of P) determine the number of pixels which need to be interpolated. For example, with 100 and 150 paths generated for a slice with 512×512 pixels, and $0.4 \leqslant P \leqslant 0.7$, the constructed paths cover between 85 %–95 % of the pixels. A large number of paths could be generated to cover almost every pixel, significantly reducing

the requirement for interpolation. However, experience has shown that dense path distribution is not required in the outer regions of the slice, as the phase varies sufficiently slowly in these regions.

6.3.3 *Calculating Fourier series order*

As the distance to the implant decreases, the sharpness of the features in the phase function increases. At the same time, the number of pixels along each path decreases. To achieve a particular accuracy of fit, N must therefore increase as the paths are traversed from the outer boundary to the inner boundary.

Initially, it was intended that the order of the Fourier series, N, would be determined *a priori* using a model of the phase shift, such as that shown in Fig. 6.2. To find the best N for each path, successive terms were added to the Fourier approximation until the goodness of fit reached a desired threshold. A mean square error in decibels (MSE_{dB}) of less than 20 dB was used as the threshold. MSE_{dB} is given by

$$MSE_{dB} = 20 \log_{10} \left[\frac{1}{D} \sum_{i=1}^{D} \left(F^N(r_i) - \phi_m(i) \right) \right], \qquad (6.20)$$

where $F^N(r_i)$ is the Fourier series approximation and $\phi_m(i)$ is the model phase along the path. Figure 6.21 shows the calculated N values for 140 paths generated across the central slice of the Implant 1 simulated phase shift, as shown in Fig. 6.2.

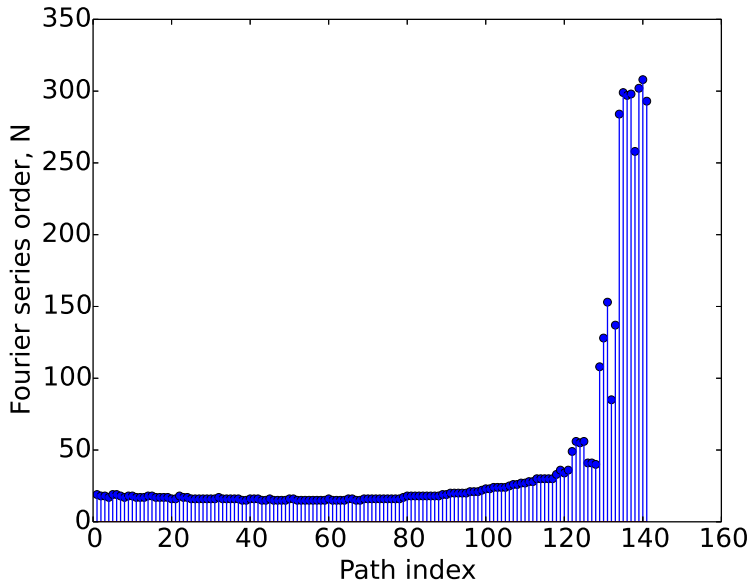

Figure 6.21: Calculated Fourier series order for 150 paths generated across the central slice of the Implant 1 simulated phase.

However, while conducting initial experiments of POP on the phantom data (as described in the following chapter), it was observed that this method produced unusual results for the inner paths. This corresponded to the sudden increase in N as demonstrated in Fig. 6.21.

For these paths, the calculated N value required to reach a threshold of $MSE_{dB} < 20\,dB$ exceeded 200. It is likely that the unusual results occurred due to the objective function minimisation failing to converge to the correct set of values for such a large number of coefficients. This suggests that the Fourier series may not be the best basis for approximating the phase along the inner paths. This is a topic which is discussed further in Chapter 10, *Investigating a better basis*.

Instead, the Fourier series order used for the paths generated for each slice was calculated by linearly distributing the set of N values across the paths. The outermost path for the majority of the slices processed in this thesis used $N = 20$, and the N value for the innermost path ranged between 50 and 150, depending on the type of implant present. This is described further in Sec. 8.1.3. While this method is not optimal, it produced sufficiently accurate and reliable results. It also relies on less prior knowledge of the implant, compared to the previously described method.

7

Phantom Results

In this chapter, results are presented for imaging performed on the three phantoms described in Chapter 5, using POP. These are compared with the performance of existing phase unwrapping techniques, with results shown for the unweighted and weighted branch cut and minimum-norm phase unwrapping methods. Three phantom data sets are tested for each method. Results are shown for the central slice and one outer slice of each phantom.

- Mask formulation:

The 3D voxelised geometry of Implant 1, acquired during the voxelisation process described in Sec. 5.1, was registered with the approximate position and orientation of the implant in the Phantom 1 FSE data. Slices were extracted from the matrix to generate a mask of the implant boundary for each FSE slice.

Boundary masks for Phantom 1 were generated by applying a manual threshold to the magnitude FSE images. The largest connected component in the resulting binary images was identified. The pixels corresponding to this connected component were assigned as the initial phantom mask. Holes within the initial mask were then filled to obtain the phantom mask. This was done using the MATLAB hole-filling operation in the `imfill` function [1].

A similar method was used to generate the implant masks for Phantoms 2 and 3. The connected component which corresponded to the implant boundary was manually selected. This was generally the second largest component. The holes in the connected component were then filled to obtain the implant mask. It should be noted that it is not possible to determine the true implant boundary using this method. The signal loss produced near the implant causes the generated mask to be larger than the actual boundary. This is discussed further in Sec. 8.3.

[1] In this function a hole is defined as being a set of background pixels (or non-mask pixels) which are not reached by performing a flood-fill operation from the edge of the image.

7.1 PHANTOM 1: CENTRAL SLICE

In this section, results are shown for the central slice of Phantom 1, using POP, and both the unweighted and weighted minimum-norm and branch cut phase unwrapping methods.

Figure 7.1 shows the wrapped phase shift ϕ_w for the central slice of Phantom 1, extracted using Eq. 6.12. Figure 7.2 shows the estimated phase shift ϕ (rad) and the fat and water separated images obtained using POP. This result was acquired using $K = 150$ paths distributed with $P = 0.6$. N ranged between 25 and 100 [2]. The fat in the three vials has been successfully suppressed. A number of small areas close to the boundary of the implant have been incorrectly identified as fat. These are indicated with red arrows. A "perfect" fat image would contain no signal from the agar gel and a perfect water image would contain no signal from the vials of peanut oil.

Note that the image intensity throughout the fat (b) and water (c) images is non-uniform, with a much brighter intensity in the centre of the slice compared to the outer regions. This may be due to B_1 (or RF) inhomogeneities, as RF pulses become distorted by large metal implants. Errors in the automatic shimming process may have also contributed to the intensity variation, as the shimming may have been affected by the small volume of agar surrounding the implant in the phantom.

Figure 7.1: Phantom 1, central slice, wrapped phase.

[2] Refer to Secs. 6.2 and 6.3.3 for the definition of these parameters.

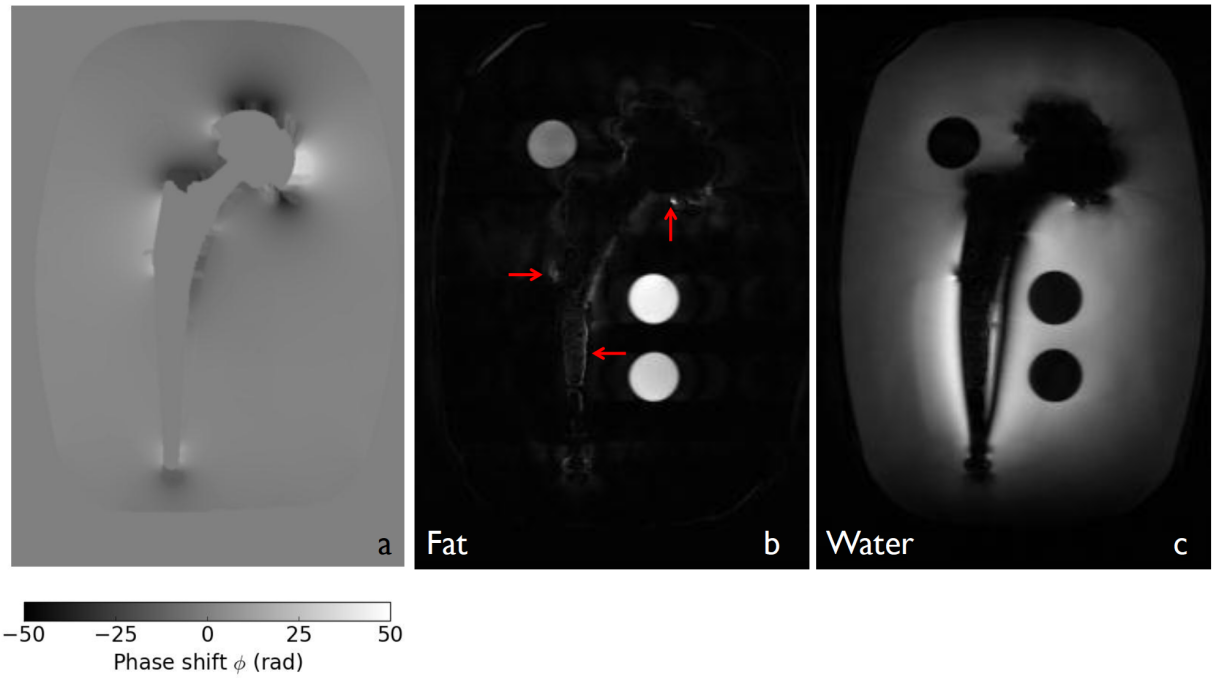

Figure 7.2: Phase shift (a), fat (b), and water (c) images of Phantom 1, central slice, obtained using the POP method.

7.1.1 *Unweighted methods*

Recall from Chapter 4 that in the standard unweighted minimum-norm and branch cut phase unwrapping methods, the wrapped phase at every pixel is assigned equal importance. Figure 7.3 shows the phase shift, fat, and water images obtained using the unweighted minimum-norm method. Figure 7.4 shows the phase shift, fat, and water images obtained using the unweighted branch cut method.

In Fig. 7.3, the calculated phase has been underestimated, particularly near the implant boundary. The range of the estimated phase, $[-20, 20]$ rad, is much smaller than the POP estimated phase range of $[-50, 50]$ rad. This has produced significant errors which are spread throughout the fat and water images, with fat-water swaps present in two of the fat vials.

Although the fat has been successfully suppressed in all three vials in Fig. 7.4, the branch cut phase unwrapping has failed severely. This is likely due to unbalanced residues present at a number of pixels located on or near the implant boundary [3]. The phase unwrapping has failed at these pixels. These errors have spread during the flood-fill stage of the branch cuts algorithm, producing streaks throughout the estimated phase, fat, and water images.

[3] Refer to Sec. 4.3.

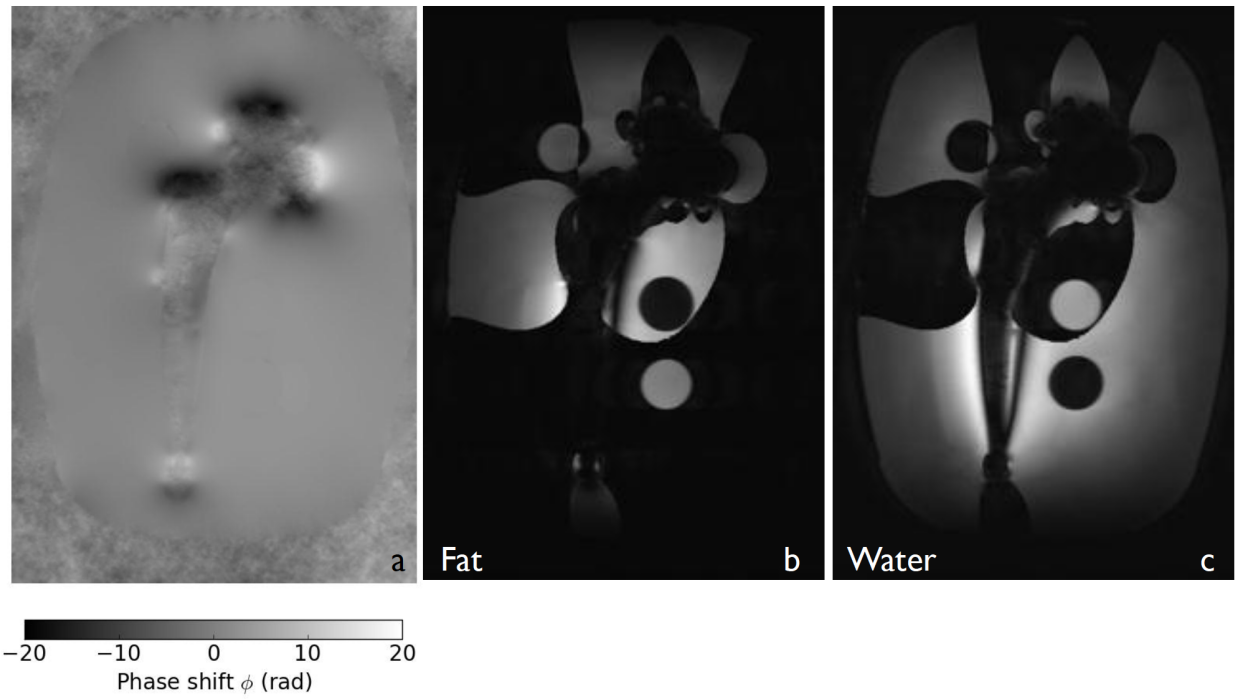

Figure 7.3: Phase shift (a), fat (b), and water (c) images of Phantom 1, central slice, obtained using the unweighted minimum-norm method.

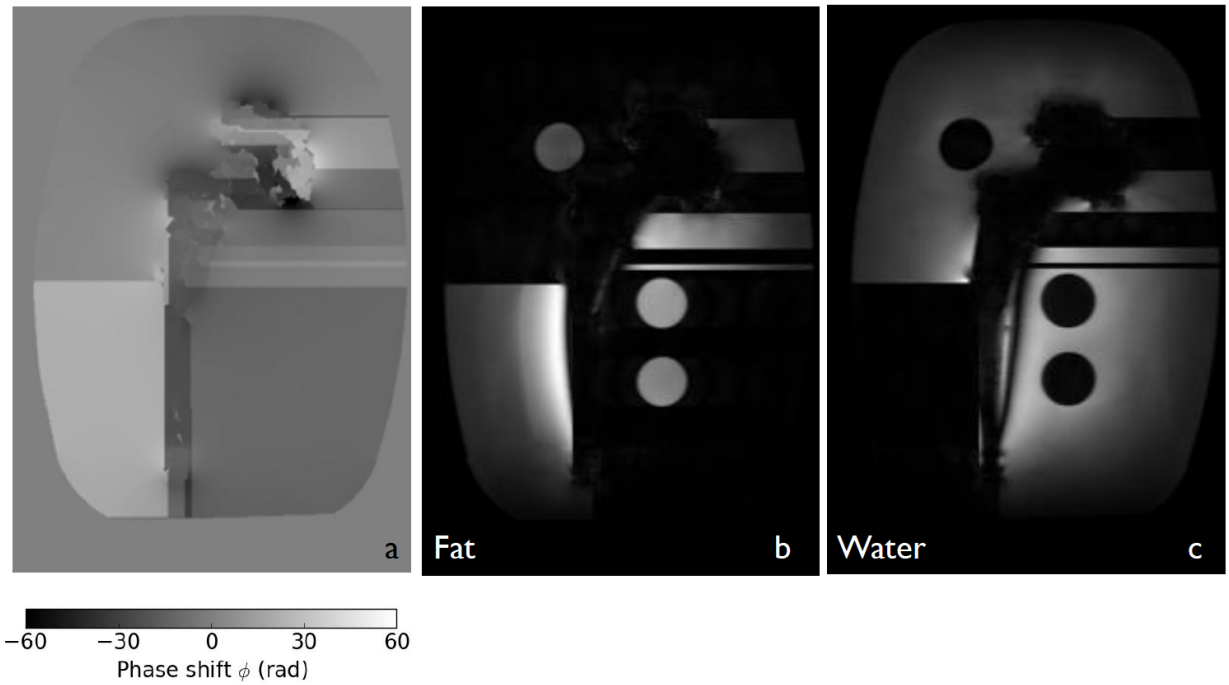

Figure 7.4: Phase shift (a), fat (b), and water (c) images of Phantom 1, central slice, obtained using the unweighted branch cut method.

7.1.2 *Weighted methods*

In this subsection, results are presented for the weighted minimum-norm and branch cut methods. Clearly the unweighted methods have not performed well. Experience has demonstrated that pixels situated inside the implant mask boundary and outside the phantom mask boundary have an undue effect on the unwrapped phase. In the weighted methods, these pixels are given a weighting of zero. This prevents the phase in these regions from influencing the minimum-norm and branch cut unwrapping methods.

Figure 7.5 and 7.6 show the phase shift, fat, and water images obtained using the weighted minimum-norm and branch cut methods. The fat-water separation is significantly improved by avoiding unwrapping across the implant boundary. However, both methods are unable to resolve the rapid phase variations in regions near the implant boundary, where POP succeeds. Experience with these phase unwrapping methods has indicated that notably improved results are obtained with the weighted methods compared to the unweighted methods. Therefore, only the weighted results are shown in the remainder of this chapter.

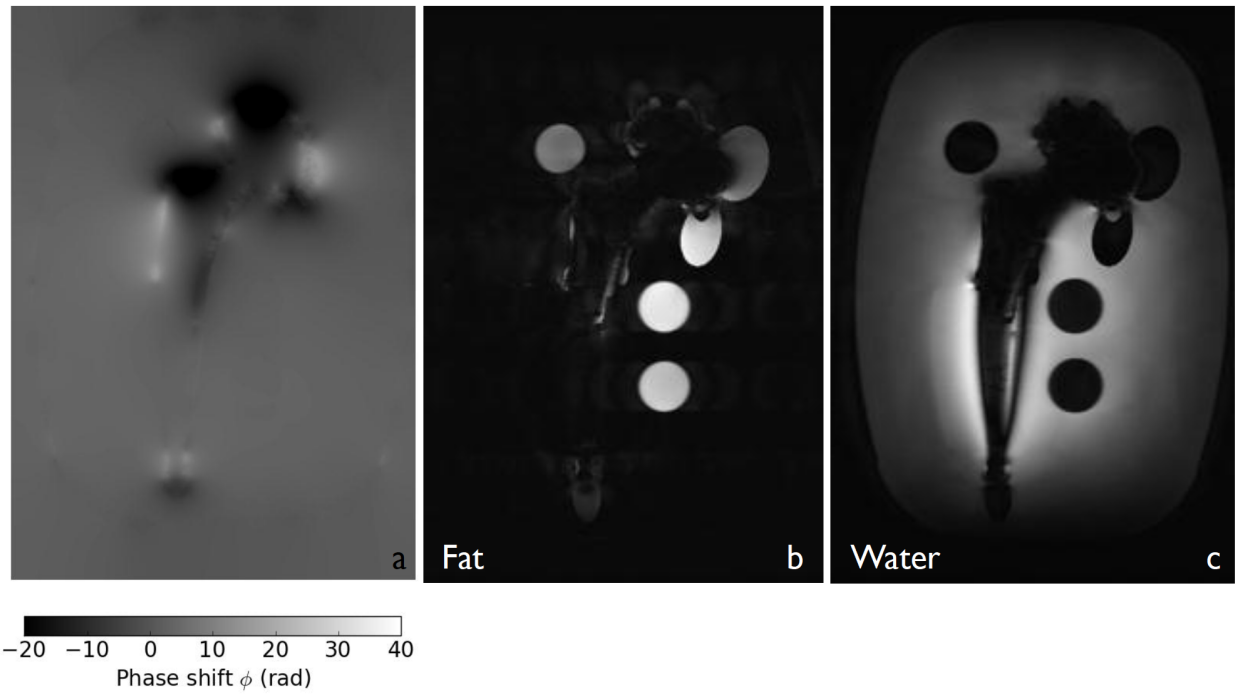

Figure 7.5: Phase shift (a), fat (b), and water (c) images of Phantom 1, central slice, obtained using the weighted minimum-norm method.

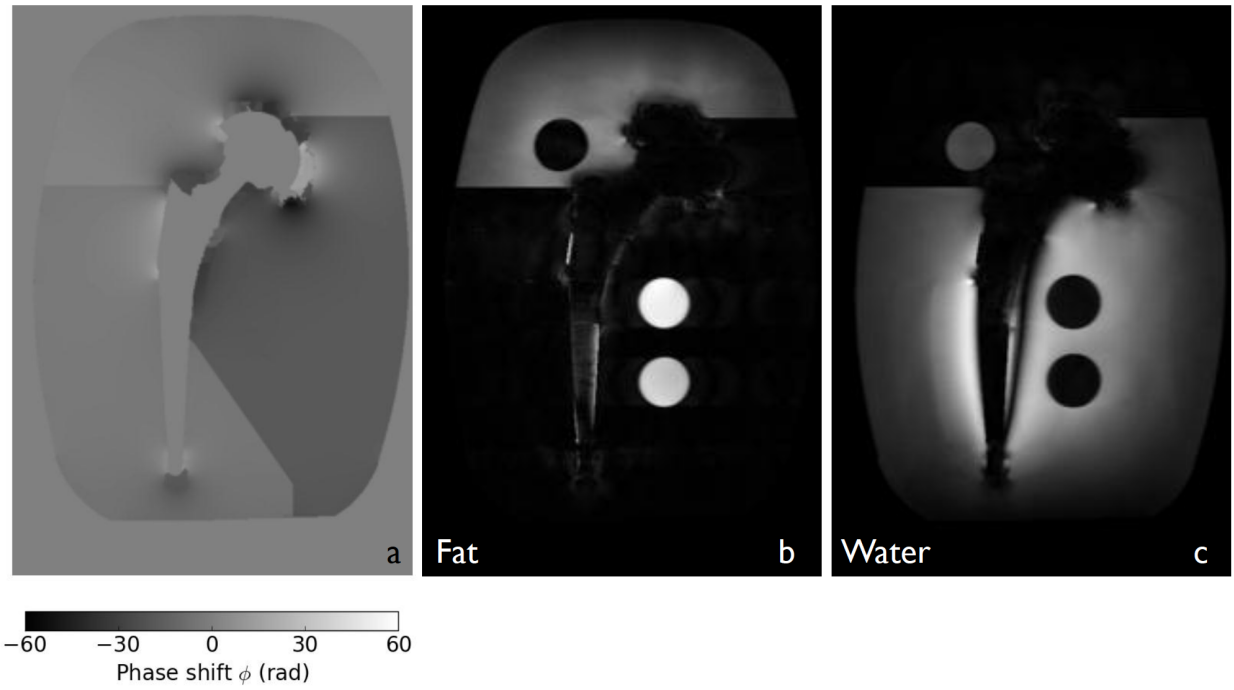

Figure 7.6: Phase shift (a), fat (b), and water (c) images of Phantom 1, central slice, obtained using the weighted branch cut method.

7.2 PHANTOM 1: SLICE 4

Slice 4 is offset from the central slice of Phantom 1 by 12 mm [4]. Figure 7.7 shows the wrapped phase shift ϕ_w. The implant boundary for this slice has two components. Figure 7.8 shows the phase shift, fat, and water images obtained with POP. This result was acquired using $K = 100$ levels [5], with 139 paths in total. The levels were distributed with $P = 0.45$. N ranged between 25 and 70. The images have been cropped and magnified to more clearly show that while the method has succeeded in the majority of the slice, it has failed in the space between the two implant boundaries. This is marked with a red arrow.

Figure 7.9 and 7.10 show the phase shift, fat, and water images obtained using the weighted minimum-norm and branch cut methods. Results are similar to the weighted methods for the central slice. The weighted minimum-norm method has successfully unwrapped the phase in the region between the two implants where POP has failed. However, the minimum-norm method has failed in the vicinity of the implant, where the phase varies rapidly.

[4] Recall that 16 slices were obtained for Phantoms 1 and 2 (Table 5.1).

[5] Recall that the term *levels* is used when more than one object is present in the slice, as defined in Sec. 6.2.3.

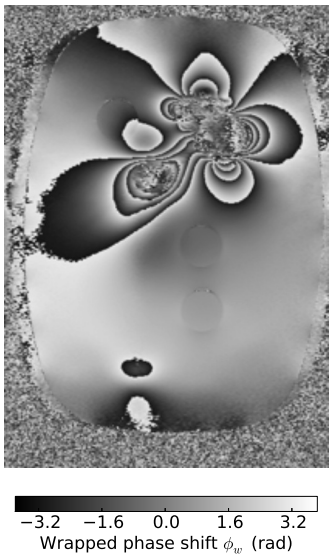

Figure 7.7: Phantom 1, Slice 4, wrapped phase.

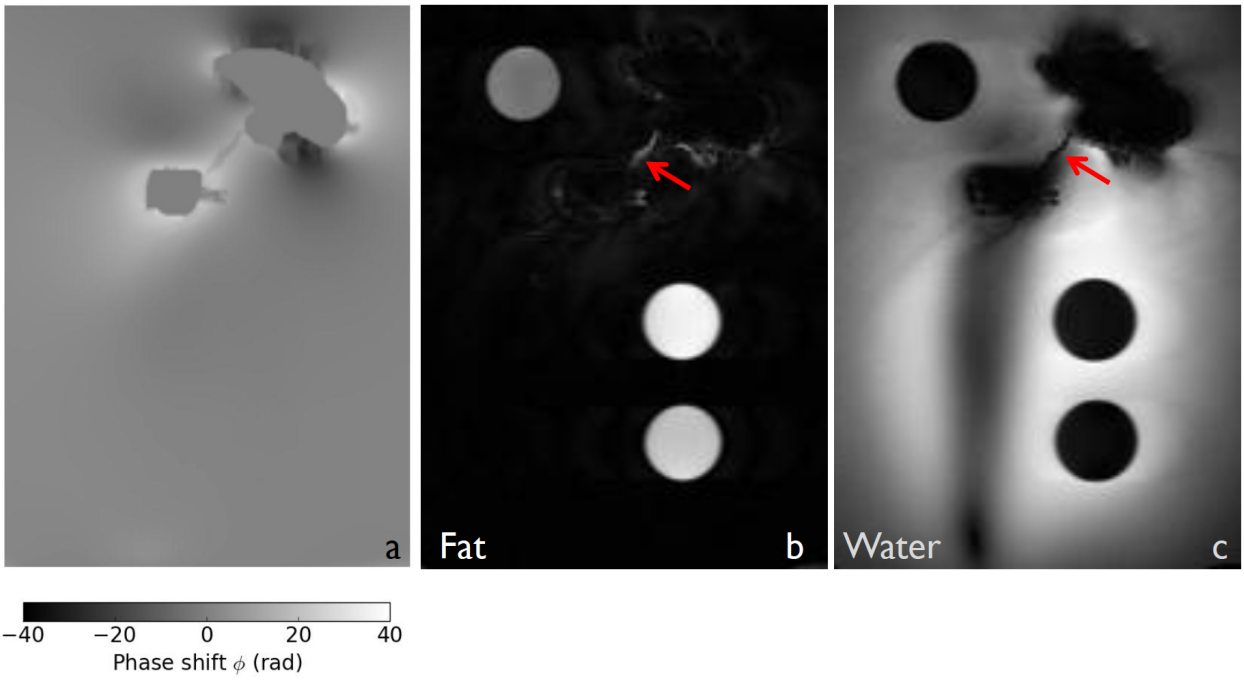

Figure 7.8: Phase shift (a), fat (b), and water (c) images of Phantom 1, Slice 4, obtained using the POP method.

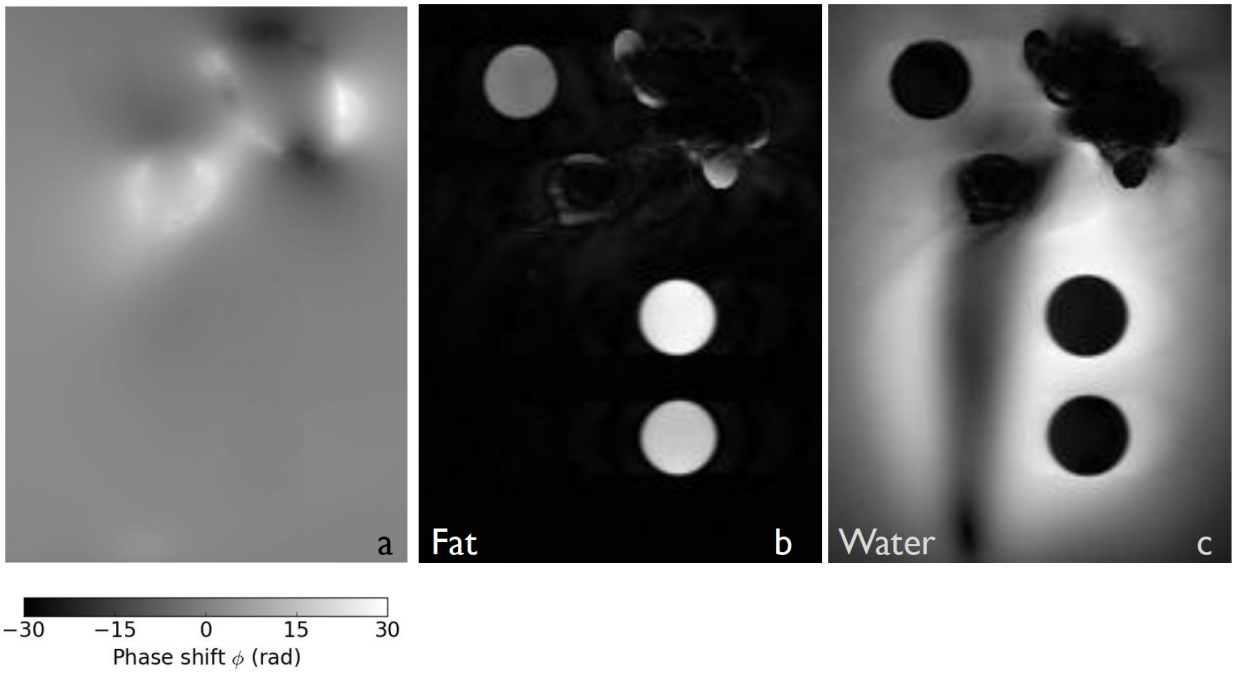

Figure 7.9: Phase shift (a), fat (b), and water (c) images of Phantom 1, Slice 4, obtained using the weighted minimum-norm method.

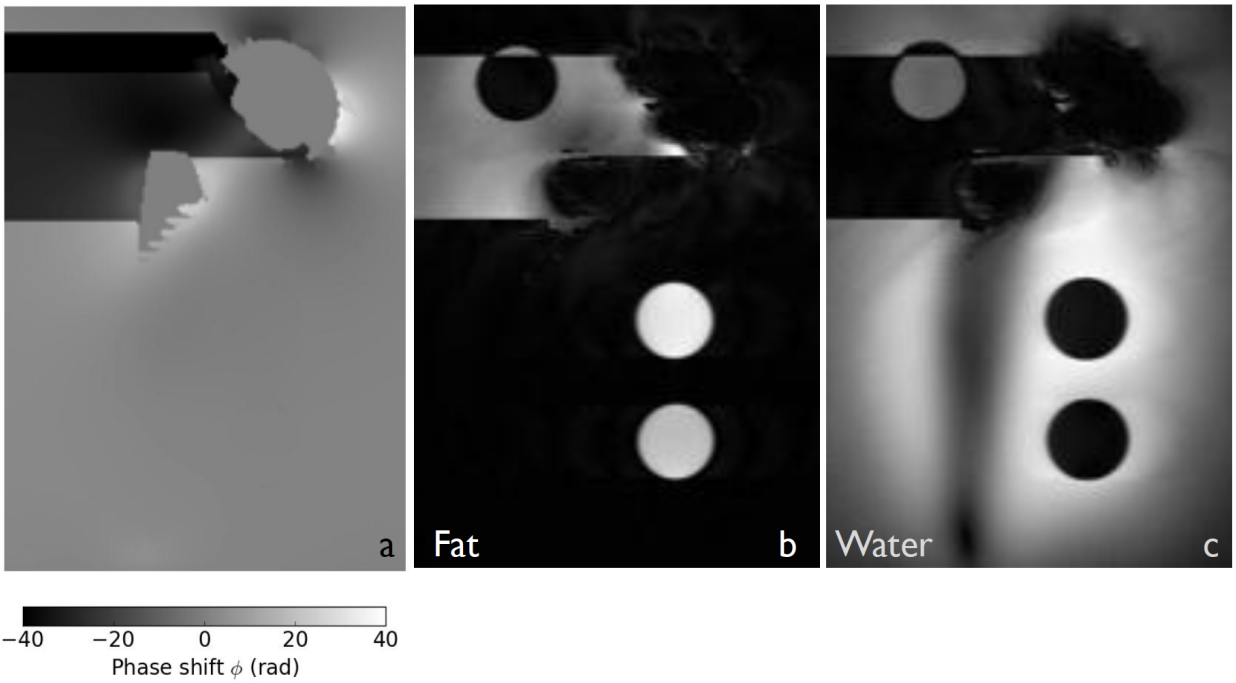

Figure 7.10: Phase shift (a), fat (b), and water (c) images of Phantom 1, Slice 4, obtained using the weighted branch cut method.

7.3 PHANTOM 2: CENTRAL SLICE

As described in Chapter 5, Phantom 2 contained a cobalt-chromium and titanium hip replacement embedded inside a plastic grid, which was suspended in agar gel. No vials of peanut oil were present in this phantom. Figure 7.11 shows the wrapped phase shift ϕ_w for the central slice of Phantom 2. Figure 7.12 shows the phase shift, fat, and water images using POP. This result was acquired using $K = 100$ paths distributed with $P = 0.74$. N ranged between 20 and 100. This method has generally succeeded, apart from several small regions labelled with red arrows which have been incorrectly identified as fat.

Figure 7.13 and 7.14 show the phase shift, fat, and water images obtained using the weighted minimum-norm and branch cut methods. Both these methods have again failed to correctly separate fat and water, with errors spreading throughout the images. The failure of fat suppression is generally more significant than for Phantom 1, as the phase shift gradient is steeper than the phase shift estimated for the central slice of Phantom 1 (Fig. 7.2). This is because Phantom 2 contained an implant with titanium and cobalt-chromium components, whereas Phantom 1 was comprised of titanium and ceramic components. The resonant frequency variation, $\Delta f[\mathbf{x}]$, (and so the phase shift) induced by the cobalt-chromium components is larger and contains steeper gradients than the $\Delta f[\mathbf{x}]$ variation induced by the titanium components [6].

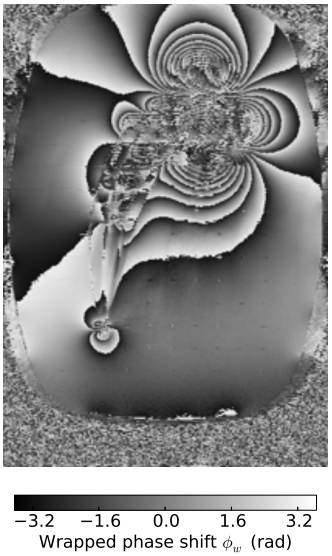

Figure 7.11: Phantom 2, central slice, wrapped phase.

[6] Recall from Sec. 2.2, the susceptibility value for cobalt-chromium is larger than the susceptibility value for titanium. The $\Delta f[\mathbf{x}]$ variation is proportional to the susceptibility value.

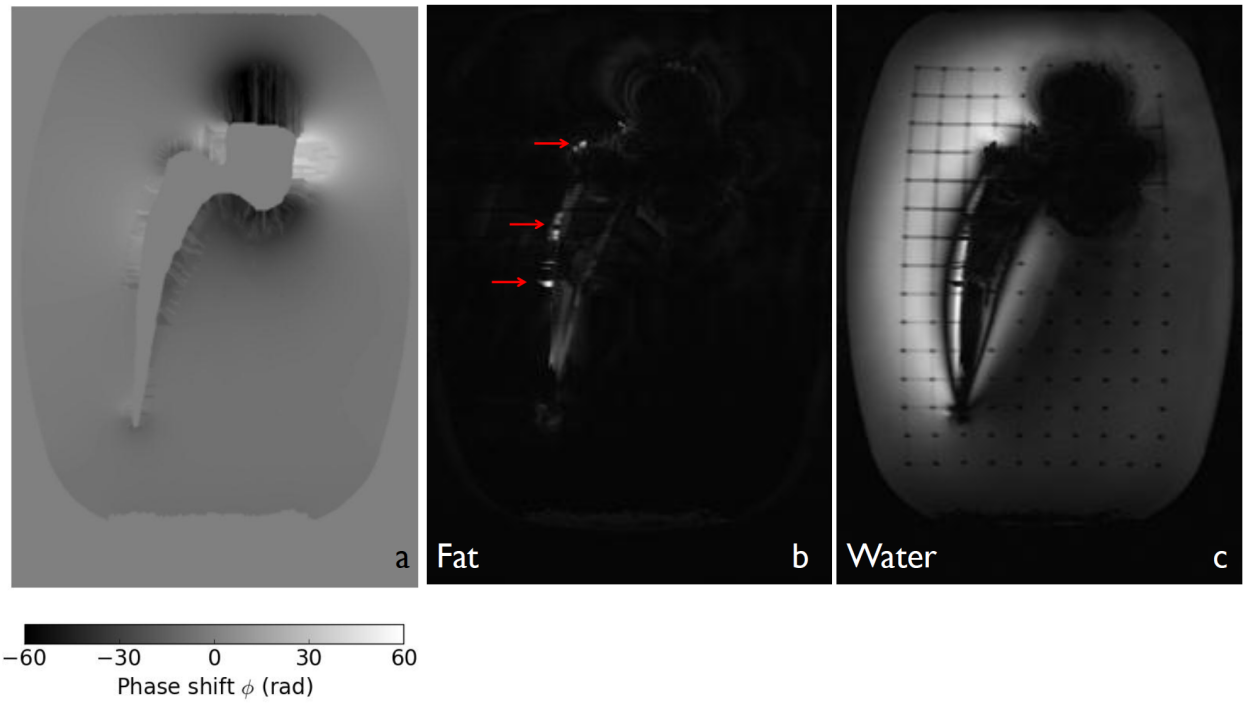

Figure 7.12: Phase shift (a), fat (b), and water (c) images of Phantom 2, central slice, obtained using the POP method.

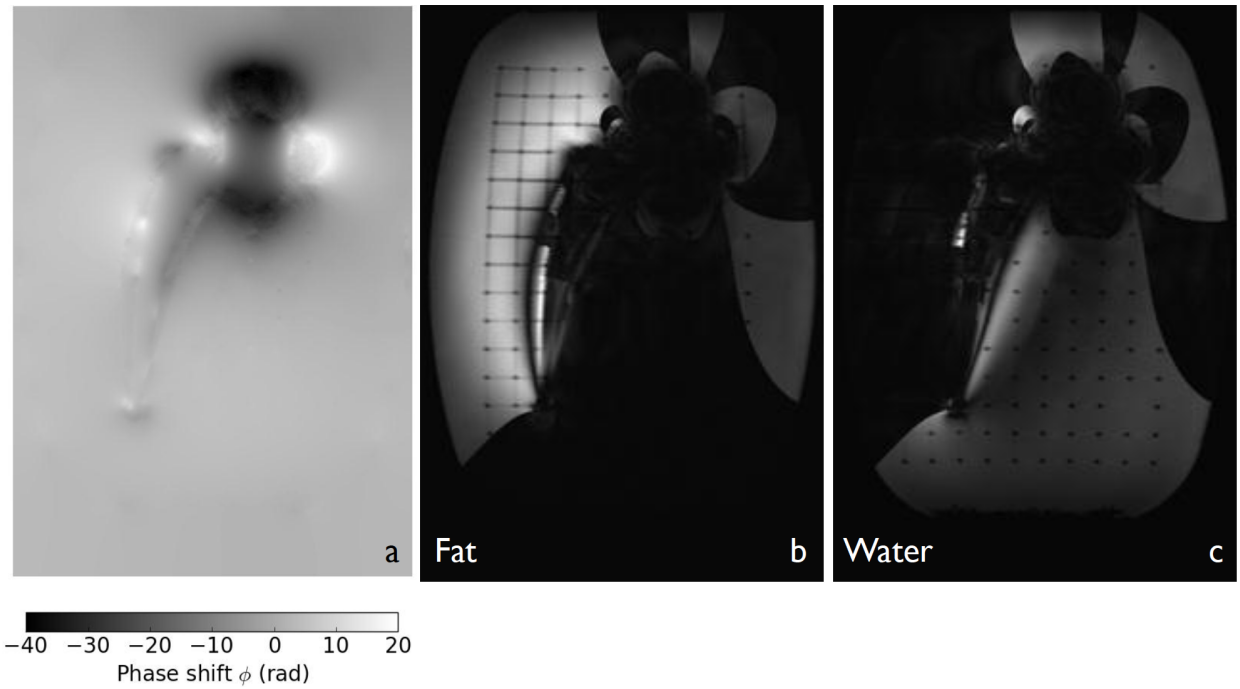

Figure 7.13: Phase shift (a), fat (b), and water (c) images of Phantom 2, central slice, obtained using the weighted minimum-norm method.

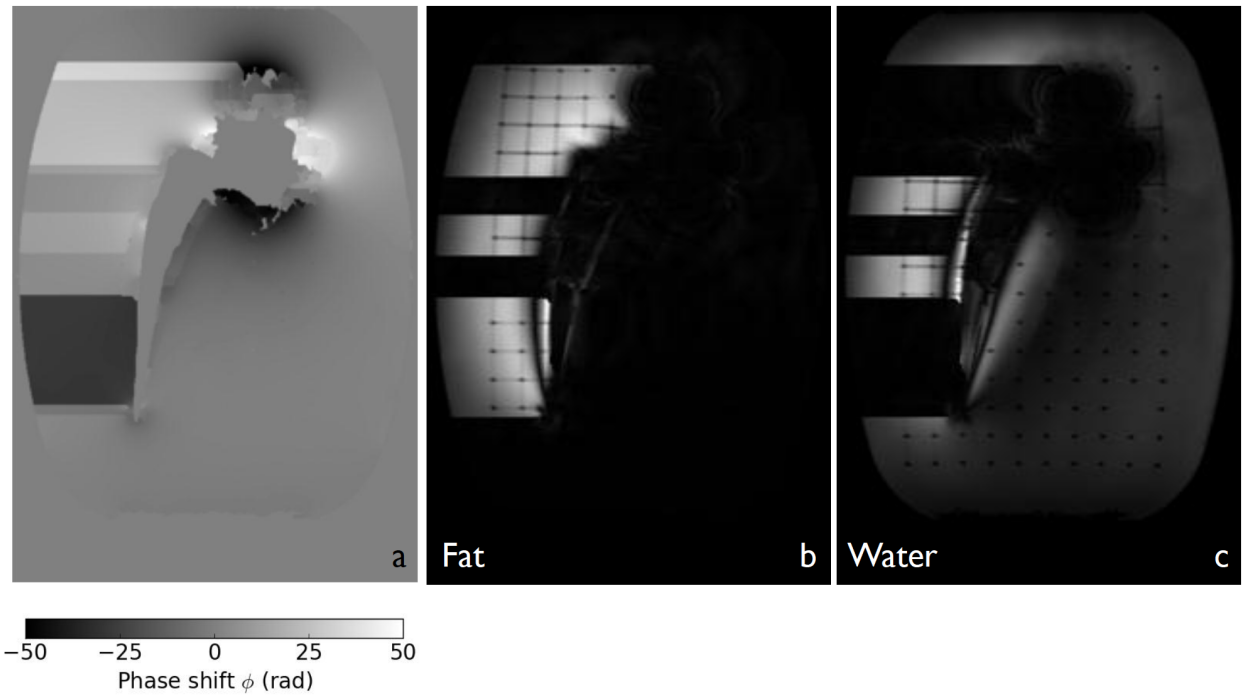

Figure 7.14: Phase shift (a), fat (b), and water (c) images of Phantom 2, central slice, obtained using the weighted branch cut method.

7.4 PHANTOM 2: SLICE 2

Slice 2 is separated from the central slice of Phantom 2 by 18 mm. Figure 7.15 shows the wrapped phase shift ϕ_w. Figure 7.16 shows the phase shift, fat, and water images using POP. This result was acquired using K = 100 paths distributed with P = 0.8. N ranged between 20 and 100. This method has again succeeded throughout most of the image, but has failed in several regions close to the implant boundary, with one region indicated with a red arrow.

Figure 7.17 and 7.18 show the phase shift, fat, and water images obtained using the weighted minimum-norm and branch cut methods. These methods have failed in a similar manner to the central slice of Phantom 2. Note that in these figures the plastic grid has a different appearance to the central slice figures, Figs. 7.12–7.14. This is because this slice does not intersect with a plane of horizontal cross links in the grid.

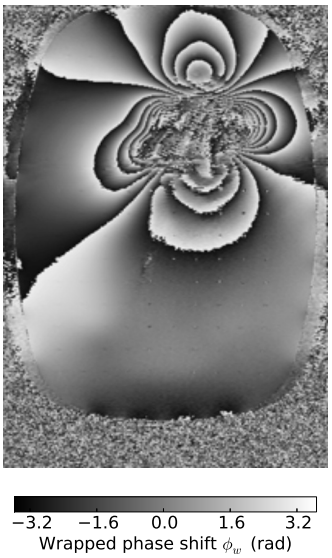

Figure 7.15: Phantom 2, Slice 2, wrapped phase.

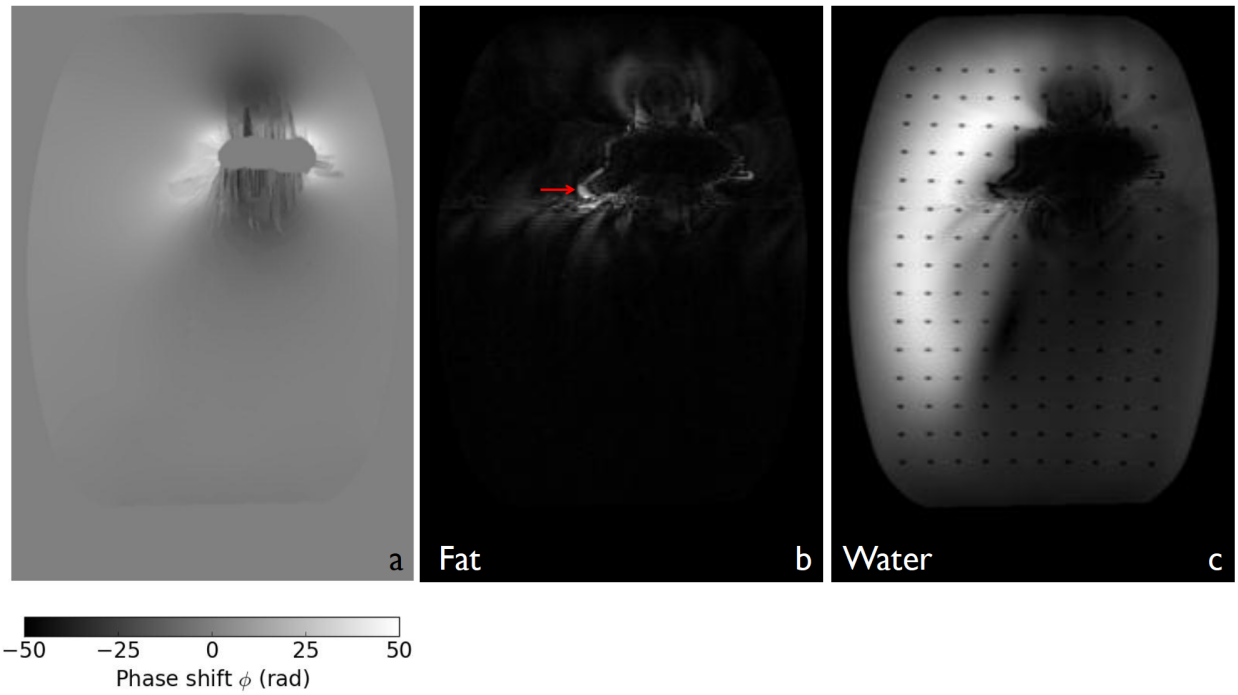

Figure 7.16: Phase shift (a), fat (b), and water (c) images of Phantom 2, Slice 2, obtained using the POP method.

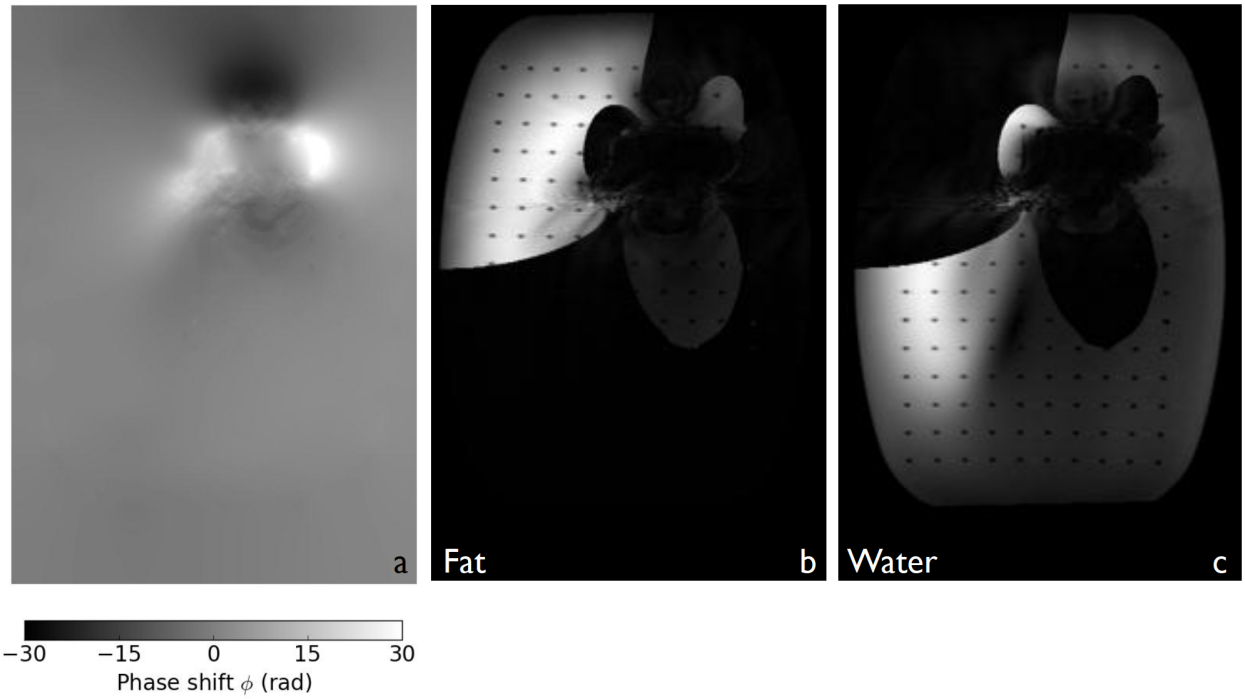

Figure 7.17: Phase shift (a), fat (b), and water (c) images of Phantom 2, Slice 2, obtained using the weighted minimum-norm method.

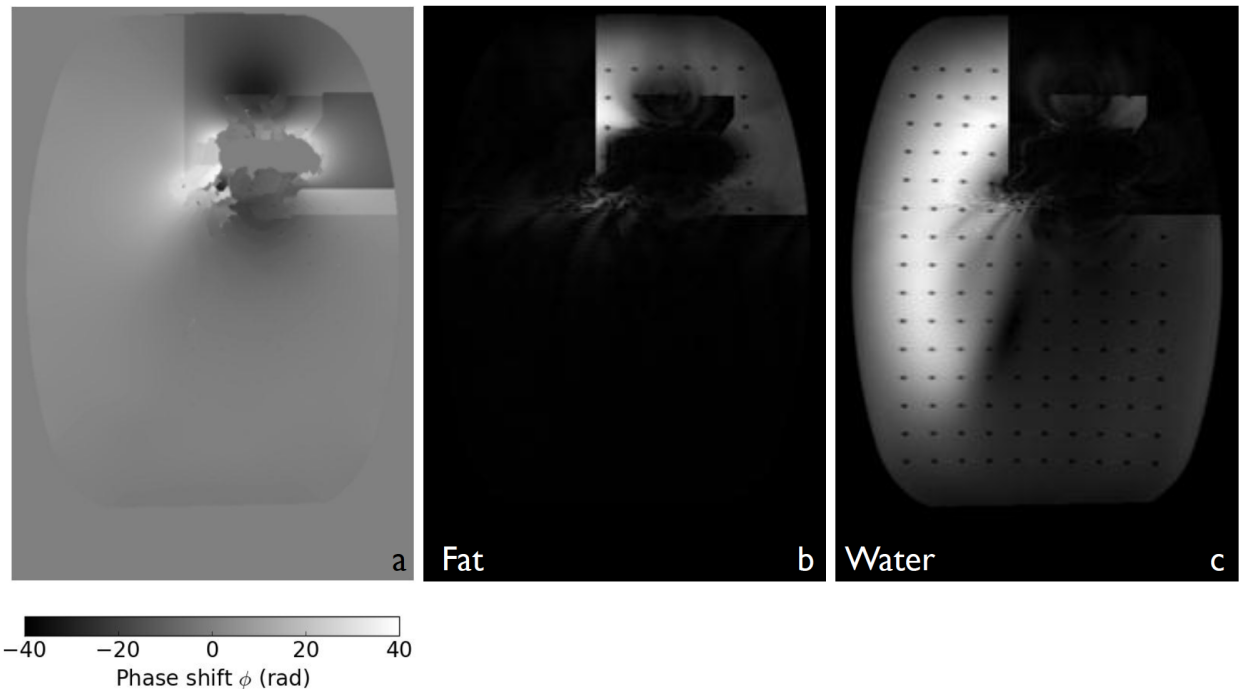

Figure 7.18: Phase shift (a), fat (b), and water (c) images of Phantom 2, Slice 2, obtained using the weighted branch cut method.

7.5 PHANTOM 3: CENTRAL SLICE

Phantom 3 contained a stainless steel femur replacement suspended in agar gel. The implant was surrounded by six vials of peanut oil. Figure 7.19 shows the wrapped phase shift ϕ_w for the central slice of Phantom 3.

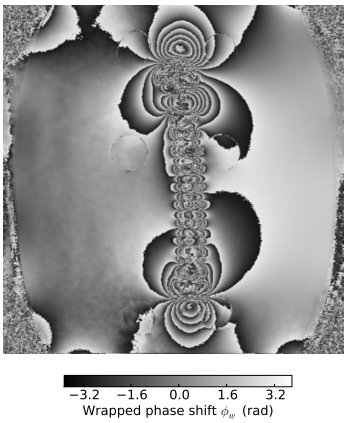

Figure 7.19: Phantom 3, central slice, wrapped phase.

Figure 7.20 shows the phase shift, fat, and water images using POP. This result was acquired using $K = 100$ paths distributed with $P = 0.6$. N ranged between 20 and 200. Five of the six fat vials have been separated from the water successfully. The fat separation has failed in parts of the lowest right-hand vial, as marked with a red arrow.

Figure 7.21 and 7.22 show the phase shift, fat, and water images obtained using the weighted minimum-norm and branch cut methods. Similar to the branch cut results for Phantoms 1 and 2, the fat and water images contain artifacts in the form of several streaks. The minimum-norm method has also failed to correctly separate fat and water, but the effect is more subtle. The errors in the phase unwrapping are spread throughout Fig. 7.21(a). This affects the intensity values at all pixels in the reconstructed images. As a result, in the fat image, the water pixels appear brighter than they should. Likewise, in the water image, the fat vials are not completely suppressed. This is most noticeable in the bottom two vials.

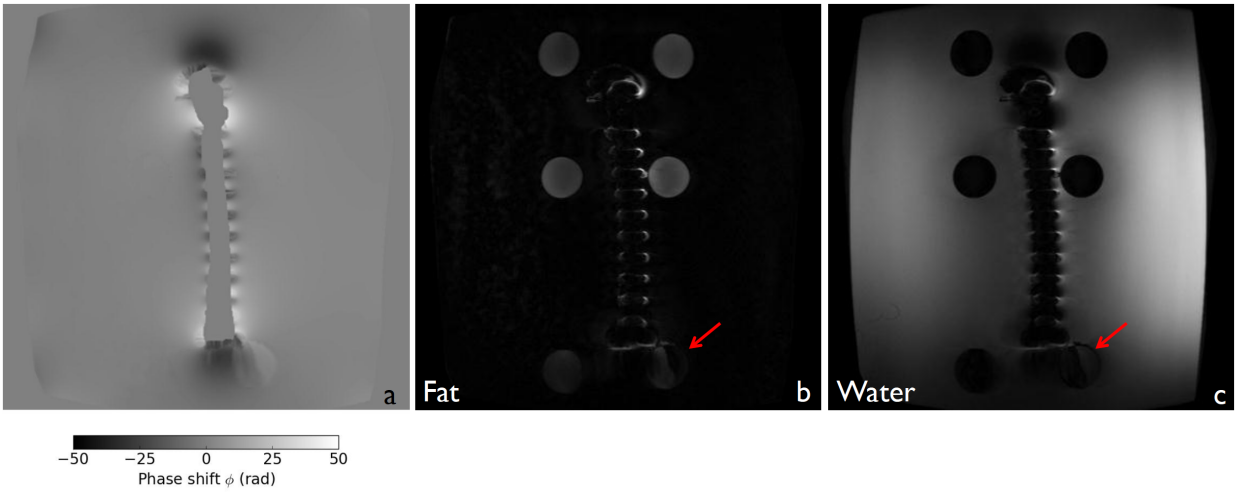

Figure 7.20: Phase shift (a), fat (b), and water (c) images of Phantom 3, central slice, obtained using the POP method.

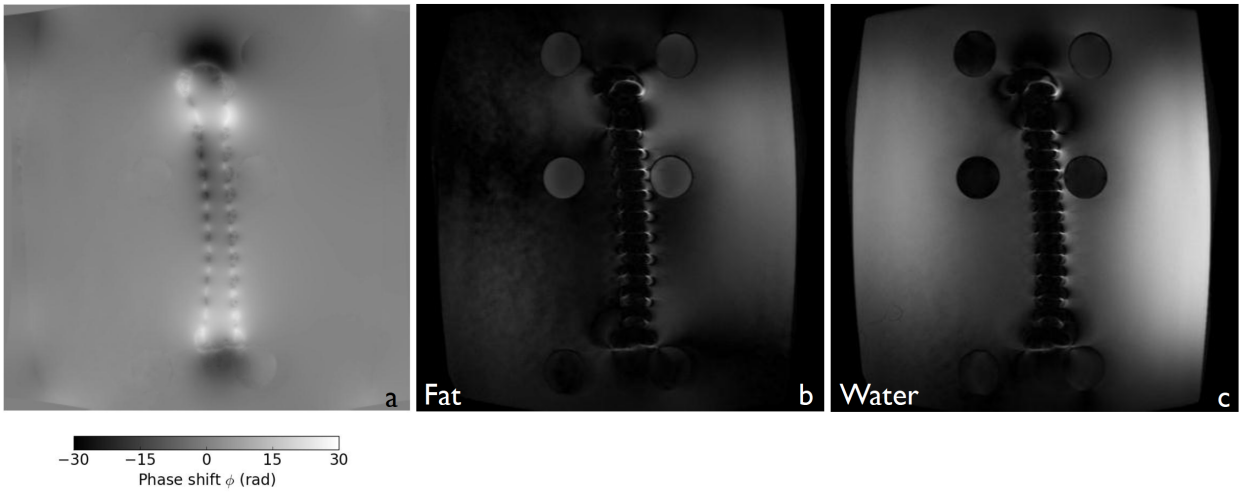

Figure 7.21: Phase shift (a), fat (b), and water (c) images of Phantom 3, central slice, obtained using the weighted minimum-norm method.

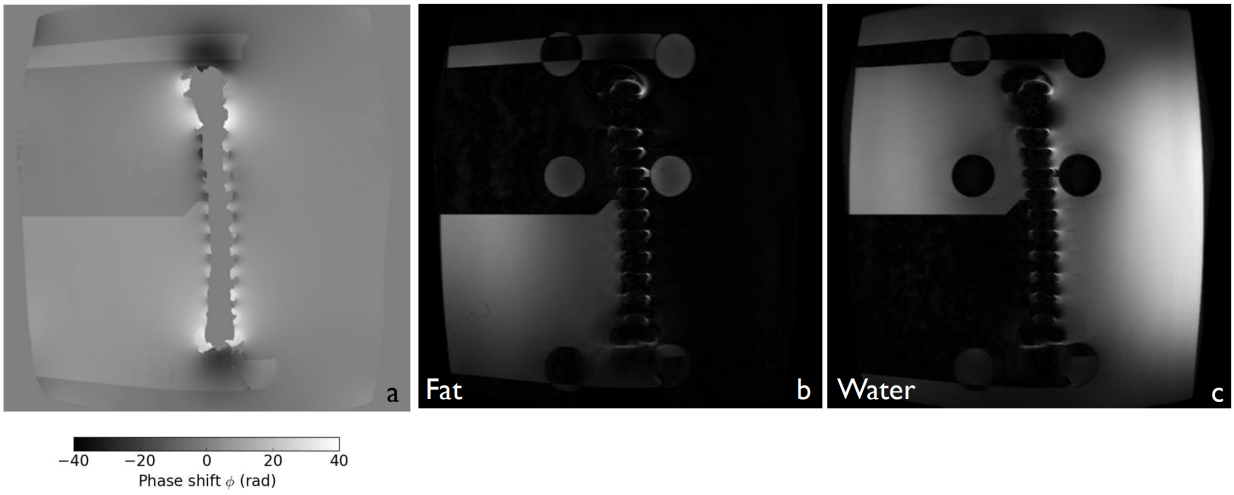

Figure 7.22: Phase shift (a), fat (b), and water (c) images of Phantom 3, central slice, obtained using the weighted branch cut method.

7.5.1 *POP with a cropped slice*

The imaged field of view for Phantom 3 was 390×390 mm. The outer phantom boundary is considerably larger than the corresponding boundary would be for an in-vivo femur implant, as discussed in Sec. 5.6. The outermost generated path is a significant distance from the implant boundary, where the phase is slowly varying. In order to simulate a more realistic scenario, where the implant is situated close to the outer boundary, POP was used to estimate the phase in a cropped slice.

The acquired FSE images were cropped from 512 pixels to 150 in the horizontal dimension. The corresponding phantom boundary mask for the slice was also cropped. The POP method then proceeded as normal. 60 paths were used, instead of 100 paths in Fig. 7.20.

Figure 7.23 shows the obtained phase shift, fat, and water images for a cropped central slice of Phantom 3. The resulting fat and water images have similar results to Fig. 7.20, with slightly improved fat-water separation in the lowest right-hand fat vial. The reasons for this are examined in Sec. 7.7, *Discussion*.

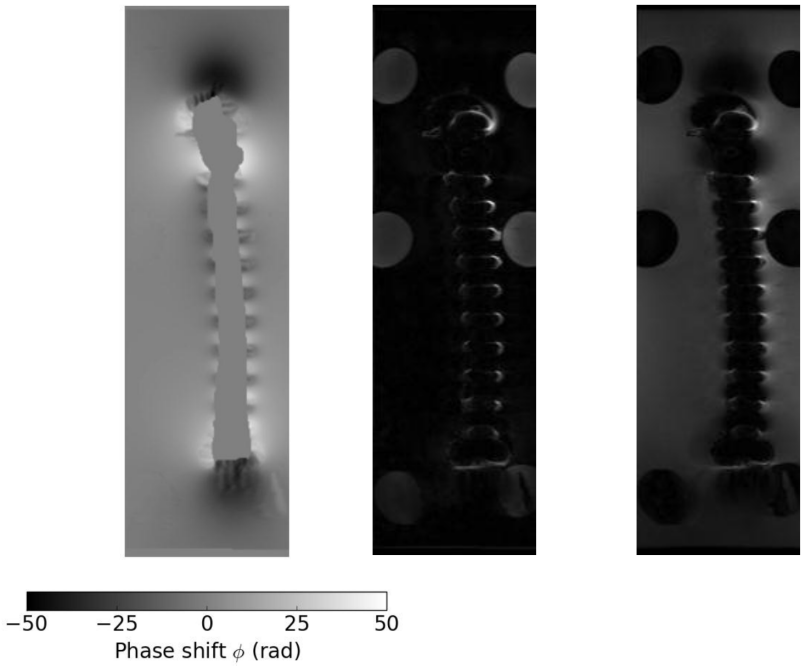

Figure 7.23: Phase shift (left), fat (middle), and water (right) images of Phantom 3, cropped central slice, obtained using the POP method.

POP is capable of separating the fat and water in slices where the phantom boundary is close to the implant boundary. However, the requirement that the phase along the outermost path must vary sufficiently slowly that it can be unwrapped successfully still exists.

7.5.2 *STIR and fat saturation*

Phantom 3 was also scanned using STIR and fat saturation sequences. The fat suppressed images for the central slice are shown in Fig. 7.24.

All six fat vials have been successfully suppressed using STIR, but the SNR is lower than in the images acquired using the Dixon technique. Fat saturation has failed to suppress the fat in three of the six vials, and artifacts are present throughout a significant proportion of the image.

It should be noted that the default iterative IDEAL algorithm on the scanner was also used to reconstruct the Phantom 3 images acquired with the IDEAL protocol [7]. The performance of this algorithm at separating fat and water near metal is discussed in Chapter 9, *Iterative resonant frequency estimation near metal*.

[7] Recall that this algorithm is described in Sec. 3.3.4.

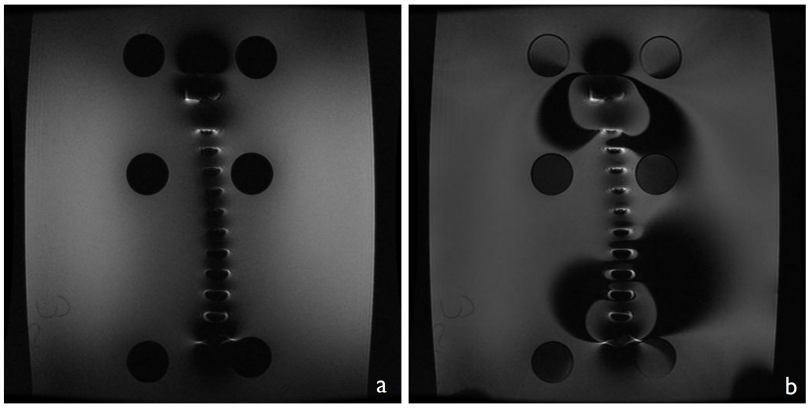

Figure 7.24: Fat suppressed images of Phantom 3 obtained using STIR (a) and fat saturation (b).

7.6 PHANTOM 3: SLICE 10

Slice 10 is offset from the central slice of Phantom 3 by 21 mm [8]. In this case the slice intercepted only a small part of the implant. Figure 7.25 shows the wrapped phase shift ϕ_w.

[8] Recall that 33 slices were acquired for Phantom 3 (Table 5.3).

Figure 7.26 shows the phase shift, fat, and water images using POP. This result was acquired using $K = 100$ paths distributed with $P = 0.6$. N ranged between 20 and 150. This method has succeeded relatively well at separating the fat in the vials but has failed significantly in the water-filled central region of the image near the implant boundary.

Figure 7.27 and 7.28 show the phase shift, fat, and water images obtained using the weighted minimum-norm and branch cut methods. Both these methods have shown improved performance over POP in the central region of the slice. However, the images contain similar artifacts to the results for the central slice of Phantom 3 (Figs. 7.21 and 7.22). The intensity values at all pixels throughout the minimum-norm images have been altered, with the bottom two fat vials the most affected. Streak artifacts are present throughout significant proportions of the branch cut images, with numerous streaks originating from pixels located near the implant boundary.

Figure 7.25: Phantom 3, Slice 10 wrapped phase.

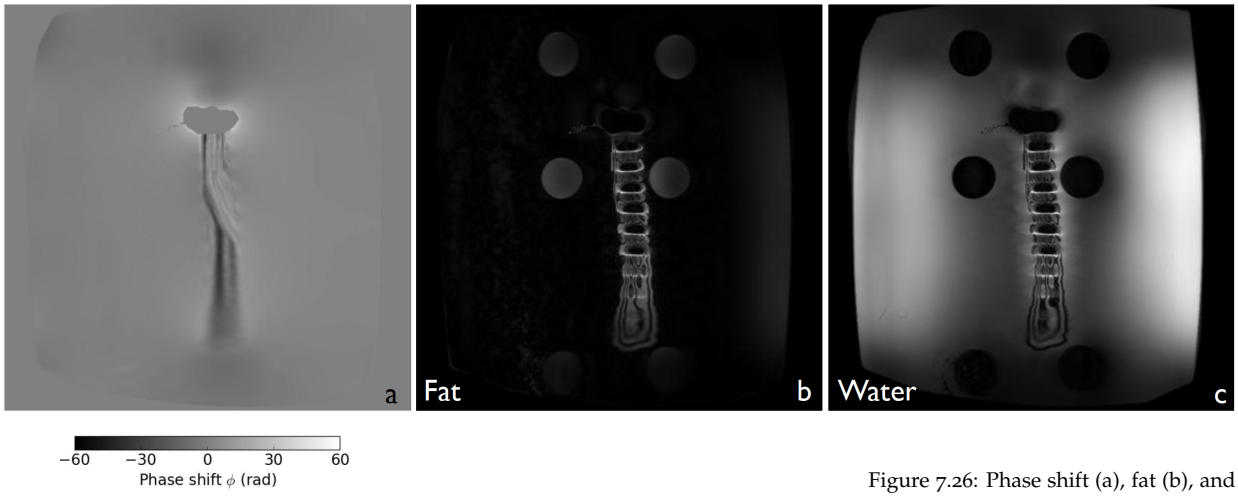

Figure 7.26: Phase shift (a), fat (b), and water (c) images of Phantom 3, Slice 10, obtained using the POP method.

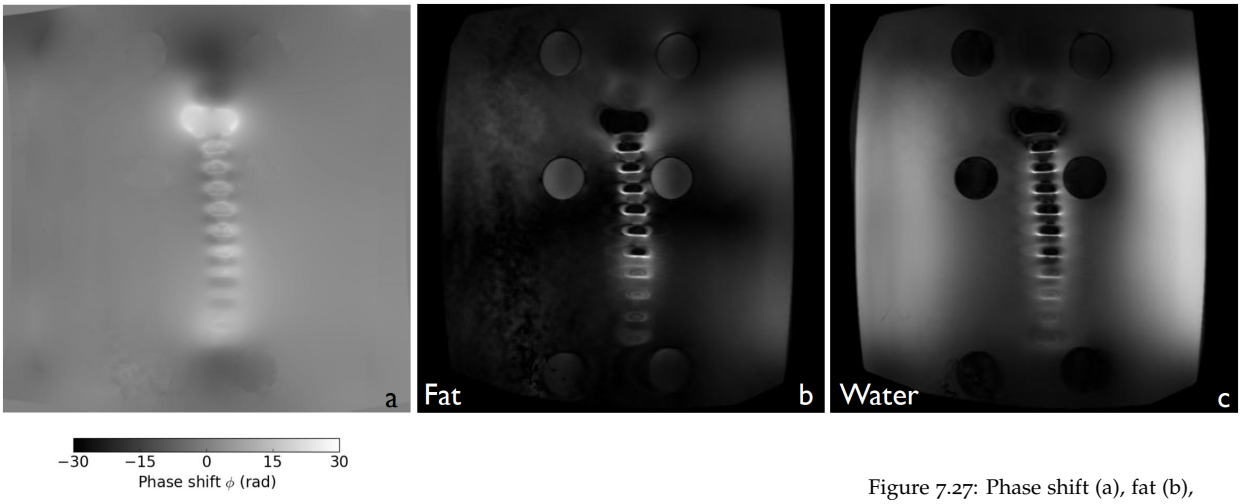

Figure 7.27: Phase shift (a), fat (b), and water (c) images of Phantom 3, Slice 10, obtained using the weighted minimum-norm method.

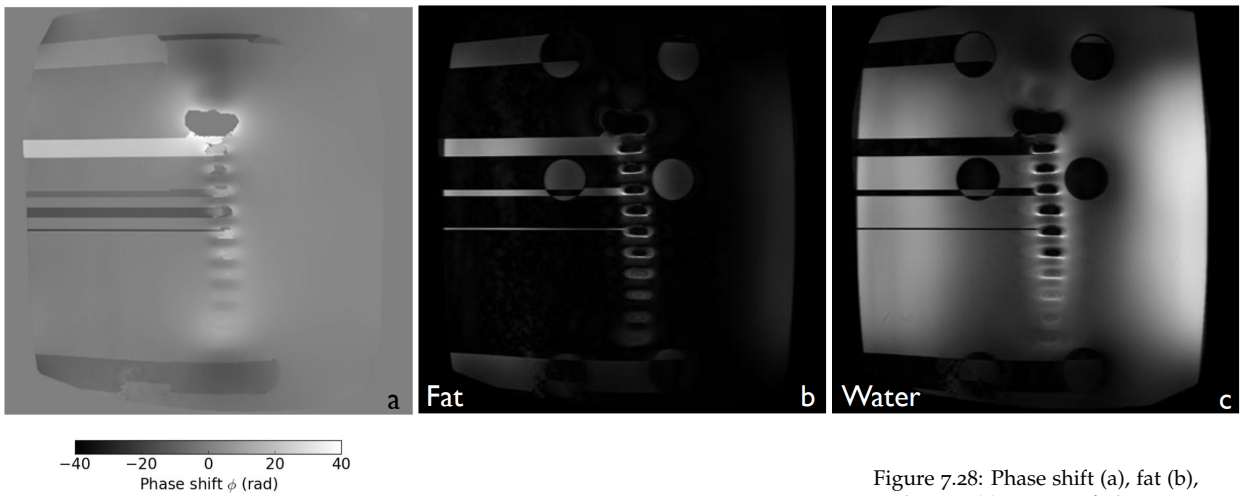

Figure 7.28: Phase shift (a), fat (b), and water (c) images of Phantom 3, Slice 10, obtained using the weighted branch cut method.

7.7 DISCUSSION

Phase Onion Peeling (POP) was tested on the three sets of phantom data. The performance of POP was compared with branch cut and minimum-norm phase unwrapping methods. Results were shown for two slices for each phantom. POP has generally performed better at fat-water separation than the branch cut and minimum-norm methods.

In general, the branch cut and minimum-norm methods are not able to unwrap the phase successfully near the implant boundary. This is shown by large streaks in the branch cut results, which tend to propagate throughout the image. This happens when the phase is unwrapped across one or more unbalanced residues [9]. Even a single unbalanced residue can produce significant errors in the unwrapped phase.

[9] Recall that residues and branch cuts are discussed in Secs. 4.2 and 4.3.

The severity of the streaks produced depends on the location of the first, or seed, pixel. This pixel is unwrapped first in the flood-fill stage of the algorithm. If it is situated close to an unbalanced residue, the errors from unwrapping across this residue spread throughout a larger proportion of the image. Figure 7.29 shows the unwrapped phase obtained by starting the branch cut algorithm at four different locations. Four different solutions have been calculated.

In comparison, the minimum-norm method produces errors which are distributed throughout the unwrapped phase. This is because the minimum-norm method unwraps the phase by taking the DCT of the wrapped phase differences, and scaling the transformed values [Ghiglia and Romero, 1994]. The unwrapped phase is then obtained by the inverse DCT. Poor quality wrapped phase values will therefore alter the value of the unwrapped phase across the entire image. This can cause the fat-water separation to fail in subtle ways, as shown in Figs. 7.21 and 7.21. Both the weighted branch cut and weighted minimum-norm methods perform significantly better than their unweighted equivalents.

POP fails to achieve accurate fat and water separation in two distinct situations. The first situation occurs in regions close to the implant boundary. This is most pronounced in the results for Phantom 3, which contained a stainless steel implant [10]. The failure may be due to multiple reasons. First, the optimisation routine may have converged to an incorrect solution. Second, the signal magnitude is low in these regions, so the extracted phase is noisy. Finally, there are significant in-plane and through-plane artifacts. The extracted phase at each pixel is therefore a distorted version of the true phase. The POP estimated phase shift contains significant ripple-like artifacts in these regions, as shown in Fig. 7.26. The underlying assumption that the phase is smooth and can be estimated by a Fourier series may not be valid in these circumstances. This is discussed further in Chapter 10, and in Sec. 11.2, as a topic of future work.

[10] Recall that stainless steel has a susceptibility of 3000-5000 ppm, and so induces the largest resonant frequency variations.

POP also fails to successfully estimate the phase at all points between multiple implant boundaries. This is shown in Fig. 7.8. This is

likely because the path density is insufficient in these areas. This is a known flaw of the described path generation method, as discussed in Sec. 6.2.3. This is also a topic for future work.

Finally, the POP fat-water separation in the cropped central slice of Phantom 3 (Fig. 7.23) displayed improved performance in the lowest right-hand fat vial compared to the full slice (Fig. 7.20). As discussed above, due to in-plane and through-plane distortions the assumption that the phase is smooth along paths which intersect with this vial may not be valid. POP has likely converged to two different solutions for the phase in the cropped slice compared to the full slice, producing different error patterns in Fig. 7.20 and Fig. 7.23. This demonstrates that POP may be susceptible to producing inconsistent results in regions of steep phase (or resonant frequency) variations.

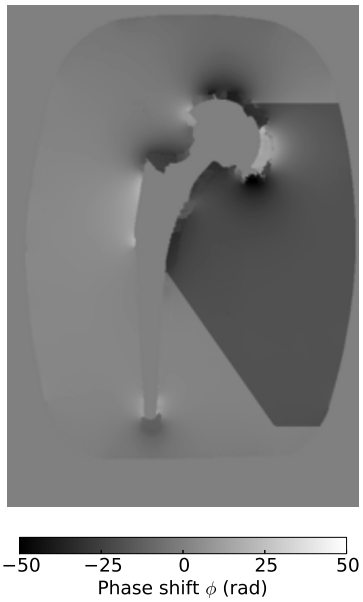

(a) Starting pixel origin: top left

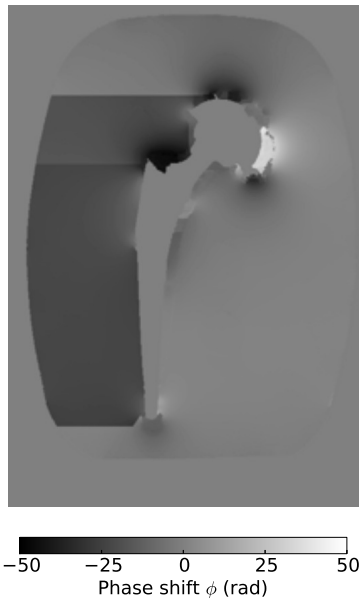

(b) Starting pixel origin: top right

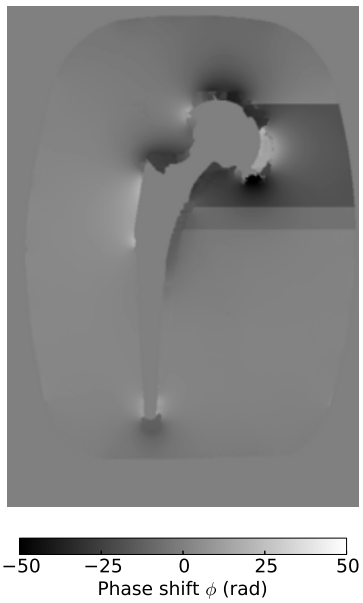

(c) Starting pixel origin: bottom left

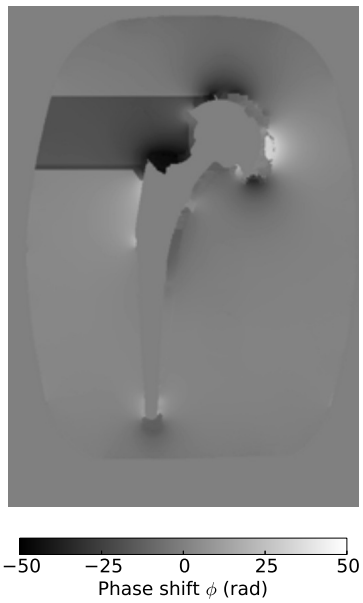

(d) Starting pixel origin: bottom right

Figure 7.29: Unwrapped phase for the central slice of Phantom 1 using the weighted branch cut method. In each plot the algorithm was started from a different initial pixel location.

8

Human Study

This chapter presents results from imaging seven human subjects with orthopaedic hip replacements. The overall aim of the study was to assess the performance of POP for reducing fat suppression artifacts in MR images of participants with metal implants. The study sought to answer two research questions:

1. How does the performance of POP compare with existing phase unwrapping algorithms?
2. How does the performance of POP for the Dixon technique compare with IDEAL?

▶ The chapter is separated into three sections:

- Section 8.1, *Method*, first outlines the process of recruiting participants and acquiring data for the study. The data reconstruction is then described, including the aspects of the POP algorithm which are adjusted for the human study. Finally, the methods used to analyse the reconstructed data are explained.
- Section 8.2, *Results*, presents the results of analysing the obtained participant data. Samples of the processed slices are displayed first. This is followed by a summary of the statistics calculated to compare the performance of each fat-water separation method.
- The final section, Sec. 8.3, *Discussion*, provides context to the results presented, with respect to the two aims of the study. The limitations of POP are also examined in detail, and possible future developments are briefly outlined as a precursor to Chapter 11.

8.1 METHOD

Human ethics approval for this study was obtained by the Central Health and Disability Ethics Committee of the New Zealand Ministry of Health. The study title was *Improving fat suppression in magnetic resonance imaging of patients with metal implants.* The ethics reference number was 16/CEN/106.

This was an observational study designed to demonstrate proof-of-concept of the POP algorithm. MRI data were collected for a sample size of seven participants. Two participants had ceramic and titanium hip replacements, and five had cobalt-chromium and titanium replacements.

8.1.1 Participants

Participants were recruited using the Canterbury Orthopaedic and Bone Research Association (COBRA) database. This database stores patient demographics and pre-operative and post-operative information, including:

- Pre-operative body mass index (BMI).
- Reason for orthopaedic surgery, such as osteoarthritis.
- Post-operative Oxford score [1].

The potential participants were selected from those in the COBRA database who had recently completed a five year follow up study after their joint replacement surgery between 2009 and 2010. This study compared the progress of patients with ceramic-on-ceramic hip replacements, with those with metal-on-metal replacements [2]. Each patient underwent a yearly questionnaire, X-ray and blood test. Potential participants were randomly selected from those in the study meeting the following inclusion and exclusion criteria:

[1] The Oxford hip and knee scores are short questionnaires which are completed by the patient after surgery (such as six months post-surgery). The questions are designed to assess function and pain experienced while carrying out standard daily activities [Dawson et al., 1996, 1998].

[2] In a *ceramic-on-ceramic* replacement, the liner and femoral head are both ceramic. In a *metal-on-metal* replacement, the liner and head are cobalt-chromium. This is explained in further detail in the inclusion criteria below. Refer to Fig. 5.1 for a diagram of the main components.

▶ INCLUSION CRITERIA:

1. Participant has a non-ferrous MRI safe metal orthopaedic hip implant made of either titanium or cobalt-chromium.
2. Half of the participants have a ceramic-on-ceramic De Puy hip replacement made of the following materials:
   - Titanium femoral stem,
   - Titanium acetabular shell,
   - Ceramic acetabular liner,
   - Ceramic femoral head.

   The other half have a metal-on-metal De Puy hip replacement, made of the following materials:
   - Titanium femoral stem,

- Titanium acetabular shell,
- Cobalt-chromium acetabular liner,
- Cobalt-chromium femoral head.

3. Participant's post-operative Oxford score is higher than 37 at one year after surgery.
4. Participant has undergone primary joint replacement surgery.
5. Participant has undergone joint replacement surgery due to osteoarthritis.
6. The participant's address is situated within ten kilometres of the study locality.
7. Participant is able to lie in a supine position for at least 30 minutes.
8. Participant is able to read written English and understand spoken English.
9. Participant is willing to give voluntary, written consent to participate in the study.
10. Participant, in the opinion of the investigators, is able to understand the study, and is willing and able to perform all study procedures.

► Exclusion criteria:

1. Participant has other implants which are not MRI-safe, including pacemakers, catheters, cochlear implants, or metal hardware made of a ferrous material.
2. Participant has undergone revision surgery or is on the waiting list for a revision surgery.
3. In addition to osteoarthritis, the participant has other pre-existing conditions such as inflammatory arthritis or cancer that could potentially alter MRI outcomes.
4. Participant is claustrophobic.
5. Participant has a medical condition which means they are unable to provide informed consent or understand the study.
6. Participant's BMI exceeds 30. This is necessary to ensure their body mass and girth does not exceed the maximum limits for the MRI scanner, which are 150 kg and 60 cm, respectively.

There were no specific requirements on the participants' age, ethnicity, or gender. Ten participants were initially contacted, with seven agreeing to take part in the study.

8.1.2 *Data acquisition*

Each participant made one visit to the GE 750 3 T MRI scanner at the New Zealand Brain Research Institute (NZBRI) in Christchurch. The total scan time for each participant was approximately 30 minutes.

The following scan protocols were run:

1. FSE-IDEAL Dixon sequence, with the following symmetric echo time offset parameters: $t_n = [0, 1.1, 2.2]$ ms.
2. FSE-IDEAL Dixon sequence, with the following echo time offset parameters: $t_n = [-1.1, 0, 1.1]$ ms.
3. FSE-IDEAL Dixon sequence, with the default echo time offset parameters of $t_n = [-0.2, 0.6, 1.4]$ ms.
4. STIR inversion recovery sequence.
5. FAT-SAT fat saturation sequence.

The scan parameters used were similar to the Phantom 1 and 2 scan parameters given in Table 5.1. The parameters which were different to those used for the phantoms are given in Tables 8.1 and 8.2.

Parameter	Value
Echo time (TE)	12 ms
Number of slices	26
Coil	Eight-channel cardiac coil

Table 8.1: Scan parameters which were altered for all participant scans.

Participant	Matrix size	Field of view (mm)
1	384×192	390×390
2	416×192	420×420
3 - 7	448×224	460×460

Table 8.2: Scan parameters which were altered for each participant's scan.

All protocols were reconstructed by the MRI scanner software at the time of acquisition. For protocols 1-3 the raw data was also acquired and was reconstructed offline using `orchestra-sdk-1.4-722`, as described in Sec. 5.5. All images were reconstructed in DICOM format.

8.1.3 *Reconstruction*

This subsection first outlines the methods used to reconstruct the acquired data. This is followed by descriptions of the components of the POP method which were altered for the participant data. The three components are: the mask acquisition process, the method for unwrapping the outermost path, and the parameter values used.

The data from each protocol was reconstructed using the algorithms described in Table 8.3.

Protocol	Reconstruction Algorithm
1	POP Weighted minimum-norm Weighted branch cut Standard IDEAL with symmetric echo time offsets (scanner implementation)
3	Standard IDEAL with default asymmetric echo time offsets (scanner implementation)
4	Standard STIR
5	Standard FAT-SAT

Data from Protocol 2 was not reconstructed with POP. It was acquired as a backup dataset in case of any corruption of the p-files acquired in Protocol 1.

Table 8.3: Reconstruction methods used for each protocol.

For each acquired dataset, every third slice was analysed. This method was used as it allowed for the performance in the outer slices to be assessed along with the central slices. Nine slices were analysed for each participant, giving 63 slices in total [3].

[3] For Participant 7, the scan slices were not centred around the implant. A significant number of slices did not contain the implant. Nine central slices containing the implant were used instead of analysing every third slice.

- MASK FORMULATION:
Two masks were calculated for each slice: a mask of the outer boundary of the participant anatomy, M_o, and a mask of the estimated implant boundary, M_i. These were generated using the same method as for Phantoms 2 and 3. A manual threshold was applied, with the connected components corresponding to each mask then selected [4].

The hip replacement for Participant 7 also had two screws situated near the top of the femoral stem. Three masks were used in the processed slices: a mask for the main hip implant, and two small masks for each of the screws.

[4] Refer to the beginning of Chapter 7, *Mask formulation*, for details.

- UNWRAPPING OUTERMOST PATH:
As described in Sec. 6.3.2, the outermost path in POP is unwrapped using standard 1D phase unwrapping. This was a suitable approach for the phantom data, where the agar simulated a simplistic, uniform tissue. There was a distinct boundary at the outer edge of the phantom. In comparison, the outer boundaries in the acquired participant data were located near the edge of the coil used, and so the signal magnitude along the outermost path is much lower than for central regions of the image. The extracted wrapped phase along this path is noisy, but slowly varying. The presence of residues, or inconsistent pixels, along this path mean it cannot be assumed that the phase can be unwrapped successfully with a 1D method. Figure 8.1 shows the water image produced from an initial attempt at reconstructing a slice by using 1D unwrapping on the outermost path. In this example the 1D path unwrapping has failed and significant errors have propagated throughout the image.

Figure 8.1: Water-only image of Participant 2, Slice 18, produced by performing 1D phase unwrapping on the outermost path, and then proceeding with the POP algorithm.

Instead, the outermost paths of the participant slices were unwrapped by first performing 2D phase unwrapping on a thin strip near the outer boundary. After the paths were generated for a particular slice, a third temporary mask was calculated, M_t. The boundary of this mask, Γ_t, was obtained from the mth path in the list, ρ_m. The strip of pixels between the two masks, M_o and M_t, was then unwrapped using the weighted branch cut method. In the acquired slices, $m = 5$ was used. Figure 8.2 shows M_o and M_t for a sample slice, and the corresponding strip of unwrapped phase. Figure 8.3 shows the resulting water image for Slice 18, Participant 2, obtained with the described unwrapping method on the outer paths.

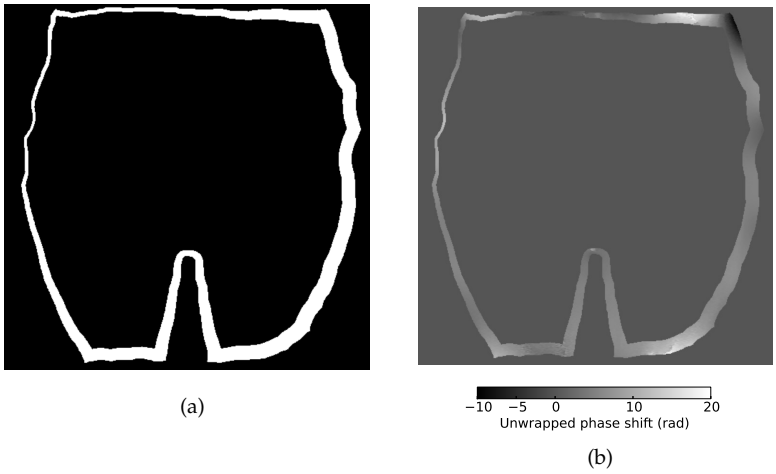

(a) (b)

Figure 8.2:
a) The two masks M_o and M_t are shown in black, with the area which is unwrapped within the strip shown in white.
b) The strip of unwrapped phase, obtained before proceeding with POP.

▶ PARAMETER VALUES:
The following range of parameter values were used for the processed slices:

- The number of levels, or paths, K, was 150 for all slices. This value was chosen as it struck an appropriate balance between generating sufficient paths to cover a significant proportion of the image, and keeping the processing time acceptably low.
- P, the constant which controls how closely the paths are distributed, lay in the range $[0.3, 0.6]$. The results were found to be relatively insensitive to the value used. Lower values were used for the datasets containing cobalt-chromium implants, and higher values for the titanium implants. This allowed the paths for the cobalt-chromium implants to be more closely spaced near the implant boundary, where the phase varies more rapidly compared to the titanium implants.
- The order of the Fourier series used, N, was linearly spaced between 20 for the outermost path, and between 50 and 90 for the innermost path. Again the results were fairly insensitive to the value. A higher order for the innermost path was used for the cobalt-chromium implants, compared to the titanium implants. A higher order was used to enable correct fitting of the phase along

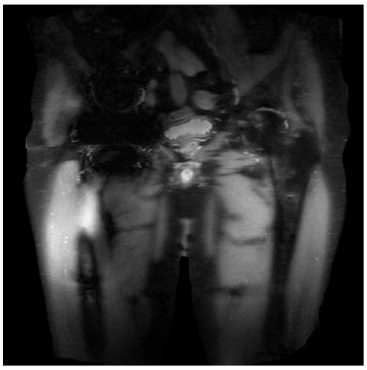

Figure 8.3: Water-only image of Participant 2, Slice 18, produced by performing 2D phase unwrapping on a thin strip of outer paths, and then proceeding with the POP algorithm.

the inner paths, which contain steeper gradients compared to the titanium implants.

Five slices from three participants were initially processed with the parameters used in the phantom datasets. Reconstructions were then repeated with different parameter settings to derive the values listed above.

8.1.4 Analysis

The analysis of the reconstructed slices intended to answer the two research questions stated at the beginning of this chapter.

- FIRSTLY, a comparison was made between POP and the weighted minimum-norm and weighted branch cut methods at separating fat and water. The water-only images were assessed for each of the 63 slices processed with the three methods. The regions in each processed slice where obvious fat-water swap artifacts had occurred were measured. This was done by manually tracing the boundary of the regions using the OsiriX region of interest (ROI) measurement tool [OsiriX, 2015]. The total measured area of all the regions in each slice, in pixels^2, was exported and collated. This was then converted to a proportion of the total pixels in the image.

  It was intended that only regions corresponding to fat-water swap artifacts were measured. Regions where other near-metal artifacts had occurred would not be included, such as signal loss and distortion. However, close to the implant boundary, it is difficult to distinguish between signal loss and an incorrectly fat-suppressed area. Therefore, the values presented in Sec. 8.2.2 are an approximate indication of the severity of the fat-water swap artifacts.

- SECONDLY, an assessment was carried out to ascertain how POP performed compared to other fat-water separation techniques, especially IDEAL. An independent fully trained radiologist compared the water images in the following datasets:

  1. Comparison 1: the Protocol 1 slices reconstructed with POP, and the Protocol 3 slices reconstructed with the default IDEAL algorithm on the scanner. For reference, the STIR images were provided as a third dataset.

  2. Comparison 2: the Protocol 1 slices reconstructed with POP, and the Protocol 1 slices reconstructed with the IDEAL scanner algorithm. The STIR images were also shown for reference.

  The datasets were anonymised by removing all personal information pertaining to the participant, with the name replaced by a randomly generated three digit identification number. The order in which the POP and IDEAL datasets appeared during the inspection was randomised. The method used was unknown to the radiologist, with the name replaced by "Method A" or "Method B". All STIR images

were designated as the third method, with the name remaining as STIR.

For each of the seven participant datasets, the radiologist answered the following two quality questions:

1. Do these slices have homogeneous fat suppression?

2. Are these slices diagnostic?

A rating system from 1-5 was used to answer both quality questions, where 1 indicated poor quality, and 5 indicated excellent quality. Figure 8.4 shows two example slices where the level of fat suppression homogeneity corresponds to ratings of 1 and 5.

Two ratings were applied across the entire set of nine processed slices for each participant: a rating answering question 1, and a rating answering question 2. This system was chosen for two reasons. First, in practice radiologists consider a series of slices when making decisions, and can "read through" or ignore occasional slices which contain artifacts. Second, this reduced the time needed to evaluate the datasets, compared to assigning a separate rating for each individual slice.

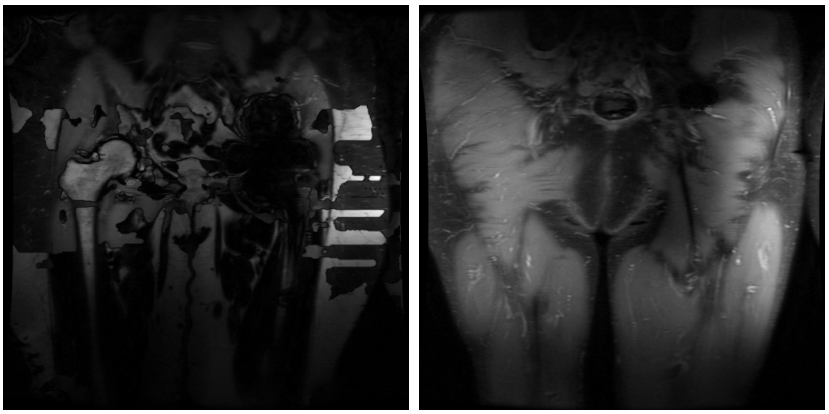

(a) (b)

Figure 8.4:
a) Typical slice with inhomogeneous fat suppression corresponding to a quality rating of 1, or "poor".
b) Typical slice with relatively homogeneous fat suppression corresponding to a quality rating of 5, or "excellent".

8.2 RESULTS

This section is separated into three components. First, a selection of the slices processed with the described reconstruction methods are shown. Second, the results of measuring the fat-water swap artifacts in the processed slices are summarised with a set of box plots. Finally, the ratings assigned by the radiologist to each dataset are presented.

8.2.1 Illustrated results

This subsection displays results obtained for a small subset of the processed slices. The presented slices are typical of the study results. Figure 8.5 shows the phase shift, fat, and water images reconstructed using the POP, weighted minimum-norm, and branch cut methods, for Participant 3, Slice 15. Similarly, Fig. 8.6 shows the phase shift, fat, and water images processed with the POP, weighted minimum-norm, and branch cut methods, for Participant 4, Slice 5. Both implants shown in these two slices are metal-on-metal.

Similar to the presented phantom results, POP has achieved a more accurate and consistent fat-water separation compared to the weighted minimum-norm and branch cut methods. POP has successfully separated the fat and water throughout both slices, but there are a number of small regions near the implant boundary where fat-water swap artifacts are present. Two regions are marked with red arrows. In particular the performance of POP in Participant 4, Slice 5 near the implant boundary is very similar to Phantom 2, Slice 2 (Fig. 7.16) [5].

[5] Recall that Phantom 2 also contained a metal-on-metal implant.

The weighted minimum-norm method has again failed to estimate the phase correctly near the implant boundary, with "clover-leaf" artifacts present in the fat and water images. In Fig. 8.6, Row 2, this method has underestimated the phase, with the estimated phase covering the range $[-20, 40]$ rad, compared to the estimated POP phase range of $[-40, 40]$ rad. The branch cut method has also produced streak-like artifacts in the two displayed slices.

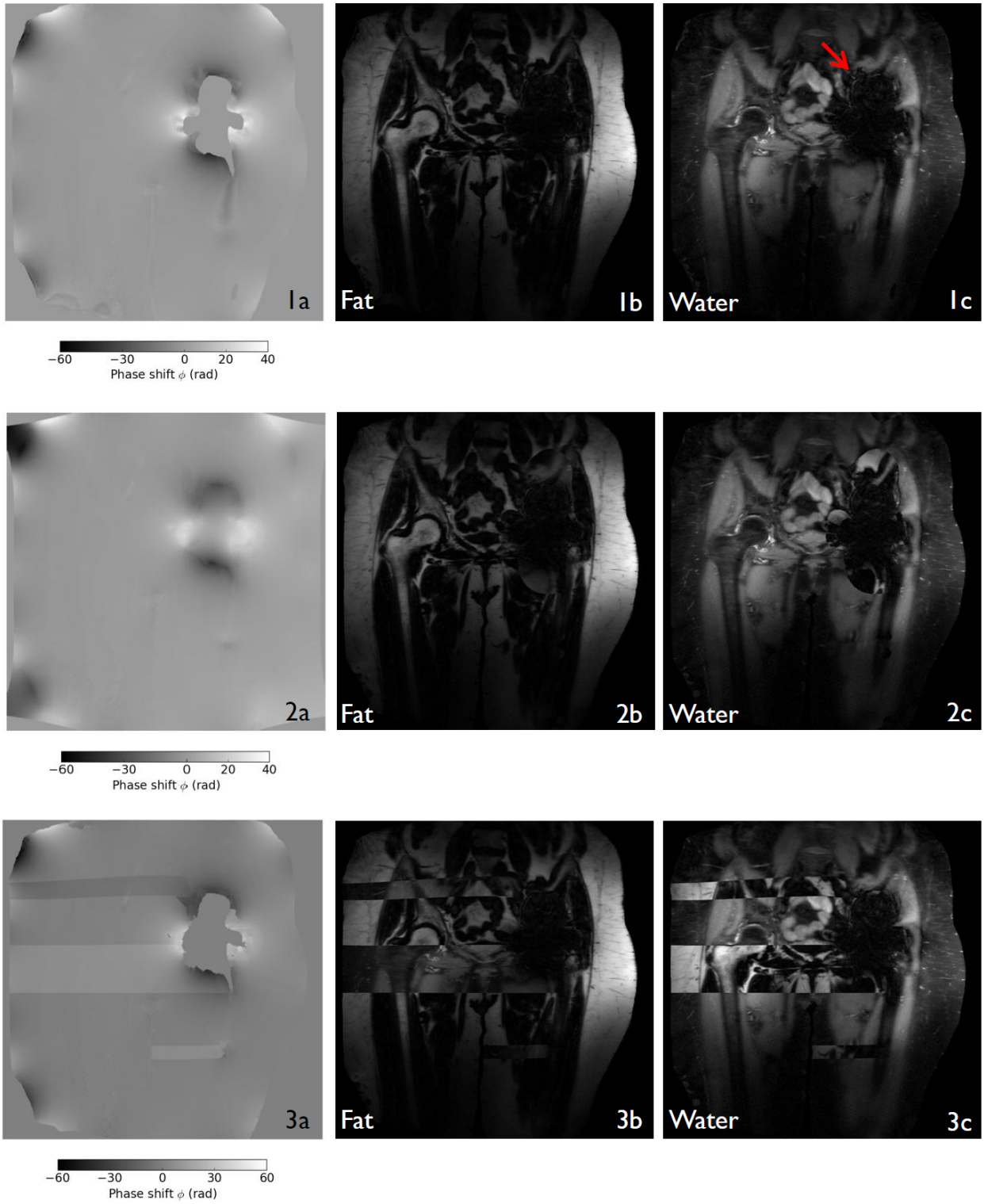

Figure 8.5: Phase shift (a), fat (b), and water (c) images of Participant 3, Slice 15, obtained using the following methods:
Row 1: POP.
Row 2: Weighted minimum-norm.
Row 3: Weighted branch cut.

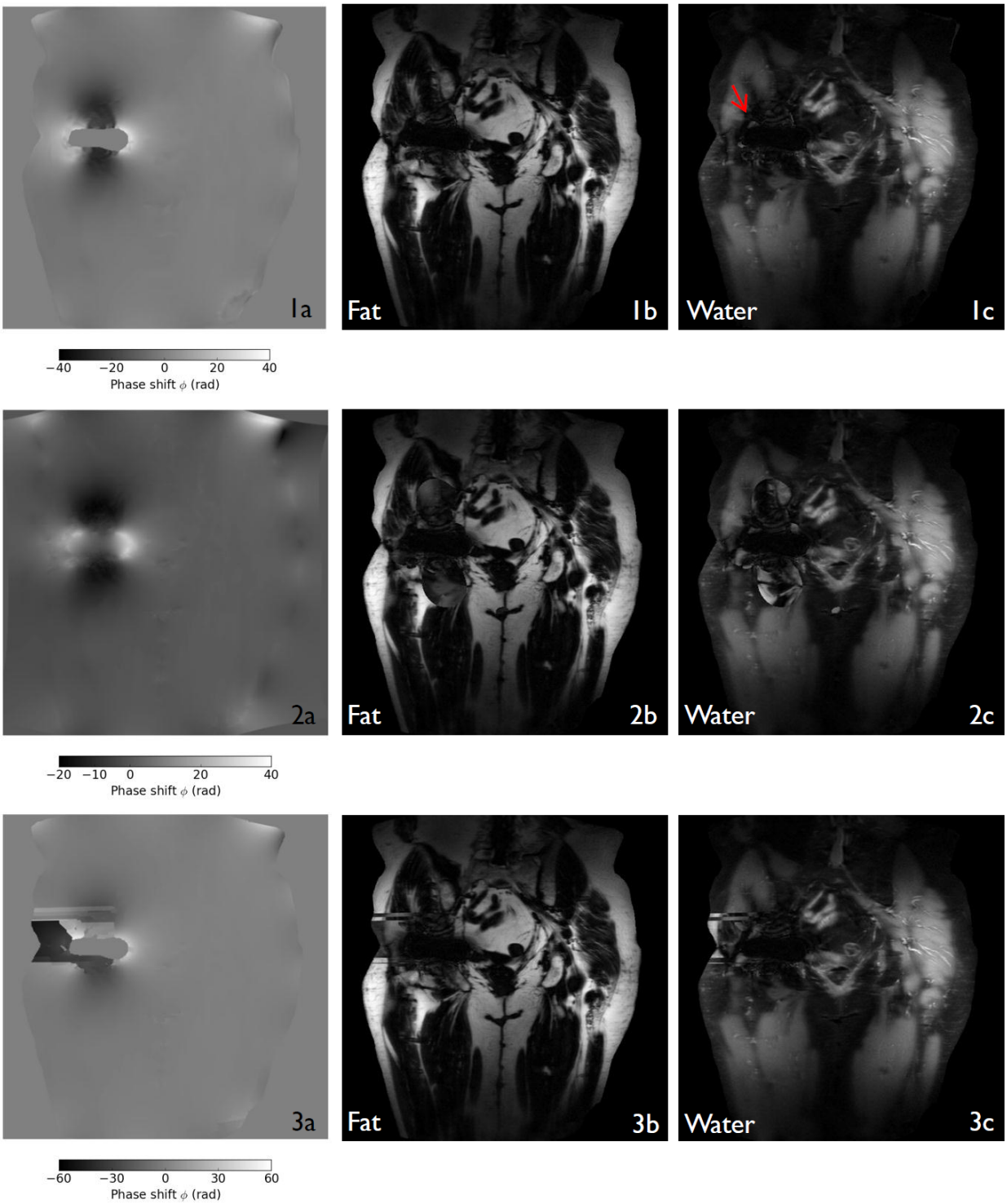

Figure 8.6: Phase shift (a), fat (b), and water (c) images of Participant 4, Slice 5, obtained using the following methods:
Row 1: POP.
Row 2: Weighted minimum-norm.
Row 3: Weighted branch cut.

▶ FIGURE 8.7 shows the water images acquired using POP, the default IDEAL reconstruction (Protocol 3), and the symmetric IDEAL reconstruction (Protocol 1) [6]. Results for the following four slices are shown:

1. Row 1: Participant 3, Slice 15.
2. Row 2: Participant 4, Slice 5.
3. Row 3: Participant 6, Slice 22. The implant shown is metal-on-metal [7].
4. Row 4: Participant 7, Slice 14. The implant shown is ceramic-on-ceramic [8].

[6] Recall that the Protocol 3 used the default asymmetric echo time offsets and Protocol 1 used the symmetric three-point Dixon echo time offsets.

[7] Recall that a metal-on-metal implant contains a combination of titanium and cobalt-chromium components.

[8] Recall that a ceramic-on-ceramic implant contains a combination of titanium and ceramic components.

In the third and fourth rows, POP has again successfully separated the fat and water throughout the majority of the slice, with a few residual artifacts remaining near the implant boundary. In the first three rows, POP has achieved a more accurate fat-water separation compared to the IDEAL and symmetric IDEAL (IDEAL-s) reconstructions.

In the fourth row, POP has performed better than the IDEAL–s reconstruction but slightly worse than the IDEAL reconstruction. The improved performance of the IDEAL algorithm may be due to the fact that the implant in this slice is titanium and ceramic. The induced $\mathbf{B}_0$ field variation is smaller than in the first three slices, which contain a titanium and cobalt-chromium implant.

The IDEAL reconstruction has generally performed better than the IDEAL-s reconstruction, but both methods have produced images with significant artifacts. In particular the IDEAL-s reconstruction for Participant 3, Slice 15 (Row 1) has performed very poorly, with artifacts spread throughout at least half of the slice. In comparison, in Rows 2 and 3 the IDEAL and IDEAL-s reconstructions have yielded similar results. All implants in these three slices contain the same composition of materials, illustrating that it may be difficult to predict the reliability of IDEAL for a given implant. The performance of IDEAL across multiple slices is discussed in more detail in Chapter 9.

Figure 8.8 shows the water images acquired using the STIR and fat saturation techniques for Participant 3, Slice 15 (Row 1) and Participant 4, Slice 5 (Row 2). Similarly to the Phantom 3 results displayed in Sec. 7.5.2, STIR has successfully suppressed the fat throughout the two slices but the images have lower SNR than the IDEAL reconstructed images. Fat saturation has again failed throughout significant proportions of the displayed slices. It should be noted that the STIR and fat saturation sequences were not optimised for image quality, so the the images are of a poorer quality than standard STIR and fat saturation images.

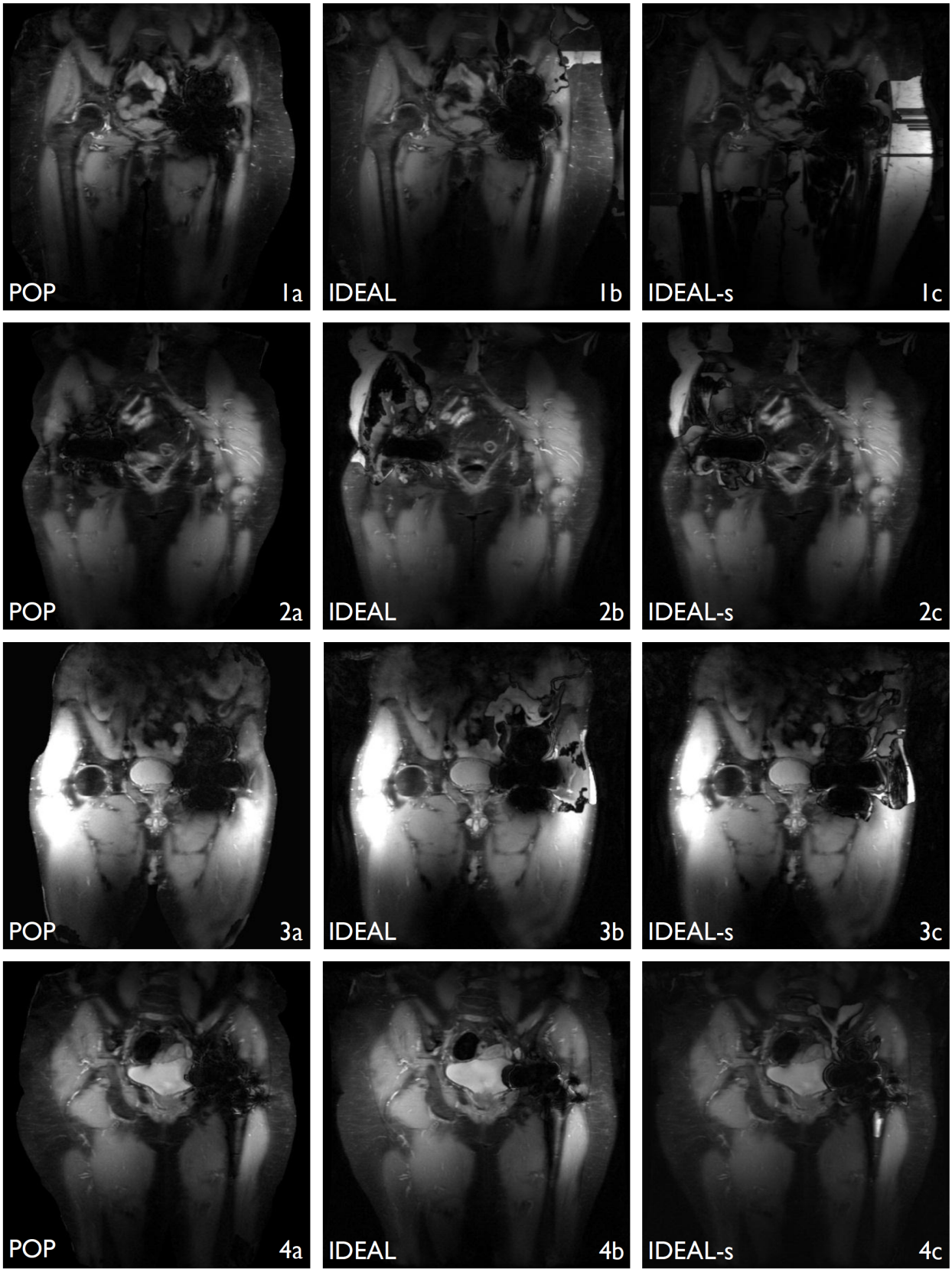

Figure 8.7: Water-only images obtained using the POP (a), default IDEAL (b), and symmetric IDEAL (labelled with IDEAL-s and (c)) methods. Note that the contrast in the images in the third row has been adjusted to better display the artifacts in the upper right of the slice.

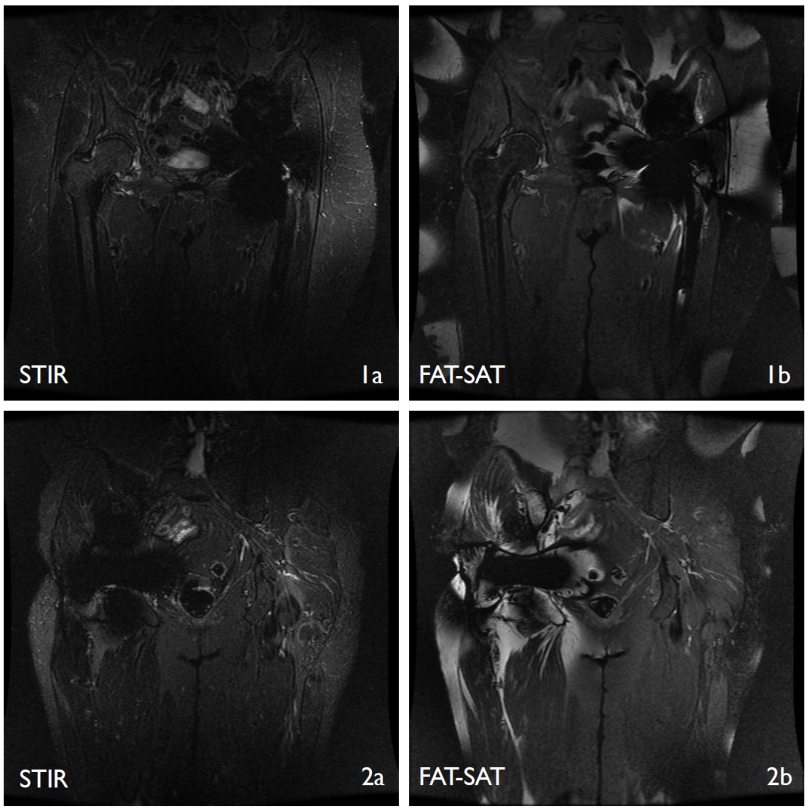

Figure 8.8: Water-only images obtained using the STIR and default fat saturation (FAT-SAT) methods for the following participants:
Row 1: Participant 3, Slice 15.
Row 2: Participant 4, Slice 5.

8.2.2 *Comparison of phase unwrapping methods*

Fat-water swap artifacts were measured[9] for the 63 slices processed with the three phase unwrapping methods: POP, weighted minimum-norm, and weighted branch cut. 189 images were analysed in total. For the nine slices processed for each participant, the measured area of artifacts varied over a wide range. This is particularly true for the minimum-norm and branch cut methods, where the proportion of the image covered with artifacts fluctuated significantly between the outer and inner slices. Box plots are used to present the results for each participant, as these succinctly illustrate the performance of the phase unwrapping methods.

Figures 8.9 - 8.15 show box plots depicting statistics calculated for the percentage of the processed slices which are covered by fat-water swap artifacts. Figure 8.16 shows an aggregated plot of the median percentage for each participant, across the three methods. For all seven participants, the median percentage is significantly lower for POP, compared with the other two methods. The slices processed with POP had a smaller measured region of fat-water swaps for 56 out of 63 slices, compared to the slices processed with the minimum-norm and branch cut methods. The range across the slices is also much smaller for POP. This is indicated by the size of the box and extent of the whiskers in the box plots.

In comparison, the minimum-norm and branch cut methods both have a higher median percentage of fat-water swap artifacts, for all

[9] Recall that the method is described in Sec. 8.1.4.

seven participants. In some slices processed with these two methods, fat-water swap artifacts occurred in less than 2 % of the image. This is shown by the box plots where the whisker tails are located close to zero. However, the upper end of the whiskers and marked outliers show that for other slices processed for the same participant, up to 60 % of the image pixels had fat-water swap artifacts. This indicates that the minimum-norm and branch cut methods perform inconsistently across multiple slices.

The time required to process each slice with POP depends on the values of the parameters K, P, and N. With $K = 150$, $P = 0.5$, and $N = [20, 70]$, a typical slice is processed in around 120-140 seconds. This includes the time taken to generate the paths, perform the iterative stages of POP, and reconstruct the phase, water and fat images. In comparison, slices processed with the weighted branch cut method took approximately 15-20 seconds. Slices processed with the weighted minimum-norm method required 410-420 seconds. However, these algorithms were written in MATLAB and were not implemented with speed as a priority. It is likely that the processing time of all methods could be reduced with more efficient code.

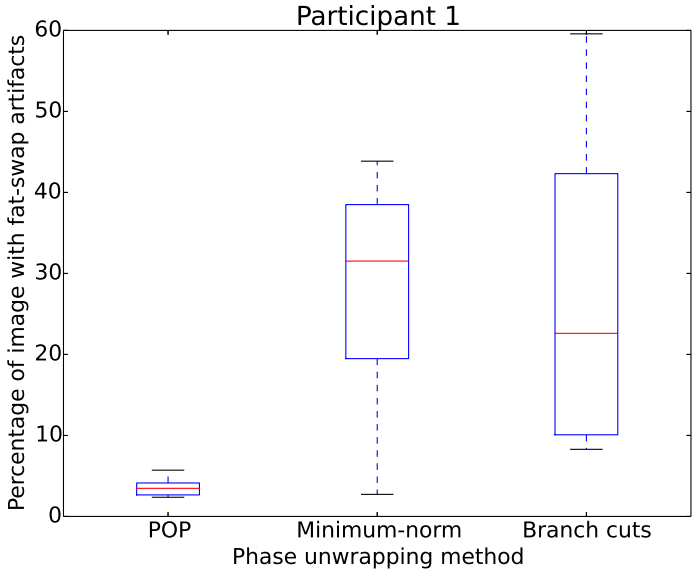

Figure 8.9: Box plot for the measured area of fat-water swaps in nine slices, for Participant 1. In this set of box plots, the red line indicates the median measured area. The top and bottom of the box are the third and first quartiles of the measured area. The lower end of the whisker indicates the lowest value within 1.5 of the interquartile range (IQR), and the higher end indicates the highest value within 1.5 of the IQR. Outliers are marked with blue crosses.

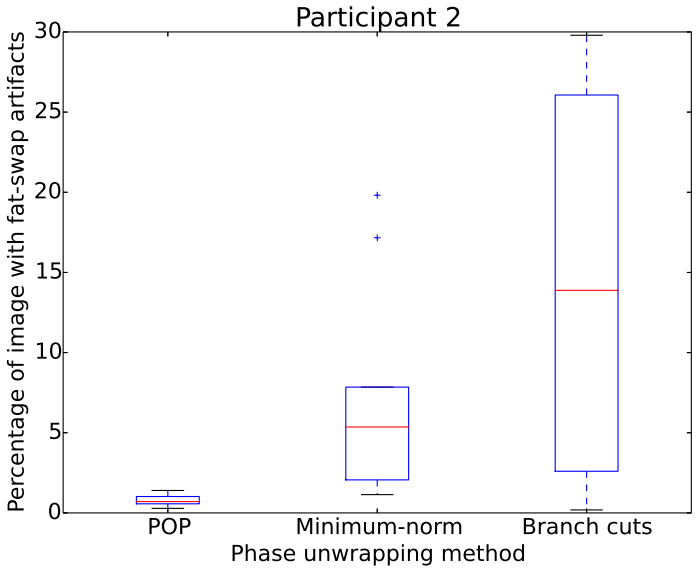

Figure 8.10: Box plot for the measured area of fat-water swaps in nine slices, for Participant 2.

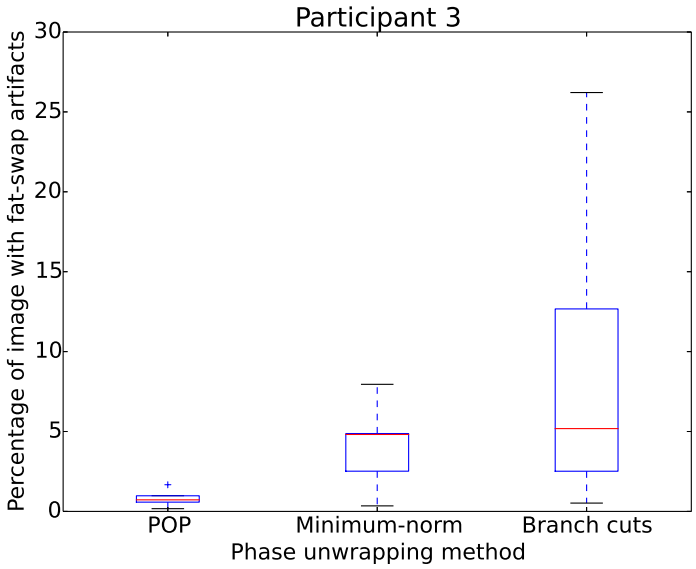

Figure 8.11: Box plot for the measured area of fat-water swaps in nine slices, for Participant 3.

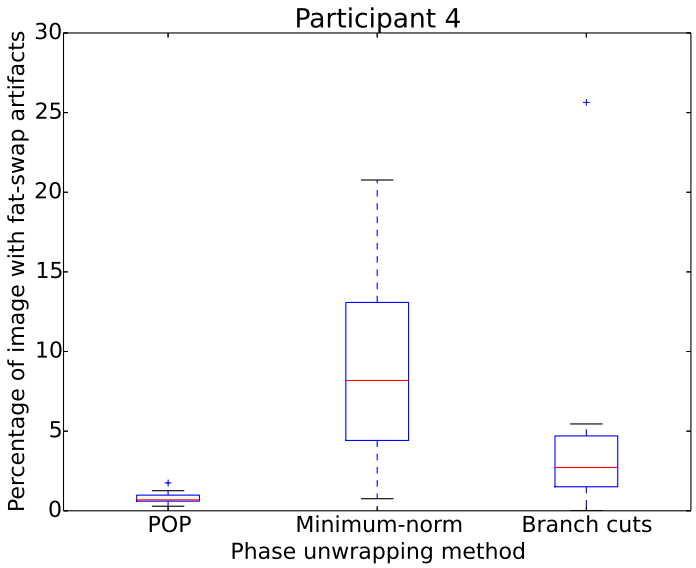

Figure 8.12: Box plot for the measured area of fat-water swaps in nine slices, for Participant 4.

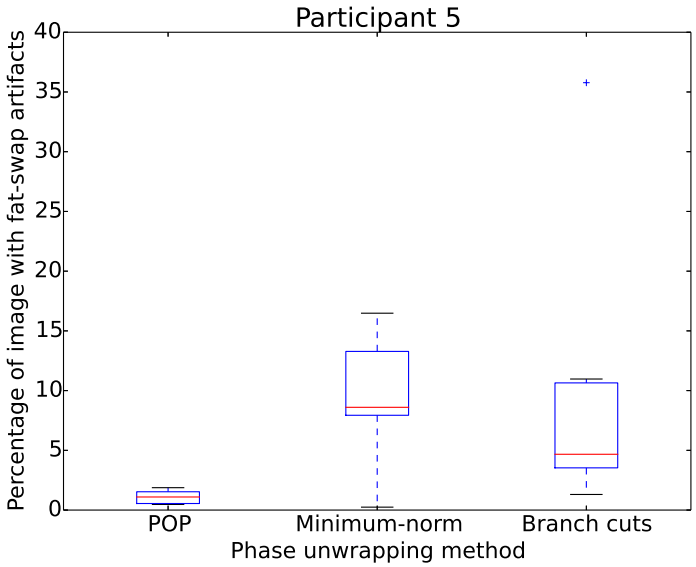

Figure 8.13: Box plot for the measured area of fat-water swaps in nine slices, for Participant 5.

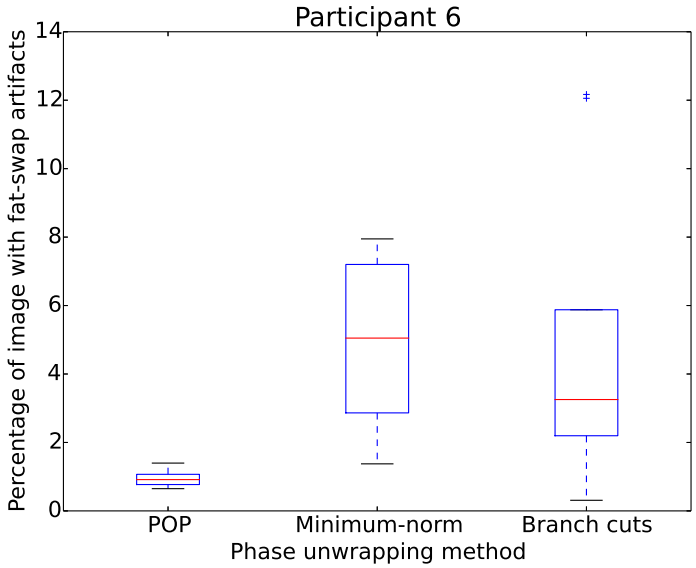

Figure 8.14: Box plot for the measured area of fat-water swaps in nine slices, for Participant 6.

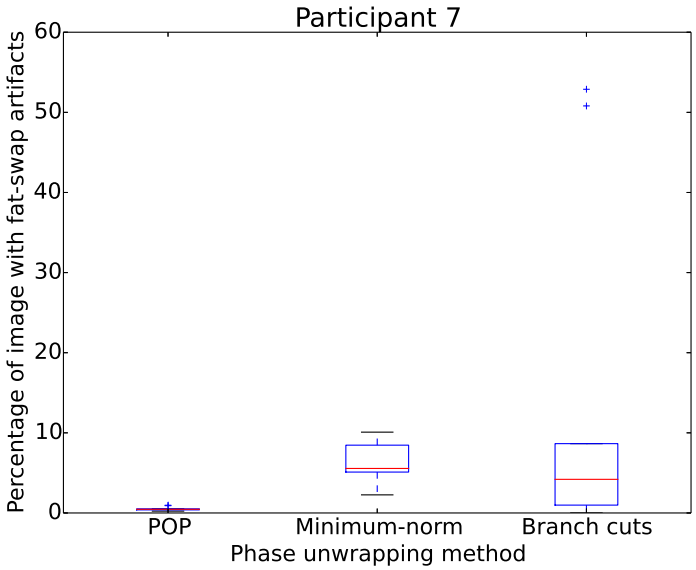

Figure 8.15: Box plot for the measured area of fat-water swaps in nine slices, for Participant 7.

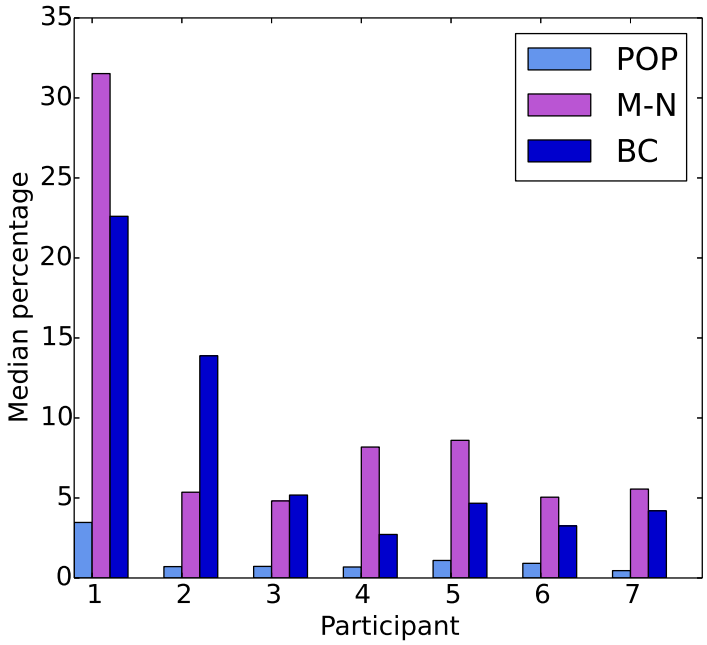

Figure 8.16: Median percentage of the processed slices which are covered by fat-water swap artifacts for each participant, across the three methods: POP, minimum-norm (M-N) and branch cut (BC).

8.2.3 *Radiologist rating of fat suppression methods*

Table 8.4 shows the ratings for Comparison 1, Quality Question 1 determined by the radiologist. Likewise, Table 8.5 shows the ratings for Comparison 2, Quality Question 1. Ratings of 1-3 were assigned as all datasets produced less homogeneous fat suppression compared to the STIR images provided for reference.

In four of the seven datasets for Comparison 1, POP was determined to produce slightly improved fat suppression compared to the default IDEAL reconstruction. In the remaining three datasets, POP produced comparable fat suppression with the default IDEAL reconstruction. Across all seven datasets for Comparison 2, POP produced significantly improved fat suppression compared to the symmetric (or three-point Dixon) IDEAL reconstruction. Overall, the radiologist concluded that some slices reconstructed with IDEAL contained varying degrees of block-like inhomogeneity about the implants, and the symmetric IDEAL reconstruction clearly produced the poorest quality images.

Ratings of 1 were assigned across all datasets for Quality Question 2: *Are these slices diagnostic?*, as none of the datasets were determined to be diagnostic, including the STIR images. This is mainly due to the significant metal-induced artifacts obscuring the anatomy near the implants, including in-plane and through-plane distortion.

	Comparison 1, Quality Question 1	
	POP	IDEAL - default
Participant		
1	3	3
2	3	3
3	3	2
4	3	2
5	3	3
6	3	2
7	3	2

Table 8.4: Comparison 1 ratings answering Quality Question 1: *Do these slices have homogeneous fat suppression?* Ratings are given by the radiologist on a scale of 1-5, where 1 is poor and 5 is excellent.

	Comparison 2, Quality Question 1	
	POP	IDEAL - symmetric
Participant		
1	3	1
2	3	1
3	3	1
4	3	1
5	3	1
6	3	1
7	3	1

Table 8.5: Comparison 2 ratings answering Quality Question 1.

8.3 DISCUSSION

Overall, POP has displayed superior fat and water separation compared to the weighted minimum-norm and branch cut phase unwrapping methods. This supports the phantom results presented in Chapter 7. POP has produced better results in the illustrated slices, especially near the implant boundary. In Sec. 8.2.2, where the extent of the fat-water swap artifacts were measured across the processed slices, POP has performed more consistently.

In the four displayed slices in Fig. 8.7, POP has achieved a better or comparable fat-water separation with the IDEAL and symmetric IDEAL algorithms. In the radiologist analysis, POP produced more homogeneous fat suppression compared to IDEAL for four participants, and comparable performance for three participants. POP also produced more homogeneous fat suppression compared to the symmetric IDEAL algorithm for all seven participants. However, all algorithms require further development as the datasets were determined not to achieve diagnostic quality.

In the displayed slices, the artifacts produced by POP are constrained to be close to the implant boundary. In comparison, the phase unwrapping methods and IDEAL reconstruction methods have produced artifacts which have spread throughout varying proportions of the slice, affecting the ability to identify anatomical features in these regions. It should be noted however that POP is also vulner-

able to the propagation of errors. This is discussed in the following section.

8.3.1 Limitations

The slices assessed by the radiologist were not contiguous, as only nine of the 26 acquired slices were reconstructed to reduce the assessment workload. Ideally it would have been preferable to analyse the entire set of acquired images. In addition, the STIR and FAT-SAT sequences (Protocols 4 and 5) were not optimised for image quality, as the same scan parameters were used as in the IDEAL sequences (Protocols 1-3). The resulting images have low SNR.

The reasons for the failure of POP near the implant boundaries are likely to be similar to those outlined for the phantom results in Sec. 7.7. This is due to a combination of POP failing to converge to the correct result along the paths near the boundary, and the algorithm not accounting for in-plane and through-plane distortions.

For both the illustrated phantom and participant results, the phase shifts estimated by POP covered the range of between $[-40, 40]$ and $[-60, 60]$ rad. By Eq. 6.1, this corresponds to a resonant frequency variation of between $[-2.9, 2.9]$ and $[-4.3, 4.3]$ kHz. This is smaller than the simulated resonant frequency variations in Fig. 5.7, and values reported by Koch et al. [2010], which are in the order of tens of kilohertz. This demonstrates that POP may underestimate the phase in regions close to the implant boundary. However, the spins at pixels which experience this magnitude of resonant frequency variation suffer from signal loss and pile-up. The extracted phase at these pixels may be noisy and meaningless. It is therefore unrealistic to expect that the phase could be accurately estimated in these regions without first correcting for the signal loss and pile-up.

A more comprehensive method for quantifying the extent of the fat-water swap artifacts across the slices would allow for the performance of each method to be more easily compared. This could be based on the method used for evaluating submissions for the 2012 ISMRM challenge on fat-water separation [Cui et al., 2014]. Fat and water separated images reconstructed using algorithms submitted for the challenge were obtained using a three-point IDEAL acquisition. These images were evaluated against "ground-truth" or reference fat and water images, which were acquired using a seven-point fat-water separation method to obtain images at seven echo times. The reference images were then reconstructed using a multipeak signal model [10]. A similar approach could be used to compare the performance of POP with IDEAL, but would require additional data acquisition to obtain the reference images. The ability to quantify the accuracy of the fat and water separation would allow for a more robust evaluation of POP.

[10] Refer to Sec. 3.3.5 for a description of the multipeak signal model.

▶ There are several aspects of POP which should be addressed to improve the accuracy and efficiency of the algorithm. First, the cur-

rent implementation of POP requires a significant amount of manual intervention during the mask acquisition, and determining the values of the parameters used.

Two mask acquisition methods have been tested. The first used the 3D voxelised geometry of Implant 1 and was applied successfully to the Phantom 1 data. However, this process requires the model geometry to be accurately aligned with the true position and orientation of the scanned implant. This is difficult to guarantee, as implants such as hip replacements have several degrees of freedom. The second method used manual thresholding of the magnitude images. This does not capture the true boundary of the implant geometry, as the signal loss near the implant is included in the mask. This method is also impractical for processing a large number of slices, as the connected component corresponding to the implant has to be manually selected. The thresholding process should be automated. Alternatively, a different method could be used to identify the masks, such as by using a phase quality map.

For the participant datasets, the parameter values K, P, and N were determined empirically. A more comprehensive study into how the POP results depend on these values should be undertaken. Sets of training data could be used to develop a automatic method for calculating these parameters, to eliminate the need for manual input. As described in Sec. 6.3.3, the set of N values was linearly spaced across the paths for each slice. This approach is not ideal, as the sharpness of the features from the outermost to innermost path does not increase in a linear manner. A more sophisticated method of determining N should be investigated.

The method described for estimating the phase along the outermost path by first unwrapping a thin 2D strip is inefficient and not robust. It also requires manual input, as the location of the seed pixel for the branch cut algorithm must be indicated. Error checking should be implemented, so that POP does not proceed if the branch cuts method fails. Alternatively, a better approach would be to replace this step with a different method which does not rely on existing phase unwrapping techniques.

The use of the Fourier series assumes that the phase along each path is smooth and continuous. This is valid for the vast majority of the phase in the acquired images. However, some anatomical features cause discontinuities in the phase. These can occur at the boundaries between different tissues, or in air gaps. The current POP implementation does not have any mechanism to deal with discontinuous regions of phase.

These discontinuous regions can cause errors to propagate throughout the image, as the current POP algorithm does not incorporate error checking to prevent errors from spreading between adjacent paths. Figure 8.17 shows an example of a cropped slice where POP has failed to estimate the phase along paths crossing two anatomical features. The errors along these paths have subsequently spread inwards towards the implant boundary.

Figure 8.17: Cropped water-only image of Slice 1, Participant 6, obtained using POP. The red arrows indicate where the fat-water separation has failed, causing errors to propagate towards the implant boundary.

These issues could be addressed in multiple ways. First, regions of poor quality or discontinuous phase could be identified before proceeding with the phase unwrapping using phase quality maps, as described in Sec. 4.5. Additional masks could then be applied, forcing the path generation process to construct paths which avoid these regions. A different basis could be employed in the discontinuous regions, as described further in Chapter 10, *Investigating a better basis*. Alternatively, the phase could be expanded along a set of radial paths in conjunction with the existing closed paths, or the properties of the objective function could be exploited to indicate when the algorithm has failed. These two suggestions are discussed in Sec. 11.2.

Finally, POP does not reliably separate the fat and water in the space between the multiple implants in Participant 7. This is shown in Fig. 8.7, Image 4a, where fat-water swap artifacts are present in the region between the screws and the hip replacement. This is similar to the phantom results in Fig. 7.8, and further demonstrates that more research is needed to address this problem.

9

Iterative Resonant Frequency Estimation Near Metal

The IDEAL protocol is the standard multipoint fat suppression sequence implemented on GE scanners, and is widely used. It offers greater flexibility and more robust performance compared to the three-point Dixon technique. IDEAL was used in the human study described in the previous chapter to compare with POP. This chapter intends to assist with understanding the human study results, with the performance of IDEAL in areas of rapid resonant frequency variation discussed first. An extension to the POP method is then introduced, which is used in conjunction with the VARPRO iterative algorithm.

Recall that IDEAL acquires N_S images at any combination of echo time offsets, as detailed in Sec. 3.3.5. Phase unwrapping cannot be used to directly estimate the phase shift due to the resonant frequency variation, as the images may not be acquired symmetrically. Instead, an iterative least squares algorithm is used to simultaneously estimate the resonant frequency variation, fat, and water. The default IDEAL sequence acquires three images at an asymmetric set of echo times optimised to produce the best noise performance.

A major disadvantage of the standard three-point Dixon technique is that symmetrically acquired images can fail to achieve an accurate estimation in voxels which contain equal proportions of fat and water signal [Reeder et al., 2005]. This was a key motivator for the development of the asymmetric IDEAL acquisition. However, the existing IDEAL implementation uses a region growing method which assumes the resonant frequency variation is slowly changing. An alternative approach is necessary in regions of rapid resonant frequency variation induced by metal. This chapter lays the groundwork for developing POP so it can be used in conjunction with asymmetrically acquired images near metal.

The first section in this chapter explores the convergence of IDEAL using simulations, to understand how IDEAL can fail in regions of

rapid resonant frequency variation. The second section expands on the IDEAL results presented in the previous chapter and analyses how IDEAL performs across adjacent slices for the same implant. The third section describes an extension to POP, where the objective function is altered to have a similar form to VARPRO. With further development, this method could be used to separate fat and water near metal from images acquired at any combination of echo times. Results are displayed for one phantom and two participant slices.

9.1 ANALYSIS OF IDEAL

This section first considers a simulated scenario where IDEAL can converge to a range of incorrect estimated resonant frequency variations at a single pixel. It then examines how errors can be amplified during the iterative process used to refine the estimate of the resonant frequency variation. Finally, results of a simplistic implementation of the IDEAL algorithm are displayed for Phantom 1. This section comprises early work conducted on understanding the performance of IDEAL near simulated metal implants. It is largely based on the analysis presented by Yu et al. [2005].

As outlined in Sec. 3.3.4, the iterative reconstruction method introduced by Reeder et al. [2004] simultaneously estimates the fat, water, and resonant frequency variation on a pixel-by-pixel basis by minimising the residual, R, given in the following equation:

$$R = \|\mathbf{S}(t_n) - (W + Fe^{j2\pi f_{cs} t_n})e^{j2\pi \Delta f t_n}\|_2. \tag{9.1}$$

In the simplest situation where the pixel contains only water, this equation simplifies to:

$$R_w = \|\mathbf{S}(t_n) - We^{j2\pi \Delta f t_n}\|_2, \tag{9.2}$$

Figure 9.1 shows a plot of R_w, over a range of Δf values, $-2000 \leqslant \Delta f \leqslant 2000$ Hz. This plot was simulated using $B_0 = 3$ T and the symmetric three-point Dixon echo time offsets $t_n = [0, 1/2f_{cs}, 1/f_{cs}] = [0, 1.1, 2.2]$ ms. The residual has numerous local minima at integer multiples of $f_{cs} = 440$ Hz [1].

[1] For pixels which contain a mixture of fat and water, the locations of the residual minima are dependent on the ratio of fat and water in the pixel [Yu et al., 2005].

If the initial estimate for the resonant frequency variation, Δf_0, is not sufficiently close to the true value Δf, the algorithm converges to an aliased solution. For example, if $\Delta f_{true} = 0$ Hz, but $\Delta f_0 = 300$ Hz, as marked by a red dot on Fig. 9.1, the final estimate of the field variation is $\Delta f_{final} = 440$ Hz, marked by a blue dot. In this situation the true water pixel "looks" like it is a fat pixel, and the two species are swapped. This example shows that the estimated values of the fat and water signals are dependent on the initial estimate of the resonant frequency variation for that particular pixel.

In comparison, Fig. 9.2 shows a plot of R_w over $-2000 \leqslant \Delta f \leqslant 2000$ Hz, simulated using the default IDEAL asymmetric echo time offsets, $t_n = [-0.2, 0.6, 1.4]$ ms. While local minima are still present in the residual, there are fewer, shallower minima and one obvious

global minimum. This illustrates that images reconstructed with the IDEAL echo time offsets may be less sensitive to the initial Δf value for each pixel. This supports the discussion of the problem of fat-water swapping presented by Yu et al. [2005].

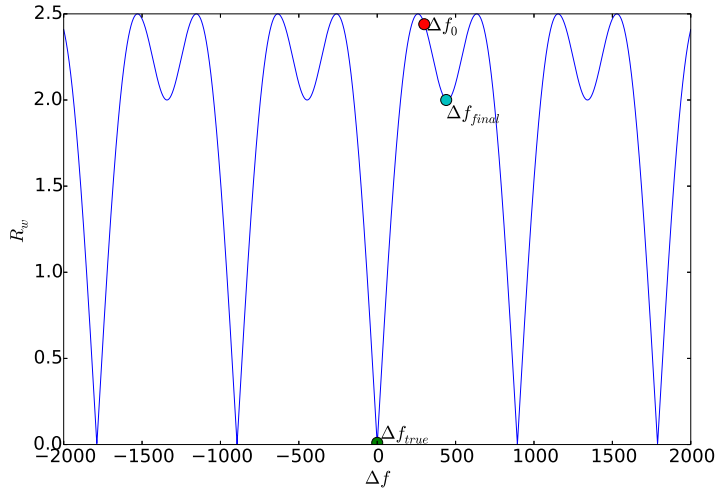

Figure 9.1: Locations of residual minima for a pixel which contains only water, simulated using symmetric three-point Dixon echo time offsets.

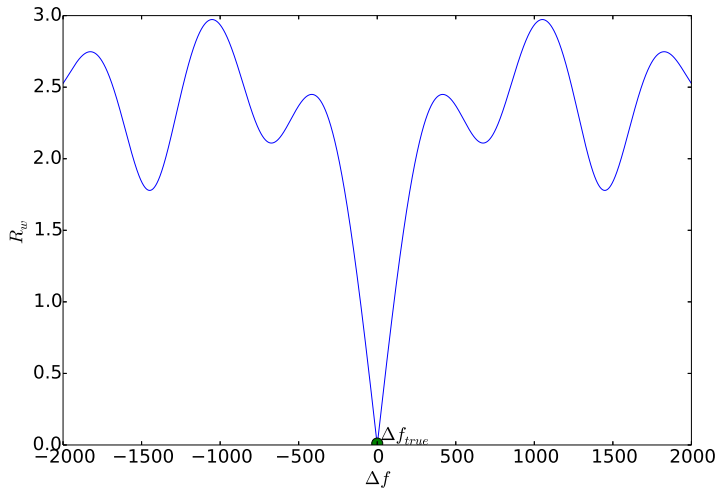

Figure 9.2: Locations of residual minima for a pixel which contains only water, simulated using default IDEAL asymmetric echo time offsets.

Near metal, the resonant frequency variation changes rapidly between pixels, and it is difficult to determine an accurate initial estimate for the resonant frequency variation of every pixel. Between adjacent pixels, the resonant frequency variation may change by several hundred hertz [2]. If the initial resonant frequency variation for these pixels is calculated using the estimated values of the adjacent pixels, numerous incorrect solutions may be possible [3]. In conclusion, the iterative linear least squares method may not produce reliable results in regions of large resonant frequency variation.

[2] In the case of the simulated resonant frequency variation near Implant 3 shown in Fig. 5.7(b), near the implant boundary the resonant frequency variation changes by between 1000-3000 Hz between adjacent pixels.

[3] Recall from Sec. 3.3.4 the region-growing IDEAL algorithm determines the initial Δf value for each pixel using the neighbouring pixel values.

9.1.1 *Convergence or divergence?*

If an unsuitable value is used as the initial estimate of the field variation in the IDEAL iterative least squares algorithm, there is the possibility it may converge to an erroneous solution. Figure 9.3(a) shows the final estimated resonant frequency variation Δf_{final} for a single pixel, plotted over a range of initial values, $-2000 \leqslant \Delta f_0 \leqslant 2000$ Hz. The true resonant frequency variation is 0 Hz. In this simulation the symmetric three-point Dixon echo time offsets were used and the pixel contained only water ($W = 1$, $F = 0$). The spikes in the estimated solution can be understood by considering how the initial value is refined at each iteration of the algorithm.

In the full derivation of the iterative method described in Sec. 3.3.4, Reeder et al. [2004] show that given an estimate of Δf_0, W, and F are obtained by solving the following system of equations using linear least squares:

$$\hat{\mathbf{S}} = A\mathbf{y}, \tag{9.3}$$

where $\mathbf{y} = [W\ F]^T$. Δf_0 is then refined by solving a similar linear system of equations for the error in each of the three parameters, $\mathbf{e} = [\epsilon_{\Delta f}\ \epsilon_W\ \epsilon_F]^T$:

$$\tilde{\mathbf{S}} = B\mathbf{e}. \tag{9.4}$$

B is obtained by assuming that the error in the estimated resonant frequency variation, $\epsilon_{\Delta f}$, is small. If Δf_0 is not close to a local minimum, the error $\epsilon_{\Delta f}$ is large, and B may be ill-conditioned. When Eq. 9.4 is solved, the estimated value of $\epsilon_{\Delta f}$ may be abnormally large. This abnormal result is added to Δf_0, and errors propagate through the following iterations, resulting in a final estimate of Δf_{final} which may make no sense.

Figure 9.3(b) shows a plot of the initial condition number of B over $-2000 \leqslant \Delta f_0 \leqslant 2000$ Hz. The peaks of the condition number approximately match the peaks of the residual in Fig. 9.1 and the spikes in Fig. 9.3(a). This indicates that the ability of this algorithm to converge to a sensible solution is dependent on the location of Δf_0 in relation to the nearest local minimum. The location of the minima are not known in advance.

It should be noted that for a simulation using the asymmetric IDEAL echo time offsets and a pixel containing only water, fewer spikes were identified in the plots of the final estimated resonant frequency variation and condition number. Fewer convergence issues were also encountered when the pixel contained a mixture of fat and water. Figure 9.4 shows the Δf_{final} value for a simulation where the pixel contained an equal ratio of fat and water ($W = F$). In this result, for each initial Δf_0 value the algorithm has converged to the nearest local minimum as marked on Fig. 9.2. Asymmetrically acquired images may therefore offer more reliable convergence when the initial resonant frequency variation is not close to the nearest local minimum.

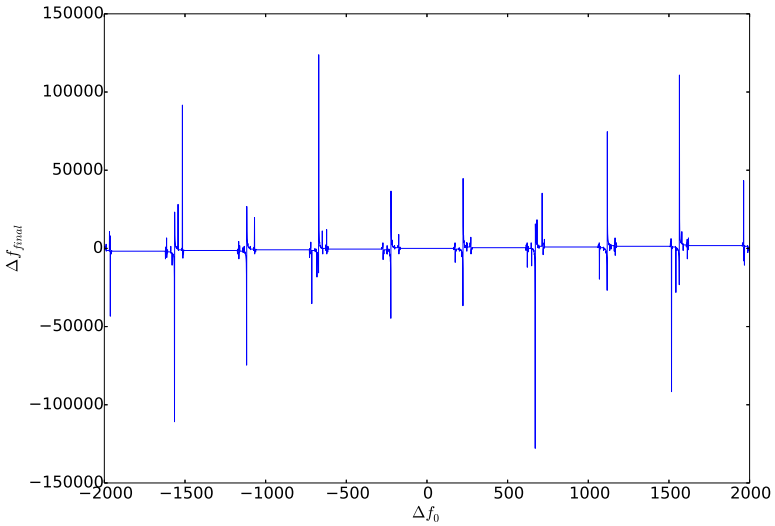

(a) Final estimated resonant frequency variation Δf_{final} versus initial value Δf_0

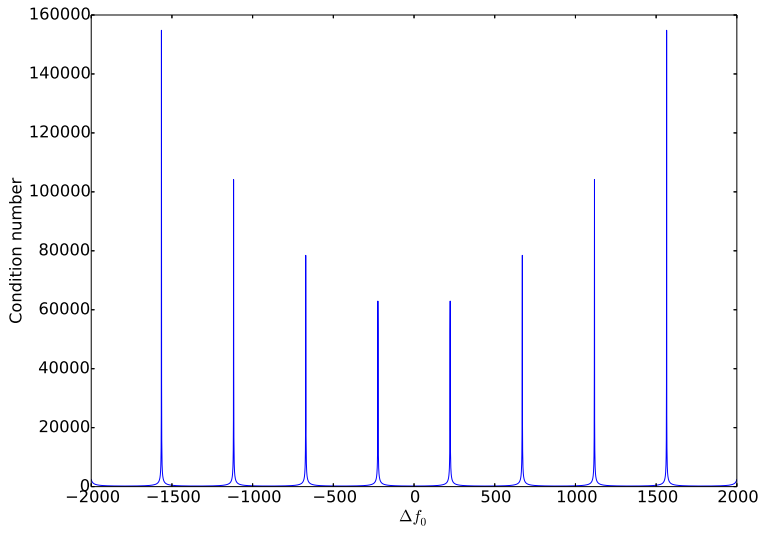

(b) Initial condition number of B versus Δf_0

Figure 9.3: Influence of the initial resonant frequency variation on the final result for a pixel containing only water, shown over a range of initial values, $-2000 \leqslant \Delta f_0 \leqslant 2000$ Hz.

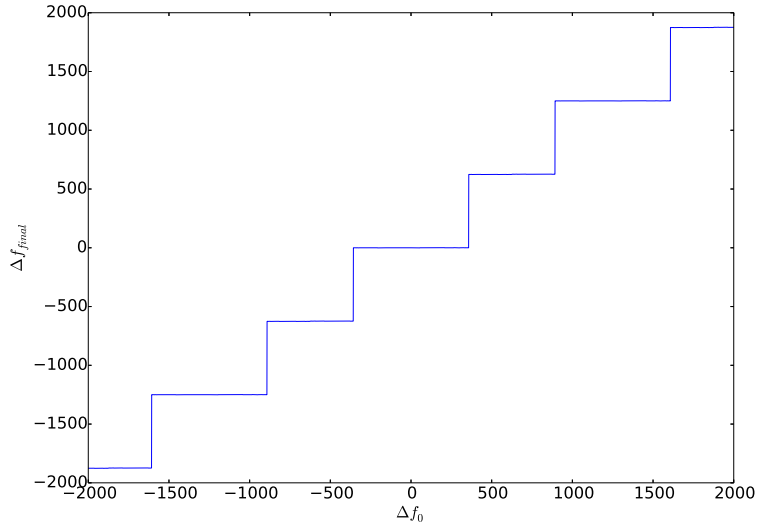

Figure 9.4: Final estimated resonant frequency variation Δf_{final} over a range of initial Δf_0 values, for a simulation using the asymmetric IDEAL echo time offsets and a pixel containing an equal mixture of fat and water.

- A SIMPLISTIC "PIXEL-INDEPENDENT" VERSION of the iterative IDEAL algorithm was implemented, with the resonant frequency variation at each pixel estimated independently from the other pixels. Figure 9.5(a) shows the cropped estimated resonant frequency variation for the central slice of Phantom 1, obtained using the pixel-independent algorithm. This result contains numerous pixels where the algorithm has converged to abnormally large values. To better visualise the estimated resonant frequency variation without the interference of the abnormal pixels, a median filter was applied to Fig. 9.5(a). Figure 9.5(b) shows the estimated resonant frequency variation after the median filter was applied. Figure 9.6 shows the obtained fat and water images. The red arrows indicate where fat and water have been swapped in one vial. Overall, the fat-water separation has failed severely.

  It should be noted that in the original description of the IDEAL iterative least squares algorithm, the final resonant frequency variation estimate is smoothed with a low-pass filter [Reeder et al., 2004]. The region-growing method was subsequently developed to reduce the likelihood of the algorithm converging to incorrect resonant frequency variation values [Yu et al., 2005].

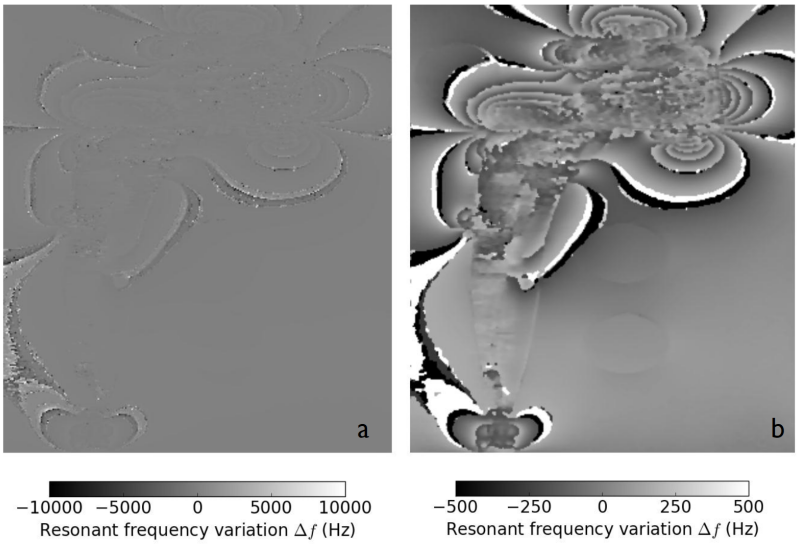

Figure 9.5: Estimated resonant frequency variation for Phantom 1, cropped central slice, using pixel-independent IDEAL. a) shows the unfiltered result and b) shows the median filtered result, obtained using a median filter kernel of size 3. The true estimated values covered the range $[-75000, 50000]$ Hz, but a) shows the results over a compressed range. Similarly, in the median-filtered result the true estimated values covered the range $[-3000, 6000]$ Hz, but again a compressed range is displayed in b). This is necessary to show details of the spatial variation throughout the image.

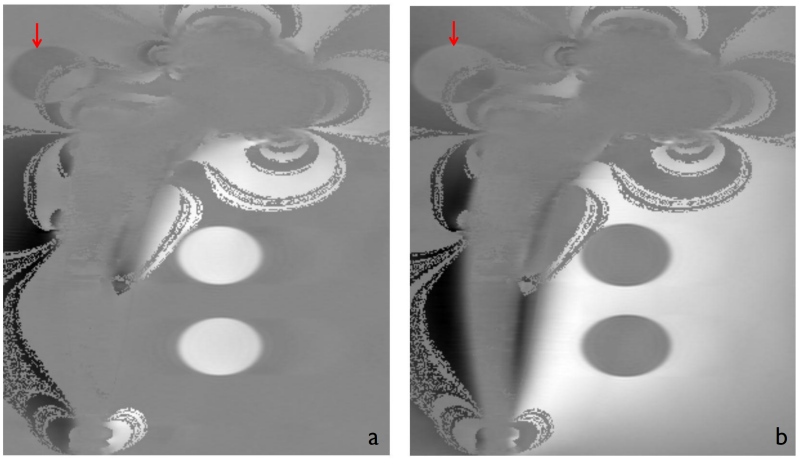

Figure 9.6: Estimated fat (a) and water (b) images of Phantom 1, cropped central slice, using pixel-independent IDEAL.

9.2 PERFORMANCE OF EXISTING ITERATIVE METHODS

This section assesses the performance of existing iterative methods for performing fat-water separation, comparing adjacent slices. It briefly expands on the results described in Sec. 8.2 in the previous chapter. The standard implementation of the IDEAL algorithm on GE scanners using the symmetric Dixon echo time offsets is compared with the default asymmetric echo time offsets.

Overall, in the seven participant datasets, the default asymmetric IDEAL implementation achieved a more accurate fat-water separation near metal than the symmetric Dixon implementation. This is demonstrated in the displayed slices and radiologist results presented in Sec. 8.2. This supports the argument presented in the original IDEAL paper by Reeder et al. [2005], and the analysis in the previous section, which suggested that the algorithm has better convergence properties for asymmetrically acquired images compared to symmetrically acquired images.

In general, IDEAL was observed to perform inconsistently between adjacent slices, in both phantom and participant datasets. Figure 9.7 shows the water images for six central slices across Phantom 3. In the first and third columns, the default IDEAL asymmetric echo time offsets were used. In the second and fourth columns, the symmetric three-point Dixon echo time offsets were used. The images were processed with the IDEAL reconstruction algorithm on the scanner. All slices suffer from significant fat-water swap artifacts, with the location and pattern of the artifacts varying widely from slice to slice.

A similar pattern is shown in Fig. 9.8 which displays cropped water images for five central slices obtained for Participant 4. While the artifacts are not as severe as Phantom 3, the fat-water separation performs erratically across the slices. This behaviour is likely due to the region-growing component of the algorithm. Similarly to the branch cut phase unwrapping method, the presence of one or two pixels can cause errors to propagate throughout the image.

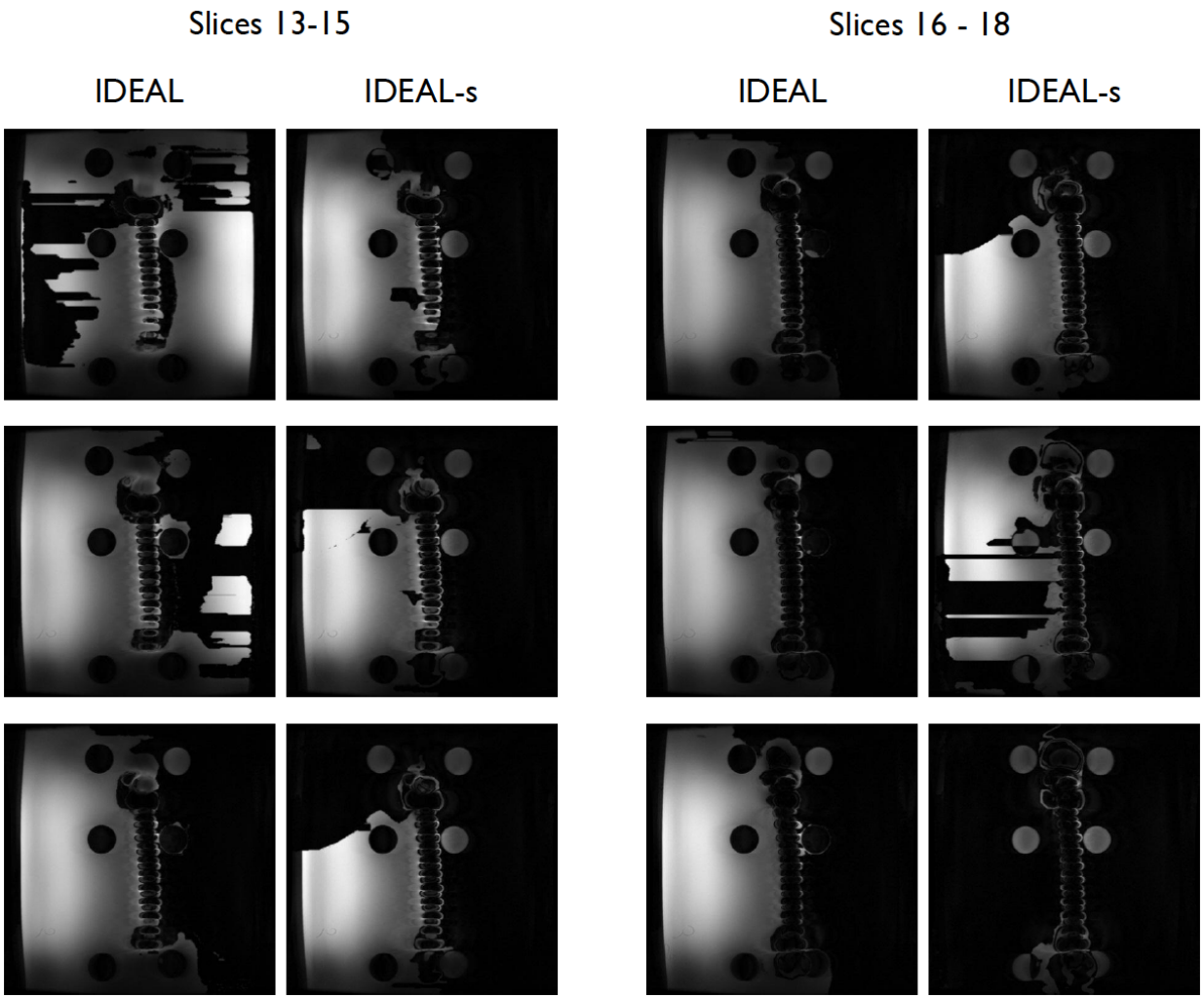

Figure 9.7: Reconstructed water-only images for six central slices across Phantom 3. The first and third columns show images acquired with the IDEAL default asymmetric echo times (IDEAL), and the second and fourth columns show images acquired with the Dixon symmetric echo times (IDEAL-s).

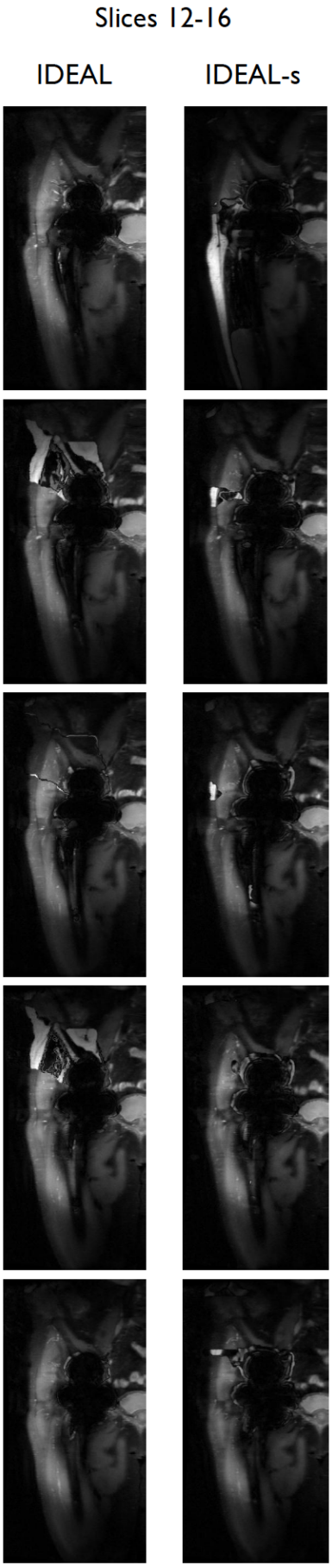

Figure 9.8: Reconstructed and cropped water-only images for five central slices across Participant 4. The first column shows images acquired with the IDEAL default asymmetric echo times (IDEAL), and the second column shows images acquired with the Dixon symmetric echo times (IDEAL-s).

9.3 AN EXTENSION TO VARPRO

In this section a variation on the VARPRO least squares approach is described, based on the POP method presented in Chapter 6. This variation is called POP-VARPRO. Results of implementing POP-VARPRO are displayed for the central slice of Phantom 1 and two participant slices.

Recall from Sec. 3.3.4 that the VARPRO cost function for an individual voxel $\mathbf{x} = [x, y, z]$ is

$$R_V = \|[I - \Psi(\Delta f)\Psi(\Delta f)^+]\mathbf{S}_V\|_2, \tag{9.5}$$

where I is the $N_S \times N_S$ identity matrix, $\Psi(\Delta f)$ is dependent on the non-linear parameter Δf, and $\mathbf{S}_V$ contains the measured signal data. Minimising this function for a single voxel does not guarantee the correct solution, as R_V has many local minima, and the Δf value at each voxel is not independent of all other voxels. As described in Sec. 3.3.4, Hernando et al. [2010a] minimise the cost function for all voxels in the field map simultaneously, using a graph cuts algorithm. Smoothness constraints are placed on the estimated resonant frequency variation by adding a regularisation term to Eq. 9.5.

As described in Chapter 6, the phase along a path, $\phi(i)$, is smooth and can be represented with an Nth order basis. A similar expression can be written for the resonant frequency variation along the path,

$$\Delta f(i) = \sum_{n=1}^{N} \alpha_n \beta_n(i), \tag{9.6}$$

where $\{\alpha_n\}$ are the parameters to estimate and $\{\beta_n\}$ is the set of basis functions.

Using Eq. 9.5, the aim is to find the set of parameters $\{\alpha_n\}$ which minimises the residual sum along each path,

$$R_P = \sum_{i=1}^{D} \|[I - \Psi(\{\alpha_n\})\Psi(\{\alpha_n\})^+]\mathbf{S}_P(i)\|_2, \tag{9.7}$$

where

$$\mathbf{S}_P(i) = \begin{bmatrix} S(t_1)|_{i=1}^{i=D} \\ S(t_2)|_{i=1}^{i=D} \\ S(t_3)|_{i=1}^{i=D} \end{bmatrix}$$

$$\Psi(\{\alpha_n\}) = \begin{bmatrix} e^{j2\pi f_{cs} t_1} & e^{j2\pi(f_{cs} + \sum_{n=1}^{N} \alpha_n \beta_n(i))t_1} \\ e^{j2\pi f_{cs} t_2} & e^{j2\pi(f_{cs} + \sum_{n=1}^{N} \alpha_n \beta_n(i))t_2} \\ e^{j2\pi f_{cs} t_3} & e^{j2\pi(f_{cs} + \sum_{n=1}^{N} \alpha_n \beta_n(i))t_3} \end{bmatrix}. \tag{9.8}$$

Equation 9.7 has a similar form to the objective function used for POP as presented in Eq. 6.17. The POP method described in Section 6.3 can be generalised to data acquired at any combination of echo times, with the main difference being that the objective function defined by Eq. 6.17 is replaced with Equation 9.7. As in POP, an Nth order Fourier series is used as the basis.

The main components of the POP algorithm can largely be applied to POP-VARPRO without modification, including the path generation (Sec. 6.2) and iterative stages (Sec. 6.3.2). The two elements of the POP algorithm which are altered to implement POP-VARPRO are as follows. First, instead of extracting the complex data along each path, $e^{j\hat{\phi}(i)}$, the data from the three echo time offset images are extracted and stored as $\mathbf{S}_P(i)$. Second, the objective function form in Eq. 9.7 does not lend itself easily to gradient-based optimisation methods. The BFGS quasi-Newton algorithm implemented by the MATLAB function `fminunc` is used instead.

Estimating the resonant frequency variation along the outermost path (or thin strip of paths) is difficult as direct phase unwrapping cannot be used. In the results shown in this chapter, POP-VARPRO is used to reconstruct the resonant frequency variation in the symmetric Dixon three-point images. An existing 2D phase unwrapping method is then used to unwrap the strip of outermost paths, as described in Sec. 8.1.3. Further work is required to develop a suitable method for estimating the resonant frequency variation along the outer paths which can be applied to any combination of echo times.

9.3.1 *Results*

Results are shown for one phantom slice and two participant slices. Figure 9.9 shows the water image reconstructed for the central slice of Phantom 1. This figure demonstrates very similar performance to the POP water image in Fig. 7.2. Likewise, Figs. 9.10 and 9.11 show the resonant frequency variation, fat, and water images for Slice 15, Participant 3, and Slice 4, Participant 5. These images also display similar performance to the POP reconstructed images in Figs. 8.5 (Row 1) and 8.6 (Row 1). However, there are more regions where fat-water swaps have occurred. These are indicated with red arrows. Situations where error propagation has occurred during estimation of the resonant frequency variation are also marked with arrows in Figs. 9.10(a) and 9.10(a).

Figure 9.9: Water image for central slice of Phantom 1, obtained using POP-VARPRO and the symmetric three-point Dixon images.

The processing time required for POP-VARPRO was observed to be much higher than the methods reported in Sec. 8.2, with each slice taking approximately 3.5 hours to be reconstructed. This is around 100 times longer than the reported POP reconstruction time of 120-140 seconds. This indicates that the objective function in Eq. 9.7 is much slower to converge compared with Eq. 6.17.

9.3.2 *Discussion*

The three illustrated slices show that POP-VARPRO can be used to accurately separate the fat and water in the three-point Dixon technique, with comparable performance to the standard POP method. This demonstrates that POP can be extended or altered to use different objective function forms and achieve similar results. However, further development of the method used to estimate the resonant frequency variation along the outer paths is needed before

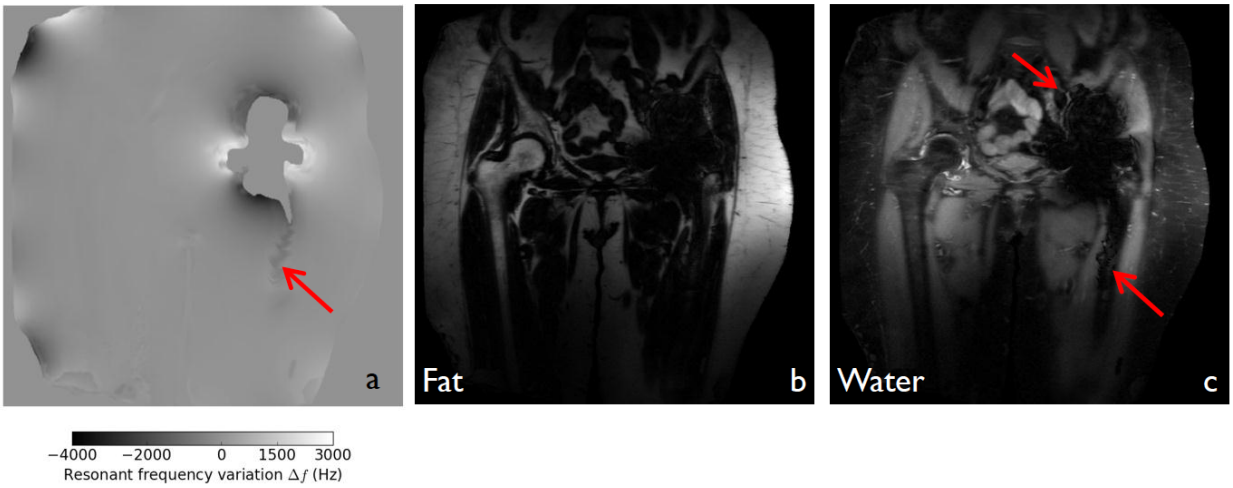

Figure 9.10: Resonant frequency variation (a), fat (b), and water (c) images of Participant 3, Slice 15, obtained using POP-VARPRO and the symmetric three-point Dixon images.

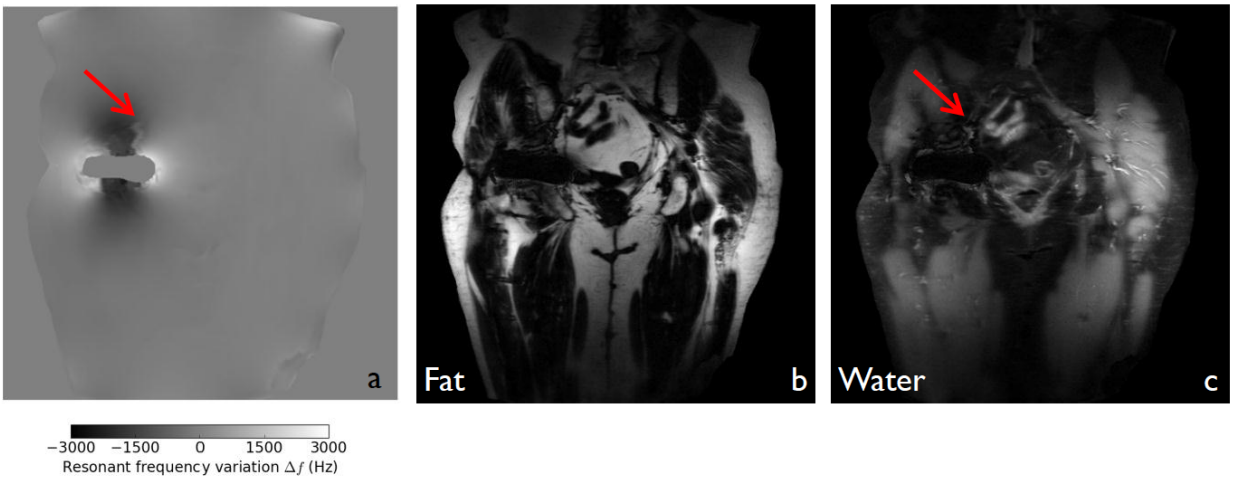

Figure 9.11: Resonant frequency variation (a), fat (b), and water (c) images of Participant 4, Slice 5, obtained using POP-VARPRO and the symmetric three-point Dixon images.

POP-VARPRO can be used to separate the fat and water in images acquired with any combination of echo times.

It should be noted that the IDEAL region-growing algorithm initially downsamples the acquired images to a low resolution. It then estimates the resonant frequency variation for pixels in the low resolution images by applying the pixel-independent algorithm. These pixels are then used as starting "super-pixels" in the region-growing method, which is applied to the acquired (full sized) images. It is anticipated that a similar approach could be applied to POP-VARPRO, where the IDEAL region-growing method is applied to estimate the resonant frequency variation along a thin strip of outer paths. POP-VARPRO would then proceed as described, using the estimated resonant frequency variation along the initial outer paths as a starting point.

In addition, the very slow reconstruction time indicates that the POP-VARPRO objective function is unlikely to be the most suitable objective function to use for images acquired with any combination of echo times. Furthermore, the objective function fails to converge to the correct result in some situations where POP succeeds, as marked in Fig. 9.10. This signifies that the POP-VARPRO objective function may have poor convergence properties. It would be worthwhile to investigate the best form of objective function for POP which converges to its minimum value rapidly and accurately.

It would also be useful to evaluate the performance of the graph cuts algorithm near metal implants [Hernando et al., 2010a]. This method is likely to provide valuable insights into how to develop a robust method for estimating the resonant frequency variation near metal. The multipeak model of the fat spectrum described in Sec. 3.3.5 could be used to assist with the estimation of the resonant frequency variation [Yu et al., 2012, Smith et al., 2015].

Finally, the object-based method described by Sharma et al. [2015] uses the predicted resonant frequency variation induced by susceptibility changes across the anatomy to aid the fat-water separation [4]. This method was only applied to images of human anatomy without metal implants, but is likely to prove useful in understanding how to achieve fat-water separation in asymmetrically acquired images near metal.

[4] This approach is similar to the methods described in Appendix A, where the model phase shift is subtracted from the acquired signal before performing phase unwrapping.

9.4 SUMMARY

In conclusion, this chapter consisted of three main components. First, a summary of initial work performed on simulating IDEAL was presented. This included an analysis of the convergence of the basic iterative reconstruction algorithm in regions of rapid resonant frequency variation. The second section briefly summarised the performance of IDEAL, referring to the participant results described in Chapter 8. Water images were also shown for multiple adjacent slices for Phantom 3 and Participant 4, demonstrating that the IDEAL algorithm can perform erratically from slice to slice. In the third and

final section, a new algorithm called POP-VARPRO was described, where the VARPRO objective function was altered to be used in conjunction with POP. The displayed results demonstrate the potential of this method, but further work is needed before it can be used with any combination of echo times.

10

Investigating a Better Basis

This chapter presents an alternative to the Fourier series basis used in the main POP method, as described in Chapter 6. First, the motivation for an improved set of basis functions is discussed. This is followed by an introduction to over-complete basis functions and the matching pursuit algorithm. A variation on this algorithm is then presented and applied to the POP algorithm.

10.1 MOTIVATION

This section outlines the main motivating factor for investigating a different basis for POP: the number of Fourier series coefficients required to accurately represent the phase along the inner paths is large. This was first observed when developing the initial method for determining the order of the Fourier series, as described in Sec. 6.3.3. Further simulation confirmed the need to consider an alternative basis, and is explained in this section using two main points. First, an example is described where POP is used to estimate the simulated phase induced by Implant 1. With a low order Fourier series, POP fails to correctly estimate the phase along the inner paths.

This is followed by Sec. 10.1.1, *Fourier series analysis*. This section investigates the number of coefficients needed to achieve two error thresholds for paths generated across ten simulated slices. It is demonstrated that a very high number of coefficients is necessary to accurately represent the sharp features present in the phase along the inner paths.

▶ Recall that the phase along a path is represented by a set of basis functions,

$$\phi(i) = \sum_{n=1}^{N} \alpha_n \beta_n(i). \tag{10.1}$$

In the work presented to this point in the thesis, an Nth order Fourier series is used as a basis in POP. While this is arguably the most straightforward basis, it is not the most appropriate model for sharp

variations in the phase along paths near the implant boundary. This is demonstrated in Fig. 10.1, which shows a 30th order Fourier series[1] fitted to the simulated phase along one sample path near the boundary of Implant 1, and two paths near the boundary of Implant 3 [2]. The Fourier series is not able to accurately fit the spikes and rapid changes in the phase along the plotted paths. Gibbs ringing is also observed on either side of the spikes. Figure 10.1 also shows the error (ϵ) between the fitted Fourier series phase (ϕ_{FS}) and the simulated phase (ϕ_M). Regions of significant error are noted near spikes in the simulated phase.

[1] With an order of $N = 30$ there are $2N + 1 = 61$ coefficients.

[2] It should be noted that these paths are situated closer to the implant boundary than those marked in Figs. 6.2–6.6.

The effect of using a low order Fourier series on the POP optimisation process can be observed in the following example. Gaussian white noise was added to the simulated model phase shift for Implant 1, as shown in Fig. 6.2. The variance of the noise was set so the SNR of the simulated model phase was 20 dB. The noisy model, ϕ_{NS}, was then encoded in the complex exponential,

$$s_N = e^{j\phi_{NS}}. \tag{10.2}$$

The phase was then estimated using POP. 80 paths were generated and the order of the Fourier series across the paths ranged over $N = [20, 80]$. Figure 10.2(a) shows the reconstructed phase. Figure 10.2(b) shows the absolute error between the estimated and simulated model phase. It can be seen that there are significant errors in the estimated phase near the implant boundary.

Figure 10.3 shows the final value of the objective function H across the paths [3]. At path index 65, the value of H jumps from 12 to 73. Figure 10.4 shows the estimated and model phase along path index 65. POP has converged to an incorrect solution. This is likely because the Fourier series is not able to resolve the sharp peaks in this path.

[3] Recall that H is defined by Eq. 6.17.

Similar patterns were observed during the POP optimisation steps for the phantom and participant data, with the final value of H increasing considerably at the inner paths. This is likely to contribute to the failure of POP to accurately separate the fat and water near the implant in Phantom 3, and in some processed slices for participants with cobalt-chromium implants [4].

[4] As discussed in Sec. 7.7, it should be noted that signal loss and distortion are also present along the inner paths, adding to the difficulty of converging to the correct solution.

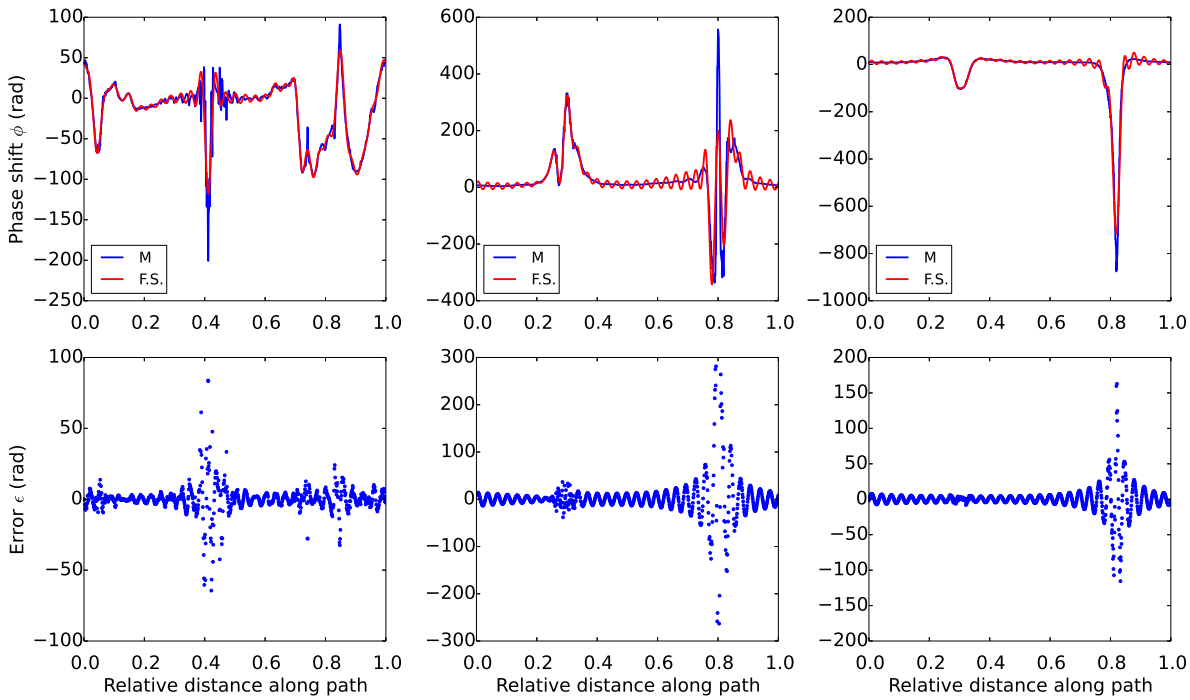

Figure 10.1: The top row of plots shows the rapidly varying modelled phase (M) along one sample path for Implant 1 (left) and two from Implant 3 (middle and right), with a 30th order Fourier series fitted to both (F.S.). The bottom row of plots shows the error between the fitted Fourier series phase and the modelled phase, $\epsilon = \Phi_{FS} - \Phi_{M}$.

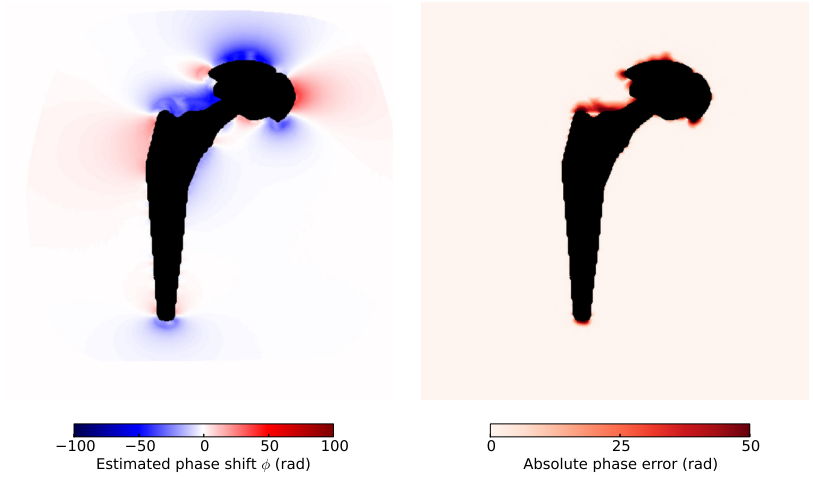

(a) Estimated phase

(b) Absolute error

Figure 10.2: Estimated phase obtained using POP (a) and absolute error between estimated and simulated model phase (b).

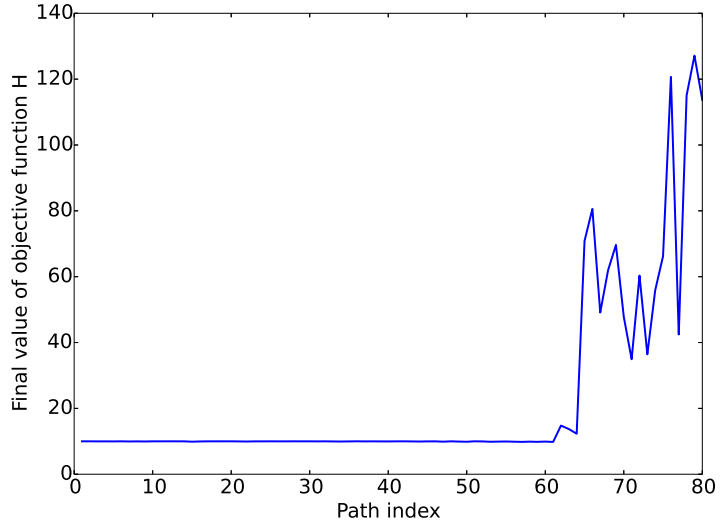

Figure 10.3: Final value of the objective function from outermost path (index 1) to innermost path (index 80).

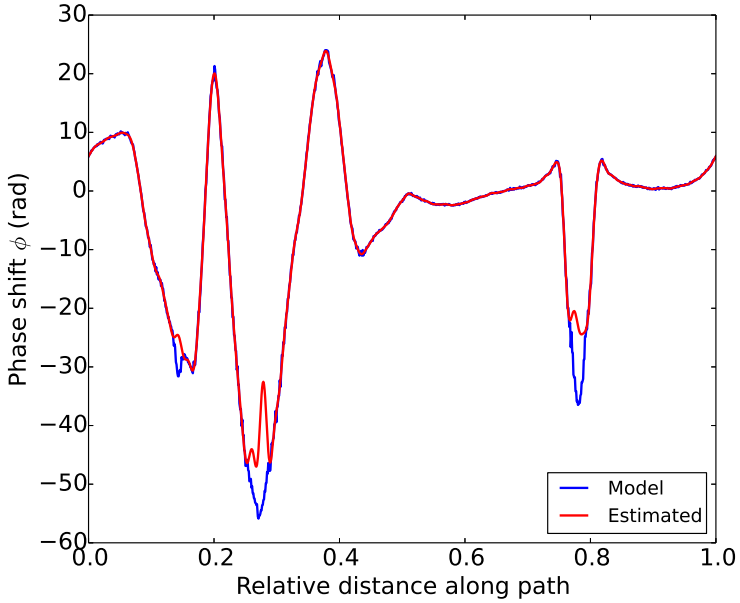

Figure 10.4: Estimated phase obtained using POP and simulated model phase along path 65.

10.1.1 *Fourier series analysis*

This section expands on the initial method used to determine the Fourier series order described in Sec. 6.3.3. The Fourier series was fitted to the phase along paths generated from the simulated phase for Implant 1 and Implant 3. Paths were generated from five slices for Implant 1, and five slices for Implant 3. For each slice, the Fourier series was fitted to 80-90 paths.

Two metrics were used to assess the goodness of fit: the mean square error and the maximum absolute error. Recall from Eq. 6.20 that the mean square error in decibels (MSE_{dB}) is given by

$$MSE_{dB} = 20\log_{10}\left[\frac{1}{D}\sum_{i=1}^{D}(F^N(r_i) - \phi_S(i))\right], \tag{10.3}$$

where $\phi_S(i)$ is the simulated phase along the path [5]. The maximum absolute error (MAE) along the path is given by

$$MAE = \max|F^N(r_i) - \phi_S(i)|. \tag{10.4}$$

[5] Recall that D is the number of pixels in the path and $F^N(r_i)$ is the Fourier series representation of the phase.

For each path, the number of Fourier series coefficients required to reach the following thresholds were recorded:

1. $MSE < 10\,dB$
2. $MAE < \pi$.

For the Fourier series, the number of coefficients is equal to $2N + 1$.

Figure 10.5 shows the number of coefficients needed for $MSE < 10\,dB$ and $MAE < \pi$, for the paths generated over three slices for Implant 1. Tables 10.1 and 10.2 show the number of coefficients required for the outermost and innermost paths across the ten modelled slices.

The number of coefficients required to achieve the two error thresholds increases substantially across the paths, with a noticeable sudden increase for the $MSE < 10\,dB$ criterion at approximately path 70. This is similar to the sudden increase in H observed in Fig. 10.3. The number of coefficients needed to reach $MAE < \pi$ is generally larger than those needed to reach $MSE < 10\,dB$, as the former is a more stringent requirement. The innermost path requires the highest number of coefficients, as this is where the phase shift gradient is the highest.

Table 10.1: Number of coefficients required to achieve error thresholds for outermost and innermost paths across modelled slices for Implant 1.

	Number of coefficients			
	$MSE < 10\,dB$		$MAE < \pi$	
	Outermost	Innermost	Outermost	Innermost
Slice 1	7	195	9	237
2	11	719	19	863
3	11	593	19	611
4	13	247	15	261
5	9	599	17	793

	Number of coefficients			
	MSE < 10 dB		MAE $< \pi$	
	Outermost	Innermost	Outermost	Innermost
Slice 1	49	873	113	965
2	65	737	101	751
3	47	781	97	801
4	43	721	203	751
5	43	379	77	387

Table 10.2: Number of coefficients required to achieve error thresholds for outermost and innermost paths across modelled slices for Implant 3.

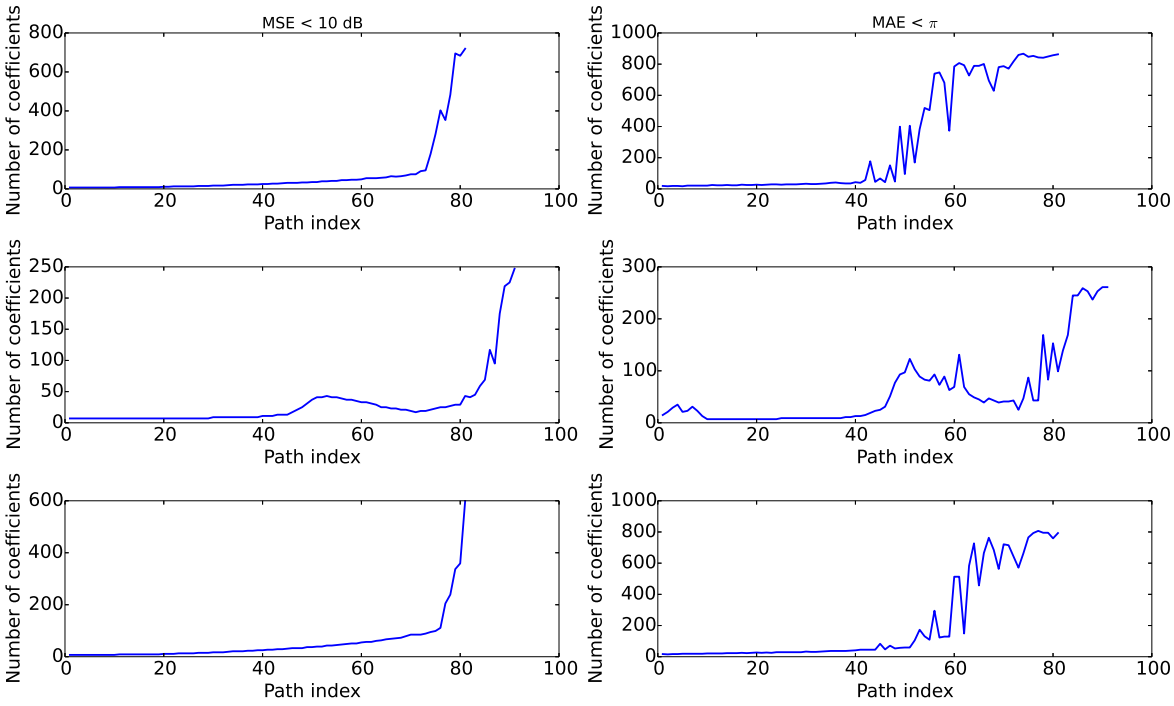

Figure 10.5: Number of coefficients required to achieve a fit where the MSE < 10 dB and MAE $< \pi$. Results are shown for 80 paths generated for slice 2 (top), slice 4 (middle) and slice 5 (bottom), for Implant 1. Similar results were obtained for slices 1 and 3 for Implant 1, and the five slices for Implant 3.

In general, the Fourier series is an appropriate basis for the slowly varying phase shift along the outer paths. However, it does not efficiently represent the rapidly varying phase close to the implant boundary, as the number of coefficients required to achieve the same goodness of fit increases significantly.

It was described in Sec. 6.3.3 that with a high value of N, the POP optimisation process produced unusual results. Therefore, with too few coefficients, the Fourier series is unable to resolve steep phase gradients, but with too many coefficients, the objective function optimisation is more difficult. In conclusion, the Fourier series is not the optimal basis for modelling the rapid phase changes near the implant boundary. Ideally, the best basis function set requires as few parameters as possible to sparsely represent the phase.

10.2 FUNCTION REPRESENTATION USING AN OVER-COMPLETE BASIS

This section first introduces the concept of an over-complete set of basis functions, or "dictionary". It then provides an overview of the matching pursuit algorithm, and the phase along three sample paths is decomposed using three matching pursuit dictionaries. This is followed by Sec. 10.2.2, *Matching pursuit analysis*, which compares the number of coefficients required to achieve the error metrics described in Sec. 10.1.1. The suitability of the three dictionaries for representing the phase along the simulated paths is discussed.

The background information presented in this section is comprised from a collection of papers by Mallat and Zhang [1993], Leone et al. [2005], Donoho et al. [2006], and the review article by Tosic and Frossard [2011].

▶ THE REPRESENTATION OF REAL-WORLD SIGNALS by basis functions is a common problem addressed in many signal processing applications. Orthogonal basis sets, such as the Fourier series, are commonly used as the vectors of the set are linearly independent. This allows the unique coefficients α_n to be efficiently obtained by taking the inner product of the vectors β_n with the signal ϕ,

$$\alpha_n = \langle \phi, \beta_n \rangle \quad n = \{1, ..., N\}. \tag{10.5}$$

However, many real-world signals cannot be efficiently represented by a single basis. For example, the phase along the paths in Fig. 10.1 consists of three or four sharp impulsive features and an underlying smooth, continuous phase. Instead, the signal can be represented by an over-complete set of basis functions, or "dictionary". The dictionary can be comprised of a combination of several orthogonal bases, such as sinusoids and wavelets [6]. The functions do not have to be orthogonal. Each element of the dictionary is a unit-norm vector called a word. The dictionary contains many more words than are chosen to represent the signal [Donoho et al., 2006].

[6] Dictionaries can also be built from "fit-for-purpose" functions obtained by running dictionary learning algorithms on training data.

▶ A DIRECT ANALOGY can be made to the literal dictionary:

Imagine an English dictionary which only has around 1000 words. Any idea or object could be described using these words, but it would require very long sentences, i.e. "A meal or snack which can be topped with ingredients such as tomato and cheese." Now, consider a dictionary with 100,000 words. These ideas can be described with much shorter sentences, or perhaps a single word, i.e. "Pizza." Also, the same idea can be expressed using several different combinations of words [Leone et al., 2005].

▶ LET $\{w_k\}$ form K unit-norm words chosen from a dictionary D_w. The true phase along a path, $\phi(i)$, can therefore be modelled by

$$\phi(i) = \sum_{k=1}^{K} c_k w_k(i). \tag{10.6}$$

The dictionary is redundant, unlike an orthogonal basis, so the words are not linearly independent. In addition, the representation is not unique. Finding the optimal set of words is an NP-hard problem,

but a sub-optimal representation can be found using the matching pursuit algorithm.

10.2.1 Matching pursuit

Matching pursuit is a greedy algorithm which iteratively decomposes a signal into a linear expansion of words from a redundant dictionary D_w. It was first introduced by Mallat and Zhang [1993], and has been applied to a wide range of signal processing and machine learning applications.

The algorithm selects the set of words $\{w_k\}$ from the dictionary D_w and calculates the corresponding set of coefficients, $\{c_k\} = \{c_1, c_2, ..., c_K\}$. There are K iterations. The basic steps are:

1. In the first iteration $k = 1$, execute the following steps:

   (a) Calculate the inner product of each word of the dictionary with the signal,

   $$c_m = \langle \phi, w_m \rangle \quad m = \{1, ..., M\}, \tag{10.7}$$

   where M is the total number of words in the dictionary.

   (b) Select the index of the word which gives the largest inner product,

   $$m_1 = \arg\max_m |c_m|. \tag{10.8}$$

   This gives the first element in the sets $\{w_k\}$ and $\{c_k\}$, $c_1 = c_{m_1}$ and $w_1 = w_{m_1}$. w_{m_1} is the word which has the maximum correlation with the signal.

   (c) Subtract $c_{m_1} w_{m_1}$ from the signal. This gives the residual of the first iteration,

   $$R_1 = \phi - c_{m_1} w_{m_1}. \tag{10.9}$$

2. For successive iterations, $k = 2, ..., K$, execute the following steps generalised from the first iteration:

   (a) Calculate the inner product of each word with the residual from the previous iteration, $c_m = \langle R_{k-1}, w_m \rangle \quad m = \{1, ..., M\}$.

   (b) Calculate $m_k = \arg\max_m |c_m|$. This gives the kth element in the sets $\{w_k\}$ and $\{c_k\}$, $c_k = c_{m_k}$ and $w_k = w_{m_k}$.

   (c) Subtract $c_{m_k} w_{m_k}$ from the signal to get the kth residual, $R_k = R_{k-1} - c_{m_k} w_{m_k}$.

   (d) Increment k and repeat Steps 2a - 2c.

▶ THE PHASE ALONG THE PATHS analysed in Sec. 10.1 was decomposed using MATLAB's matching pursuit algorithm, `wmpalg`. Three types of dictionaries were used:

1. Dictionary comprised of the discrete cosine transform basis (DCT).
2. Daubechies least-asymmetric wavelet functions (SYM).
3. A combination of the DCT and SYM bases.

Examples of the phase fitted with each method along the three paths in Fig. 10.1 are shown in Figures 10.6-10.8. 61 coefficients were used for each method [7]. The error between the fitted phase and the simulated phase is also shown for each method. The DCT dictionary has performed better than the 30th order Fourier series, but has still failed to accurately fit the phase over the sharp spikes. The wavelet (SYM) and combined DCT-SYM dictionaries performed similarly, with both accurately modelling the phase over the three displayed paths. The relative performance of these three dictionaries across the simulated paths is explored further in the following section.

[7] In Fig. 10.1 61 coefficients were also used as this corresponds to a Fourier series order of $N = 30$.

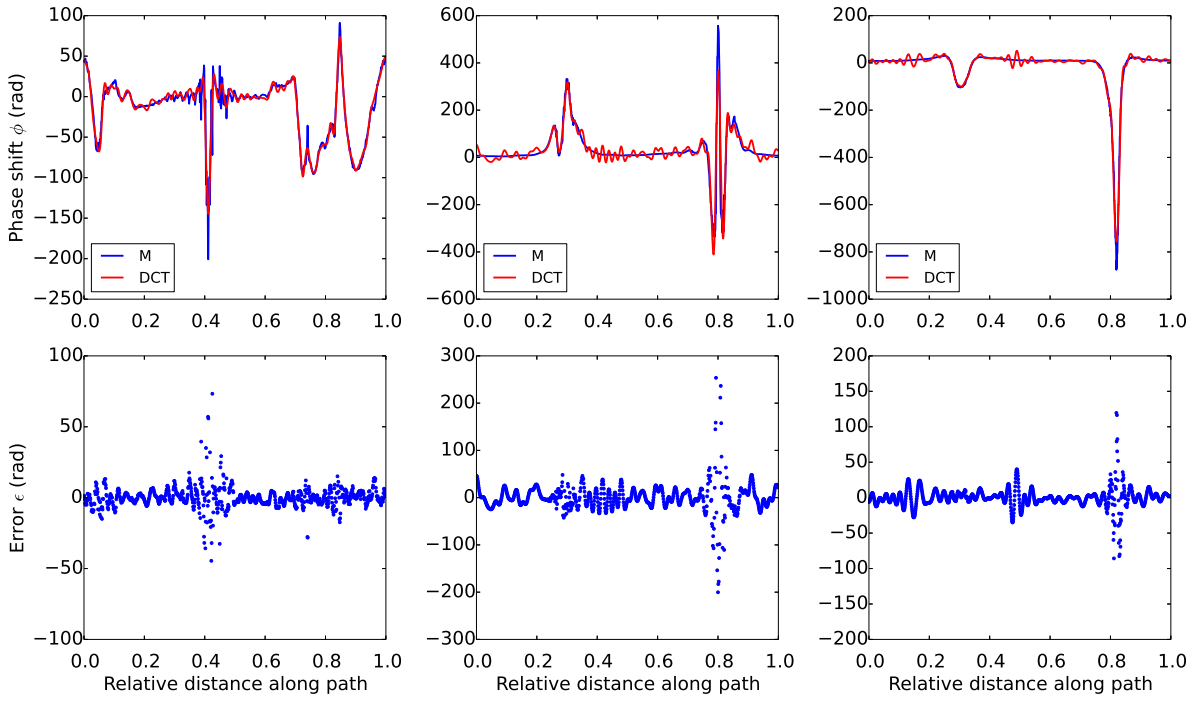

Figure 10.6: The top row of plots shows the modelled phase (M) and estimated phase (DCT) along one sample path for Implant 1 (left) and two from Implant 3 (middle and right). The phase was fitted using a DCT dictionary. The bottom row of plots shows the error in the fitted phase.

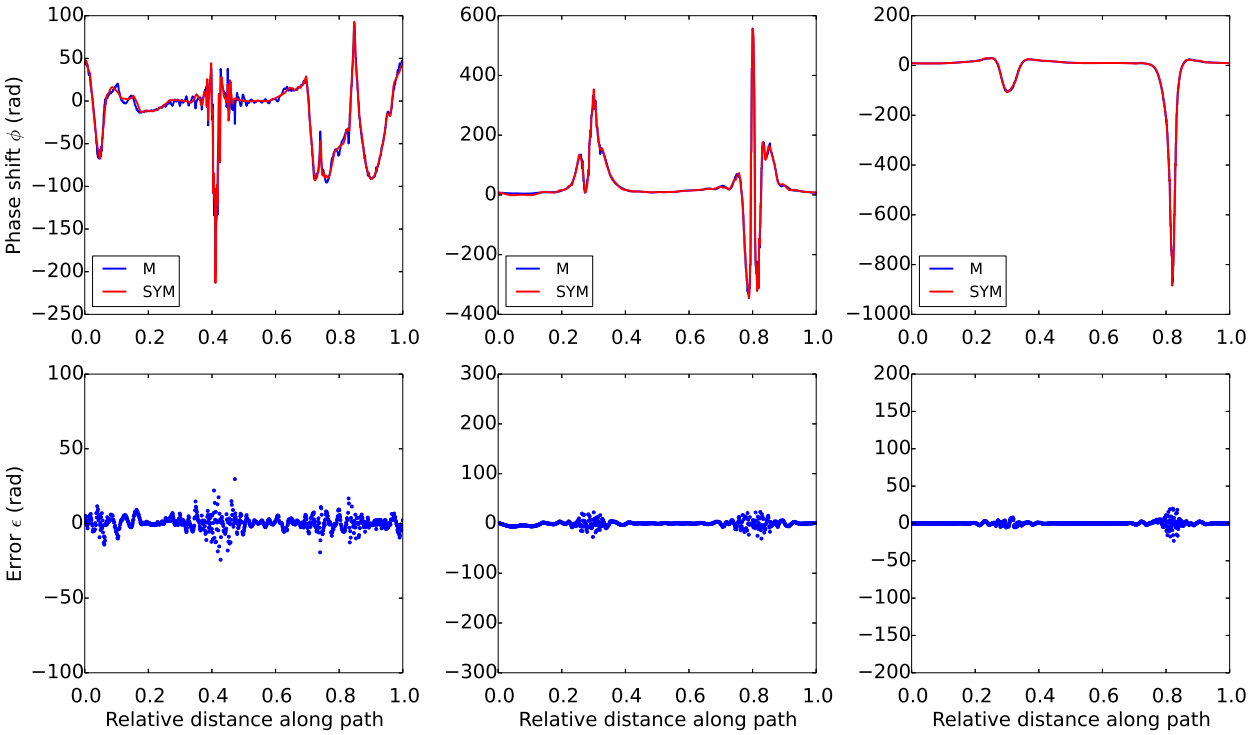

Figure 10.7: The top row of plots shows the modelled phase (M) and estimated phase (SYM) along one sample path for Implant 1 (left) and two from Implant 3 (middle and right). The phase was fitted using a wavelet dictionary. The bottom row of plots shows the error in the fitted phase.

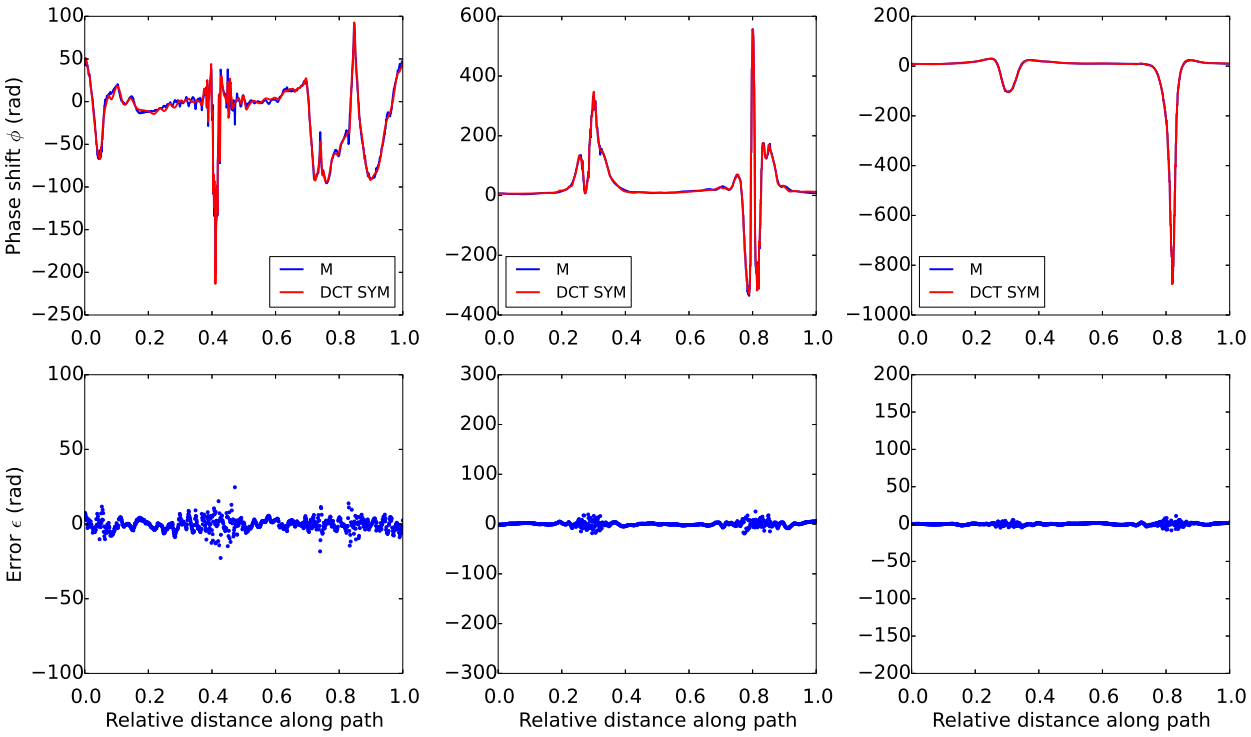

Figure 10.8: The top row of plots shows the modelled phase (M) and estimated phase (DCT-SYM) along one sample path for Implant 1 (left) and two from Implant 3 (middle and right). The phase was fitted using a DCT and wavelet dictionary. The bottom row of plots shows the error in the fitted phase.

10.2.2 *Matching pursuit analysis*

Tables 10.3 and 10.4 compare the number of coefficients required for each dictionary to reach $\mathrm{MSE}_{\mathrm{dB}} < 10\,\mathrm{dB}$ and $\mathrm{MAE} < \pi$, for the innermost and outermost paths for two slices in Implant 1 and Implant 3. These tables demonstrate that compared to the Fourier orthogonal basis, the tested dictionaries require far fewer coefficients to achieve the same error thresholds. This is particularly noticeable for the innermost paths. The combined dictionary comprised of the DCT and wavelet (SYM) bases required the smallest number of coefficients to reach the error thresholds. Similar results were obtained for the eight additional slices.

Figures 10.9 and 10.10 compare the $\mathrm{MSE}_{\mathrm{dB}}$ and MAE for 20 coefficients fitted using each dictionary to the paths for the same two slices. These figures illustrate how each basis performs with a fixed, low number of coefficients. The DCT dictionary has a similar performance to the Fourier series orthogonal basis, as both consist of smooth continuous functions. Both have low error metrics for the outermost paths, and the error increases with the path index. However, the DCT dictionary performs slightly better than the Fourier series basis. This is because the latter uses just the first 20 terms in the Fourier series, whereas the DCT dictionary uses the best 20 words across the entire dictionary.

The wavelet dictionary is made up of shifted wavelet functions. It performs poorly for smoothly varying paths, but performs well at fitting the rapidly changing phase along the inner paths. However, the dictionary with both DCT and wavelet functions had the lowest error metric across all the tested paths. At the outer paths, the selected dictionary words consist of mostly DCT functions. Wavelet functions are gradually introduced, and the selected words at the inner paths are mostly wavelet functions. This is shown in Figure 10.11, which shows the first ten selected words from the DCT-SYM dictionary for two paths. Note the predominance of narrow-extent functions for the inner path compared to the outer path. Overall, the combined DCT-SYM dictionary was determined to be the most appropriate of the tested dictionaries for modelling the phase across the simulated paths.

	Number of coefficients			
	$\mathrm{MSE} < 10\,\mathrm{dB}$		$\mathrm{MAE} < \pi$	
Basis	Outermost	Innermost	Outermost	Innermost
Fourier	*11*	*719*	*19*	*863*
DCT	7	229	10	558
SYM	7	69	10	139
DCT and SYM	5	68	7	138

Table 10.3: Number of coefficients required for each dictionary to achieve error thresholds. Results are shown for outermost and innermost paths across Slice 2, Implant 1. The number of coefficients for the Fourier series orthogonal basis is given in italics for comparison.

	Number of coefficients			
	MSE < 10 dB		MAE $< \pi$	
Basis	Outermost	Innermost	Outermost	Innermost
Fourier	*47*	*781*	*97*	*801*
DCT	39	525	91	569
SYM	40	227	52	298
DCT and SYM	17	206	26	278

Table 10.4: Number of coefficients required for each dictionary to achieve error thresholds. Results are shown for Slice 3, Implant 3.

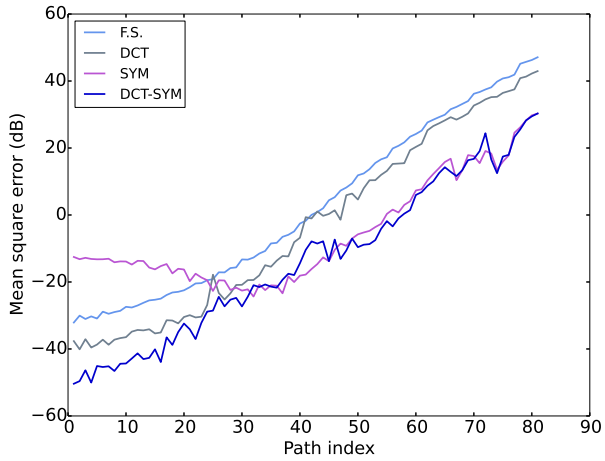

(a) Mean square error, MSE (dB)

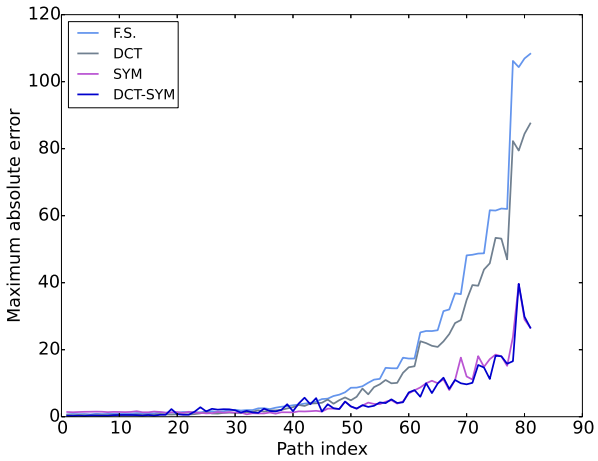

(b) Maximum absolute error, MAE

Figure 10.9: MSE and MAE between modelled and fitted phase using the three matching pursuit dictionaries (DCT, SYM, DCT-SYM), and the Fourier series orthogonal basis (F.S.). 20 coefficients were fitted for each basis. Results are shown for 80 paths generated for Slice 2, Implant 1.

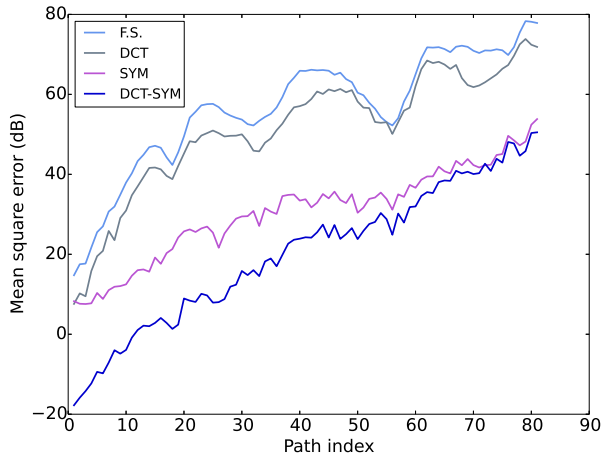

(a) Mean square error, MSE (dB)

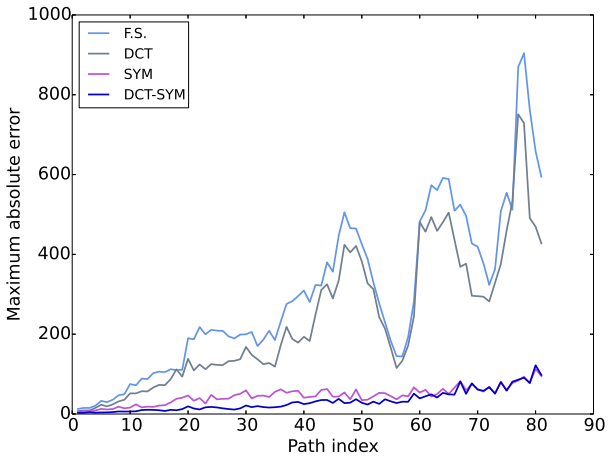

(b) Maximum absolute error, MAE

Figure 10.10: MSE and MAE between modelled and fitted phase using the three matching pursuit dictionaries (DCT, SYM, DCT-SYM), and the Fourier series orthogonal basis (F.S.). 20 coefficients were fitted for each basis. Results are shown for 80 paths generated for Slice 3, Implant 3.

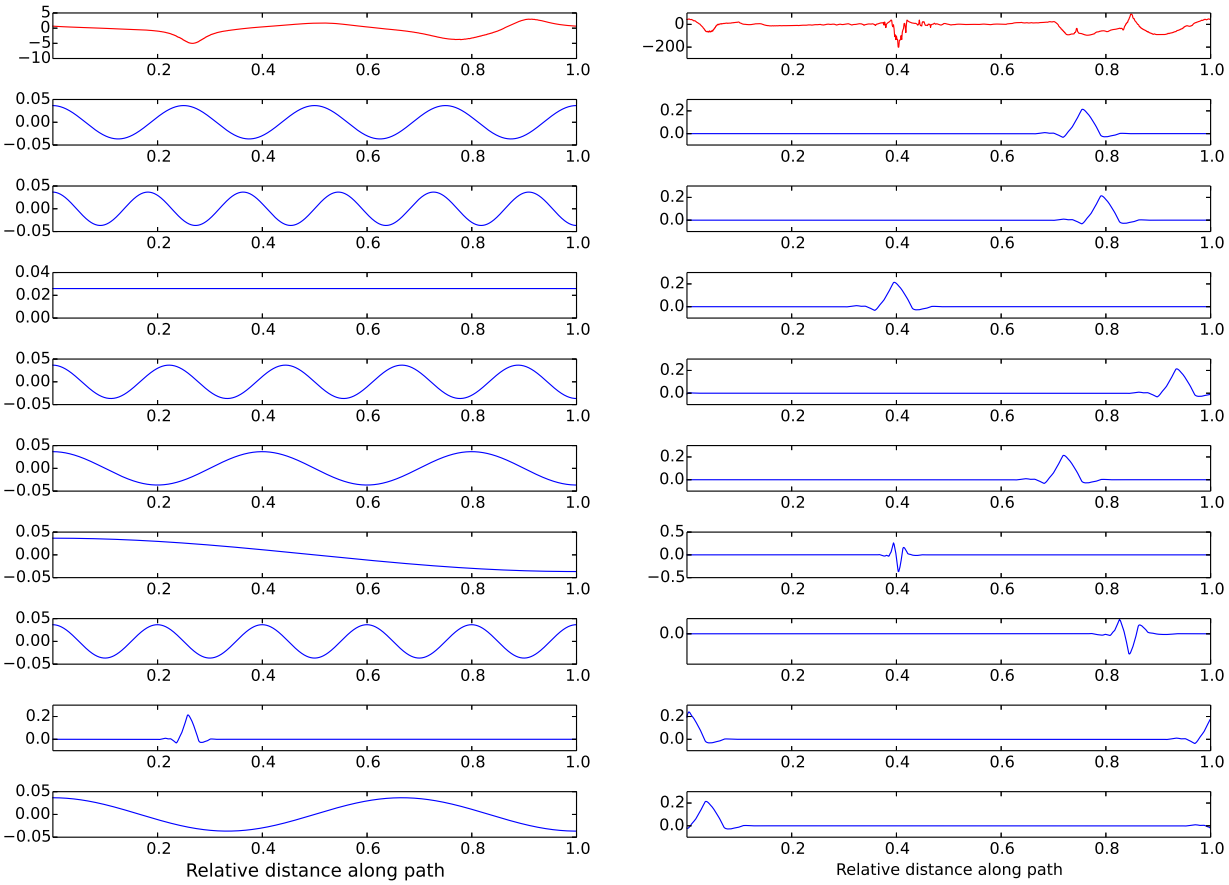

(a) Outer path

(b) Inner path

Figure 10.11: First ten selected words from the DCT-SYM dictionary for two paths in Slice 2, Implant 1: the outermost path (a), and an inner path (b). The phase along each path is plotted in red in the top plot. The normalised dictionary words are plotted in blue.

10.3 APPLICATION TO PHASE ONION PEELING

This section introduces a potential method for estimating the phase along a path by differentiating the words of an over-complete dictionary. Results are shown for three sample paths generated for Implant 1. The limitations of this method are also discussed.

▶ DECOMPOSING A KNOWN SIGNAL with matching pursuit is a straightforward process. However, in the three-point Dixon technique, the true signal phase is not known. The phase along a path is encoded in the complex exponential,

Refer to Sec. 6.3.1 for details.

$$s(i) = e^{j\hat{\phi}(i)}. \tag{10.10}$$

Consider that the phase along each path, $\phi(i)$, is modelled by K words from an over-complete dictionary, as described first in Eq. 10.6,

$$\phi(i) = \sum_{k=1}^{K} c_k w_k(i). \tag{10.11}$$

It is necessary to determine the coefficients $\{c_k\}$ to obtain the unwrapped phase estimate. This can be done with the assistance of the approximate prior knowledge of the phase shift. Let $\phi_M(i)$ be a model of the phase shift along the path, such as the simulated phase in Fig. 6.2. This can be approximated by K words by

$$\phi_M(i) = \sum_{k=1}^{K} a_k w_k(i). \tag{10.12}$$

Performing matching pursuit on the model phase gives the set of words $\{w_k\}$. Assuming that the model is well-fitted to the measured data, these words form a suitable basis for the true phase.

The coefficients $\{c_k\}$ can be directly calculated using the first order derivative of the measured complex data, $s(i)$. This can be calculated by differentiating and rearranging Eq. 10.10 [8],

[8] Refer to Liang [1996] for details.

$$\begin{aligned} \frac{ds(i)}{di} &= j\frac{d\hat{\phi}(i)}{di}e^{j\hat{\phi}(i)} \\ \frac{d\hat{\phi}(i)}{di} &= -je^{-j\hat{\phi}(i)}\frac{ds(i)}{di} \\ &= -js(i)^*\frac{ds(i)}{di}. \end{aligned} \tag{10.13}$$

The derivative $\frac{d\hat{\phi}(i)}{di}$ is estimated using the derivative property of the Fourier transform.

It is assumed that the dictionary words $\{w_k\}$ are real and differentiable, so Eq. 10.11 can be differentiated to give

$$\frac{d\phi(i)}{di} = \sum_{k=1}^{K} c_k \frac{dw_k(i)}{di}. \tag{10.14}$$

The coefficients $\{c_k\}$ are calculated by evaluating the inner products

$$c_k = \left\langle \frac{d\hat{\phi}(i)}{di}, \frac{dw_k(i)}{di} \right\rangle \quad k = \{1, ..., K\}. \tag{10.15}$$

Once the coefficients are calculated, the unwrapped phase along the path is then estimated by Eq. 10.11. This estimate can then be refined using the optimisation steps in the POP algorithm, outlined in Sec. 6.3.

▶ THE DESCRIBED METHOD WAS APPLIED to estimate the phase shift for the central slice of Phantom 1. 80 paths were generated across both the central slice of the Implant 1 modelled phase shift, $\phi_M[\mathbf{x}]$, and the central slice of the acquired complex data, $\hat{s}[\mathbf{x}]$. For the model phase along each path, $\phi_M(i)$, the model basis words $\{w_k\}$ were decomposed using the matching pursuit algorithm. The number of words in each basis, K, were the number required for the basis to fit the model phase with $MAE < \pi$. The bases were then used to estimate the phase along the paths generated for Phantom 1, $\phi(i)$, by the following steps:

1. The model basis words, $\{w_k\}$, were differentiated using the derivative property of the Fourier transform.
2. The acquired complex phantom data, $s(i)$, was differentiated by Eq. 10.13, and using the derivative property of the Fourier transform.
3. The coefficients, $\{c_k\}$, were calculated by Eq. 10.15.
4. The phase, $\phi(i)$, was estimated by Eq. 10.11.

10.3.1 Results

Figures 10.12-10.14 show the "true" phase along three paths generated for the central slice of Phantom 1. This was obtained using the standard POP algorithm. The estimated phase along these paths, calculated using the described matching pursuit method, is shown in red. In general, this method succeeded at directly estimating the phase along the outer and central paths, but failed in some regions along the inner paths. The reasons for this are discussed in the following section.

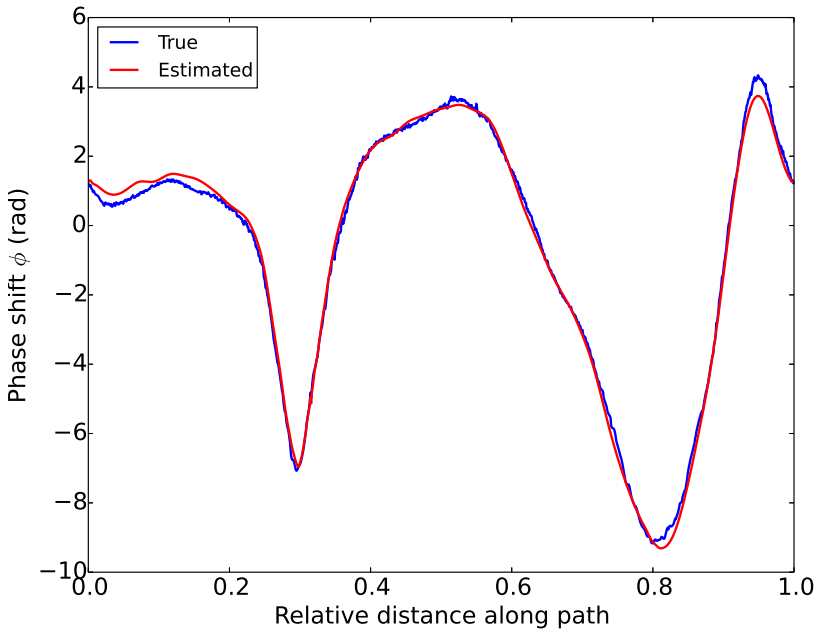

Figure 10.12: True phase unwrapped using POP, and estimated phase obtained using matching pursuit, for an outer path.

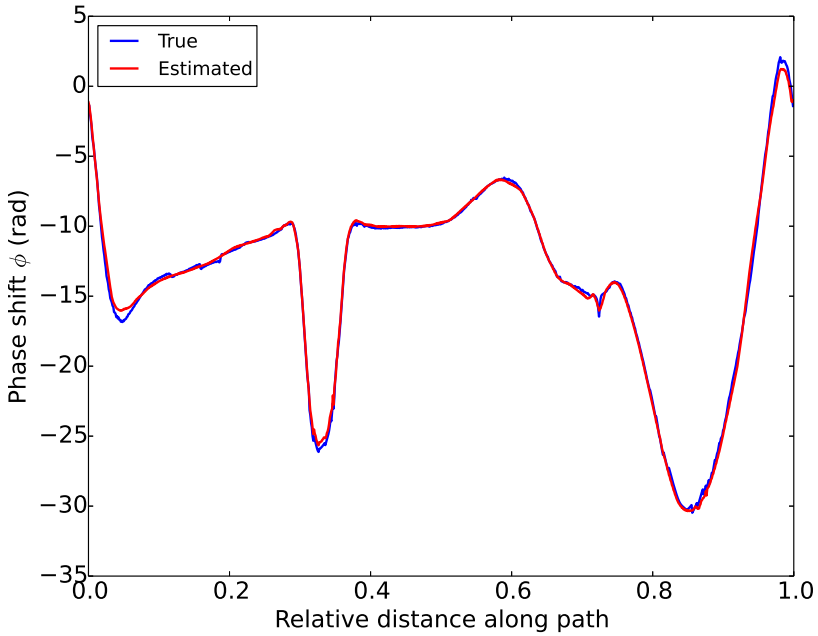

Figure 10.13: True phase unwrapped using POP, and estimated phase obtained using matching pursuit, for a centrally located path.

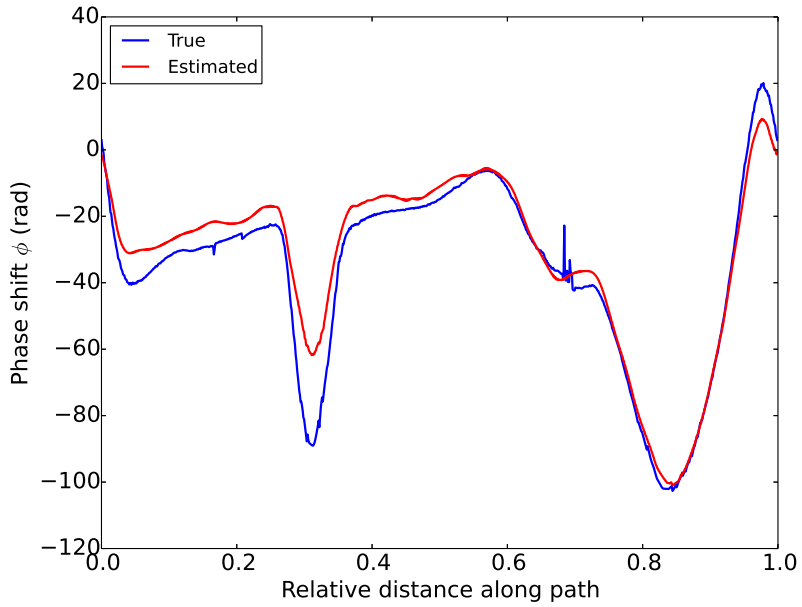

Figure 10.14: "True" phase and estimated phase obtained using matching pursuit, for an inner path. To simulate the behaviour of the phase along an inner path, the "true" phase was obtained by multiplying the POP-obtained phase along a central path by a scaling factor. This is because the POP-estimated phase shift for Phantom 1 only covers the range ± 50 rad, but it was important to consider how the proposed matching pursuit method performed in regions of steeper phase variation.

10.3.2 Discussion

The described method of calculating the matching pursuit coefficients using a model of the phase shift and the derivative of the true phase has several advantages. First, it allows for efficient and direct estimation of the phase in a single iteration. It does not rely on the performance of existing phase unwrapping methods at the outer paths, so may provide an improved approach for estimating the phase along the outermost path. Finally, the method offers a flexible way of incorporating prior knowledge of the phase induced by any type of implant, or combination of implants. For example, the phase induced by titanium and cobalt-chromium hip implants contains features of a similar shape, but a different magnitude. The normalised model basis words for both implants would include similar information, so only one basis may need to be generated. The variation in calculated coefficient values would represent the difference in magnitude.

However, there are a number of issues with this approach. First, the model must be well-fitted to the true phase. If it is not, the selected words from the dictionary will not form an appropriate basis. For example, the peaks in the model phase may occur at a slightly different location to the peaks in the true phase. Figure 10.15(a) shows an example where the simulated model phase (in purple), which the model basis words $\{w_k\}$ are obtained from, is not well-fitted to the "true" phase obtained with POP. The wavelet functions selected for the model basis words are shifted in location from the best words for the true phase. This can result in unusual features being present in the final estimated phase. This is demonstrated in Fig. 10.15(b). The estimated phase, in red, was obtained using the

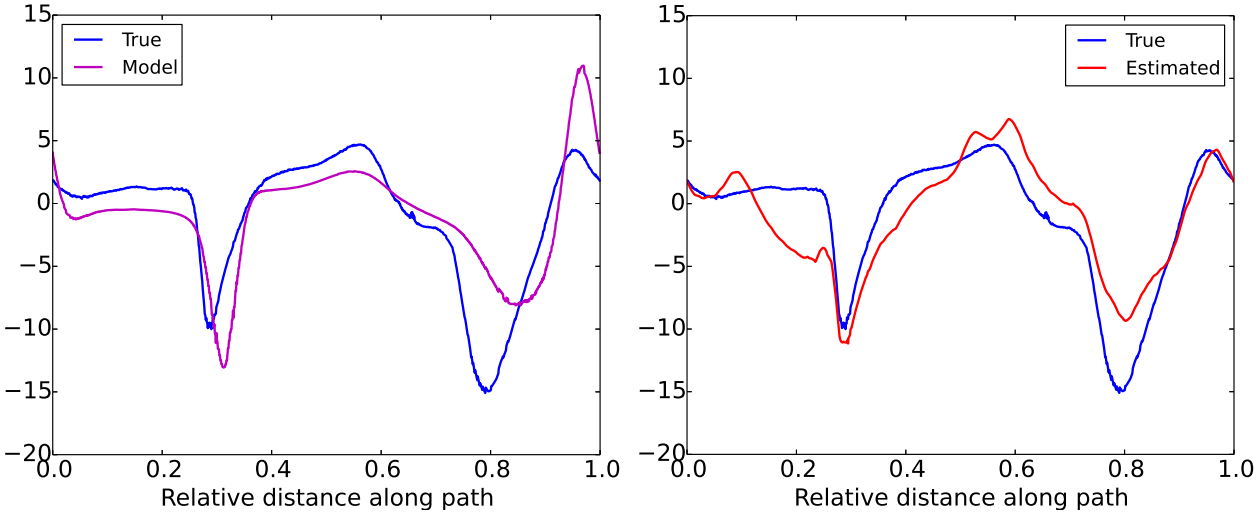

(a) (b)

Figure 10.15: a) shows the "true" phase along a path unwrapped with POP in blue, and the poorly fitted simulated model phase along the same path in purple. Note that the peak features in the model phase are offset from those in the true phase. b) shows the true phase in blue, and the red line shows the phase estimated using the basis obtained from the simulated model phase in a).

basis calculated for the simulated model phase in Fig. 10.15(a).

The second problem with this approach is that an accurate estimate of the derivative of the phase is necessary. Taking the derivative of the phase amplifies the noise present in the measured data. This affects the value of the calculated basis function coefficients, and consequently, the unwrapped phase. Coefficients corresponding to features in the decomposed basis which are similar to noise are given a higher weighting than if the noise was absent.

Additionally, if the phase is undersampled, the derivative cannot be evaluated correctly [9]. This is demonstrated in Figs. 10.16 and 10.17. The model phase $\phi_M(i)$ was differentiated using two methods:

1. Standard differentiation. This is the "true" derivative.
2. Encoding the phase in the complex exponential $e^{j\phi_M(i)}$ and taking the derivative using Eq. 10.13. This is the "estimated" derivative.

Figures 10.16(b) and 10.17(b) show the true and estimated derivative[10]. In Fig. 10.16 the phase is fully sampled, so the derivative can be estimated correctly. The phase in Fig. 10.17 is undersampled across the sharpest peak, so the derivative cannot be estimated accurately by Eq. 10.13 in this region. A more sophisticated way of incorporating prior knowledge is needed in regions where this sampling condition is violated.

[9] Recall that for the phase to be sufficiently sampled, the difference in phase must be less than π in magnitude, $|\Delta\phi[x]| \leqslant \pi$.

[10] It should be noted that the derivative is not a smooth function. The voxelisation process, as described in Sec. 5.2, causes the geometry of Implant 1 to appear voxelated. This reduces the smoothness of the simulated phase shift, with the effects amplified when the phase is differentiated.

10.4 SUMMARY

The Fourier series is not the ideal basis for representing the rapidly varying phase near the implant boundary. Matching pursuit offers a more flexible approach, as it allows for the use of tailor-made basis

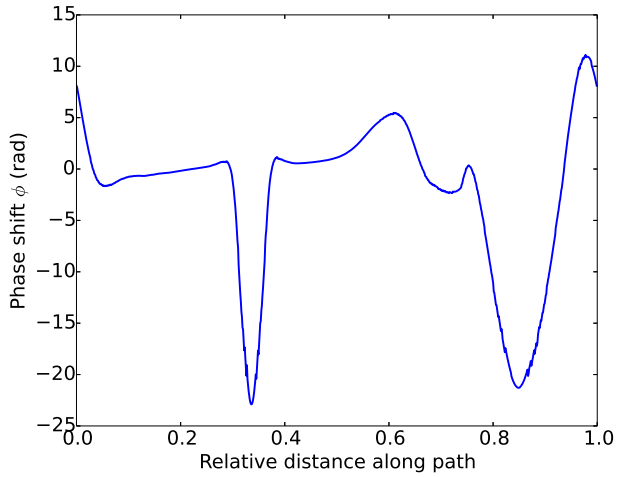

(a)

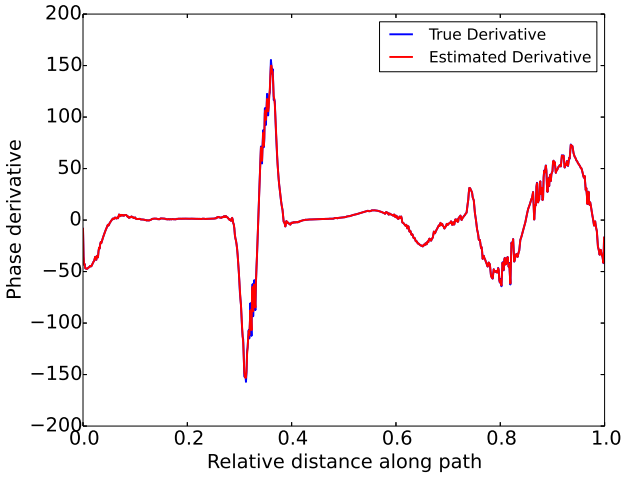

(b)

Figure 10.16: Model phase (a) and derivative (b) along a path where the phase is adequately sampled. This path is 941 pixels in length.

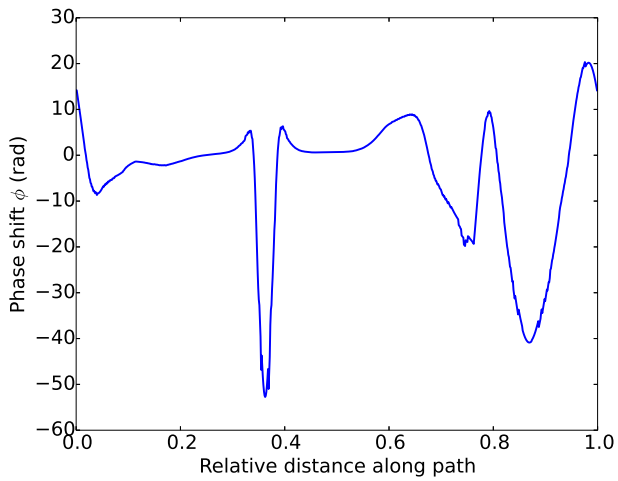

(a)

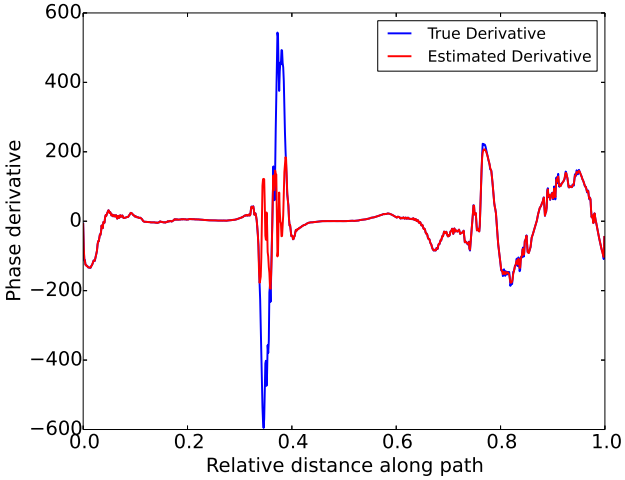

(b)

Figure 10.17: Model phase (a) and derivative (b) along a path where the phase is undersampled. This path is 905 pixels in length.

functions which better fit the phase. A well-fitted basis requires far fewer coefficients to achieve the same error thresholds as a poorly fitted basis.

Matching pursuit cannot be directly applied to the three-point Dixon technique when only the wrapped phase is known. One described method uses the derivative of a set of model basis functions to directly calculate the coefficients. However, the issues associated with this approach require further investigation, as described in the following chapter, *Conclusions and Future Work*.

11

Conclusions and Future Work

This chapter summarises the main contributions made by this thesis, and draws conclusions from the research performed. Recommendations for suggested future work are also made.

11.1 THESIS SUMMARY AND CONCLUSIONS

The primary aim of the research presented in this thesis was to answer the following question: *'is it possible to develop an improved method for phase unwrapping in the three-point Dixon technique near metal implants, using some degree of prior knowledge?'*. The development of the Phase Onion Peeling (POP) algorithm confirms the answer to this question.

This thesis has explored many aspects of the problem of phase estimation near metal, culminating in the results produced by the POP algorithm. As outlined in Part I, the literature covering the topics of MR imaging near metal, fat suppression, and phase unwrapping was examined in depth. This established the need for an improved resonant frequency estimation method in multipoint fat suppression techniques. In particular, such a method would allow for easier visualisation of fluid-based complications near the implant boundary, and would improve the ability to identify abnormalities such as tumours, inflammation, or scar tissue in contrast-enhanced imaging.

Part II began with an overview of the phantoms which were constructed and scanned. The geometries of two implants were obtained using a white light scanner, and processed using a voxelisation algorithm. The geometries were then used to simulate the resonant frequency variation near the implants. These provided valuable tools used in the development of POP.

Chapter 6 then gave a comprehensive outline of the POP algorithm, including the motivating factors, the path generation method, and the objective function used by POP. The development of POP arose from two key pieces of knowledge obtained from the simulations. First, the gradient of the phase shift induced by the metal is highest at the boundary of the metal. It decreases as the distance

from the boundary increases. Second, the phase along a closed loop around the implant can be modelled by a smooth periodic function; the Fourier series was chosen for simplicity. By adjusting the Fourier coefficients instead of the phase at each pixel, only $2N + 1$ parameters need to be estimated. The phase estimation is therefore simplified, while a degree of smoothness is automatically enforced.

In Chapter 7, three sets of phantom results were presented and analysed. POP was shown to achieve a more accurate phase unwrapping, and therefore fat-water separation, compared to the weighted branch cut and minimum-norm methods. This is especially noticeable in rapidly varying regions of phase where the existing techniques fail. The unweighted branch cut and minimum-norm methods were also shown to perform poorly compared to the weighted methods. In general, the branch cut method produced images containing large streak-like artifacts, whereas the minimum-norm method produced errors which were spread throughout the images in a range of different forms. In comparison, POP produced images where the errors tended to be well-contained near the implant boundary.

In the human study results presented in Chapter 8, POP was also shown to produce a more accurate and reliable fat-water separation than the weighted branch cut and minimum-norm methods. The latter two methods were observed to generate similar artifacts to the phantom results. Across the processed slices for each participant, POP produced images with both a smaller median percentage of artifacts and a smaller variation in the percentage of the image covered with artifacts across multiple slices. POP was also shown to achieve better or comparable fat suppression compared to the default IDEAL algorithm, and significantly better fat suppression compared to the symmetric IDEAL algorithm. This is demonstrated in the illustrated slices and in the results of the analysis performed by the radiologist.

Overall, POP has achieved a superior fat-water separation compared to existing phase unwrapping methods, and better or comparable separation compared to the default IDEAL algorithm. This is validated by the results of the three phantom datasets and the human study.

POP has been extended to be used in conjunction with the VARPRO objective function, with preliminary results shown in Chapter 9. With further development, this method could be used to estimate the resonant frequency variation in images acquired at asymmetric echo times. The performance of the existing IDEAL algorithm was also analysed and shown to perform inconsistently from slice to slice.

The resonant frequency variation simulations described earlier also provided important insight into how POP could be improved. As described in Chapter 10, an analysis of the limitations of the Fourier series at estimating the phase was carried out. This was followed by an investigation into the suitability of using matching pursuit dictionaries to represent the phase. This is an area which requires further study, and is discussed in the following section.

Preliminary phase unwrapping methods concentrated on using an

imperfect model of the resonant frequency variation to simplify the phase unwrapping, and are described in Appendix A. The simulated resonant frequency variations were also essential in developing and evaluating these methods.

▶ ONE MAJOR ADVANTAGE of POP is that errors in the estimated phase shift tend to be restricted to small regions of the image. For example, if the phase is underestimated in a sharp spike along a path, the error is local to this spike. In comparison, errors in the branch cut, minimum-norm, or IDEAL region-growing methods tend to spread throughout the image. This can produce large streaks in regions which have relatively slowly varying phase.

Another key advantage of POP lies in its flexibility. The described method for path generation can be used with a broad range of inner (or implant) and outer boundaries, including with multiple objects in the same slice. The Fourier series, used to model the phase along the paths, can be easily replaced by an alternative set of basis functions. The objective function and optimisation method can also be altered to suit the application. In general, the algorithm provides an adaptable structure for phase estimation, and could potentially be used in a variety of phase unwrapping applications, beyond the three-point Dixon technique.

11.2 SUGGESTED FUTURE WORK

The contributions in this thesis form significant steps towards solving the problem of fat-water separation near metal. However, there are a number of possible developments which would improve the performance of POP, and form interesting research questions. The suggested future work can be separated into two main categories: improvements to the existing POP algorithm, and extending the range of applications of POP.

11.2.1 Improvements to POP

The objective function used for POP, as defined in Eq. 6.17 [1] will have many local minima and is unlikely to be convex. A global minimum of H can be obtained with multiple values of $F^N(r_i)$, so this objective function is not unique. POP assumes that as long as the paths in rapidly varying regions of phase are sufficiently closely spaced, the relative similarity of the phase along adjacent paths generally ensures convergence to the correct solution. However, this assumption may not be valid for regions with steep phase gradients. Also, using the previous path as an estimate for the next path can cause errors to propagate throughout the image, as discussed in Sec. 8.3.

One approach to deal with this issue may involve expanding the phase along a set of radial paths from the implant boundary. The paths which circumnavigate the implant would enforce data smoothness, whereas the radial set would enforce data consistency between

[1] Recall that the objective function used is:

$$H = \sum_{i=1}^{D} |e^{j\Phi(i)} - e^{jF^N(r_i)}|. \quad (11.1)$$

adjacent paths. This would significantly increase the number of parameters required to estimate the phase at each pixel. Alternatively, a more sophisticated global optimisation approach could be used. Finally, a different objective function may improve convergence in areas of steep or discontinuous phase.

The objective function H is a summation, with each value of $|e^{j\phi(i)} - e^{jF^N(r_i)}|$ defined at each pixel along the path. It is also bounded by a maximum value at each pixel, of 2. These two properties could be exploited to identify when the estimated phase $F^N(r_i)$ does not accurately match the data. A thresholding method could be used to identify if failure has occurred over a restricted interval along the path, such as when the value of $|e^{j\phi(i)} - e^{jF^N(r_i)}|$ suddenly increases or reaches its peak value. This could also be used in conjunction with a phase quality map to indicate when the path crosses a discontinuous region of phase [2].

[2] Refer to Sec. 4.5.

There are a number of stages in POP which require manual input and should be automated, as discussed in Sec. 8.3. One way of improving the mask generation process could involve using a phase quality map such as the phase derivative variance. However, by using these maps, there is no way of distinguishing between the region of undersampled phase near the implant boundary, and the implant boundary itself. Additional information, such as data from a MAVRIC-SL acquisition, could also be used. However, this would require the MAVRIC-SL sequence to always be run in the same protocol as the IDEAL sequence, and careful calibration between the slices in the two datasets.

The sensitivity of the final unwrapped phase to the values of the parameters P and N requires further investigation. Currently these parameters are determined manually and empirically. This requirement could be removed by using training datasets to determine a range of acceptable parameter values. To remove the reliance on existing phase unwrapping techniques, a more sophisticated method for estimating the phase along the outer paths is recommended, as discussed in Sec. 8.3.

The described path generation method should be extended to provide better path distribution in the following situations:

- Within the region between multiple objects in the same slice.
- Within sharp concavities along an object boundary. This could be addressed by applying a convex hull to the boundary, and generating the paths inside the concavity in a separate step from those outside it.
- Around objects which are only partially present in the slice. Currently POP requires the outer boundary to fully envelop the inner implant boundary.

Furthermore, the current path generation method may produce paths with common pixels near the implant boundary, particularly with low values of P. This leads to redundancy in the main POP method,

as the phase at pixels along some paths is estimated twice. A better approach would involve ensuring that each pixel is only assigned to one path. Finally, in the case of a slice containing multiple implants, the method described on page 83 for performing the nearest-neighbour mapping between pixels on adjacent sub-paths is inefficient. For every pixel on the new sub-path, all pixels in all sub-paths on the previous level must be checked. A better approach would be to arrange the sub-paths in groups, where all sub-paths "belonging" to the same implant boundary are in the same group.

11.2.2 *Extensions to POP*

POP has been described and demonstrated for 2D images. The unwrapped phase is estimated using a set of 1D functions distributed over each 2D slice. A useful extension would be to extend the algorithm to 3D imaging, as described in Bones et al. [2016]. This could be done by forming a series of closed surfaces, or shells, in the space between the outside surface of the implant and the enclosing boundary of the imaged volume. Each shell would totally enclose the previous one. The outermost shell would be located where the phase is relatively slowly varying, and conventional 2D phase unwrapping would be performed. The estimated unwrapped phase could be represented by spherical harmonic functions over the shell, with a "surface distance" function used to assign approximate polar and azimuthal angle values to voxels lying on the shell. The remaining steps of the algorithm would be directly analogous to those described for 2D images in Sec. 6.3. However, significantly more coefficients would be required for the 2D expansions compared to the 1D Fourier series, with an associated increase in computational effort.

The resonant frequency variation $\Delta f[\mathbf{x}]$ induced by a particular implant can be estimated, and MAVRIC-SL acquisitions can also be used to obtain $\Delta f[\mathbf{x}]$ [3]. In principle a unique model of the resonant frequency variation (and so phase shift) exists for any specific implant. However, it is unlikely that the precise location or material of the implant is known. It is anticipated that there may be alternative ways of using this prior knowledge to guide the objective function minimisation, particularly in areas where the phase gradients are known to have high magnitude.

[3] Recall that these modelling techniques are described in Sec. 2.3.1.

POP should be expanded to a method which can estimate the resonant frequency variation, fat, and water in images which have been acquired using any combination of echo times. Extending POP to estimate the resonant frequency variation in conjunction with VARPRO has been demonstrated in concept, but requires further development. The processing time could be reduced by using a basis function set with fewer parameters, or a different optimisation method. The multipeak model of the fat spectrum may provide valuable assistance in developing a more sophisticated method for estimating the resonant frequency variation.

The feasibility of using matching pursuit or another dictionary learning method to estimate the phase should be explored further. The suitability of other basis function dictionaries should be considered, including Gabor functions and a custom-made dictionary derived from the model phase. The possibility of using matching pursuit in conjunction with VARPRO should also be investigated.

The requirement to estimate the phase derivative in the described application of matching pursuit to POP (Sec. 10.3) could be avoided by taking a linear transform of the signal. The distribution derivative method (DDM) is an algorithm used to estimate the parameters of the signal $s(t)$ which is modelled by

$$s(t) = e^{\sum_{n=1}^{N} \alpha_n p_n(t)}, \tag{11.2}$$

where α_n are the complex parameters and $p_n(t)$ are the real basis functions. DDM transforms the signal to another domain using a linear transform, such as the Fourier or wavelet transforms [Betser, 2009, Hamilton and Depalle, 2012]. The parameter estimation is done in this domain. By exploiting the properties of linear transforms, DDM eliminates the need for signal derivatives, which are often not known. It would be interesting to investigate whether the distribution derivative method can be applied to matching pursuit and POP.

In the current implementation of POP, the effects of image distortion artifacts near metal have been ignored. In reality, near metal the extracted wrapped phase at each pixel is not indicative of the true phase. The ΔB_0 variation causes spins to shift in location in the frequency-encoding and slice-selection directions. Each slice in the acquired Dixon images suffers from in-plane and through-plane distortions, so the extracted phase at each pixel is a summed contribution from the shifted spins. This could be addressed in several ways. First, POP could be extended to 3D (as described above) and combined with an imaging technique such as MAVRIC-SL. Alternatively, the signal models in Eq. 3.15 could be adjusted so the phase is estimated at the same time as correcting for geometric distortion. Such a method would be computationally expensive.

The success of multipoint fat suppression techniques is based on the assumption that fat and water precess at different resonant frequencies, and so have distinct spectral peaks. However, near the boundary of metal the gradient of the resonant frequency variation affecting the spins across a single voxel varies significantly. As described in Smith et al. [2015], this causes a broadening of the fat and water spectral peaks to the point where they appear to be a single, wide peak. The fundamental assumption behind multipoint fat suppression therefore disintegrates in these regions. The ability to achieve truly accurate fat-water separation near metal is limited with imaging sequences which perform frequency encoding (including fast spin echo and multispectral imaging methods) and so single point imaging techniques may be required.

Further clinical testing is required to evaluate the performance of POP. A set of more realistic phantoms could be built, as described in

Sec. 5.6. Only hip replacements were scanned in the human participant study, and all participants were generally healthy with no complications arising from their replacement. A broader study would incorporate participants with complications and a wider range of implants. This may include knee and shoulder replacements, and implants such as screws and plates. A particular emphasis should be made on imaging cobalt-chromium and stainless steel implants, as these produce the largest resonant frequency variations. A more extensive set of imaging scenarios should be considered, including with multiple implants present in the same slice, implants which are situated close to the skin, and implants which only protrude part way into the slice. The performance of POP in conjunction with contrast-enhanced imaging should also be compared with other fat suppression techniques. Finally, a larger clinical study with a greater number of participants would allow for more significant statistical conclusions to be made.

This thesis has focused on developing methods to estimate the phase shift with some degree of prior knowledge. It is recommended that future research addresses the issues raised in this chapter. The ultimate goal should be to further develop POP into a technique which accurately estimates the water, fat, and resonant frequency variation, in a broad range of imaging scenarios, and with minimal distortions in the reconstructed images.

References

Osirix DICOM image library. http://www.osirix-viewer.com/resources/dicom-image-library/. Accessed: 01-11-2016.

MeshLab. http://meshlab.sourceforge.net/, 2014. Version 1.3.3.

Arctec 3D. *Arctec Eva*. Arctec Europe, Luxembourg, 2015.

N.S. Artz, D. Hernando, V. Taviani, A. Samsonov, J.H. Brittain, and S.B. Reeder. Spectrally resolved fully phase-encoded three-dimensional fast spin-echo imaging. *Magnetic Resonance in Medicine*, 71(2):681–690, March 2013.

N.S. Artz, C.N. Wiens, M.R. Smith, D. Hernando, A. Samsonov, and S.B. Reeder. Accelerating fully phase-encoded MRI near metal using multiband radiofrequency excitation. *Magnetic Resonance in Medicine*, 2016.

K. Bartusek, Z. Dokoupil, and E. Gescheidtova. Magnetic field mapping around metal implants using an asymmetric spin-echo MRI sequence. *Measurement Science and Technology*, 17(12):3293–3300, December 2006.

M.A. Bernstein, K.F. King, and X.J. Zhou. Dixon's Method. In *Handbook of MRI Pulse Sequences*, chapter 17.3, pages 857–887. Elsevier, 2004a.

M.A. Bernstein, K.F. King, and X.J. Zhou. Spectrally selective pulses. In *Handbook of MRI Pulse Sequences*, chapter 4.3, pages 115–124. Elsevier, 2004b.

M.A. Bernstein, K.F. King, and X.J. Zhou. Adiabatic excitation pulses. In *Handbook of MRI Pulse Sequences*, chapter 6.1, pages 177–189. Elsevier, 2004c.

M. Bertalmio, G. Sapiro, V. Caselles, and C. Ballester. Image inpainting. In *Proceedings of the 27th International Conference on Computer Graphics and Interactive Techniques*, pages 417–424, 2000.

M. Betser. Sinusoidal polynomial parameter estimation using the distribution derivative. *IEEE Transactions on Signal Processing*, 57 (12):4633–4645, 2009.

T.A. Bley, O. Wieben, C.J. François, J.H. Brittain, and S.B. Reeder. Fat and water magnetic resonance imaging. *Journal of Magnetic Resonance Imaging*, 31(1):4–18, January 2010.

P.J. Bones, L.J. King, and R.P. Millane. Phase estimation for magnetic resonance imaging near metal prostheses. In *Proceedings of the SPIE 9600, Image Reconstruction from Incomplete Data VIII*, 2015.

P.J. Bones, L.J. King, and R.P. Millane. MR imaging near metal: the POP algorithm. In *Proceedings of the 31st International Conference on Image and Vision Computing New Zealand*, 2016.

K. Butts, J.M. Pauly, B.L. Daniel, S. Kee, and A.M. Norbash. Management of biopsy needle artifacts: techniques for RF-refocused MRI. *Journal of Magnetic Resonance Imaging*, 9(4):586–595, April 1999.

K. Butts, J.M Pauly, and G.E. Gold. Reduction of blurring in view angle tilting MRI. *Magnetic Resonance in Medicine*, 53(2):418–424, 2005.

P. Campbell, E. Ebramzadeh, S. Nelson, K. Takamura, K. De Smet, and H. Amstutz. Histological features of pseudotumor-like tissues from metal-on-metal hips. *Clinical Orthopaedics and Related Research*, 468(9):2321–2327, 2010.

H. Chang and J.M. Fitzpatrick. A technique for accurate magnetic resonance imaging in the presence of field inhomogeneities. *IEEE Transactions on Medical Imaging*, 11(3):319–329, January 1992.

Z.H. Cho, D.J. Kim, and Y.K. Kim. Total inhomogeneity correction including chemical shifts and susceptibility by view angle tilting. *Medical Physics*, 15(1):7–11, 1988.

A.R. Conn, N. Gould, and P.L. Toint. *Trust Region Methods*, volume 1. SIAM, 2000.

B.D. Coombs, J. Szumowski, and W. Coshow. Two-point Dixon technique for water-fat signal decomposition with Bo inhomogeneity correction. *Magnetic Resonance in Medicine*, 38(6):884–889, 1997.

M. Costantini. A novel phase unwrapping method based on network programming. *IEEE Transactions on Geoscience and Remote Sensing*, 36(3):813–821, 1998.

C. Cui, X. Wu, J.D. Newell, and M. Jacob. Fat water decomposition using globally optimal surface estimation (GOOSE) algorithm. *Magnetic Resonance in Medicine*, pages 1–11, 2014.

P. Dalla Pria. Evolution and new application of the alumina ceramics in joint replacement. *European Journal of Orthopaedic Surgery and Traumatology*, 17(3):253–256, 2007.

D.L. Davis and J.J. Morrison. Hip arthroplasty pseudotumors: pathogenesis, imaging, and clinical decision making. *Journal of Clinical Imaging Science*, 6, 2016.

J. Dawson, R. Fitzpatrick, A. Carr, and D. Murray. Questionnaire on the perceptions of patients about total hip replacement. *Bone & Joint Journal*, 78(2):185–190, 1996.

J. Dawson, R. Fitzpatrick, D. Murray, and A. Carr. Questionnaire on the perceptions of patients about total knee replacement. *Bone & Joint Journal*, 80(1):63–69, 1998.

F. Del Grande, F. Santini, D. Herzka, M.R. Aro, C.W. Dean, G.E. Gold, and J. Carrino. Fat-suppression techniques for 3-T MR imaging of the musculoskeletal system. *RadioGraphics*, 34(1):217–233, 2014.

E.M. Delfaut, J. Beltran, G. Johnson, Rousseau J., X. Marchandise, and A. Cotten. Fat suppression in MR imaging: techniques and pitfalls. *RadioGraphics*, 19:373–382, 1999.

J. D'Errico. *Inpaint NaNs*. https://au.mathworks.com/matlabcentral/fileexchange/4551-inpaint-nans, 2014. Accessed: 15-10-2015.

W.T. Dixon. Simple proton spectroscopic imaging. *Radiology*, 153: 189–194, 1984.

D.L. Donoho, M. Elad, and V.N. Temlyakov. Stable recovery of sparse overcomplete representations in the presence of noise. *IEEE Transactions on Information Theory*, 52(1):6–18, 2006.

T.J. Flynn. Two-dimensional phase unwrapping with minimum weighted discontinuity. *Journal of the Optical Society of America*, 14 (10):2692–2701, 1997.

J. Gallo, P. Kamínek, V. Tichá, P. Riháková, and R. Ditmar. Particle disease. A comprehensive theory of periprosthetic osteolysis: a review. *Biomedical Papers*, 146(2):21–28, 2002.

D.S. Garbuz, B.A. Hargreaves, C.P. Duncan, B.A. Masri, D.R. Wilson, and B.B. Forster. The John Charnley award: Diagnostic accuracy of MRI versus ultrasound for detecting pseudotumors in asymptomatic metal-on-metal THA. *Clinical Orthopaedics and Related Research*, 472(2):417–423, 2014.

D.C. Ghiglia and M.D. Pritt. *Two-Dimensional Phase Unwrapping. Theory, Algorithms and Software*. Wiley, 1998a.

D.C. Ghiglia and M.D. Pritt. Path-following methods. In *Two-Dimensional Phase Unwrapping. Theory, Algorithms and Software*, chapter 4, pages 100–176. Wiley, 1998b.

D.C. Ghiglia and M.D. Pritt. Line integrals, residues, and 2D phase unwrapping. In *Two-Dimensional Phase Unwrapping. Theory, Algorithms and Software*, pages 32–58. Wiley, 1998c.

D.C. Ghiglia and L.A. Romero. Robust two-dimensional weighted and unweighted phase unwrapping that uses fast transforms and iterative methods. *Journal of the Optical Society of America A*, 11(1): 107–116, January 1994.

G.H. Glover and E. Schneider. Three-point Dixon technique for true water/fat decomposition with Bo inhomogeneity correction. *Magnetic Resonance in Medicine*, 18:371–383, 1991.

R.M. Goldstein, H.A. Zebker, and C.L. Warner. Satellite radar interferometry: two-dimensional phase unwrapping. *Radio Science*, 23 (4):713–720, 1988.

G. Golub and V. Pereyra. Separable nonlinear least squares: the variable projection method and its applications. *Inverse Problems*, 19(2):R1–R26, 2003.

E.M. Haacke, R.W. Brown, M.R. Thompson, and R. Venkatesan. Magnetic properties of tissues: theory and measurement. In *Magnetic Resonance Imaging: Physical Priciples and Sequence Design*, chapter 25, pages 741–781. Wiley, New York, 1999.

B. Hamilton and P. Depalle. A unified view of non-stationary sinusoidal parameter estimation methods using signal derivatives. *Proceedings of the IEEE International Conference on Acoustics, Speech and Signal Processing*, (1):369–372, 2012.

B.A. Hargreaves, W. Chen, W. Lu, M.T. Alley, G.E. Gold, A.C. Brau, J.M. Pauly, and K.B. Pauly. Accelerated slice encoding for metal artifact correction. *Journal of Magnetic Resonance Imaging*, 31(4):987–996, April 2010.

B.A. Hargreaves, P.W. Worters, K.B. Pauly, J.M. Pauly, K.M. Koch, and G.E. Gold. Metal-induced artifacts in MRI. *American Journal of Roentgenology*, 197(3):547–555, September 2011.

D. Hernando, J.P. Haldar, B.P. Sutton, J. Ma, P. Kellman, and Z.-P. Liang. Joint estimation of water/fat images and field inhomogeneity map. *Magnetic Resonance in Medicine*, 59(3):571–580, March 2008.

D. Hernando, K.M. Koch, K.F. King, and Z.-P. Liang. Generalized reconstruction of multi-spectral MR acquisitions for imaging near metal implants. In *Proceedings of the ISMRM*, volume 17, page 2860, 2009.

D. Hernando, P. Kellman, J.P. Haldar, and Z.-P. Liang. Robust water/fat separation in the presence of large field inhomogeneities using a graph cut algorithm. *Magnetic Resonance in Medicine*, 63(1): 79–90, 2010a.

D. Hernando, Z.-P. Liang, and P. Kellman. Chemical shift-based water/fat separation: a comparison of signal models. *Magnetic Resonance in Medicine*, 64(3):811–822, September 2010b.

T.J. Heyse, L.R. Chong, J. Davis, F. Boettner, S.B. Haas, and H.G. Potter. MRI analysis of the component-bone interface after TKA. *The Knee*, 19(4):290–294, August 2012.

G. Hooper. The ageing population and the increasing demand for joint replacement. *Journal of the New Zealand Medical Association*, 126(1377), 2013.

B.R. Hunt. Matrix formulation of the reconstruction of phase values from phase differences. *Journal of the Optical Society of America*, 69 (3):393–399, March 1979.

S.S. Kaushik, A. Gaddipati, B.A. Hargreaves, D. Gui, R. Peters, T. Muftuler, and K. Koch. Clinically viable diffusion-weighted imaging near metal using 2D-MSI PROPELLER DUO. In *Proceedings of the ISMRM*, volume 24, page 370, 2016.

L.J. King, R.P. Millane, and P.J. Bones. Phase unwrapping for magnetic resonance imaging near metal prostheses. In *Proceedings of the 29th International Conference on Image and Vision Computing New Zealand*, pages 124–129, 2014.

L.J. King, R.P. Millane, and P.J. Bones. Phase unwrapping near metal implants with prior knowledge of the implant geometry. In *Proceedings of the ISMRM*, volume 23, 2015.

L.J. King, R.P. Millane, H. Weber, B.A. Hargreaves, and P.J. Bones. Path-based estimation for fat suppression near metal implants. In *Proceedings of the ISMRM*, volume 24, 2016.

K.M. Koch and R.S. Hinks. Empirical and computed Bo perturbations induced by metallic implants. In *Proceedings of the ISMRM*, volume 16, page 1180, 2008.

K.M. Koch and K.F. King. Combined parallel imaging and compressed sensing on 3D multi-spectral imaging near metal implants. In *Proceedings of the ISMRM*, volume 19, page 19, 2011.

K.M. Koch, X. Papademetris, D.L. Rothman, and R.A. de Graaf. Rapid calculations of susceptibility-induced magnetostatic field perturbations for in vivo magnetic resonance. *Physics in Medicine and Biology*, 51(24):6381–6402, December 2006.

K.M. Koch, J.E. Lorbiecki, R.S. Hinks, and K.F. King. A multispectral three-dimensional acquisition technique for imaging near metal implants. *Magnetic Resonance in Medicine*, 61(2):381–390, February 2009.

K.M. Koch, B.A. Hargreaves, K. Butts Pauly, W. Chen, G.E. Gold, and K.F. King. Magnetic resonance imaging near metal implants. *Journal of Magnetic Resonance Imaging*, 32(4):773–787, October 2010.

K.M. Koch, A.C. Brau, W. Chen, G.E. Gold, B.A. Hargreaves, M. Koff, G.C. McKinnon, H.G. Potter, and K.F. King. Imaging near metal with a MAVRIC-SEMAC hybrid. *Magnetic Resonance in Medicine*, 65(1):71–82, January 2011a.

K.M. Koch, K.F. King, W. Chen, G.E. Gold, and B.A. Hargreaves. Frequency encoding in the presence of extreme static field gradients. In *Proceedings of the ISMRM*, volume 19, page 293, 2011b.

K.M. Koch, K.F. King, M.F. Koff, and H.G. Potter. Metallic implant reconstruction from MAVRIC Bo field maps. In *Proceedings of the ISMRM*, volume 21, 2013.

S.H. Kolind, A.L. MacKay, P.L. Munk, and Q-S. Xiang. Quantitative evaluation of metal artifact reduction techniques. *Journal of Magnetic Resonance Imaging*, 20(3):487–495, September 2004.

S. Kurtz, F. Mowat, K. Ong, N. Chan, E. Lau, and M. Halpern. Prevalence of primary and revision total hip and knee arthroplasty in the United States from 1990 through 2002. *Journal of Bone and Joint Surgery*, 87(7):1487–1497, July 2005.

S. Kurtz, K. Ong, E. Lau, F. Mowat, and M. Halpern. Projections of primary and revision hip and knee arthroplasty in the United States from 2005 to 2030. *Journal of Bone and Joint Surgery*, 89(4): 780–785, 2007.

G. Labek, M. Thaler, W. Janda, M. Agreiter, and B. Stöckl. Revision rates after total joint replacement: cumulative results from worldwide joint register datasets. *Journal of Bone and Joint Surgery*, 93(3): 293–297, March 2011.

M.J. Lee, D.L. Janzen, P.L. Munk, A. MacKay, Q.S. Xiang, and A. McGowen. Quantitative assessment of an MR technique for reducing metal artifact: application to spin-echo imaging in a phantom. *Skeletal Radiology*, 30(7):398–401, July 2001.

A. Leone, C. Distante, N. Ancona, K.C. Persaud, E. Stella, and P. Siciliano. A powerful method for feature extraction and compression of electronic nose responses. *Sensors and Actuators B: Chemical*, 105 (2):378–392, 2005.

Z.-P. Liang. A model-based method for phase unwrapping. *IEEE Transactions on Medical Imaging*, 15(6):893–897, 1996.

W. Lu, K. Butts Pauly, G.E. Gold, J.M. Pauly, and B.A. Hargreaves. SEMAC: Slice Encoding for Metal Artifact Correction in MRI. *Magnetic Resonance in Medicine*, 62(1):66–76, July 2009.

J. Ma. Dixon techniques for water and fat imaging. *Journal of Magnetic Resonance Imaging*, 28(3):543–558, 2008.

S.G. Mallat and Z. Zhang. Matching pursuits with time-frequency dictionaries. *IEEE Transactions on Signal Processing*, 41(12):3397–3415, 1993.

J.P. Marques and R. Bowtell. Application of a Fourier-based method for rapid calculation of field inhomogeneity due to spatial variation of magnetic susceptibility. *Concepts in Magnetic Resonance Part B: Magnetic Resonance Engineering*, 25B(1):65–78, April 2005.

MATLAB. *Version 8.6 (R2015b)*. The MathWorks Inc., Natick, Massachusetts, 2015.

D.W. McRobbie, E.A. Moore, M.J. Graves, and M.R. Prince. *MRI from Picture to Proton*. Cambridge University Press, New York, 2 edition, 2006a.

D.W. McRobbie, E.A. Moore, M.J. Graves, and M.R. Prince. Susceptibility and metal artifacts. In *MRI From Picture to Proton*, chapter 6.8, pages 101–103. Cambridge University Press, New York, 2 edition, 2006b.

M.D. Mitchell, H.L. Kundel, P.M. Joseph, and L. Axel. Agarose as a tissue equivalent material. *Magnetic Resonance Imaging*, 4:263–266, 1986.

P.S. Morgan, R.W. Bowtell, D.J.O. McIntyre, and B.S. Worthington. Correction of spatial distortion in EPI due to inhomogeneous static magnetic fields using the reversed gradient method. *Journal of Magnetic Resonance Imaging*, 19(4):499–507, April 2004.

G. Nico, G. Palubinskas, and M. Datcu. Bayesian approaches to phase unwrapping: theoretical study. *IEEE Transactions on Signal Processing*, 48(9):2545–2556, 2000.

D.G. Nishimura. *Principles of Magnetic Resonance Imaging*. Department of Electrical Engineering, Stanford University, 1995a.

D.G. Nishimura. Inversion Recovery. In *Principles of Magnetic Resonance Imaging*, pages 157–159. Department of Electrical Engineering, Stanford University, 1995b.

D.P. O'Leary and B.W. Rust. Variable projection for nonlinear least squares problems. *Computational Optimization and Applications*, 54 (3):579–593, 2013.

Orchestra. *Version 1.4-722*. General Electric Healthcare, Milwaukee, Wisconsin, 2015.

OsiriX. *OsiriX Lite*. Pixmeo SARL, Geneva, Switzerland, 2015.

S. Ostlere. How to image metal-on-metal prostheses and their complications. *American Journal of Roentgenology*, 197(3):558–567, 2011.

S. Patil and B. Ravi. Voxel-based representation, display and thickness analysis of intricate shapes. In *Proceedings of the Ninth International Conference on Computer Aided Design and Computer Graphics*, pages 415–420, 2005.

B. Quist, X. Shi, H. Weber, and B.A. Hargreaves. Improved field-map estimation and deblurring for MAVRIC-SL. In *Proceedings of the ISMRM*, volume 24, page 4241, 2016.

P. Ramos-Cabrer, J.P.M. van Duynhoven, A. Van der Toorn, and K. Nicolay. MRI of hip prostheses using single-point methods: in vitro studies towards the artifact-free imaging of individuals with metal implants. *Magnetic Resonance Imaging*, 22(8):1097–1103, October 2004.

S.B. Reeder, Z. Wen, H. Yu, A.R. Pineda, G.E. Gold, M. Markl, and N.J. Pelc. Multicoil Dixon chemical species separation with an iterative least-squares estimation method. *Magnetic Resonance in Medicine*, 51(1):35–45, January 2004.

S.B. Reeder, A.R. Pineda, Z. Wen, A. Shimakawa, H. Yu, J.H. Brittain, G.E. Gold, C.H. Beaulieu, and N.J. Pelc. Iterative decomposition of water and fat with echo asymmetry and least-squares estimation (IDEAL): application with fast spin-echo imaging. *Magnetic Resonance in Medicine*, 54(3):636–644, September 2005.

R. Salomir, B.D. De Senneville, and C.T.W. Moonen. A fast calculation method for magnetic field inhomogeneity due to an arbitrary distribution of bulk susceptibility. *Concepts in Magnetic Resonance Part B: Magnetic Resonance Engineering*, 19(1):26–34, 2003.

J.F. Schenck. The role of magnetic susceptibility in magnetic resonance imaging: MRI magnetic compatibility of the first and second kinds. *Medical Physics*, 23(6):815, 1996.

S.D. Sharma, N.S. Artz, D. Hernando, D.E. Horng, and S.B. Reeder. Improving chemical shift encoded water-fat separation using object-based information of the magnetic field inhomogeneity. *Magnetic Resonance in Medicine*, 73:597–604, 2015.

F.G. Shellock. Magnetic resonance safety update 2002: implants and devices. *Journal of Magnetic Resonance Imaging*, 16(5):485–496, 2002.

X. Shi, E.G. Levine, and B.A. Hargreaves. Accelerated imaging of metallic implants using model-based nonlinear reconstruction. In *Proceedings of the ISMRM*, volume 24, page 47, 2016.

S. Skare and J.L.R. Andersson. Correction of MR image distortions induced by metallic objects using a 3D cubic B-spline basis set: application to stereotactic surgical planning. *Magnetic Resonance in Medicine*, 54(1):169–181, July 2005.

T.E. Skinner and G.H. Glover. An extended two-point Dixon algorithm for calculating separate water, fat, and Bo images. *Magnetic Resonance in Medicine*, 37(4):628–630, April 1997.

M.R. Smith, N.S. Artz, K.M. Koch, A. Samsonov, and S.B. Reeder. Accelerating sequences in the presence of metal by exploiting the spatial distribution of off-resonance. *Magnetic Resonance in Medicine*, 72(6):1658–1667, 2014.

M.R. Smith, N.S. Artz, C. Wiens, D. Hernando, and S.B. Reeder. Characterizing the limits of MRI near metallic prostheses. *Magnetic Resonance in Medicine*, 74:1564–1573, 2015.

P. Stradiotti, A. Curti, G. Castellazzi, and A. Zerbi. Metal-related artifacts in instrumented spine. Techniques for reducing artifacts in CT and MRI: state of the art. *European Spine Journal*, 18(1):102–108, 2009.

S. Stramaglia, A. Refice, and L. Guerriero. Statistical mechanics approach to the phase unwrapping problem. *Physica A: Statistical Mechanics and its Applications*, 276(3):521–534, 2000.

A.P. Toms, T.J. Marshall, J. Cahir, C. Darrah, J. Nolan, S.T. Donell, T. Barker, and J.K. Tucker. MRI of early symptomatic metal-on-metal total hip arthroplasty: a retrospective review of radiological findings in 20 hips. *Clinical Radiology*, 63(1):49–58, January 2008.

I. Tosic and P. Frossard. Dictionary learning. *IEEE Signal Processing Magazine*, 28(2):27–38, 2011.

J.E. Vandevenne, F.M. Vanhoenacker, P.M. Parizel, K. Butts, and P.K. Lang. Reduction of metal artifacts in musculoskeletal MR imaging. *JBR-BTR*, 90(5):345–349, 2007.

R.D. Venook, N.I. Matter, M. Ramachandran, S.E. Ungersma, G.E. Gold, N.J. Giori, A. Macovski, G.C. Scott, and S.M. Conolly. Prepolarized magnetic resonance imaging around metal orthopedic implants. *Magnetic Resonance in Medicine*, 56(1):177–186, July 2006.

J.M. Verburg and J. Seco. CT metal artifact reduction method correcting for beam hardening and missing projections. *Physics in Medicine and Biology*, 57(9):2803–2818, 2012.

A.M. Viano, S.A. Gronemeyer, M. Haliloglu, and F.A. Hoffer. Improved MR imaging for patients with metallic implants. *Magnetic Resonance Imaging*, 18(3):287–295, April 2000.

L.M. White, J.K. Kim, M. Mehta, N. Merchant, M.E. Schweitzer, W.B. Morrison, C.R. Hutchison, and A.E. Gross. Complications of total hip arthroplasty: MR imaging-initial experience. *Radiology*, 215(1): 254–262, April 2000.

P.W. Worters, K. Sung, K.J. Stevens, K.M. Koch, and B.A. Hargreaves. Compressed sensing multispectral imaging of the postoperative spine. *Journal of Magnetic Resonance Imaging*, 37:243–248, 2012.

L. Ying, Z.P. Liang, D.C. Munson, R. Koetter, and B.J. Frey. Unwrapping of MR phase images using a Markov random field model. *IEEE Transactions on Medical Imaging*, 25(1):128–136, 2006.

H. Yu, S.B. Reeder, A. Shimakawa, J.H. Brittain, and N.J. Pelc. Field map estimation with a region growing scheme for iterative 3-point water-fat decomposition. *Magnetic Resonance in Medicine*, 54(4): 1032–1039, October 2005.

H. Yu, C.A. McKenzie, A. Shimakawa, A.T. Vu, A.C. Brau, P.J. Beatty, A.R. Pineda, J.H. Brittain, and S.B. Reeder. Multiecho reconstruction for simultaneous water-fat decomposition and T2* estimation. *Journal of Magnetic Resonance Imaging*, 26(4):1153–1161, October 2007.

H. Yu, A. Shimakawa, C.A. McKenzie, E. Brodsky, J.H. Brittain, and S.B. Reeder. Multiecho water-fat separation and simultaneous R2* estimation with multifrequency fat spectrum modeling. *Magnetic Resonance in Medicine*, 60(5):1122–1134, November 2008.

H. Yu, S.B. Reeder, A. Shimakawa, C.A. McKenzie, and J.H. Brittain. Robust multipoint water-fat separation using fat likelihood analysis. *Magnetic Resonance in Medicine*, 67(4):1065–1076, April 2012.

A

Methods for Reducing Phase Unwrapping Complexity

This chapter describes three techniques to reduce the complexity of the phase unwrapping in the three-point Dixon technique using prior knowledge of the phase shift. It is attached as an appendix as it constitutes preliminary work carried out before the development of POP.

▶ In general, the phase shift can be expressed as

$$\phi[\mathbf{x}] = \phi_M[\mathbf{x}] + \epsilon[\mathbf{x}], \tag{A.1}$$

where $\phi_M[\mathbf{x}]$ is an imperfect model of the phase shift and $\epsilon[\mathbf{x}]$ is the residual error in the model. Instead of estimating $\phi[\mathbf{x}]$ from the wrapped values $\phi_w[\mathbf{x}]$, the phase unwrapping problem is converted to estimating the model error $\epsilon[\mathbf{x}]$,

$$\epsilon[\mathbf{x}] = \phi[\mathbf{x}] - \phi_M[\mathbf{x}]. \tag{A.2}$$

This is done by removing the contribution by the model to the phase $\phi[\mathbf{x}]$, before extracting the wrapped phase,

$$\alpha[\mathbf{x}] = e^{j\epsilon[\mathbf{x}]} = e^{j\phi[\mathbf{x}]}e^{-j\phi_M[\mathbf{x}]}. \tag{A.3}$$

The model error can be extracted by taking the phase of $\alpha[\mathbf{x}]$. This produces a wrapped estimate of the residual, $\epsilon_w[\mathbf{x}]$. If the model is sufficiently close to the true phase, $\epsilon[\mathbf{x}]$ is slowly varying and can be estimated from $\epsilon_w[\mathbf{x}]$ using existing two-dimensional phase unwrapping techniques.

▶ Figure A.1(a) shows the simulated phase induced by a cobalt-chromium acetabular shell. This was obtained using the STL geometry of the Implant 1 acetabular shell. In this section, this is the "true phase", $\phi[\mathbf{x}]$. The shell is then displaced and rotated from its original position. This introduces error in the simulated phase, as shown in Fig. A.1(b). This is the imperfect "model phase", $\phi_M[\mathbf{x}]$. Figure

A.2 shows the wrapped phase extracted from Fig. A.1(a) and the wrapped residual. In this section 2D $x-z$ slices are considered. For simplicity, it is assumed that the geometry of the implant is known exactly but the position is not.

By considering the number of phase wraps E in the wrapped phase, it can be observed from Fig. A.2 that removing the model simplifies the phase unwrapping required [1]. There are 2903 phase wraps in the wrapped phase $\phi_w[x,z]$, compared with 1722 in the wrapped residual $\epsilon_w[x,z]$.

[1] Recall that a measure of the complexity of 2D phase unwrapping is obtained by calculating the number of phase wraps, E, in an image. This is defined by Eq. 4.13.

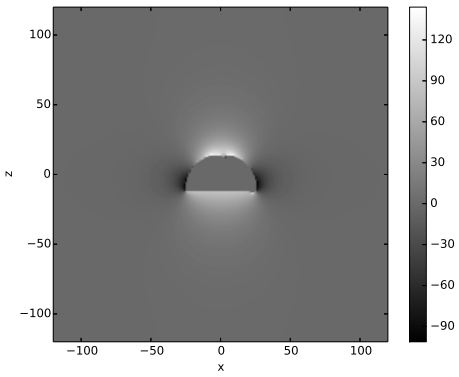

(a) True phase shift in radians.

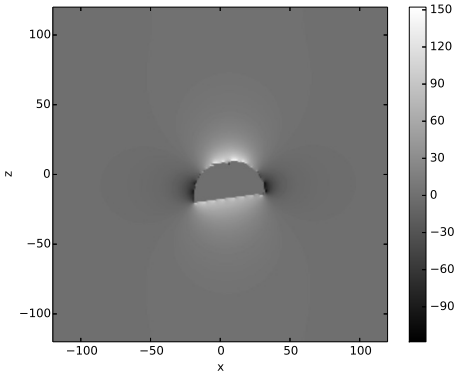

(b) Model phase shift in radians.

Figure A.1: Simulated true phase shift and corresponding imperfect model. The model implant is offset from the true implant by $\Delta x = 5$ mm, $\Delta z = -4$ mm, and $\Delta\theta = 8°$.

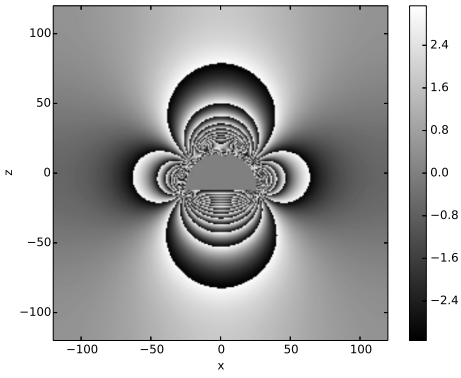

(a) Extracted, wrapped phase.

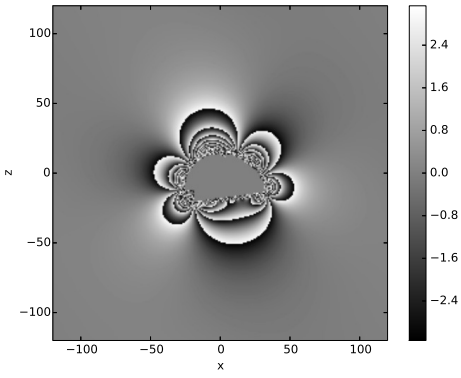

(b) Extracted, wrapped residual.

Figure A.2: Comparison between phase wrapping complexity without a model (a) and with a model (b).

A.1 MODEL ERROR DERIVATIVE

By removing the model from the true phase, the unwrapping is reduced to estimating the model error $\epsilon[x, z]$. However, if the model is not well fitted to the true phase, the residual gradient $\Delta\epsilon[x, z]$ may exceed $|\pi|$/pixel and standard phase unwrapping does not succeed as the residual is undersampled. This section describes a method for unwrapping the undersampled residual with a poorly fitted model.

Instead of extracting the model error $\epsilon[x, z]$ directly from Eq. A.3, $\alpha[x, z]$ can be manipulated to extract the derivative of $\epsilon[x, z]$. Using finite differences, the first order derivatives of $\epsilon[x, z]$ can be approximated on a pixel-by-pixel basis as:

$$\frac{\partial \epsilon}{\partial x} \approx \Delta\epsilon^x[x, z] = \epsilon[x + 1, z] - \epsilon[x, z] \tag{A.4}$$

$$\frac{\partial \epsilon}{\partial z} \approx \Delta\epsilon^z[x, z] = \epsilon[x, z + 1] - \epsilon[x, z]. \tag{A.5}$$

Substituting Eq. A.4 into Eq. A.3 gives

$$e^{j\Delta\epsilon^x[x,z]} = e^{j\epsilon[x+1,z]}e^{-j\epsilon[x,z]} \tag{A.6}$$

$$e^{j\Delta\epsilon^x[x,z]} = \alpha[x + 1, z]\alpha[x, z]^*, \tag{A.7}$$

where $*$ denotes the complex conjugate. The derivative of the model error in the x-direction can be estimated by evaluating Eq. A.7 and then extracting the phase. The derivative in the z-direction can be estimated in a similar manner. This gives wrapped estimates of the derivatives, $\Delta\epsilon^x_w[x, z]$ and $\Delta\epsilon^z_w[x, z]$, as the true derivative of $\epsilon[x, z]$ exceeds the range $[-\pi, \pi]$.

The wrapped derivatives $\Delta\epsilon^x_w[x, z]$ and $\Delta\epsilon^z_w[x, z]$ can be unwrapped using standard methods, including branch cut and minimum-norm algorithms. A weighted method is necessary to avoid unwrapping across the discontinuity present at the implant boundary. Once an unwrapped estimate of $\Delta\epsilon^x[x, z]$ and $\Delta\epsilon^z[x, z]$ is obtained, path integration is used to calculate an accurate, smooth estimate of the model error $\epsilon[x, z]$. This can then be added to the model $\phi_M[x, z]$ to estimate the true phase shift $\phi[x, z]$, as given in Eq. A.1.

▶ METHOD OVERVIEW

The described method can be summarised by the following steps:

1. Model the expected phase shift near the implant, using the estimated size, shape, location, and material of the object.
2. Subtract the model ϕ_M from the phase shift using Eq. A.3.
3. Estimate the derivative of the model error using Eq. A.7.
4. Extract the phase of Eq. A.7 to get $\Delta\epsilon^x_w[x, z]$ (and similarly for $\Delta\epsilon^z_w[x, z]$).
5. Unwrap $\Delta\epsilon^x_w[x, z]$ and $\Delta\epsilon^z_w[x, z]$.

6. Integrate $\Delta\epsilon^x[x,z]$ and $\Delta\epsilon^z[x,z]$ to get $\epsilon[x,z]$.

7. Add $\epsilon[x,z]$ to the model, as shown in Eq. A.1.

- FIGURE A.3(A) SHOWS the wrapped derivative of the residual, obtained from Fig. A.2(b). Figure A.3(b) shows the unwrapped derivative of the residual, calculated using a branch cut phase unwrapping algorithm. Figure A.4 shows the wrapped and unwrapped residual derivative for the central slice of Phantom 1.

- THIS METHOD IS AN EFFICIENT APPROACH for unwrapping an undersampled phase shift with the guidance of a model. By removing the model from the phase, and extracting the derivative of the model error, the phase unwrapping is simplified. However, although the proposed method reduces the severity of the phase wrapping and number of phase wraps, it also amplifies the noise present during the phase unwrapping process. This is due to two reasons. First, removing the model from the true phase shift reduces the amplitude of the phase, but the level of noise remains the same. This effectively reduces the SNR of $\epsilon[x,z]$. Second, taking the derivative of $\epsilon[x,z]$ amplifies the noise present, further reducing the SNR of $\epsilon[x,z]$. Using the finite differences method to calculate the derivative of the residual also amplifies errors and noise. A better approach would be to use the derivative property of the Fourier transform, as described in Sec. 10.3.

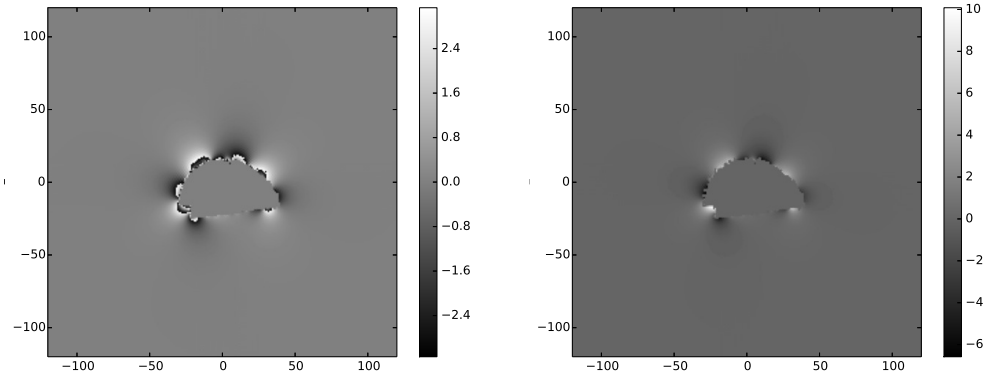

(a) Extracted, wrapped derivative of the residual

(b) Unwrapped derivative of the residual

Figure A.3: Wrapped residual derivative $\Delta\epsilon^x_w[x,z]$ (a) and unwrapped residual derivative $\Delta\epsilon^x[x,z]$ (b).

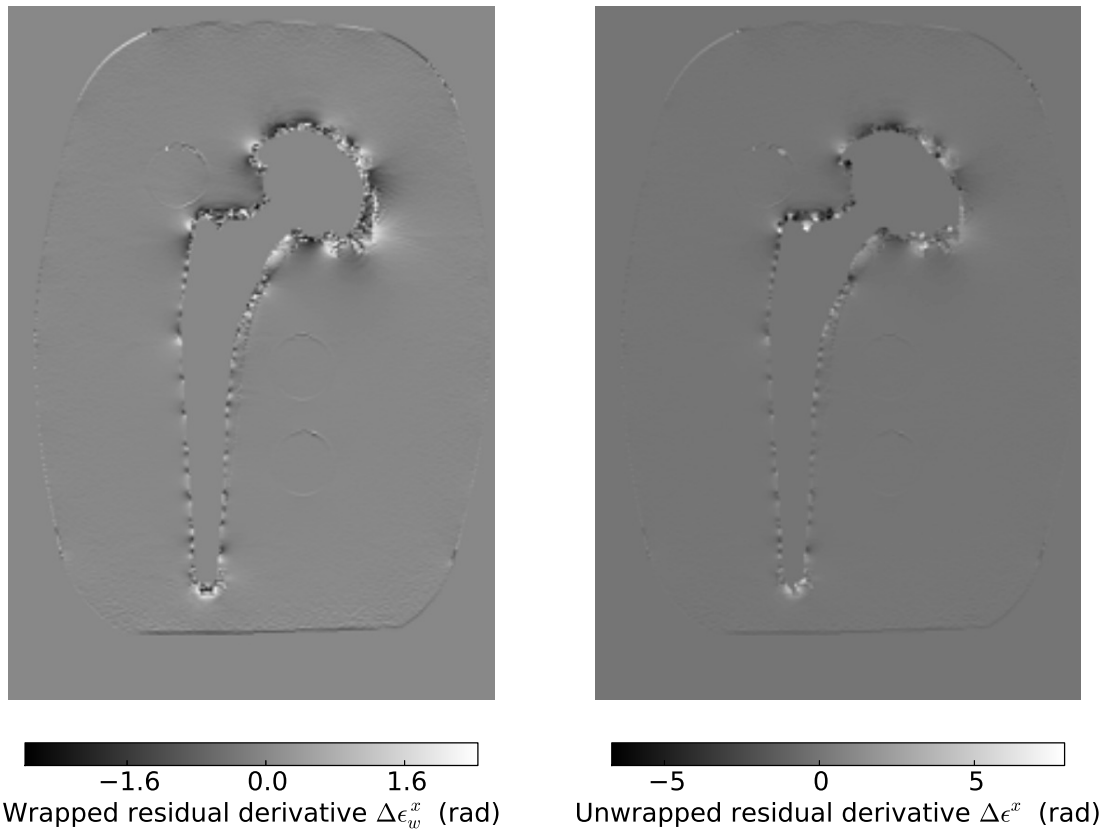

(a) (b)

Figure A.4: Wrapped residual derivative $\Delta\epsilon_w^x[x,z]$ (a) and unwrapped residual derivative $\Delta\epsilon^x[x,z]$ (b) for the central slice of Phantom 1.

A.2 MODEL ADJUSTMENT

If the model is poorly fitted, the wrapped residual is undersampled and it is necessary to use the derivative of the residual, as described in the previous section. In this section an alternative approach is described, where the initial model is iteratively adapted so it has a better fit to the true phase. The aim is to find the model which minimises the number of discontinuities or phase wraps, E, in the residual. For simplification, only two-dimensional (or translational) adjustment is considered.

The initial model shape is translated and rotated before voxelisation. In 3D, the position $\mathbf{x}$ and orientation θ of an object with known geometry can be described by six parameters: $\mathbf{x} = [x, y, z], \theta = [\theta_x, \theta_y, \theta_z]$. These parameters can be translated by Δx, Δy, and Δz, and rotated by $\Delta\theta_x$, $\Delta\theta_y$, and $\Delta\theta_z$ using affine transforms. This is done by multiplying the STL coordinates by the following affine transform matrices,

$$
\begin{aligned}
T &= \begin{bmatrix} 1 & 0 & 0 & \Delta x \\ 0 & 1 & 0 & \Delta y \\ 0 & 0 & 1 & \Delta z \end{bmatrix} \\
R_x &= \begin{bmatrix} 1 & 0 & 0 & 0 \\ 0 & \cos(\theta_x) & -\sin(\theta_x) & 0 \\ 0 & \sin(\theta_x) & \cos(\theta_x) & 0 \\ 0 & 0 & 0 & 1 \end{bmatrix} \\
R_y &= \begin{bmatrix} \cos(\theta_y) & 0 & \sin(\theta_y) & 0 \\ 0 & 1 & 0 & 0 \\ \sin(\theta_y) & 0 & \cos(\theta_y) & 0 \\ 0 & 0 & 0 & 1 \end{bmatrix} \\
R_z &= \begin{bmatrix} \cos(\theta_z) & -\sin(\theta_z) & 0 & 0 \\ \sin(\theta_z) & \cos(\theta_z) & 0 & 0 \\ 0 & 0 & 1 & 0 \\ 0 & 0 & 0 & 1 \end{bmatrix}.
\end{aligned}
\tag{A.8}
$$

T is the translation matrix and R_x, R_y, and R_z are the rotation matrices about the x, y, and z axes, respectively. The transformations can be applied in succession by multiplying the object coordinates by the following matrix

$$M = TR_xR_yR_z. \tag{A.9}$$

▶ FOR SIMPLIFICATION, it is initially assumed that y, θ_x, and θ_z is known exactly, but we only have approximate knowledge of the 2D position x, z, and orientation θ_y. This reduces the number of parameters to refine to three. The imperfect model of the phase shift, ϕ_M, is generated by simulating an implant which is offset from the true position of the object (x_t, z_t, θ_t) by Δx, Δz, and $\Delta\theta_y$. For example, Fig. A.6 shows the residual extracted using an initial model with an offset of $\Delta x = -8.1$ mm, $\Delta z = 1$ mm, and $\Delta\theta_y = 4.8^o$ from the true object position. The wrapped phase has been extracted from simu-

lated images with a SNR of 10 dB. There are 2345 discontinuities in the residual.

The imperfect model is iteratively adjusted by Δx, Δz, and $\Delta\theta_y$ to find the model parameter values x, z, and θ_y which minimise the number of discontinuities E in ϵ_w. E is calculated by evaluating Eq. 4.13 for each new model. A coarse grid search is used to find an approximate set of parameters which produce the lowest number of phase wraps. This is refined using a series of grids, each with a finer resolution than the previous.

Figure A.7 shows ϵ_w after adjusting the model in Fig. A.6 using a grid search. The final estimate of the parameters is $\Delta x = 0.1$ mm, $\Delta z = 0.1$ mm, and $\Delta\theta_y = -0.3^o$. There are 20 discontinuities in this residual. The wrapped phase with no model is shown for reference in Fig. A.5. There are 4640 discontinuities in this figure. These three figures show that modifying the model to better fit the true phase significantly reduces the complexity of the phase unwrapping required.

However, if the model phase is not well-fitted to the true phase, this method can introduce discontinuities at pixels where there were previously none. Figure A.8 shows the wrapped phase for the central slice of Phantom 1, with the implant and outer masks applied. There are 5774 discontinuities in this figure. Figure A.9 shows the wrapped residual acquired using the initial model phase, with 5374 discontinuities present. Finally, Fig. A.10 shows the wrapped residual with the adjusted model, with 4452 discontinuities. Although this method has reduced the phase unwrapping required in the outer regions of the slice, near the implant boundary, numerous phase wraps have been introduced due to the inclusion of the model. This increases the difficulty of the phase unwrapping required in these regions.

It should be noted that the residual in Fig. A.9 indicates that the simulated model phase is not well-fitted to the measured Phantom 1 phase. This may be due to two main reasons. First, it is likely that the 3D orientation of the STL model geometry was not correctly aligned with the orientation of the implant in the phantom. Second, the estimated susceptibility value used in the simulated model phase may have been different to the true susceptibility of the implant.

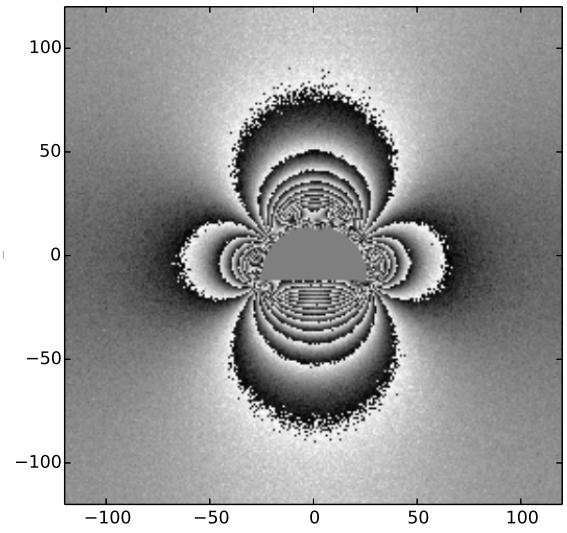

Figure A.5: Extracted wrapped phase with no model.

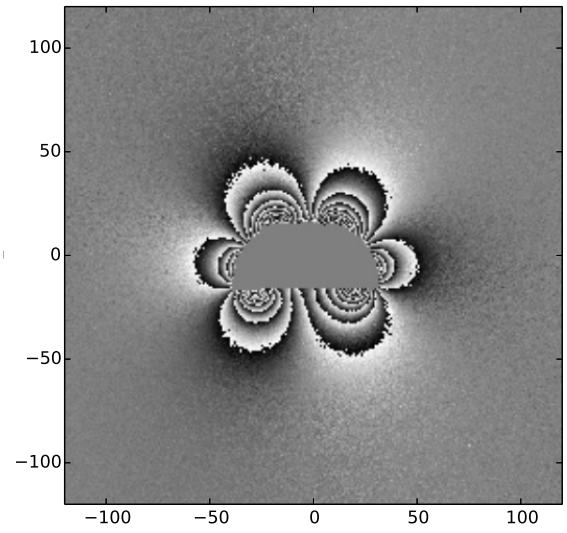

Figure A.6: Wrapped residual with initial imperfect model offset by $\Delta x = 8.1\,\text{mm}$, $\Delta z = 1\,\text{mm}$, and $\Delta\theta_y = 4.8^o$.

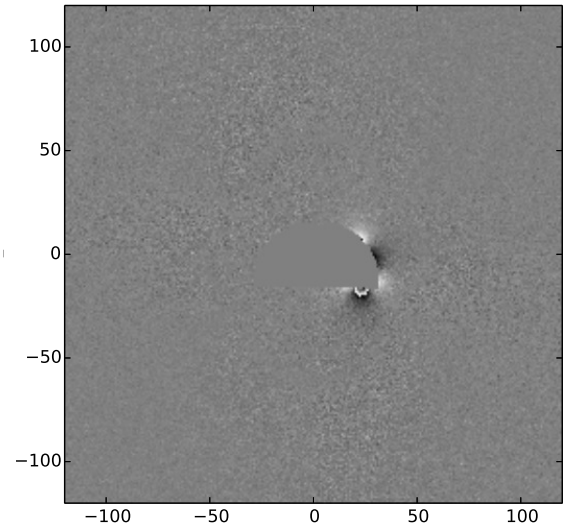

Figure A.7: Wrapped residual with adjusted model offset by $\Delta x = 0.1\,\text{mm}$, $\Delta z = 0.1\,\text{mm}$, and $\Delta\theta_y = -0.3^o$.

Figure A.8: Extracted wrapped phase for the central slice of Phantom 1, with no model.

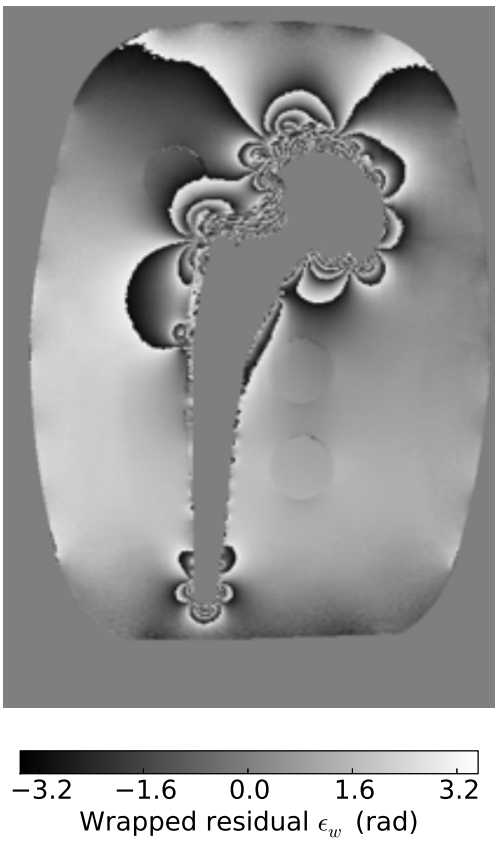

Figure A.9: Wrapped residual for the central slice of Phantom 1, with initial imperfect model.

Figure A.10: Wrapped residual for the central slice of Phantom 1, with adjusted model, shifted from the initial model by $\Delta x = 7$ mm, $\Delta z = 5$ mm, and $\Delta\theta_y = -3^o$.

- In reality, six parameters must be refined to estimate the model which minimises E in three dimensions. Furthermore, in a hip replacement the acetabular liner and shell rotates relative to the femoral head. This introduces three additional parameters to estimate: the 3D orientation of the acetabular component with respect to the femoral component. If the nine parameters are discretised to n values each, there are n^9 possible models to evaluate. The number of affine transformations to perform rapidly explodes, even with low values of n. This method is therefore impractical unless the initial model position and orientation is already well fitted.

  Finally, the metric of the phase unwrapping complexity, E, is a global measure. In reality the model may be well-fitted in some regions of the image but ill-fitted in others. A localised measure such as the density of the phase wraps in small regions may be more useful for iterative model refinement.

A.3 MAVRIC MODEL

The third technique uses the field map acquired during a MAVRIC-SL acquisition to produce a model of the phase shift. This approach does not require any prior knowledge of the implant geometry or position. However, it is necessary that a MAVRIC-SL sequence is run alongside the three-point Dixon technique.

MAVRIC-SL images were acquired for Phantoms 1 and 2. The basic scan parameters, such as the field of view and number of slices, were the same as described in Table 5.1. For both phantoms, 24 MAVRIC bin images were acquired over the following range of discrete resonant frequency offset values,
$\{f_b\} = \{-11000, -10000, ..., 0, ..., 11000, 12000\}$ Hz. The bin width was 1 kHz.

Figure A.11 shows the resonant frequency variation and reconstructed MAVRIC-SL image for the central slice of Phantom 1. The resonant frequency variation was calculated using Eq. 2.21, and was converted to the model phase, ϕ_M, using Eq. 6.1. The residual wrapped phase, $\epsilon_w[x, z]$, was then obtained using Eq. A.3. Figure A.12 shows the residual wrapped phase.

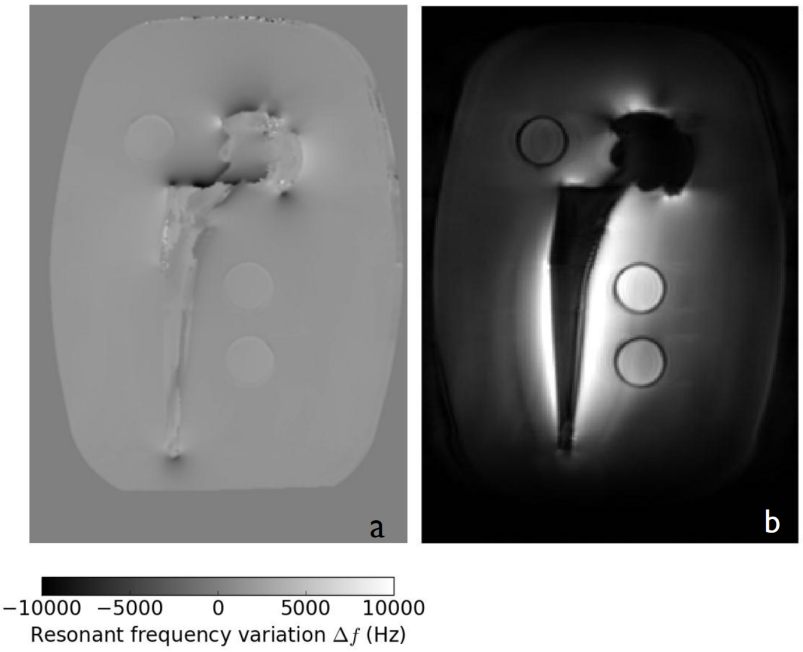

Figure A.11: Reconstructed images for central slice of Phantom 1. a) shows the estimated resonant frequency variation (in hertz) generated during the MAVRIC-SL reconstruction process. Note that the resonant frequency offset in the fat vials (of approximately 440 Hz at 3 T) has not been removed. b) shows the reconstructed MAVRIC-SL image.

The resolution of the MAVRIC resonant frequency variation in Fig. A.11 is limited, as it is calculated using a weighted sum of the discrete $\{f_b\}$ values. The model phase is therefore a discrete approximation to the true phase. This is the likely reason for the "noisy" appearance of the wrapped residual. Also, if this method was to be used in practice, it would be important to ensure that the MAVRIC-SL and the three-point Dixon images were correctly aligned. Any movement between the scans would need to be accounted for.

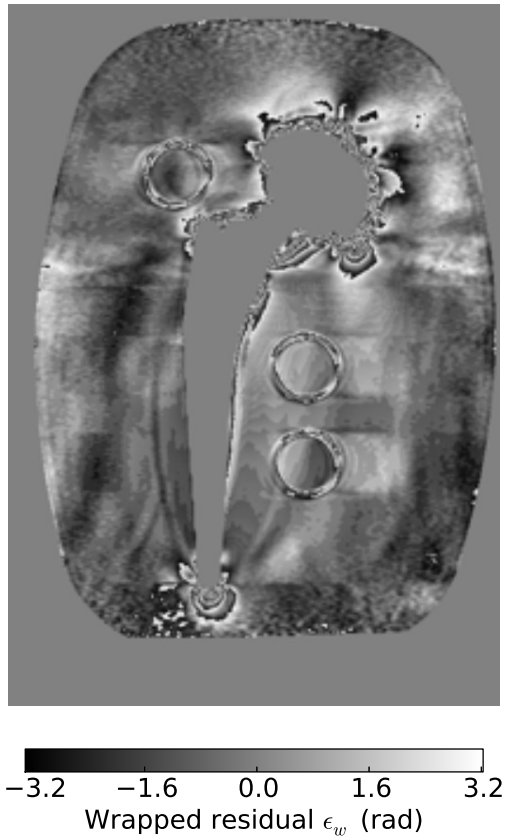

Figure A.12: Wrapped residual for the central slice of Phantom 1, acquired by removing the MAVRIC model phase from the complex data.

A.4 SUMMARY

Three methods for using a model of the phase shift have been described. These have been shown to significantly reduce the complexity of the phase unwrapping required. However, it is important that the model phase is well-fitted to the true phase. A model which is offset in position by just one or two pixels may not reduce the number of phase wraps in regions of steep field gradients near the implant boundary. By Eq. A.3, if the model overestimates the true phase, the number of phase wraps increases. In addition, there are regions of significant signal loss near the implant, so the extracted phase is noisy. In these regions, the model phase has a large magnitude. Removing the model from these regions will not reduce the number of phase wraps. These limitations were the key motivating factors in developing a more sophisticated method for incorporating some degree of prior knowledge in the phase unwrapping process, by modelling the phase with a set of basis functions.

This document was typeset in LaTeX using a combination of the `tufte-style` book template based on the style developed by Edward Tufte, and the `classicthesis` template developed by André Miede. Figures were produced using CorelDRAW, Python's `matplotlib`, and Ti*k*Z.